ATOMIC STRUCTURE
AND NONELECTRONIC PROPERTIES
OF SEMICONDUCTORS

Formation of Selenium-Containing Complexes in Silicon

A. A. Taskin* and E. G. Tishkovskiĭ

Institute of Semiconductor Physics, Siberian Division, Russian Academy of Sciences,
pr. Akademika Lavrent'eva 13, Novosibirsk, 630090 Russia
*e-mail: taskin@thermo.isp.nsc.ru
Submitted November 8, 2001; accepted for publication November 21, 2001

Abstract—The results of studying the formation of selenium-related complexes in silicon are reported. On the basis of analyzing the kinetics of the donor-center formation, the composition of the simplest complexes and the main parameters of their formation were determined. The polymerization process $Se + Se_{n-1} \longleftrightarrow Se_n$ of selenium atoms was analyzed; this analysis made it possible to describe quantitatively the features of in-diffusion of selenium atoms from the implanted region to the crystal bulk. The equilibrium solubility of selenium in silicon is regarded as a result of the formation of monomers with limited concentration in the course of formation of the complexes. © *2002 MAIK "Nauka/Interperiodica".*

1. INTRODUCTION

In the last few decades, silicon doped with chalcogens (sulfur, selenium, or tellurium) has been actively studied. The interest in this system, in addition to the use of these materials in detectors of infrared radiation, is related to the active interaction of impurity atoms in the silicon lattice and the possibility of the detailed study of the process of the formation of complexes (stable associations) containing chalcogen atoms.

A number of special features of the system under consideration make it possible to regard this system as a model one in studying the interaction between impurity atoms in solids. First of all, these features include the electrical activity centers related to complexes (at least, the simplest of these complexes). Isolated chalcogen atoms at the silicon lattice sites are doubly charged donors. The ionization energies of their ground states are equal to 0.32 eV (0.61 eV) for S^0 (S^+), 0.30 eV (0.59 eV) for Se^0 (Se^+), and 0.20 eV (0.41 eV) for Te^0 (Te^+) [1–3]. The formation of the main complex being studied (a dimer composed of two chalcogen atoms at the neighboring crystal-lattice sites) also yields a doubly charged donor with a somewhat lower ionization energy: 0.187 eV (0.371 eV) for S_2^0 (S_2^+), 0.206 eV (0.248 eV) for Se_2^0 (Se_2^+), and 0.158 eV for Te_2^0 [2, 3]. Under certain conditions of heat treatment of silicon wafers doped with chalcogens, more shallow donor states with an ionization energy of $\lesssim 0.1$ eV have also been observed; these states are apparently related to the formation of more complex associations [2–7]. The electrical activity of complexes and appreciable distinctions in the ionization energies of the corresponding states make it possible to experimentally determine, easily and reliably, the concentration of complexes of various compositions in the course of their transforma-tion. Another special feature that makes silicon doped with chalcogens attractive for studying the interaction of impurity atoms is the intermediate equilibrium solubility of chalcogen atoms in the silicon lattice. The highest chalcogen solubility amounts to $\sim 10^{17}$ cm^{-3}, which is much higher than the solubility of the majority of metallic elements in silicon but is much lower than the solubility of the main doping impurities (the elements of Groups III and V of the periodic table) in silicon. This circumstance makes it possible to ensure a wide dynamic concentration range of impurities in the crystal for studying the processes of association of defects, starting with low concentrations when the initial stage of formation of complexes is observed and ending with concentrations for which a large degree of supersaturation (exceeding by three–four orders of magnitude the solubility limit) is observed.

Selenium is of the most interest among chalcogens from the standpoint of studying complex formation; the reason is that selenium occupies an intermediate position in the S–Se–Te sequence in all physicochemical properties in silicon (solubility, diffusivity, reactivity, positions of energy levels in the band gap, the degree of matching to the silicon covalent radius, and so on). Previously [8], we reported the results of studying the formation kinetics for Se_2 complexes. The objective of this study was to gain insight into the formation of complexes composed of a larger number of selenium atoms and to determine the composition of these complexes and their role in the establishment of limiting equilibrium concentrations of impurity atoms in the silicon lattice.

2. EXPERIMENTAL

We used ion implantation to dope the silicon wafers with selenium. The 125-keV selenium ions with a dose range of 6×10^{14}–3×10^{15} cm^{-2} were implanted into

wafers of p-Si:B ($\rho = 20\ \Omega$ cm) and also into wafers of n-Si:P ($\rho = 7.5\ \Omega$ cm), p-Si:B ($\rho = 10\ \Omega$ cm), p-Si:B ($\rho = 40\ \Omega$ cm), and floating-zone p-Si:B ($\rho = 20\,000\ \Omega$ cm) through an oxide layer 3- to 50-nm thick. The projected range of selenium ions was no larger than ~0.1 μm. The in-diffusion of selenium was accomplished by heat treatments of various durations at different temperatures.

In order to study the kinetics of formation of the simplest impurity-related complexes containing two, three, or more selenium atoms, we used high-temperature (1200°C) and long-term (up to 76 h) heat treatments to form initial selenium diffusion distributions with doped-layer thicknesses of ~100–300 μm and an impurity concentration no higher than ~10^{17} cm^{-3}. In this situation, almost all of the implanted impurity penetrated into the bulk of the wafers. Variations in the concentrations of the centers related to the complexes containing selenium atoms were measured in the course of additional low-temperature heat treatments (at 550–700°C). The diffusion-induced distribution of selenium atoms preliminarily formed in the starting samples was not much affected by the duration of these heat treatments in the selected temperature range. Distributions of electrically active centers and their concentration and microscopic parameters (ionization energies, degeneracy factors, and so on) were determined from the measurements and analysis of temperature dependences of the Hall voltage and electrical conductivity using layer-by-layer etching of silicon according to previously reported methods [8].

In order to study both the spatial redistribution of selenium atoms from implanted layers into the sample bulk and the establishment of limiting equilibrium concentrations of impurity atoms in the silicon lattice, we subjected a number of wafers (immediately after implantation) to heat treatments for $t = 10$, 50, and 120 min at $T = 1200$, 1100, and 1050°C. As a result of these treatments, the major portion of impurity atoms remained in the implanted region (within ~0.1 μm from the surface), whereas 1–4% of implanted atoms penetrated into the bulk. The temperatures and durations of heat treatments were chosen so that the thicknesses of the doped layers were the same for all samples in this series. In addition to studying the spatial distribution of electrically active centers in these experiments (see above), we used secondary-ion mass-spectrometry (SIMS) to determine the spatial distribution of selenium atoms in the samples (the method used has been described in detail elsewhere [9]).

3. RESULTS AND DISCUSSION

3.1. The Complex-Formation Kinetics

As has been shown previously [8], low-temperature heat treatments of silicon wafers give rise to three types of donor centers, C_1, C_2, and C_3, with ionization energies that correspond to the transition from the neutral to the singly charged state and are equal to 0.3, 0.2, and 0.13 eV, respectively. It has also been shown [8] that the following quantity remains unchanged when the concentration of the centers varies in the temperature range of 670–1000°C:

$$N_{s1} + 2N_{s2} + 3N_{s3} = N_{s0}. \qquad (1)$$

Here, N_{s1}, N_{s2}, and N_{s3} are the total number of centers C_1, C_2, and C_3 (expressed in atoms per square centimeter), respectively.
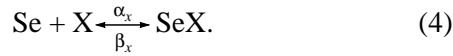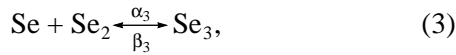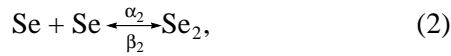
In [8], much attention was concentrated on studying the mutual transformations of the C_1 centers corresponding to isolated selenium atoms in the silicon lattice and the C_2 centers corresponding to two selenium atoms at two neighboring lattice sites. The conditions for the predominant formation of these centers were formulated in [8] and amounted to the following: the implantation dose should be no higher than ~1.5×10^{15} cm^{-2}, and the temperature of additional heat treatments should be no lower than ~670°C.

In this study, we are interested in the characteristics of the formation of the C_3 centers, whose buildup to appreciable concentrations in the samples under investigation was observed at temperatures below 650°C.

In Fig. 1, we show variations in the total (or sheet) concentration (N_s) of the C_1, C_2, and C_3 centers in the course of isothermal annealing at a temperature of 600°C. Similar kinetic curves were also obtained after heat treatments at other temperatures in the range $T = 550$–700°C.

It is characteristic of all studied samples that the concentration of the C_1 centers decreases, whereas the concentration of the C_2 and C_3 centers increases as a result of heat treatments. Steady-state concentrations of the centers are attained in all samples; i.e., a further increase in the heat-treatment duration does not result in an increase in the concentrations of the centers. The time needed to attain the steady state of the centers increases as the temperature of the isochronous heat treatment decreases and can be as long as ~150 h at a temperature of 550°C. Condition (1) is approximately satisfied for all samples, although a slight decrease in N_{s0} as the isochronous-annealing temperature is lowered is observed (this decrease may amount to ~25% at a temperature of 550°C). A repeat short-term (for no longer than 5 min) annealing of the samples at a temperature of 1200°C results in a return to the initial ratio between the concentrations of the observed donor centers. The aforementioned special features of the kinetics of donor-center formation make it possible to suggest (as was done previously [8] for the reaction of formation of a Se$_2$ quasi-molecule) the following scheme of quasi-chemical reactions for the formation and

decomposition of impurity complexes responsible for the emergence of the above centers:

$$\text{Se} + \text{Se} \underset{\beta_2}{\overset{\alpha_2}{\rightleftarrows}} \text{Se}_2, \qquad (2)$$

$$\text{Se} + \text{Se}_2 \underset{\beta_3}{\overset{\alpha_3}{\rightleftarrows}} \text{Se}_3, \qquad (3)$$

$$\text{Se} + \text{X} \underset{\beta_x}{\overset{\alpha_x}{\rightleftarrows}} \text{SeX}. \qquad (4)$$

Here, α_2, α_3, α_x and β_2, β_3, and β_x are phenomenological constants, which account for the rates of direct and reverse reactions and are independent of the concentrations of reacting components. Reactions (2) and (3) describe the successive attachment of the mobile component (selenium atoms at the lattice sites), which gives rise to Se_2 and Se_3 complexes, respectively. Reaction (4) describes the observed decrease in N_{s0} in (1) in the course of heat treatments as a result of the formation of a neutral C_x center, and it is written in the form accounting for the interaction of a selenium atom with a component of unknown nature, i.e., an uncontrolled-impurity atom in silicon (C, O, N, and such), a structure defect, and so on.

A system of differential equations corresponding to the scheme of reactions (2)–(4) can be solved numerically. In the absence of a significant diffusion-related spread in the starting profile of atoms in the course of heat treatment, this system of kinetic equations represents the Cauchy problem with the initial conditions corresponding to the distribution of donor centers in the sample immediately after the high-temperature and long-term heat treatments. In order to solve this problem, the Runge–Kutta method of the fourth order has been used [10]. The obtained solutions were checked using *a posteriori* Runge–Romberg estimates of accuracy [11] for a series of condensed and sparse grids. In Fig. 1, the solid lines represent the results of calculating the kinetics of interconversion for the C_1, C_2, and C_3 centers at a temperature of 600°C. The adjustable parameters in the calculation were the rates of the direct and reverse reactions α_2, α_3, α_x, β_2, β_3, and β_x. As can be seen from Fig. 1, there is good agreement between the results of calculation and experimental data. For each temperature of heat treatment, we determined the rates of the direct and reverse reactions, which correspond to the best agreement between the calculated and experimental kinetic curves.

3.2. Equilibrium Constants for Reactions of Complex Formation

The reaction-rate constants α_i and β_i govern the entire run of the kinetic curves, including the section that describes the steady state of the reactants in the system. If the steady state of the system corresponds to the equilibrium state, the concentrations of reactants can be described in terms of equilibrium constants for the reactions proceeding in the system. According to
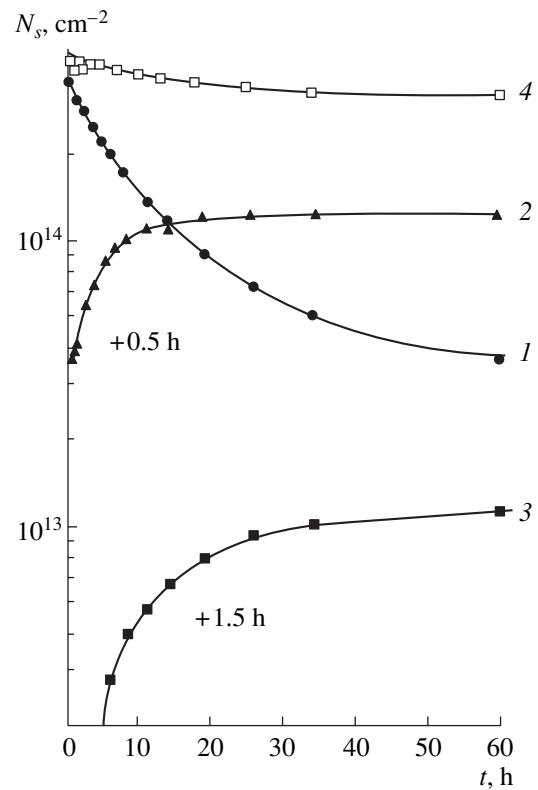

Fig. 1. Kinetics of interconversion of the C_1, C_2, and C_3 centers at a temperature of 600°C: (*1*) the sheet concentration of C_1 centers; (*2*) the sheet concentration of C_2 centers; (*3*) the sheet concentration of the C_3 centers; and (*4*) the sum of sheet concentrations of the centers $N_{s1} + 2N_{s2} + 3N_{s3}$. The selenium implantation dose was 1.2×10^{15} cm^{-2}; the in-diffusion was performed for 24 h at 1200°C.

the theory of molecular-reaction kinetics [12], the ratio between the rates of the direct (α_i) and reverse (β_i) reactions is equal to the equilibrium constant K_i of this reaction; i.e.,

$$K_i = \alpha_i / \beta_i. \qquad (5)$$

Another method for determining the equilibrium constants for reactions (2)–(4) is based on the analysis of the spatial distribution of steady-state concentrations of donor centers in the samples. If the steady-state concentrations of the centers correspond to the locally equilibrium concentrations, the equilibrium constants may be defined as the ratios between the concentrations of reactants by using the mass action law, which is valid for diluted solutions of defects [13].

For reaction (2), the equilibrium constant K_2 is equal to

$$\frac{N_2^\infty}{\left(N_1^\infty\right)^2} = K_2, \qquad (6a)$$

where N_1^∞ is the steady-state concentration of isolated selenium atoms C_1 at a specified point of the sample,
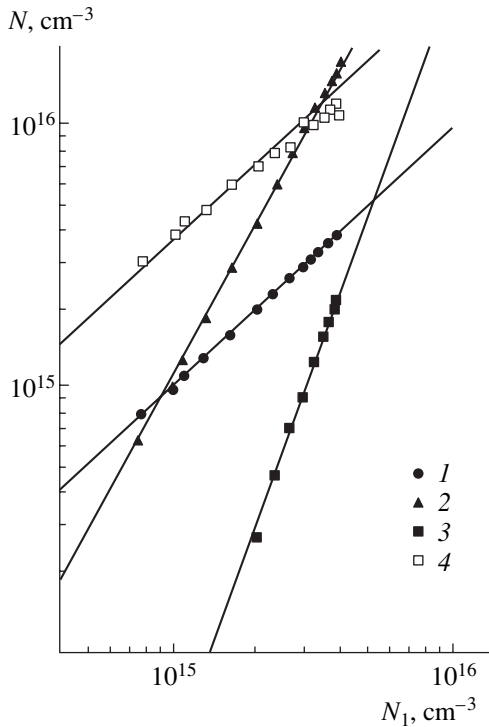
N, cm^{-3}

Fig. 2. Dependences of concentrations of various centers on the concentration of centers C_1: (*1*) C_1, (*2*) C_2, (*3*) C_3, and (*4*) C_x. The implantation dose was 1.2×10^{15} cm^{-2}; the in-diffusion of selenium was performed for 24 h at 1200°C; an additional annealing was performed for 60 h at 600°C.

and N_2^∞ is the steady-state concentration of centers C_2 at the same point.

For reaction (3), the equilibrium constant K_3 is given by

$$\frac{N_3^\infty}{N_1^\infty N_2^\infty} = K_3, \qquad (6b)$$

where N_3^∞ is the steady-state concentration of centers C_3.

For reaction (4), the equilibrium constant K_x is equal to

$$\frac{N_x^\infty}{N_1^\infty (N_x^{tot} - N_x^\infty)} = K_x, \qquad (6c)$$

where N_x^∞ is the steady-state concentration of centers C_x and N_x^{tot} is the total concentration of component X at a specified point of the sample.

As can be seen from dependences (6a)–(6c), the concentration of complexes consisting of two selenium atoms is proportional to the squared concentration of isolated selenium atoms, the concentration of complexes composed of three selenium atoms is proportional to the cubed concentration of isolated selenium atoms, and the concentration of neutral centers contain-

ing a single selenium atom depends linearly on the concentration of isolated selenium atoms if the latter concentration is not too high ($K_x N_1^\infty \ll 1$).

Since silicon wafers were doped using the drive-in diffusion of an impurity, the selenium concentration decreased as the distance from the surface increased. Consequently, experimental data on the steady-state concentrations of the centers under consideration at various points of the diffusion profile make it possible to verify the dependences given by (6a)–(6c).

In Fig. 2, the dependences of the concentrations of the centers (N) on the concentrations of isolated selenium atoms (N_1) for a sample annealed for 60 h at a temperature of 600°C are shown on the log–log scale. The slope of the straight line corresponding to the concentrations of C_2 centers is equal to two, the slope of the straight line corresponding to the concentrations of centers C_3 is equal to three, and the slope of the straight line describing approximately the concentrations of centers C_x, calculated as the variation in the sum of concentrations $N_1 + 2N_2 + 3N_3$ in reference to the initial distribution, is equal to unity.

Thus, an analysis of the spatial distribution of steady-state concentrations of the donor centers confirms the presumed composition of the complexes and shows that the equilibrium constants for reactions (2)–(4) under consideration are independent of the concentrations of reactants.

Equations (6a)–(6c) make it possible to use the data on the spatial distribution of steady-state concentrations of the donor centers to determine the numerical values of equilibrium constants for the reactions proceeding in the crystal. The values of equilibrium constants determined from Eqs. (6) coincide with those obtained from an analysis of the formation kinetics for the donor centers as the ratio between the rates of the direct (α_i) and reverse (β_i) reactions in expression (5). For diluted solutions of point defects, the equilibrium constants for the reactions of formation of impurity complexes are given by [13]

$$K_i = K_{i0}\exp\{E_{bi}/kT\}, \qquad (7)$$

where E_{bi} is the energy of the complex formation; T is the temperature at which equilibrium is established; k is the Boltzmann constant; and K_{i0} is a preexponential factor, which depends on the structure of the complex.

The temperature dependences of the equilibrium constants obtained in this study for reactions (2)–(4) have the form described by expression (7); i.e., these dependences fall on a straight line plotted as a graph of $\log(K_i)$ versus $1/kT$. The following values of the formation energies E_{bi} of the complexes were determined from the slopes of the obtained straight lines: 1.4 eV for Se$_2$, 1.15 eV for Se$_3$, and 0.8 eV for SeX.

3.3. Polymerization

The above-considered characteristic features of the formation of Se_2 and Se_3 complexes suggest that complexes of Se_n containing a larger amount of Se can be formed; the corresponding reactions are given by

$$Se + Se_{n-1} \longleftrightarrow Se_n \qquad (8)$$
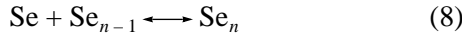
and represent an extension of reactions (2)–(4) (the so-called polymerization of selenium atoms). The formation energy of the Se_n complexes may be estimated as ~1 eV, which is an extrapolation of the formation energies for the Se_2 and Se_3 complexes. This inference is confirmed by quantum-chemical calculations that we performed recently;[1] we have shown that the character of the chemical bonds remains virtually unchanged when complexes containing a larger number of selenium atoms are formed. According to the calculations, selenium atoms occupying the neighboring lattice sites form chemical bonds with the nearest silicon atoms and do not form chemical bonds with each other. A distinction between the Se_2 and Se_3 complexes consists in the fact that both Se atoms in Se_2 have three neighboring Si atoms, whereas one of the Se atoms in Se_3 (the central one) has two neighboring Si atoms and forms with the latter a stronger chemical bond (a bond of higher order). Each successive selenium atom attached to the complex gives rise to an increased number of impurity atoms that have two neighboring silicon atoms.

An exception to the above process is the Se_6 complex, which consists of six impurity atoms that form a complete topological ring. The special feature of the spatial structure of this complex (the presence of only two neighboring silicon atoms for all six selenium atoms) is responsible for the much higher formation energy for this complex (~2 eV) compared with that of spatially nonclosed complexes. In addition, the arrangement of single-electron energy levels of this complex suggests that this complex may have the properties of a neutral center (or a donor with a very deep level).

The equilibrium concentrations of the Se_{n-1} and Se_n complexes in reactions (8) are related by the formula

$$\frac{N_n}{N_1 N_{n-1}} = K_n, \qquad (9)$$

$$K_n = \frac{\xi_n}{N_{Si}} \exp\left\{\frac{E_{bn}}{kT}\right\} \varphi_n(T), \qquad (10)$$

where ξ_n is an integer constant having an order of unity and arising in the calculation of the configurational entropy (see [8]); N_{Si} is the number of silicon lattice sites per unit volume; E_{bn} is the bonding energy of the Se_n complex; and $\varphi_n(T)$ is a factor that depends only slightly on temperature and accounts for the charge

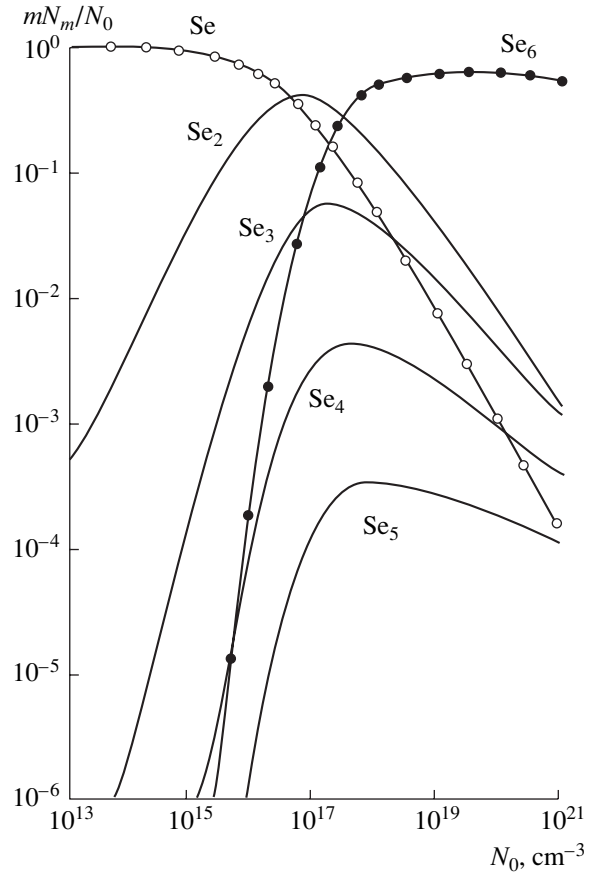[1] The results of these calculations will be reported in our next paper to be submitted to "Semiconductors."

Fig. 3. Fractions of selenium atoms contained in the Se, Se_2, Se_3, Se_4, Se_5, and Se_6 complexes under equilibrium conditions at a temperature of 900°C in relation to the total concentration of selenium atoms in the crystal.

states of defects involved in reaction (8). Taking into account the conservation of the number of selenium atoms involved in the polymerization reactions $N_1 + 2N_2 + 3N_3 + \ldots + nN_n = N_0$ (where n may formally take values as large as N_0), we may write the equation (with $K_1 \equiv 1$)

$$N_0 - \sum_{m=1}^{n}\left[m\left(\prod_{i=1}^{m} K_i\right) N_1^m \right] = 0, \qquad (11)$$

which makes it possible to determine, for a given N_0, the equilibrium concentration of monomers N_1 and, consequently, the concentration of any N_i complexes in the crystal.

Using the above-obtained values for the Se_2 and Se_3 bonding energies and assuming that this energy is equal to 1 eV for all other complexes (except for the Se_6 complex, whose bonding energy E_{b6} is set equal to 2 eV), we can calculate the distribution of selenium atoms over the complexes (mN_m) as a function of the total selenium concentration N_0 (Fig. 3).
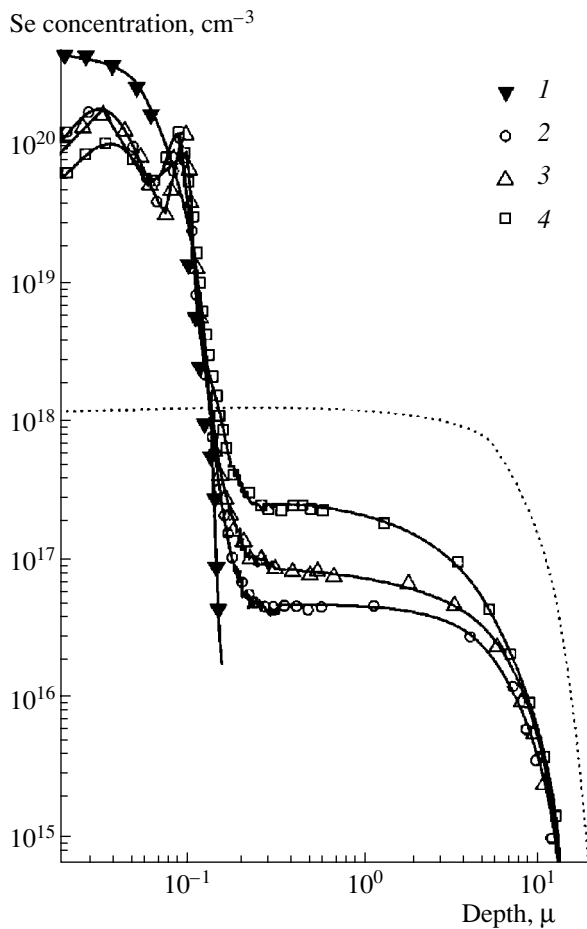
Se concentration, cm^{-3}

Fig. 4. Concentration profiles for selenium atoms (1) after implantation of selenium ions at a dose of 2.5×10^{15} cm^{-2}, (2) after postimplantation annealing for 120 min at 1050°C, (3) after annealing for 50 min at 1100°C, and (4) after annealing for 10 min at 1200°C. The lines represent the results of calculations (see the text for details).

The calculated size distribution of complexes is such that, in the entire range of selenium concentrations, the major portion of selenium atoms resides in the simplest complexes with $n \le 6$. The probability of the formation of a larger size Se$_n$ complex decreases as n increases; as a result, a series in (11) converges rapidly, and the replacement of this series by the sum of its first few terms represents a good approximation. If the concentration of selenium atoms in the crystal is low, almost all of the impurity resides in the lattice as isolated atoms. If the concentration is high, the major portion of impurity atoms is contained in the Se$_6$ complexes. This is caused by the larger bonding energy of Se$_6$ complexes compared to other complexes. In the intermediate region of selenium concentrations, the Se$_n$ complexes containing from two to five selenium atoms are observed in the crystal.

A variation in the annealing temperature does not radically affect the distribution of selenium atoms over the complexes with a different composition; only the concentration range within which we observe the transition from the predominance of isolated Se atoms in the lattice to the prevalence of the spatially closed Se$_6$ complex is shifted. As the annealing temperature is lowered, this transition region is shifted to lower impurity concentrations.

3.4. Spatial Redistributions

As follows from the obtained estimates, experimental observation of complexes containing more than three selenium atoms is very difficult in the layers with a total selenium concentration lower than 10^{17} cm^{-3} (see Fig. 3). It may be expected that these complexes will be detectable if the selenium atom concentration is no lower than 10^{18} cm^{-3}.

As has been shown previously [8], as a result of the comparatively low solubility of selenium in silicon ($\sim 10^{17}$ cm^{-3}), a spatial distribution with such a high impurity concentration can be attained only in the surface region of the crystal (Fig. 4).

The total concentration of selenium atoms in the surface regions of the wafers (up to the concentrations of $\sim (2–4) \times 10^{16}$ cm^{-3}) was determined using the SIMS method. In order to reliably determine the low concentrations of selenium atoms with allowance made for gently sloping spatial distributions of impurity atoms in the bulk of the samples, we performed an isotopic analysis in the tails of the distributions; this analysis made it possible to separate in the measurements the desired signal from noise in the range of low impurity concentrations. The concentration of selenium atoms in the bulk of the samples (at a distance from the surface greater than 1 μm) was reconstructed from the results of measuring the Hall voltage and electrical conductivity in the case of the layer-by-layer etching of silicon.

In Fig. 4, we show the selenium concentration profiles in a silicon wafer implanted with selenium ions at a dose of 2.5×10^{15} cm^{-2} and then subjected to heat treatments for 120 min at 1050°C, for 50 min at 1100°C, and for 10 min at 1200°C. It is noteworthy that the scale of the horizontal (depth) axis is logarithmic. The width of spatial distributions in the sample bulk (~ 14 μm) exceeds the width of similar distributions in the surface region (~ 0.1 μm) by about two orders of magnitude. The portions of the profiles caused by the diffusive transport of selenium atoms (the depths larger than 0.1 μm) have a shape characteristic of the diffusion of an impurity whose concentration is bounded from above. The limiting concentrations corresponding to these portions of the profiles in Fig. 4 are equal to 2.5×10^{17} cm^{-3} for 1200°C, 9×10^{16} cm^{-3} for 1100°C, and 5×10^{16} cm^{-3} for 1050°C. It is noteworthy that a change in the concentration of selenium atoms in the implanted region induced by a wide variation in the implantation dose results only in a slight change in these concentration levels.

An analysis of the contribution of the surface layer (up to a depth of 0.1 μm), in which most of the implanted impurity is concentrated, to the electrical conductivity of the sample shows that selenium atoms in this layer are hardly involved in the formation of electrically active complexes; as a result, the electron concentration in this layer is much lower than the concentration of selenium atoms. At the same time, Rutherford backscattering spectroscopy [14] indicates that, after recrystallization of the implantation-damaged layer, most of the selenium atoms (>80%) reside at the lattice sites. On the basis of the trends evident in Fig. 3, we may assume that a major portion of the selenium atoms in this layer are involved in a chain of polymerization reactions with the eventual formation of neutral centers.

In order to study the possibility of forming neutral centers and gain insight into the kinetics of accumulation of these centers, we should use sufficiently high heat-treatment temperatures, so that the implantation-damaged layer is recrystallized, radiation defects are annealed out, and the impurity is activated. At the same time, the temperatures should be low enough in order to prevent both the appreciable diffusion-related penetration of the impurity into the sample bulk and the related increase in electron concentration in the conduction band; the latter process is the opposite to that of a decrease in the charge-carrier concentration due to the formation of neutral centers in the implanted layer. The temperature range of 700–800°C satisfies the above conditions.

The kinetics of neutral-center formation was studied in the course of isothermal annealing of the samples at a temperature of 800°C; the samples were first implanted with selenium ions at a dose of 1.2×10^{15} cm^{-2} and were then annealed for 4 h at a temperature of 700°C. The total concentration of selenium atoms in the layers under investigation was measured using the SIMS method (see the inset in Fig. 5).

In Fig. 5, the triangles and blackened squares represent a decrease in the conduction-electron concentration relative to the initial electron concentration in the sample $(n_0 - n)/n_0$ as observed in the course of annealing at a temperature of 800°C. The experimental temperature dependences of electrical conductivity and the Hall voltage feature behavior typical of heavily doped semiconductors, i.e., the absence of activation energy for the donor centers and low mobility of free charge carriers (~20–40 cm^2 V^{-1} s^{-1}). In this situation, contributions of different centers to the total electrical conductivity cannot be separated. The fraction of the impurity penetrating into the sample bulk owing to diffusion is insignificant (no larger than 0.1% of the total number of atoms); consequently, a change in the electrical conductivity of the samples is wholly caused by the surface region of crystal.

Thus, the following special features are observed in the experimental studies of spatial distributions of
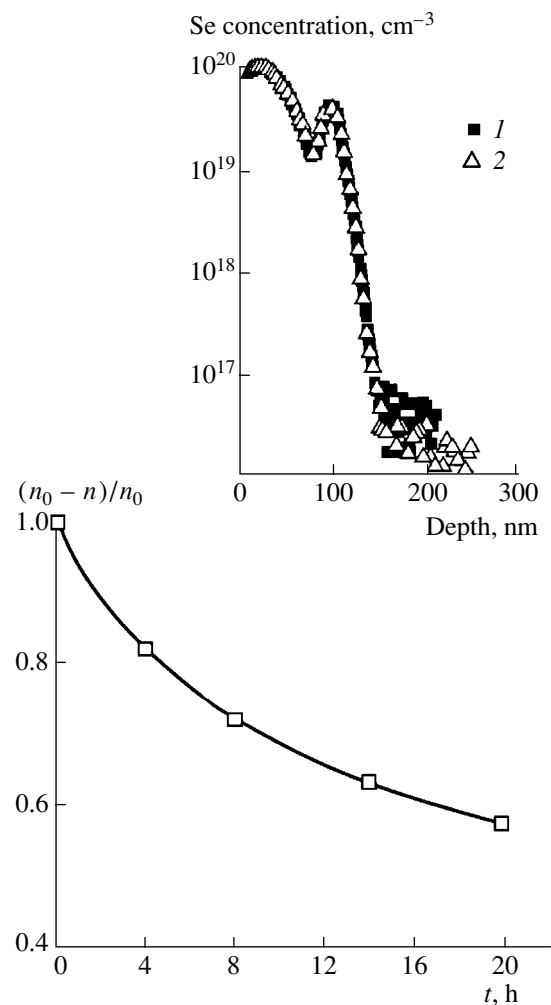

Fig. 5. Variation in the concentration of conduction electrons in the course of annealing at a temperature of 800°C in reference to the electron concentration in the starting silicon sample. The latter was obtained by implantation of selenium ions at a dose of 1.2×10^{15} cm^{-2} with subsequent annealing for 4 h at 700°C. The total concentration of selenium atoms in the sample after (*1*) 10 min and (*2*) 20 h of annealing at 800°C is shown in the inset.

impurity atoms in the crystals with a high selenium concentration (~10^{20} cm^{-3}) in the surface region: (i) formation of limiting concentrations as a result of diffusion-related penetration of selenium into the crystal bulk and (ii) formation of a high concentration of neutral centers in the surface region.

The observed patterns in the spatial distributions of selenium atoms can be naturally explained in the context of the above-considered polymerization model if it is assumed that the formed complexes are immobile (or have low mobility) in the silicon lattice and that the Se$_6$ complexes are neutral centers.

A decrease in the concentration of mobile charge carriers (Fig. 5) in the surface region of the crystal upon increasing the duration of annealing is caused in the
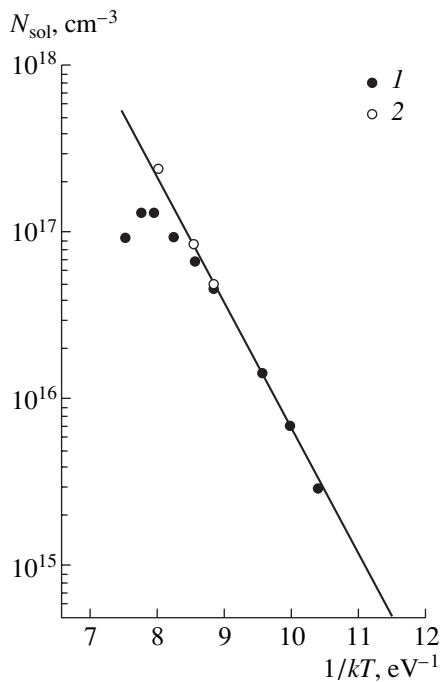
Fig. 6. Temperature dependence of selenium solubility in silicon: (*1*) the data reported in [20] and (*2*) the data obtained in this study.

model under consideration by the formation of Se_6 neutral complexes. In Fig. 5, the solid line represents the results of calculating the accumulation kinetics for these complexes in the course of annealing at a temperature of 800°C. The best fit of the results of the calculations to experimental data (Fig. 5) is obtained for the following values of the rate constants for the formation and dissociation of the Se_6 complexes: $\alpha_6 = 5 \times 10^{-21}$ cm³/s and $\beta_6 = 5 \times 10^{-9}$ s⁻¹. Attempts at interpreting the observed decrease in the concentration of mobile charge carriers on the assumption that neutral SeX complexes are formed according to reaction (4) fail for the following reasons. First, based on the rates of formation (α_x) and dissociation (β_x), the formation of SeX centers at a temperature of 800°C should proceed at a much higher rate than the observed charge-carrier removal rate. Second, estimations of the largest decrease in the conduction-electron concentration in the sample due to the formation of SeX complexes yield a value no larger than 10% of the selenium atom concentration, which is much less than the variations observed experimentally.

High concentrations of Se_6 complexes in the surface regions of the crystal play an important role in the attainment of limiting concentrations in the course of diffusion-induced penetration of the impurity into the crystal bulk. Since the major portion of the impurity is concentrated in the Se_6 complexes in the course of complex formation at high concentrations of impurity atoms (see Fig. 3), the concentration of other complexes in this region (also including mobile monomers)

is much lower than the total impurity concentration; i.e., the concentration of other complexes is limited.

If the concentration of monomers differs from that specified above in the neighboring regions of the crystal, a diffusion flow of impurity arises; as a result, the concentration of monomers changes at the point under consideration. The complexes tend to compensate the deficit or excess of isolated atoms and thus have to dissociate or form in order to restore the equilibrium distribution. Correspondingly, the concentrations of complexes of various compositions also change. Since immobile complexes (largely, Se_6) in the surface region contain a large amount of the impurity, exceeding the amount of monomers by 3–4 orders of magnitude, dissociation of multiatomic complexes can ensure that the concentration of monomers is constant in this region for a long time. The above-described process is similar to diffusion from a source with unlimited strength.

In Fig. 4, the solid lines represent the results of simulating the diffusion of selenium atoms from the surface layer; these results were obtained by numerically solving the coupled set of differential equations that describe the diffusion of monomers and the reactions of formation and dissociation for the Se_6 complexes. Good quantitative agreement is observed between the calculated profiles and the experimentally determined spatial distributions of selenium atoms. It is also possible to reproduce in calculations the observed temperature dependence of the limiting concentrations for the diffusion of impurity atoms into the bulk of the samples. For the sake of comparison, the dotted line in Fig. 4 represents a hypothetical profile, identical for all three annealing temperatures (in accordance with the chosen durations of anneals), which should be expected if all selenium atoms in the surface region are in the state of mobile monomers. An important condition that allows simulations to reproduce a difference amounting to three-to-four orders of magnitude in the concentrations of impurity atoms in the bulk and in the surface region of the samples consists in the larger bonding energy of the Se_6 complex compared to other complexes.

3.5. Solubility

The experimentally observed special features of the spatial distributions of impurity atoms in studies of diffusion in semiconductors (i.e., the formation of wings and kinks in the profiles of impurities of Groups III and V in silicon) are often used to quantitatively assess the solubility of these impurities in a crystal [15–17].

An analysis of the diffusion of selenium atoms from an implanted-layer source into the silicon bulk shows that the limitation imposed on the concentration of selenium atoms introduced into the crystal from the surrounding medium is related to the constraint on the concentration of isolated atoms (monomers) as a result of the formation of selenium-containing complexes of various composition (mainly, the Se_6 complexes for

high selenium concentrations). This means that the solubility of selenium atoms in silicon may be governed to a great extent by the processes of complex formation which are considered in this study.

The temperature dependence of the solubility of impurities in semiconductors is conventionally described by the following thermodynamic relation [13]:

$$N_{\text{sol}} = N_{\text{Si}} \exp[\Delta s/k] \exp[-\Delta h/kT]. \qquad (12)$$

Here, the solubility is governed by the enthalpy (Δh) and entropy (Δs) of mixing. Differences in the chemical nature and in the solubility mechanisms for various chemical elements in a crystal are inherent in these two thermodynamic quantities.

When devising microscopic models of solubility [18, 19], typically one has to consider the processes of incorporation of an impurity atom into the crystal lattice and, consequently, to take into account the formation of chemical bonds with lattice atoms, the elastic stresses introduced by a foreign atom into the crystal, and other factors; at the same time, precipitation and complex formation are considered in relation to the established solubility limit. In a system of silicon doped with selenium, a major role in establishing the limiting concentration of impurity atoms is apparently played by the complex-formation processes.

In Fig. 6, we show the temperature dependences of limiting concentrations of selenium atoms in silicon according to the published data on the activation of donor centers at various temperatures [20] and according to our SIMS data on limiting concentrations of selenium atoms deep inside the samples at temperatures of 1050, 1100, and 1200°C (the origin of the $1/kT$ axis corresponds to the silicon melting temperature). The temperature dependence of the solubility of selenium atoms in silicon is linear if plotted in appropriate coordinates. It corresponds to dependence (12) for the solubility of impurity atoms at lattice sites; i.e.,

$$N_{\text{solSe}} = N_{\text{Si}} 2 \exp[-1.65 \text{ eV}/kT]. \qquad (13)$$

An analysis of the temperature dependences of concentrations of isolated selenium atoms N_1 calculated using the aforementioned estimates for bonding energies of complexes shows that the dependences $N_1(T)$ are exponential and have a slope of ~1.4 eV. This means that the contribution of complex formation to the enthalpy of dissolution of these impurities can be as large as 85%.

4. CONCLUSION

Thus, we reported the results of studying the processes of formation of selenium-containing complexes in silicon.

We analyzed the kinetics of formation of donor centers and identified the composition of the simplest complexes Se_2 and Se_3 as well as the composition of the SeX neutral complex. We also determined the formation parameters of these complexes, i.e., the rates of reactions of formation and dissociation and the formation energies (1.4 eV for Se_2, 1.15 eV for Se_3, and 0.8 eV for SeX). We analyzed the process of polymerization for selenium atoms in silicon $Se + Se_{n-1} \longleftrightarrow Se_n$ and showed that a selenium concentration exceeding ~10^{18} cm^{-3} is needed for the observation of complexes containing more than three selenium atoms. We studied the diffusion of selenium atoms from the surface region of a crystal, where a selenium concentration of ~10^{20} cm^{-3} was introduced using ion implantation with subsequent heat treatment; we showed that the penetration of an impurity into the crystal bulk is bounded from above by the limiting concentration, which is temperature-dependent. We also studied the kinetics of formation of neutral centers in the surface regions of a crystal at a temperature of 800°C.

We showed that both the kinetics of formation of neutral centers in the surface regions of the crystal and the special features of selenium diffusion from the surface region into the crystal bulk can be described assuming that the complex Se_6 plays a specific role in the processes of redistribution of selenium atoms; this complex is topologically closed, electrically neutral, and has a higher formation energy compared to other complexes.

The ascertained laws of the spatial redistributions of impurity atoms make it possible to consider the equilibrium solubility of selenium atoms in silicon as a result of the attainment of a certain concentration level of monomers in the course of formation of the complexes.

REFERENCES

1. E. Janzen and H. G. Grimmeiss, J. Phys. C **15**, 5791 (1982).

2. E. Janzen, R. Stedman, G. Grossmann, and H. G. Grimmeiss, Phys. Rev. B **29**, 1907 (1984).

3. E. Janzen, G. Grossmann, R. Stedman, and H. G. Grimmeiss, Phys. Rev. B **31**, 8000 (1985).

4. S. D. Brotherton, M. J. King, and G. J. Parker, J. Appl. Phys. **52** (7), 4649 (1981).

5. H. G. Grimmeiss and E. Janzen, Mater. Res. Soc. Symp. Proc. **14**, 33 (1983).

6. V. Kalyanaraman, M. M. Chandra, and V. Kumar, J. Appl. Phys. **54**, 6417 (1983).

7. N. Sclar, J. Appl. Phys. **52**, 5207 (1981).

8. A. A. Taskin and E. G. Tishkovskiĭ, Fiz. Tekh. Poluprovodn. (St. Petersburg) **32**, 1306 (1998) [Semiconductors **32**, 1162 (1998)].

9. A. A. Taskin, B. A. Zaĭtsev, V. I. Obodnikov, and E. G. Tishkovskiĭ, Fiz. Tekh. Poluprovodn. (St. Petersburg) **34**, 318 (2000) [Semiconductors **34**, 312 (2000)].

10. A. A. Samarskiĭ, *The Theory of Difference Schemes* (Nauka, Moscow, 1983).

11. N. N. Kalitkin, *Numerical Methods* (Nauka, Moscow, 1978).

12. C. W. Gardiner, *Handbook of Stochastic Methods for Physics, Chemistry, and the Natural Sciences* (Springer-Verlag, Berlin, 1985; Mir, Moscow, 1986).

13. S. V. Bulyarskiĭ and V. I. Fistul', *Thermodynamics and Kinetics of Interacting Defects in Semiconductors* (Nauka, Moscow, 1997).

14. N. N. Gerasimenko, B. A. Zaĭtsev, V. S. Kulikauskas, *et al.*, in *Proceedings of the All-Union Conference "Ion-Beam Modification of Materials", Kaunas, 1989*, p. 56.

15. D. Nobili, S. Solmi, A. Parisini, *et al.*, Phys. Rev. B **49**, 2477 (1994).

16. A. Istratov, C. Flink, H. Hieslmair, *et al.*, Phys. Rev. Lett. **81**, 1243 (1998).

17. M. B. Huang and I. V. Mitchell, J. Appl. Phys. **85**, 174 (1999).

18. K. Weisser, J. Phys. Chem. Solids **7**, 118 (1958).

19. K. Weisser, J. Phys. Chem. Solids **17**, 149 (1960).

20. H. R. Vydyanath, J. S. Lorenzo, and F. A. Kroger, J. Appl. Phys. **49**, 5928 (1978).

Translated by A. Spitsyn

ATOMIC STRUCTURE
AND NONELECTRONIC PROPERTIES
OF SEMICONDUCTORS

Growth of Diamond Films on Crystalline Silicon by Hot-Filament Chemical Vapor Deposition

M. V. Baĭdakova*, A. Ya. Vul'*, V. G. Golubev*, S. A. Grudinkin*,
V. G. Melekhin*, N. A. Feoktistov*, and A. Krüger**

* Ioffe Physicotechnical Institute, Russian Academy of Sciences,
Politekhnicheskaya ul. 26, St. Petersburg, 184021 Russia

e-mail: grudink@gvg.ioffe.rssi.ru

** Toyohashi University of Technology, Toyohashi, 4418580 Japan

Submitted December 25, 2001; accepted for publication December 28, 2001

Abstract—The effect of hot-filament chemical vapor deposition conditions on the phase composition of diamond films grown on a silicon substrate was studied. The growth conditions providing the highest content of diamond phase at a growth rate of about 1 μm/h were ascertained. © *2002 MAIK "Nauka/Interperiodica".*

INTRODUCTION

Much attention has been given in recent years to the vapor-phase heteroepitaxy of diamond films on various substrates, because such films are very promising in a large variety of practical applications and are used for the preparation of wear-resistant and anticorrosive coatings in mechanical tools, protective and antireflective coatings for optical elements in visible and infrared light, and radiation-resistant detectors of radiation; for packaging of electronic microcircuits; and for manufacturing cold electron emitters and masks for X-ray lithography [1, 2]. Such a wide use of diamond films is due to their high thermal conductivity, chemical stability, and the wide band gap of diamond.

At present, diamond films are grown mainly by two modifications of vapor-phase deposition (VPD): hot filament chemical vapor deposition (HFCVD) and plasma-enhanced chemical vapor deposition (PECVD).

Since the growth of diamond films by vapor-phase deposition occurs at thermodynamically metastable conditions for the formation of diamond, the low growth rate and the competing process of the formation of sp^2-bonded carbon (graphite phase) are the main technological problems. The studies on VPD technology are aimed for the most part at attaining the largest fraction of sp^3-bonded carbon (the fraction of the diamond phase) and at increasing the growth rate of the films. Some additional requirements imposed on the technology are dictated by the fields of application of diamond films. For example, films with low roughness are required for optical coatings, while the main requirements for abrasive instruments are high adhesion and strength.

The aim of this study is to determine the parameters of HFCVD which provide for the growth of diamond films with the highest content of diamond phase and a growth rate no lower than 1 μm/h.

The HFCVD method was chosen because the growth rate of diamond films by this method is an order of magnitude higher than that by the PECVD method. [1]. In addition, the HFCVD method allows for the growing of diamond films with a large area and uniform thickness [3]. For example, such diamond films on silicon, which have a low transverse electrical conductivity and a high heat conductivity, can be used as a heat sink in the manufacturing of integrated microcircuits [2].

EXPERIMENTAL

The diamond films were obtained by HFCVD from a hydrogen–methane mixture. The gaseous mixture is supplied to the reactor, where methane and molecular hydrogen decompose near a heated filament into radicals and atomic hydrogen, respectively (Fig. 1). Methane also decomposes by interacting with atomic hydrogen. The film is formed from the carbon-containing radicals that reach the substrate surface. The growing film in the process of HFCVD contains carbon both in sp^3- (diamond) and sp^2-bonded states (graphite, amorphous carbon). As shown in [4], the dominant contribution to the growth of the diamond phase comes from CH_3 radicals. Because the etching rate by atomic hydrogen of sp^2-bonded carbon is much higher than that of sp^3 carbon, one can choose the parameters of deposition so that the etching rate of the nondiamond phase is greater than its growth rate [1]. The effect of atomic hydrogen consists also in the saturation of dangling bonds on the film surface. The typical parameters of the HFCVD process in our case were the following: the substrate temperature was 650–850°C; the pressure in the chamber, 12–50 Torr; the relative content of
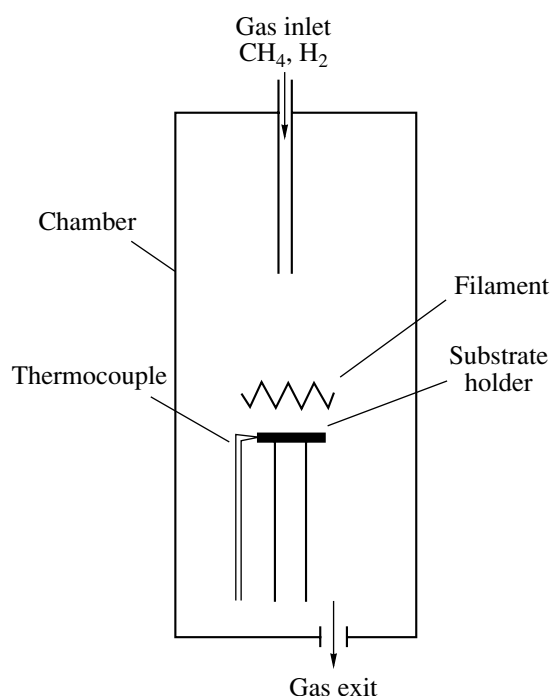
Fig. 1. Schematic diagram of a chamber for vapor-phase deposition of diamond films.

methane in the mixture, 0.5–2.5%; the gas flow rate, 100–500 sccm; and the filament temperature, 2000–2200°C.

The filament used for the dissociation of methane and hydrogen was made of a tungsten wire 0.8 mm in diameter. Prior to letting in the gas, the reactor was evacuated down to a pressure of 10^{-2} Torr. The volume of the reactor was 24 l. The temperature of the filament was measured by an optical pyrometer. The substrate holder was made of a molybdenum disk 3 mm in thickness and 20 mm in diameter. The temperature of the substrate was measured by a Pt–Pt/Rh thermocouple placed in a hole inside the substrate holder. The distance between the filament and the substrate was varied from 8 to 10 mm. A Si(100) single crystal was used as the substrate.

Because of the large difference in the surface energies of diamond (5.3 J/m²) and silicon (1.46 J/m²) [5], the density of nucleation centers of diamond on crystal-

Table 1. Parameters of HFCVD ensuring the highest content of diamond phase in the film grown on a silicon substrate

Substrate temperature	750°C
Pressure	48 Torr
Concentration of methane	1%
Gas flow rate	500 cm³/min (sccm)
Filament temperature	2200°C
Growth duration	5 h

line silicon is no higher than 10^4 cm⁻² [6], which is too small a value for the growth of a continuous film. There are several methods for increasing the density of nucleation centers during epitaxy; one of them involves grinding the substrate with a diamond powder. It was shown in [7] that such grinding gives rise to microscopic defects which stimulate the formation of nucleation centers in diamond during HFCVD. Thus, we utilized this method using commercial diamond powder (ASM 1/2) with a medium grain size of about 1 μm. The substrate was etched for 30 min in 2% solution of hydrofluoric acid to remove the layer of native silicon oxide. Next, the substrate was subjected to ultrasonic treatment with subsequent rinsing in acetone and distilled water. Additional cleaning of the substrate was performed by etching it with atomic hydrogen in the reactor for 20 min at 800°C.

The phase composition of the diamond films was studied by Raman scattering. The Raman spectra were measured using a Ramanor U-1000 monochromator. An argon laser with a radiation wavelength of 488 μm served as the excitation source. The spectral width of the monochromator slit was 5 cm⁻¹. The size of the spot on a sample was about 0.25 mm²; the power of laser radiation did not exceed 90 mW. The measurements were carried out at room temperature.

The structural quality and phase composition of the diamond films were studied using an X-ray single-crystal diffractometer in (θ, 2θ) geometry; CuK_α radiation was used (the wavelength λ = 0.154183 nm). The size of the coherent scattering area was calculated using the Selyakov–Scherrer formula [8].

The density of nucleation centers of diamond and the width and morphology of the diamond film were studied using a JSM 6300 scanning electron microscope (SEM).

RESULTS AND DISCUSSION

An SEM image of the silicon substrate surface ground by the diamond paste at the early stages of growth of the diamond film is shown in Fig. 2. The parameters of the PECVD process (Table 1) were chosen so as to provide the highest content of diamond at a growth rate no lower than 1 μm/h (the details will be explained below). After 15 and 30 min of growth, the substrate becomes covered with separately arranged diamond particles (bright spots in the micrograph), the number of which is determined by the concentration of diamond nucleation centers [9, 10]. The density of nucleation centers on the treated substrate (Fig. 2a) is equal to 10^8 cm⁻², which corresponds to the data obtained in [9, 11, 12]. Some of the diamond particles seen in Fig. 2b are monodisperse. The average growth rate of diamond particles at the stage preceding the formation of a solid film is about 0.5 μm/h. After a time lapse of about 60 min from the beginning of growth, the separate diamond particles coalesce and form a contin-

uous film (dark-and-bright background in Fig. 2c). Separately arranged white formations in Fig. 2c are the diamond particles grown on a continuous film at the sites where the nucleation centers of diamond have locally the highest density.

The phase composition of diamond film is primarily determined by the relative content of methane in the mixture, substrate temperature, and by the pressure in the chamber.

This can be illustrated by the fact that an increase of methane content in the mixture results in an increase of the growth rate both for the diamond and graphite phases; however, the growth rate of the graphite phase increases more rapidly. Since the etching rate of the graphite phase by hydrogen is almost independent of methane content, it increases if the methane content exceeds 2% the fraction of the graphite phase [1]. At a very low (usually less than 0.5%) methane content, a further change of the mixture composition towards the lowering of the methane content has almost no effect on the phase composition of the diamond film and results only in an abrupt drop in its growth rate [13]. An important parameter which also affects the VPD process of diamond film is the characteristic time the gaseous mixture is kept in the reactor; this time depends on the reactor volume. From the published data, it follows that, for the reactor used in our experiments, the content of methane in the mixture should be about 1% in order to ensure a sufficiently high film-growth rate of about 1 μm/h and to obtain a film with a high content of the diamond phase [13]. This concentration of methane was chosen in all our experiments.

Let us briefly discuss the effect of substrate temperature on the diamond phase content in a film. According to a model of carbon film growth by VPD [14], the highest content of diamond phase is attained at the optimal substrate temperature if the following conditions are satisfied:

(i) The growth rate of sp^3-bonded crystalline carbon determined by the concentration of dangling sp^3 bonds on the film surface and dependent on the desorption of hydrogen from the surface should be optimal.

(ii) The etching rate of sp^2-bonded carbon should be higher than its growth rate.

At a temperature higher than the optimal one, the etching rate of sp^2-bonded carbon (graphite) becomes lower than its growth rate, which results in the graphitization of the growing film [1]. When the substrate temperature becomes lower than the optimal one, the condensation of aromatic molecules intensifies; their subsequent decomposition gives rise to amorphous sp^2- and sp^3-bonded carbon [14]. According to numerous studies based on HFCVD technology, the highest content of diamond phase is attained in the temperature range of 500–900°C [1, 3, 13, 15].

Let us consider the effect of pressure in the reactor on the phase composition of a diamond film. As was stated above, the phase composition of a film depends
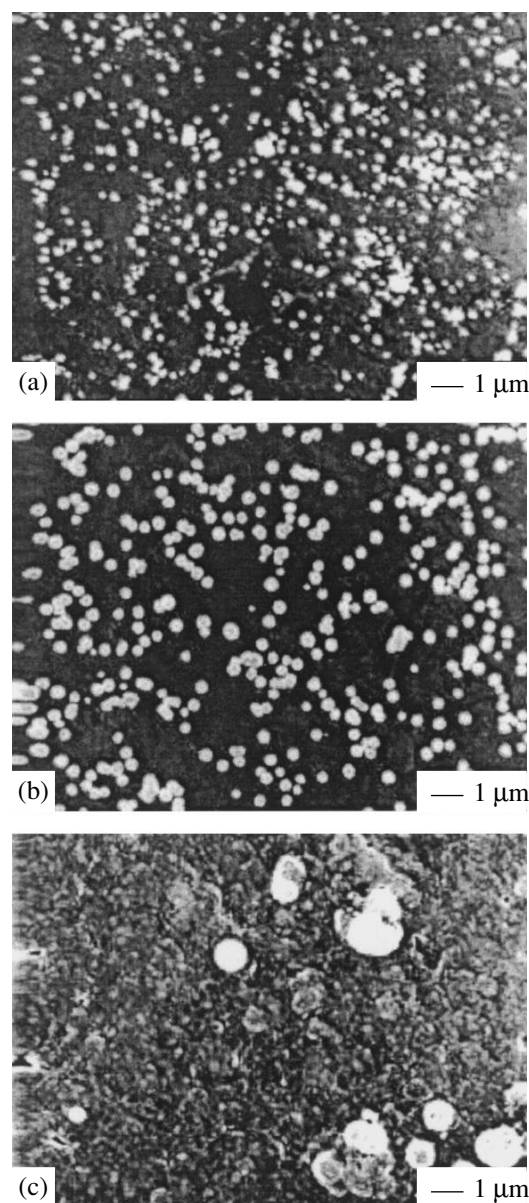

Fig. 2. SEM micrograph of silicon substrate surface after deposition of diamond film using the HFCVD method. The growth duration was equal to (a) 15, (b) 30, (c) 60 min. The parameters of the HFCVD process are shown in Table 1.

on the etching rate of sp^2-bonded carbon. The etching rate, in its turn, increases with increasing atomic-hydrogen concentration near the film surface. The concentration of atomic hydrogen depends on the pressure inside the reactor. At low pressures, the concentration of atomic hydrogen is low because of a deficit of molecular hydrogen. At high pressures, the mean free path of hydrogen atoms decreases, resulting in a decrease in the flux of atomic hydrogen from the filament to the substrate [15]. Thus, in HFCVD technology, there is only a limited pressure range within which films with a high diamond phase content are grown.
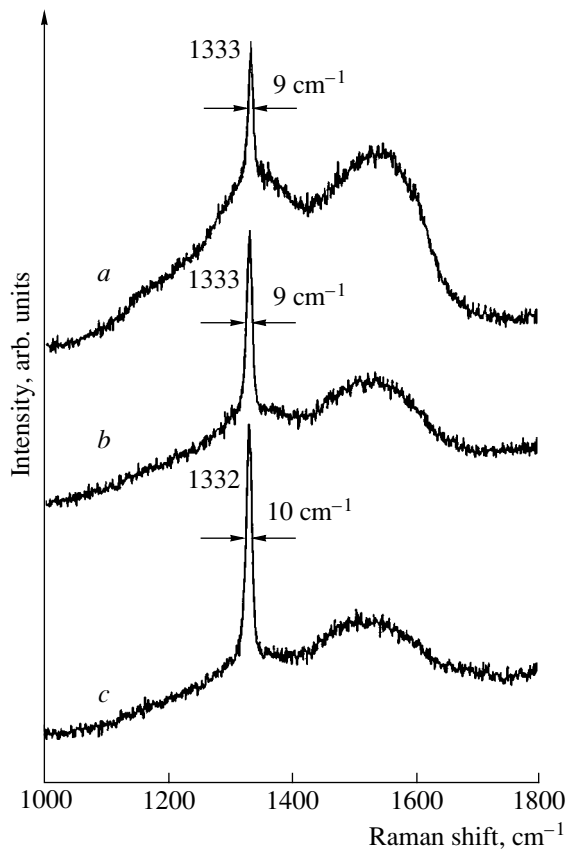
Fig. 3. Raman spectra of diamond films grown at the pressures of (*a*) 12, (*b*) 24, and (*c*) 48 Torr. Parameters of the HFCVD process: substrate temperature is 850°C, concentration of methane amounts to 1%, gas flow rate is 500 sccm, filament temperature is 2200°C, and growth duration is 5 h.

Fig. 4. Raman spectra of diamond films grown at the substrate temperatures of (*a*) 850, (*b*) 750, (*c*) 650°C. Parameters of the HFCVD process: pressure in the chamber is 48 Torr, concentration of methane amounts to 1%, gas flow rate is 500 sccm, filament temperature is 2200°C, and the growth duration is 5 h.

In order to determine the substrate temperature and the pressure of the gaseous mixture in the reactor which ensure that the conditions for the growth of a diamond film are satisfied, two sets of experiments were performed. In each set, such technical parameters as the gas flow rate (500 sccm), the methane content (1%), the filament temperature (2100°C), and the growth duration (5 h) were maintained constant. The first set of experiments consisted in the variation of pressure inside the reactor at a constant substrate temperature (850°C) in order to find the pressure that provides the highest diamond phase content in a film. The pressure thus determined was used in the second set of experiments, which consisted in the variation of the substrate temperature for determining the temperature which corresponds to the growth of the film with the highest diamond phase content. The greatest ratio of the integrated diamond peak to the integrated intensities of "nondiamond" in the Raman spectra was used as a criterion for choosing a film with the highest content of diamond phase lines.

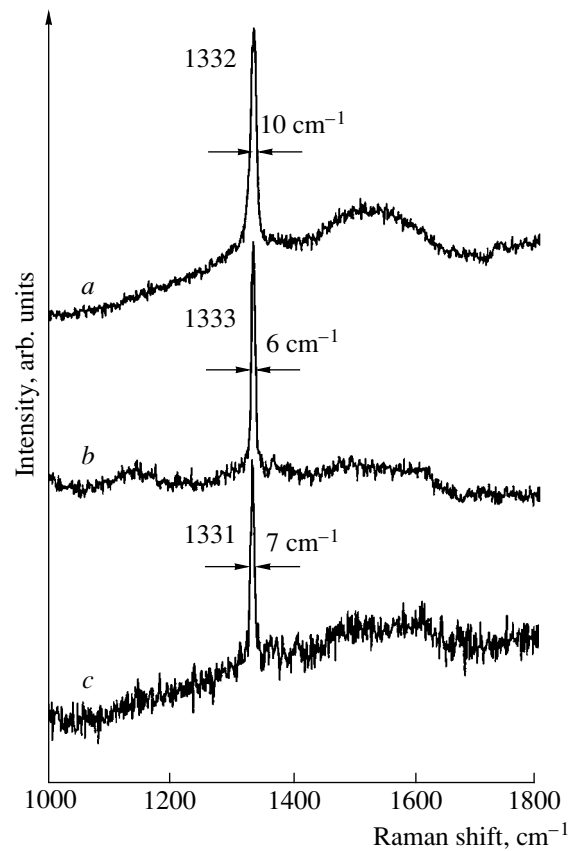The Raman spectra of the diamond films grown under various pressures in the reactor and at various substrate temperatures are shown in Figs. 3 and 4. The main features of these spectra consist in the existence of a narrow peak at a frequency of 1333 cm^{-1}, which is associated with a single-crystal diamond, and a broad peak near 1580 cm^{-1}, which corresponds to sp^2-bonded carbon [5]. A small peak at a frequency of 1150 cm^{-1} observed in some spectra is caused by the presence of a nanocrystalline diamond in the film [16]. A noticeable background signal in the region near 1350 cm^{-1} is associated with nanocrystalline and amorphous graphite [5].

The Raman spectra of diamond films obtained at various pressures in the reactor are shown in Fig 3. The highest diamond phase content is found in the film prepared at 48 Torr (Fig 3, spectrum *c*). In many studies of HFCVD (for example, in [13, 15]), the range of pressures within 20–50 Torr is considered as the optimal one.

The Raman spectra shown in Fig. 4 refer to the films grown at various substrate temperatures and at a pressure of 48 Torr. The highest content of diamond phase is found in the film grown at a substrate temperature of 750°C (Fig. 4, spectrum *b*).

The full width at the half-maximum of diamond peaks in the range of 1333 cm^{-1} is larger than the width of the diamond peak in a single-crystal diamond (3.3 cm^{-1}) [17]. The broadening of the diamond peak can be qualitatively explained in terms of the phonon confinement model [18]. This model is based on the uncertainty principle which states that the lower the size of a crystallite, the wider the range of phonon wave vectors involved in Raman scattering. As follows from the spectra shown in Figs. 3 and 4, the film with the highest diamond phase content has crystallites with the largest size. Another possible mechanism of the broadening of the diamond peak, described in [18], is related to phonon scattering by impurities and defects in diamond crystallites. We should note that because of the spread function, the true width of the diamond peak in our measurements is smaller than the width shown in Figs. 3 and 4.

Figure 5 shows the micrograph of the surface of a diamond film grown on crystalline silicon using the technical parameters corresponding to the highest diamond phase content (Table 1). The film consists of faceted crystallites, confirming a high diamond phase content. By measuring the thickness of the film from the micrograph of its cleavage and by determining the growth duration of a continuous film (which is the difference between the total time of deposition and the time of coalescence of separate diamond particles), one can determine the growth rate of a solid film. The growth rate for all processes was no lower than 1 μm/h.

The X-ray diffraction pattern of the diamond film grown by HFCVD technology using the parameters that ensured the growth of films with the highest diamond phase content is shown in Fig. 6. In this pattern, one can clearly see several maxima with angular positions corresponding to the set of reflections from the (111), (220), and (311) planes of a cubic lattice, which has the parameter $a_0 = 0.3567 \pm 0.0001$ nm characteristic of diamond [19]. The intensity ratio of the (111), (220), and (311) lines is 100 : 20 : 4. For a reference diamond powder, this ratio is 100 : 25 : 16; therefore, the crystallites in this diamond film are oriented mainly along the [111] axis.

The sizes of the coherent-scattering regions for the samples studied are given in Table 2. A comparison of the previously obtained Raman scattering data with the X-ray diffraction data shows that an increase in the diamond phase content in the film is accompanied by an increase in the size of the coherent-scattering regions. The mean size of a coherent-scattering region in the film with the highest diamond phase content, determined from three maxima, was found to be equal to 85 nm, which is almost ten times smaller than the mean size of a crystallite (1 μm) found from electron microscopy. The agreement between the sizes of the coherent-scattering region for the (111), (220), and (311) maxima indicates that the broadening of the diffraction lines is not related to internal stresses in the crystallites.
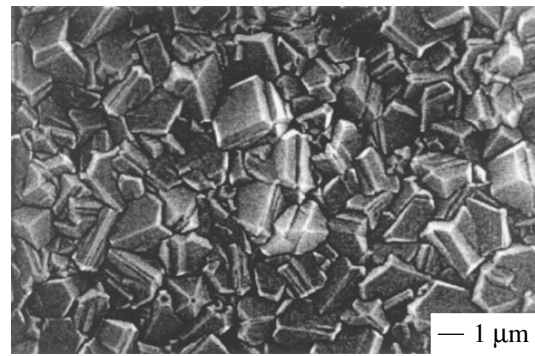
Fig. 5. Micrograph of diamond film. The parameters of the HFCVD process are given in Table 1.
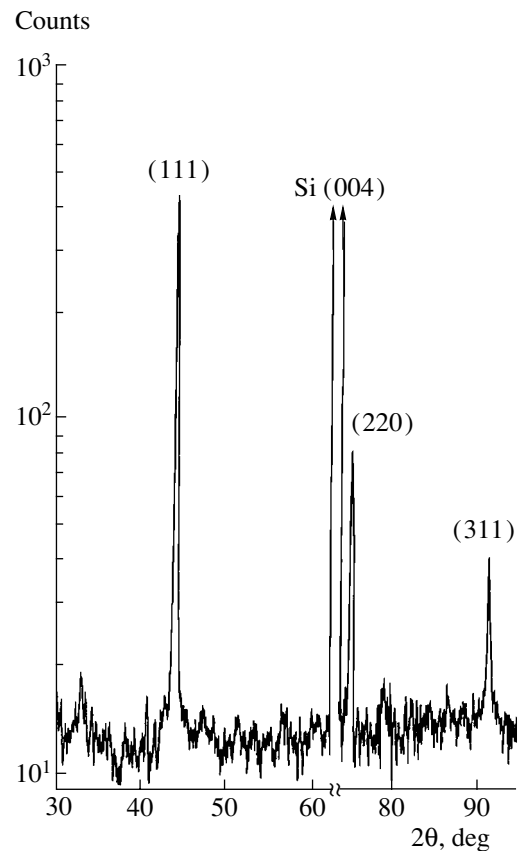

Fig. 6. Diffraction pattern of diamond film (CuK_α radiation, (θ, 2θ) geometry, background is reduced). The parameters of the HFCVD process are given in Table 1.

According to the data published in [20], the broadening of "diamond" lines in films with crystallites aligned primarily along the [111] direction can be attributed to the presence of stacking faults and twin boundaries.

The cross section for light scattering by sp^2-bonded carbon is approximately 50 times larger than that by sp^3-bonded carbon [13]. As a consequence, a weak line in the vicinity of 1580 cm^{-1} against the background of the diamond-related peak at 1333 cm^{-1} (Fig. 4, spec-

BAĬDAKOVA *et al.*

Table 2. Size of coherent-scattering regions at various parameters of HFCVD

Pressure of gaseous mixture in reactor, Torr/(substrate temperature), °C	Size of coherent-scattering region, nm
12/850	70
24/850	75
48/850	80
48/650	130
48/750	180

Note: Common parameters for all HFCVD processes: content of methane is 1%, gas flow rate is 500 sccm, and duration of growth is 5 h.

trum *c*) is indicative only of the low content of the graphite phase in the film. At the same time, the X-ray diffraction studies of the diamond film did not reveal any traces of the graphite phase (neither microcrystalline nor nanocrystalline). This means that only the amorphous graphite phase is present in the film. The amorphous graphite phase may be formed owing to the absence of atomic hydrogen in the reactor in the course of cooling the substrate to room temperature after the completion of the HFCVD process. As it was shown in [21], such graphitization of the diamond film surface can occur up to a depth of 50 nm [21]. Amorphous graphite is also present in the boundaries of diamond crystallites, since the formation of sp^2-bonded carbon in the crystallite boundaries is found to be energetically more favorable than that of structurally disordered sp^3-bonded carbon [22]. It is amorphous carbon in the crystallite boundaries that is responsible for the transverse electrical conductivity of a diamond film [22].

CONCLUSION

The technical parameters of the HFCVD process that ensure the growth of diamond films with the highest content of diamond phase at a growth rate of about 1 μm/h were ascertained. The film grown consists of [111]-oriented diamond crystallites with a mean size of about 1 μm; $sp^2$2- bonded carbon is present in this film only in its amorphous phase.

ACKNOWLEDGMENTS

REFERENCES

1. J. C. Angus and C. C. Hayman, Science **241**, 913 (1988).
2. S. Shikata, MRS Bull. **23** (9), 61 (1998).
3. V. Malcher, A. Kromka, J. Janik, *et al.*, Acta Phys. Slov. **50**, 673 (2000).
4. A. Sawabe and T. Inuzuka, Appl. Phys. Lett. **46**, 146 (1985).
5. X. C. He, H. S. Shen, Z. M. Zhang, *et al.*, Diamond Relat. Mater. **9**, 1626 (2000).
6. A. M. Stoneham, I. J. Ford, and P. R. Chalker, MRS Bull. **23** (9), 28 (1998).
7. C. Arnault, L. Demuynck, C. Speisser, and F. L. Normand, Eur. Phys. J. B **11**, 327 (1999).
8. N. S. Xu, J. Chen, S. Z. Deng, *et al.*, J. Phys. D **33**, 1572 (2000).
9. Y. Chakk, R. Brener, and A. Hoffman, Appl. Phys. Lett. **66**, 2819 (1995).
10. H. Makita, K. Nishimura, N. Jiang, *et al.*, Thin Solid Films **281**, 279 (1996).
11. P. Ascarelli and S. Fontana, Appl. Surf. Sci. **64** (4), 307 (1993).
12. B. R. Stoner, G.-H. M. Ma, S. D. Wolter, and J. T. Glass, Phys. Rev. B **45**, 11067 (1992).
13. D.-W. Kweon, J.-Y. Lee, and D. Kim, J. Appl. Phys. **69**, 8329 (1991).
14. K. E. Spear and M. Frenklach, in *Synthetic Diamond: Emerging CVD Science and Technology*, Ed. by K. E. Spear and J. P. Dismukes (Wiley, New York, 1994), p. 243.
15. A. K. Skider, A. P. Jacob, T. Sharda, *et al.*, Thin Solid Films **332**, 98 (1998).
16. S. Logothetidis, Appl. Phys. Lett. **69**, 158 (1996).
17. R. G. Buckley, T. D. Moustakas, L. Ye, and J. Varon, J. Appl. Phys. **66**, 3595 (1989).
18. L. Bergman and R. J. Nemanich, J. Appl. Phys. **78**, 6709 (1995).
19. *Powder Diffraction File 6-675* (Joint Committee on Powder Diffraction Standards, International Center for Diffraction Data, Swarthmore, 1991).
20. H. Windischmann and K. J. Gray, Diamond Relat. Mater. **4**, 837 (1995).
21. V. I. Konov, A. A. Smolin, V. G. Ralchenko, *et al.*, Diamond Relat. Mater. **4**, 1073 (1995).
22. P. Keblinski, D. Wolf, F. Cleri, *et al.*, MRS Bull. **23** (9), 36 (1998).

Translated by A. Zalesskiĭ

ELECTRONIC
AND OPTICAL PROPERTIES
OF SEMICONDUCTORS

Local Vibrational Modes of the Oxygen–Vacancy Complex in Germanium

V. V. Litvinov*, L. I. Murin**, J. L. Lindstrom***, V. P. Markevich**, and A. N. Petukh*

* Belarussian State University, ul. Leningradskaya 14, Minsk, 220050 Belarus
** Institute of Solid-State and Semiconductor Physics, Belarussian Academy of Sciences,
ul. Brovki 17, Minsk, 220072 Belarus
*** Lund University, Division of Solid State Physics, S-22100 Lund, Sweden
Submitted October 29, 2001; accepted for publication November 1, 2001

Abstract—Infrared absorption of *n*- and *p*-Ge crystals enriched with ^{16}O and/or ^{18}O isotopes was studied after irradiation with 6-MeV electrons. Absorption spectra were measured at 10 and 300 K. Along with known bands characteristic of oxygen-containing defects, new lines at 669, 944, and 990 cm^{-1} were detected. These bands are annealed at temperatures of 120–140°C; the band at 621 cm^{-1}, previously related to the vacancy–oxygen complex in Ge, is simultaneously annealed. The bands at 621 and 669 cm^{-1} showed identical temperatures (10 $\longrightarrow$ 300 K) and oxygen isotope (^{16}O $\longrightarrow$ ^{18}O) shifts. These bands were found to correspond to various charge states of a defect with an energy level near $E_v = 0.25 \pm 0.03$ eV. It is assumed that such a defect is the vacancy–oxygen complex (*A* center). The weak bands at 944 and 990 cm^{-1} were identified as combinations of asymmetric stretching modes at 621 and 669 cm^{-1} with a symmetric one at 320 cm^{-1} for neutral and negative charge states of the *A* center, respectively. © 2002 MAIK "Nauka/Interperiodica".

INTRODUCTION

The vacancy–oxygen (*VO*) complex or *A* center is one of the basic and best studied defects in Si crystals grown by the Czochralski method and irradiated with energetic particles [1, 2]. The center has negative paramagnetic (*VO*)$^-$ and neutral (*VO*)^0 states corresponding to local vibrational modes (LVM) at 836 and 885 cm^{-1}, respectively. Recently [3], additional weak bands at 1370 and 1430 cm^{-1} were detected for two charge states of the *A* center in Si, which are related to a combination of antisymmetric and symmetric modes of oxygen vibrations within the complex.

The *A* center in Ge has not been adequately identified because of insufficient informativeness of the electron spin resonance (ESR) method as applied to the defect structure in these crystals [4]. Therefore, a basic method for *A*-center determination in Ge is vibrational infrared (IR) spectroscopy. To date, only the band at 620 cm^{-1} (detected in [5, 6]) has been related to the vacancy–oxygen complex in Ge. However, the observed scatter of annealing temperatures (from 50 to 150°C) of the band at 620 cm^{-1} [5–7] makes the *A*-center determination by this band ambiguous and indicates that this band possibly corresponds to only one charge state of the complex.

This study is aimed at gaining deeper insight into the *A*-center LVMs in Ge crystals at various Fermi level positions.

EXPERIMENTAL

We studied *n*- and *p*-type crystals enriched with ^{16}O and(or) ^{18}O isotopes to concentrations of $(1–4) \times 10^{17}$ cm^{-3}. The concentration of interstitial ^{16}O and ^{18}O atoms was determined from the absorption band intensities in the regions of 856 and 812 cm^{-1} using a calibration factor of 1.25×10^{17} cm^{-2} [8]. The hole concentration in initial Ge was $p_0 = (1.3–1.7) \times 10^{15}$ cm^{-3} set by Ga doping. The electron density in initial *n*-type crystals was varied from 2×10^{14} to 2×10^{16} cm^{-3} by doping with Sb or the additional introduction of oxygen-containing quenched-in donors at 350°C for 200 h. As reference samples, we used *n*-type Ge crystals ($\rho \approx 10 \ \Omega$ cm) with a low oxygen content ($<5 \times 10^{15}$ cm^{-3}). The samples were irradiated by 6-MeV electrons ($(1–30) \times 10^{16}$ cm^{-2}) at room temperature.

The IR absorption measurements were carried out using a Bruker IPS 113v Fourier spectrometer at temperatures of 12 and 300 K with a spectral resolution of 0.5 and 1.0 cm^{-1}, respectively. The Fermi level position in the samples was determined from the temperature (80–300 K) dependences of carriers, measured by the Hall method. The conduction type of the initial and irradiated crystals was additionally determined with a hot probe.
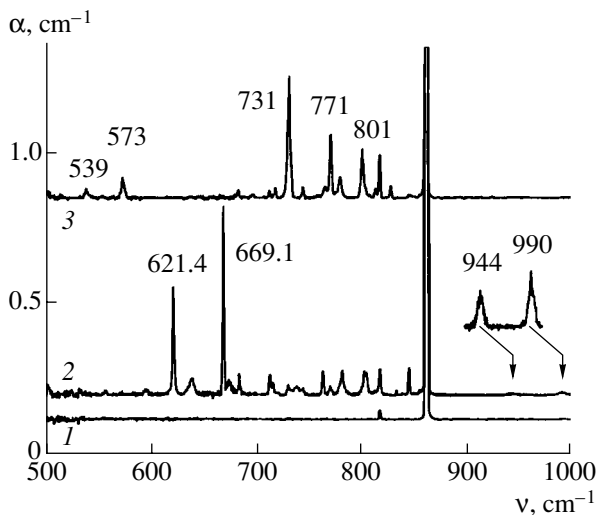
Fig. 1. Low-temperature (10 K) absorption spectra of n-Ge:^{16}O samples (*1*) in the initial state, (*2*) after irradiation by an electron flux of 1.3×10^{17} cm^{-2}, and (*3*) after subsequent 30-min annealing at $T = 160°C$ [3].

Fig. 2. Absorption spectra of n-Ge samples enriched with (*1*) ^{18}O isotope and (*2*) a mixture of ^{16}O and ^{18}O isotopes after irradiation with an electron flux of 1.3×10^{17} cm^{-2}.

RESULTS AND DISCUSSION

Figure 1 displays the low-temperature spectra of samples n-Ge:^{16}O ($n_0 = 1.8 \times 10^{14}$ cm^{-3}) in the initial state after irradiation with an electron flux of 1.3×10^{17} cm^{-2} and subsequent 30-min annealing at 160°C. The irradiation led to a $n \longrightarrow p$ conversion of the conduction type, Fermi level pinning at low temperatures in the range $E_v + 0.25 \pm 0.03$ eV, as well as to the introduction of some absorption bands. We note that none of these bands were observed after the irradiation of reference crystals with low oxygen content. The two most intense bands at 621.4 and 669.1 cm^{-1} in the spectrum of irradiated crystals are worth noting. The former was related (see [6, 7]) to the vacancy–oxygen complex; the latter was observed for the first time. The spectral positions of the bands at 621.4 and 669.1 cm^{-1} differ by a factor of 1.32 from those of corresponding LVMs at 835.8 and 885.2 cm^{-1} for neutral and negative states of the A center in Si [2, 3]. The same ratio also occurs for antisymmetric stretching modes of interstitial oxygen (O$_i$) at 862.5 and 1136.4 cm^{-1} in Ge and Si, respectively. Among previously unobserved bands are two low-intensity bands at 944 and 990 cm^{-1}, which are shifted with respect to the bands at 621 and 669 cm^{-1} by 321 and 323 cm^{-1}, respectively; by analogy with the bands at 1370 and 1430 cm^{-1} in Si [3], these low-intensity bands may represent coupled modes of antisymmetric and symmetric vibrations of oxygen in two A-center charge states.

The bands at 621.4 and 669.1 cm^{-1} are shifted to 611 and 657 cm^{-1} in the spectra measured at room temperature. The temperature shift of both bands by 11–12 cm^{-1} exceeds that for ot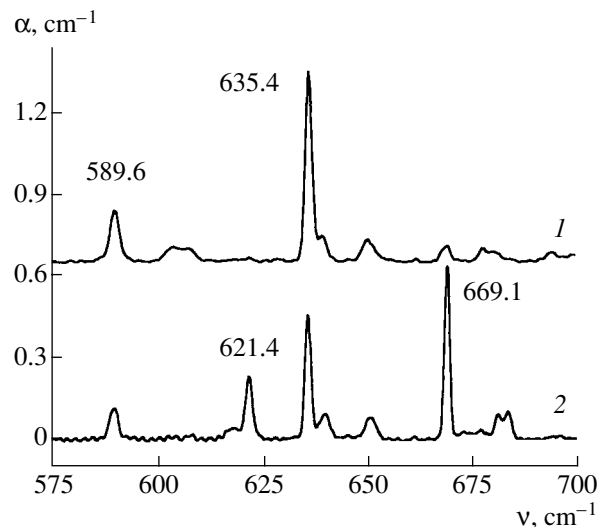her bands related to interstitial oxygen and known oxygen-containing complexes in Ge by a factor of 2–3. In the spectra of n-Ge:O samples converted by irradiation to the p-type, as in the spectra of heavily irradiated p-Ge:O crystals, the bands at 621.4 and 669.1 cm^{-1} have comparable intensities at 10 and 300 K (bands at 611 and 657 cm^{-1}). The ratio of the intensities of these bands is not appreciably changed when using filters, which prevents sample exposure to the light of the Ge intrinsic absorption range and, thus, sample recharging due to nonequilibrium carrier trapping. This points to the simultaneous existence of two charge states of the complexes due to the Fermi level pinning at the defect level in the lower part of the band gap (near $E_v + 0.25 \pm 0.03$ eV).

The low-temperature spectra in Fig. 2 for irradiated Ge:^{18}O and Ge:(^{16}O + ^{18}O) crystals show the isotopic shift (^{16}O $\longrightarrow$ ^{18}O) of both bands at 621.4 and 669.1 cm^{-1} to lower energies, 589.6 and 635.4 cm^{-3}, respectively. In this case, the squared ratio $[v(^{16}\text{O})/v(^{18}\text{O})]^2$ of frequencies for both bands is 1.11 and coincides with that for the antisymmetric stretching mode v_3 of interstitial oxygen atoms (O$_i$) in Ge: $(862/818)^2 = 1.11$. Thus, both bands at 621.4 and 669.1 cm^{-1} can be related to the antisymmetric vibrations of bivalent oxygen atoms in radiation defects. The absence of mixed modes in the spectrum of Ge enriched with a mixture of ^{16}O and ^{18}O oxygen isotopes indicates that this complex incorporates a single oxygen atom. The high intensity of the bands at 621.4 (589.6) and 669.1 (635.4) cm^{-1} in comparison with other bands of oxygen-containing defects in the spectra of irradiated Ge:^{16}O(^{18}O) crystals is consistent with the notion that they belong to complexes generated by the direct interaction between O$_i$ atoms and primary radiation defects (vacancies).
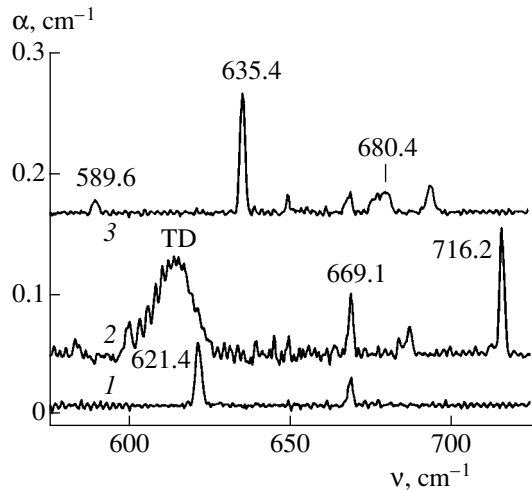
Fig. 3. Low-temperature (10 K) absorption spectra of ^{16}O-enriched samples: (1) p-Ge:^{16}O and (2) n-Ge with quenched-in donors. Spectrum 3 corresponds to the n-Ge:^{18}O sample. The integrated electron flux is 1.1×10^{16} cm^{-2}.

Fig. 4. Dependences of the band integrated intensity S on the temperature of 30-min isochronous annealing of n-Ge:^{16}O crystals irradiated with an integrated electron flux of 5×10^{16} cm^{-2}. The symbols correspond to the indicated frequencies (ν, cm^{-1}) of the peaks.

The fact that the bands at 621.4 and 669.1 cm^{-1} correspond to different charge states of the and A center in Ge is also confirmed by the observed dependence of their relative intensity on the Fermi level position in the measured samples. This dependence manifests itself after irradiation and in the course of annealing of the irradiated samples with different doping types and levels. Figure 3 displays fragments of the spectra in the region of these bands for simultaneously irradiated samples of p-Ge:^{16}O ($p_0 = 1.8 \times 10^{15}$ cm^{-3}), n-Ge:^{16}O with preliminarily introduced quenched-in donors ($n_0 = 1.8 \times 10^{16}$ cm^{-3}), and n-Ge:^{18}O ($n_0 \approx 8 \times 10^{15}$ cm^{-3}). The low electron dose (1.1×10^{16} cm^{-2}) allowed pinning of the Fermi levels near the valence band top and conduction band bottom in the irradiated samples of the p- and n-types, respectively. One can see that the bands at 669 (635) and 621 cm^{-1} dominate in the spectra after irradiation of n-Ge:^{18}O(^{18}O) and p-Ge:^{16}O, respectively.

A prominent feature of spectrum 2 (Fig. 3) for irradiated n-Ge:^{16}O with preliminarily introduced quenched-in donors is the intense band at 716.2 cm^{-1} (707.6 cm^{-1} at 300 K). An isotopic analogue of this band at 680.4 cm^{-1} has a rather low intensity after the identical irradiation of n-Ge:^{18}O without quenched-in donors (cf. spectra 2 and 3 in Fig. 3). The band at 716 cm^{-1} is imperceptible after the irradiation of p-Ge and after the radiation-induced $n \longrightarrow p$ conversion of n-Ge. This indicates that this band corresponds to centers with an energy level in the upper half of the band gap. The generation rate of these centers grows in the presence of quenched-in donors. The centers with a band at 716 cm^{-1} are annealed in the temperature range 150–160°C.
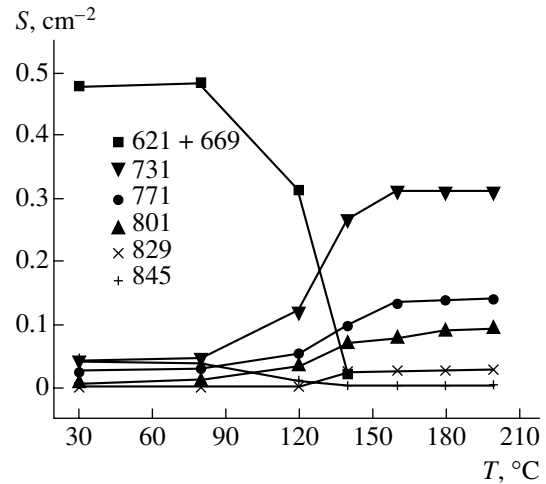
The relative intensity of the bands at 621.4 and 669.1 cm^{-1} changes in the course of isochronous annealing of n- and p-Ge crystals irradiated with various electron fluxes, though the dynamics of the total intensity of both bands is identical in the course of annealing of various samples. As is shown in Fig. 4, the center responsible for the bands at 621.4 and 669.1 cm^{-1} is annealed out at temperatures of 120–140°C. This is accompanied by the correlated (in temperature and integrated intensity) emergence of bands at 731, 771, and 801 cm^{-1}. In the same temperature range, the low-intensity modes at 845, 944, and 990 cm^{-1} are annealed out and new bands at 829, 573, and 539 cm^{-1} arise (see spectrum 3 in Fig. 1).

The above results show a total spectroscopic similarity of the bands at 621 and 669 cm^{-1}, as well as their coupled modes at 944 and 990 cm^{-1}, to corresponding LVMs for neutral and negative charge states of the VO complex in Si [1–3]. The A center in Ge is conventionally related to the acceptor level at $E_c - 0.25 \pm 0.02$ eV (see [9–11]). This statement is based on the fact that a center arises in oxygen-containing crystals, and its annealing temperature (150–160°C) is close to that of the band at 621 cm^{-1}. However, such an identification of the bands and the A-center level cannot explain the two charge states of the centers, which arose during pinning of the equilibrium Fermi level in the region of $E_v + 0.25 \pm 0.03$ eV (see spectra in Figs. 1, 2). Taking into account the results of [12, 13], it seems reasonable that the bands at 621.4 and 669.1 cm^{-1} belong to the center with an energy level in the lower half of the band gap. According to these data, irradiation of Ge crystals enriched with oxygen causes the efficient formation of centers with a level at $E_v + 0.27$ eV. The cross section of this process for the irradiation of n-Ge:O with ^{60}Co

Spectral positions of local vibrational modes (in cm^{-1}) at temperatures 10 and 300 K for vacancy–oxygen complexes in germanium

Oxygen isotope	$(VO)^0$		$(VO)^-$	
	10 K	300 K	10 K	300 K
^{16}O	621.4	611	669.1	657
^{18}O	589.6	578	635.4	624

gamma quanta was found to be close to that for the generation of separated Frenkel pairs [14]. Moreover, these centers are annealed in the same temperature range as for the bands at 621.4 and 669.1 cm^{-1}.

To establish the nature of the bands at 621.4, 669.1, and 716.2 cm^{-1} and their relation to certain defect charge states in more detail, comprehensive optical (IR absorption) and electric (deep-level transient spectroscopy) measurements of irradiated oxygen-containing *n*- and *p*-Ge crystals are being planned.

CONCLUSION

New bands at 669, 944, and 990 cm^{-1} were detected in the *n*- and *p*-Ge crystals enriched with ^{16}O and (or) ^{18}O oxygen isotopes and irradiated with fast electrons. The most intense band at 669 cm^{-1} was related to the negative state of the vacancy–oxygen $(VO)^-$ complex, and the known band at 621 cm^{-1} was identified with its neutral state $(VO)^0$. The low-intensity bands at 944 and 990 cm^{-1} were related to a combination of stretching antisymmetric modes at 621 and 669 cm^{-1} with a symmetric mode at 320 cm^{-1}. The frequencies of stretching antisymmetric modes for $(VO)^0$ and $(VO)^-$ complexes at temperatures of 10 and 300 K in Ge crystals enriched with oxygen isotopes are listed in the table. The efficient generation of complexes with a band at 716 cm^{-1} was detected during the irradiation of *n*-Ge crystals with preliminarily introduced quenched-in donors. It was concluded that the *A* center in Ge introduces a level at $E_v + 0.25 \pm 0.03$ eV.

REFERENCES

1. G. D. Watkins and J. W. Corbett, Phys. Rev. **121** (4), 1001 (1961).
2. B. Pajot, S. McQuaid, R. C. Newmann, *et al.*, Mater. Sci. Forum **143–147**, 969 (1994).
3. J. L. Lindstrom, L. I. Murin, V. P. Markevich, and T. Hallberg, Physica B (Amsterdam) **273–274**, 291 (1999).
4. J. Baldwin, Appl. Phys. **36** (3), 793 (1965).
5. R. E. Whan, Appl. Phys. Lett. **6** (11), 221 (1965).
6. R. E. Whan, Appl. Phys. Lett. **37** (6), 2435 (1966).
7. J. P. Becker and J. C. Corelli, J. Appl. Phys. **36** (11), 3606 (1965).
8. E. I. Millett, L. S. Wood, and G. Bew, Br. J. Appl. Phys. **16**, 1593 (1965).
9. N. Fukuoka, H. Saito, and Y. Kambe, Jpn. J. Appl. Phys. **22**, L353 (1983).
10. V. V. Litvinov, V. I. Urenev, and V. A. Shershel', Fiz. Tekh. Poluprovodn. (Leningrad) **17**, 1623 (1983) [Sov. Phys. Semicond. **17**, 1033 (1983)].
11. J. Fage-Pedersen and A. N. Larsen, Phys. Rev. B **62**, 10116 (2000).
12. L. A. Goncharov, V. V. Emtsev, T. V. Mashovets, and S. M. Ryvkin, Fiz. Tekh. Poluprovodn. (Leningrad) **6**, 424 (1972) [Sov. Phys. Semicond. **6**, 369 (1972)].
13. V. V. Litvinov, V. I. Urenev, and V. A. Shershel', Fiz. Tekh. Poluprovodn. (Leningrad) **18**, 1131 (1984) [Sov. Phys. Semicond. **18**, 707 (1984)].
14. V. V. Emtsev and T. V. Mashovets, *Impurities and Point Defects in Semiconductors* (Radio i Svyaz', Moscow, 1981).

Translated by A. Kazantsev

ELECTRONIC
AND OPTICAL PROPERTIES
OF SEMICONDUCTORS

Luminescent Si–Ge Solid Solution Layers Er-Doped in Molecular-Beam Epitaxy

V. G. Shengurov*, S. P. Svetlov^*, V. Yu. Chalkov*, B. A. Andreev,
Z. F. Krasil'nik**, B. Ya. Ber***, Yu. N. Drozdov**, and A. N. Yablonsky****

* Physicotechnical Research Institute, Nizhni Novgorod State University, Nizhni Novgorod, 603950 Russia
** Institute for the Physics of Microstructures, Russian Academy of Sciences, Nizhni Novgorod, 603000 Russia
*** Ioffe Physicotechnical Institute, Russian Academy of Sciences, St. Petersburg, 194021 Russia
^e-mail: svetlov@phys.unn.ru

Abstract—Erbium-doped $Si_{1-x}Ge_x$ epitaxial layers have been grown by sublimation molecular-beam epitaxy (SMBE) in an atmosphere of germane (GeH_4). Doping with erbium was done during growth, with single-crystal Si:Er as the source of Er. The $Si–Si_{1-x}Ge_x$ ($0.01 \leq x \leq 0.09$) interface was studied by secondary-ion mass spectrometry. Er and Ge show concentration profiles with abrupt boundaries and a significant decrease in their surface segregation. This means that hydrogen acts as a "surfactant." Data on the luminescent properties of the Er-doped $Si/Si_{1-x}Ge_x$ samples are reported. © *2002 MAIK "Nauka/Interperiodica".*

1. INTRODUCTION

Erbium-doped silicon has been attracting much attention owing to its emission at a wavelength of 1.54 μm, which lies in the minimum dispersion range of quartz optical communication fibers. The room-temperature electroluminescence has been reported for Si diodes doped with Er in molecular-beam epitaxy (MBE) [1, 2]. Recently, studies of Er-doped Si–Ge solid solutions have been reported [3], which opens up possibilities of creating silicon-based lasers.

However, SiGe:Er/Si layers have been studied to a much lesser extent than Si:Er/Si layers. A limited number of reports concerned with SiGe:Er/Si growth by MBE contain sparse data on the impurity content of epitaxial layers and the Er distribution in them. At the same time, the surface segregation of Er in Si layers has been demonstrated [4, 5]. The occurrence of the same effect is likely in SiGe:Er layers.

Codoping with oxygen during Si:Er layer growth stimulates the intensive incorporation of Er atoms into the growing layer [4]. Since the generation of a stable flow of Ge atoms in MBE is difficult, it is preferable to grow SiGe solid solution layers using gaseous sources [6]. However, the admission of oxygen to the growth chamber is ruled out in this case.

The present study was concerned with the composition of SiGe:Er/Si epitaxial layers, the incorporation of Er atoms into the growing layer of the SiGe solid solution, and the possibility of fabricating, by means of SMBE in a germane atmosphere, heterostructures with abrupt boundaries of doped regions which emit at a wavelength of 1.54 μm.

2. EXPERIMENTAL

The structures were grown by SMBE of silicon in a germane atmosphere according to the method reported in [7]. An atomic flow of silicon was produced by the sublimation of a Si single crystal, and the decomposition of a molecular beam of germane (GeH_4) introduced into the growth chamber at the growth surface ensured the incorporation of Ge into the growing layer. A flow of erbium atoms was produced by the evaporation of a Si:Er single crystal. The layers were deposited onto (100) Si substrates.

The structures commonly included a buffer layer ~100 nm in thickness that was grown at a substrate temperature $T_s = 1000°C$ and onto which a 50- to 100-nm-thick layer of the GeSi alloy was deposited at 500°C. The alloy layer was overgrown with a capping layer of undoped silicon.

The distribution of the Ge, Er, and O concentration across the thickness of the layers grown was studied by secondary-ion mass spectrometry (SIMS), and the Ge content in the layers was determined by X-ray diffraction.

The photoluminescence (PL) spectra of the structures were studied at a temperature $T = 4.2$ K on a BOMEM DA3 Fourier spectrometer with 1 cm^{-1} resolution, with excitation by an Ar^+ laser (514.5 nm, 200 mW) from the epitaxial layer side. The PL signal was detected with a Ge detector cooled with liquid nitrogen.

3. RESULTS AND DISCUSSION

Figure 1 shows the concentration profiles of Ge, Er, and O atoms in $Si/Si_{1-x}Ge_x$:Er/Si (100) heterostruc-

Atomic concentrations, cm^{-3}
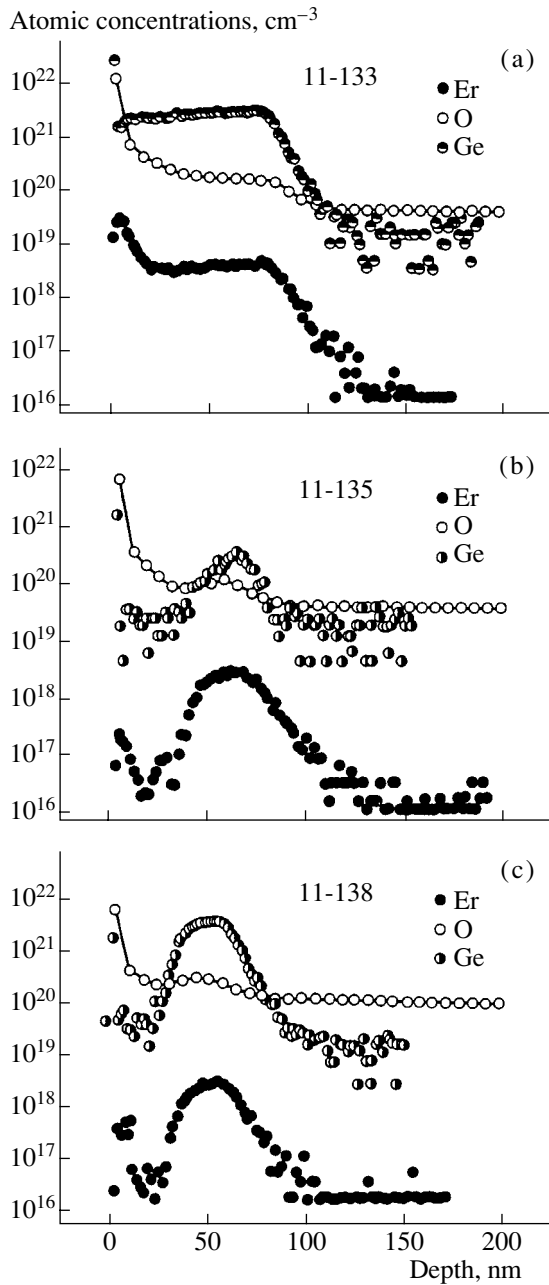

Fig. 1. Ge, Er, and O concentration profiles in Si/Si$_{1-x}$Ge$_x$:Er/Si heterostructures grown using an Er-doped silicon source: (a) $P_{\text{GeH}_4} = 2 \times 10^{-5}$ Torr, without capping layer (structure 11-133); (b) $P_{\text{GeH}_4} = 8 \times 10^{-6}$ Torr (structure 11-135); (c) $P_{\text{GeH}_4} = 8 \times 10^{-6}$ Torr, with potential $V = -300$ V applied to the substrate in Si$_{1-x}$Ge$_x$:Er layer growth (structure 11-138).

tures. The first heterostructure (11-133) was grown using an Er-doped Si source under germane pressure $P_{\text{GeH}_4} = 2 \times 10^{-5}$ Torr. This structure contained no capping layer. As seen in Fig. 1a, a sharp rise in the Ge concentration is observed beginning with the buffer layer.

In the upper portion of the profile, the Ge concentration increases by an order of magnitude within an interval of ~14 nm. The Ge concentration in the layer is quite uniform (~3×10^{21} cm^{-3} ($x = 0.06$)), with a minor decrease toward the layer surface. X-ray studies yield nearly the same Ge content, $x = 0.07$. The Er concentration in the layer varies in parallel with that of Ge, reaching its value in the source (~5×10^{18} cm^{-3}). At the same time, when a silicon layer was grown from the same source without admission of oxygen, the Er concentration did not exceed ~1×10^{17} cm^{-3} [8].

Growing a Si$_{1-x}$Ge$_x$ layer at a lower pressure $P_{\text{GeH}_4} = 8 \times 10^{-6}$ Torr (structure 11-135) results in the Ge content decreasing to $x \approx 0.01$ (Fig. 1b). In this case, the Ge concentration is not uniform across the layer thickness: after reaching its maximum value at the beginning of the Si$_{1-x}$Ge$_x$ layer, it then falls to half this value at its end. Further, after closing the germane inlet valve and growing a capping layer, the Ge concentration falls to even lower values. The Er concentration in the Si$_{1-x}$Ge$_x$ layer varies nearly in parallel with the Ge distribution. The Er concentration at the ⟨buffer layer⟩–⟨Si$_{1-x}$Ge$_x$ layer⟩ interface changes from 3×10^{17} to 3×10^{18} cm^{-3} across a thickness of ~25 nm, and at the ⟨Si$_{1-x}$Ge$_x$ layer⟩–⟨coating layer⟩ interface it changes within the same range across a thickness of ~9 nm.

Applying a negative potential ($V = -300$ V) to the substrate in the course of Si$_{1-x}$Ge$_x$:Er layer growth (structure no. 11-138) results in a considerable rise in the Ge content of the layer ($x = 0.09$, Fig. 1c), compared with that in the preceding experiment. The Ge concentration, increasing in the upper portion of the profile, changes by an order of magnitude within an interval of ~12 nm, and at the ⟨Si coating layer⟩/Si$_{1-x}$Ge$_x$:Er interface, within an interval of ~8 nm. The change in the Er concentration follows that in the concentration of germanium in the Si$_{1-x}$Ge$_x$:Er layer. The erbium concentration is comparable with that in the preceding experiments, and its rise and fall coincide with those for the Ge concentration in the same layer.

The obtained experimental data can be summarized as follows. The highest Er concentration in the layers grown is $(3-4) \times 10^{18}$ cm^{-3}, irrespective of the Ge content in a Si$_{1-x}$Ge$_x$ layer. The steepness of the rise in the Ge concentration in a Si$_{1-x}$Ge$_x$:Er layer grows with increasing the germane pressure introduced into the growth chamber and also becomes greater upon applying a negative potential to the substrate. The observed slopes of the Ge concentration profile at the ⟨Si cap layer⟩/Si$_{1-x}$Ge$_x$ interface (an order of magnitude variation of the concentration across a thickness of 8–9 nm) and at the interface between Si$_{1-x}$Ge$_x$ and the buffer layer (an order of magnitude across ~12 nm) indicates the existence of sufficiently abrupt boundaries under these experimental conditions. Moreover, the profile sharpness at the ⟨Si coating layer⟩/Si$_{1-x}$Ge$_x$:Er interface may be even greater. It is limited by the smooth
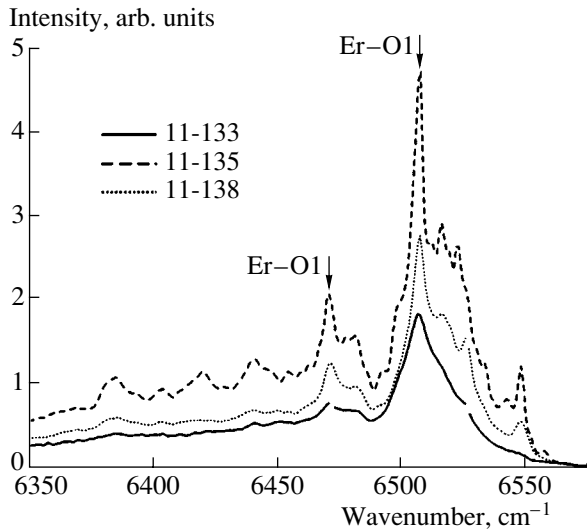
Fig. 2. PL spectra of samples 11-133, 11-135, and 11-138 (Er luminescence range). Arrows show the two strongest lines related to the Er–O1 center.
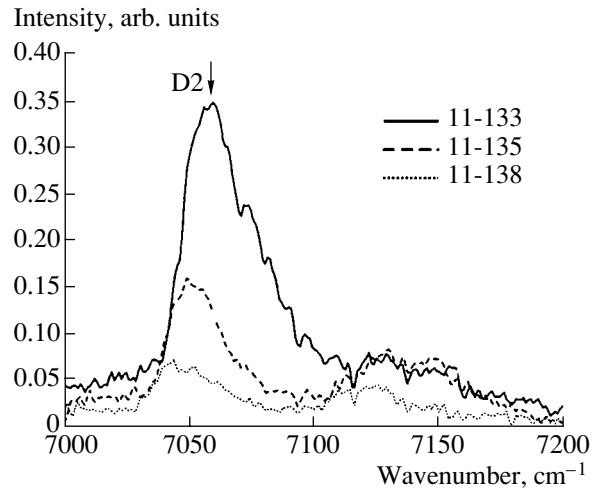

Fig. 3. PL spectra of samples 11-133, 11-135, and 11-138 (dislocation line $D2$).

variation of the germane pressure in the growth chamber after the germane flow is cutoff. On closing the germane inlet valve, a certain amount of this gas remains in the chamber, feeding germanium into the growing Si layer until the gas is completely pumped out.

Germanium is incorporated into the growing Si layer in the same way as any other impurity in MBE doping [9]. First, a surface adsorption layer of Ge is formed and feeds the growing layer. The surface segregation of Ge is responsible for the gradually sloping profile of the $Si_{1-x}Ge_x$ layer at the heterointerface.

Our data indicate that, in the process of Si sublimation in a germane atmosphere at a growth temperature of ~500°C, the Ge segregation is reduced to a minimum. This is probably stimulated by continuous coating of the surface with atomic hydrogen formed upon the dissociation of GeH_4. The surface hydrogen can affect the kinetics of Ge segregation during $Si_{1-x}Ge_x$ heterostructure formation, thereby suppressing the surface segregation. Hydrogen adsorbed on the surface behaves as a surfactant [6, 10].

The flux of Si atoms from the sublimating source contains Si^+ ions. Therefore, applying a negative potential to the substrate during $Si_{1-x}Ge_x$ layer growth accelerates the Si^+ ions toward the growth surface. They interact with Ge, Er, and O atoms, stimulating the incorporation of these atoms into the growing Si layer [8].

The fact that the Er concentration profile becomes sharper as the Ge content increases indicates that Ge affects the surface segregation of the Er impurity.

The structures under study emit at 1.54 μm (~6500 cm^{-1}) under optical excitation. Figure 2 presents the low-temperature PL spectra associated with the intracenter $^4I_{13/2} \longrightarrow {}^4I_{15/2}$ transition in the Er^{3+} ion in a $Si_{1-x}Ge_x$ solid solution. In addition, the line of dislocation luminescence, $D1$ at 6549 cm^{-1}, apparently makes a pronounced contribution to the luminescence near 6500 cm^{-1}, which is confirmed by the observation of a strong line of dislocation luminescence $D2$ at 7057 cm^{-1} [11]. The strongest in the discrete spectrum is the series of lines of an isolated Er center, Er–O1 [12], with an axial symmetry of the crystalline environment of the Er^{3+} ion (with the strongest line in this series peaked at 6508 cm^{-1}). Separate lines related to low-symmetry complexes formed by Er with oxygen and defects [12] are also observed in the range 6510–6550 cm^{-1}. The positions and relative intensities of the lines related to the Er–O1 center coincide with those for Si:Er structures grown by SMBE at a growth temperature of ≲500°C. In structures 11-135, 11-138, and 11-133, the intensity of Er luminescence decreases with increasing Ge content (especially for the discrete spectrum of isolated centers), despite an increase in the total content of Er (see Fig. 1). A possible reason for the decrease in the Er luminescence intensity is the formation of dislocations, whose density grows with increasing Ge concentration. First, this creates an alternative channel for exciton recombination [13], thus lowering the efficiency of Er center excitation; indeed, the dislocation-related line $D2$ is the strongest in the spectrum of structure 11-133, which is characterized by the highest Ge content and the lowest intensity of Er photoluminescence (Fig. 3). Second, the buildup of local stresses associated with dislocations leads to line broadening and a corresponding decrease in line intensity.

4. CONCLUSION

The obtained data indicate that in the SMBE growth of $Si_{1-x}Ge_x$:Er/Si (100) heterostructures in a germane atmosphere, germanium favors erbium incorporation

into the growing Si–Ge layer. The sharpness of the Er concentration profile grows with increasing Ge content in the layer. The distribution of germanium itself at the heterointerfaces is also rather sharp, which confirms that the surface segregation of Ge during growth is virtually suppressed. This is probably favored by the passivation of the growth surface by hydrogen, which is formed in GeH_4 dissociation and acts as a surfactant. The obtained structures exhibit high-intensity luminescence associated with an intracenter transition in the Er^{3+} ion.

ACKNOWLEDGMENTS

REFERENCES

1. H. Ennen, G. Pomrenke, A. Axmann, *et al.*, Appl. Phys. Lett. **46**, 381 (1985).
2. J. Stimmer, A. Reittinger, G. Abstreiter, *et al.*, Mater. Res. Soc. Symp. Proc. **422**, 15 (1995).
3. E. Neuteld, A. Sticht, A. Luigan, *et al.*, Appl. Phys. Lett. **73** (21), 3061 (1998).
4. R. Serna, M. Lohmeier, P. M. Zagviin, *et al.,* Appl. Phys. Lett. **66**, 1385 (1995).
5. K. Miyashito, Y. Shiraki, D. C. Hougton, and S. Fukatsu, Appl. Phys. Lett. **67** (2), 235 (1995).
6. N. Ohtani, S. Mokler, M. H. Xie, *et al.*, Jpn. J. Appl. Phys. **33**, 2311 (1994).
7. S. P. Svetlov, V. G. Shengurov, V. Yu. Chalkov, *et al.*, Izv. Akad. Nauk, Ser. Fiz. **65** (2), 204 (2001).
8. V. G. Shengurov, S. P. Svetlov, V. Yu. Chalkov, *et al.*, Fiz. Tekh. Poluprovodn. (St. Petersburg) **35** (8), 954 (2001) [Semiconductors **35**, 918 (2001)].
9. G. E. Becker and J. C. Bean, J. Appl. Phys. **48**, 3395 (1977).
10. H. Wado, T. Shimizu, M. Ishida, and T. Nakamura, J. Cryst. Growth **147**, 320 (1995).
11. R. Sauer, J. Weber, J. Stolz, *et al.*, Appl. Phys. A **36**, 1 (1985).
12. H. Przybylinska, W. Yantsch, Yu. Suprin-Belevitch, *et al.*, Phys. Rev. B **54**, 2532 (1996).
13. B. A. Andreev, Z. F. Krasil'nik, V. P. Kuznetsov, *et al.*, Fiz. Tverd. Tela (St. Petersburg) **43** (6), 979 (2001) [Phys. Solid State **43**, 1012 (2001)].

Translated by D. Mashovets

Migration of Laser-Induced Point Defects in IV–VI Compounds

S. V. Plyatsko

Institute of Semiconductor Physics, National Academy of Sciences of Ukraine, Kiev, 03028 Ukraine
e-mail: plyatsko@laser.semicond.kiev.ua
Submitted July 16, 2001; accepted for publication November 28, 2001

Abstract—The laser-induced ($h\omega < E_g$) transformation of defects in IV–VI compounds is studied. The rate of defect production is found to increase with the free carrier concentration and the electric field strength in the laser wave. The directed migration of both the intrinsic and impurity defects under the combined action of laser radiation and an external electric field is analyzed in terms of a model where the defects are believed to arise mainly from the accumulation of inclusions whose sizes are significantly smaller than the laser wavelength in the crystal. It is proposed that the directed migration and other displacements of the induced defects over the crystal are due to the drag of the activated atoms by the free charge carriers in the laser field E_L and the external electric field E_{ex}. The diffusion coefficient and the effective charge of dragged laser-induced defects are estimated. © 2002 MAIK "Nauka/Interperiodica".

INTRODUCTION

Laser irradiation with a photon energy smaller than the semiconductor band gap $\hbar\omega \lesssim E_g$ (i.e., in the absence of direct single-photon generation of free carriers) can be considered among the nondestructive methods for transforming the bulk properties of semiconductor crystals [1–3]. In the case specified, at least two mechanisms of absorption are possible: by free charge carriers and by the inclusions of intrinsic and impurity components of defects. The absorption of radiation leads to the heating of inclusions and the diffusion of their components into the crystal host. Laser-induced point defects are foreign with respect to the lattice and, thus, cause high local perturbation and a large deviation from equilibrium. The activated defects may either effectively recombine with the electrically active vacancies (originally independent of defects) or occupy a stable interstice. The local fields of elastic stress manifest themselves in a shift in the energy levels of the point defects existing in the crystal [4].

The fraction of laser-annealed equilibrium defects [3] is governed by the laser power density at the target, the time of exposure, the laser wavelength, as well as by the nature and concentration of impurities, which is basically consistent with the model of laser-induced local thermal-diffusion sources [5–6] but fails to explain the directed motion of defects [7]. Furthermore, under the condition of steady-state irradiation, which implies the uniform heating of an inclusion, this mechanism provides only an isotropic source of single atoms in the vicinity of an inclusion. These two reasons motivated recent suggestions to consider the migration of atoms activated by the laser electromagnetic field; this approach ensures the contactless application of a strong electric field to the semiconductor crystal, which could hardly be accomplished by other means, especially in the narrow-gap semiconductors. Within the context of this model, variations of the defect concentration with the time of laser irradiation should be expressed in terms of the diffusion under the action of external forces, specifically, the electric field of the laser wave E_L. The electric field E_L affects the motion of an activated particle directly if it is charged and via the interaction between free carriers and particles irrespective of whether the latter are charged or neutral. In either case, the necessary condition for the motion of particles over the crystal lattice is a change in their kinetic energy which should be sufficient for them to surmount the potential barrier and enter into a stable state, i.e., a lattice site or interstice.

It is, therefore, reasonable to expect that experiments will confirm the dependence of the defect production rate on both the concentration of free carriers (for the constant laser power density W = const) and the electric field of the laser wave E_L for crystals with identical concentrations of free carriers. Anisotropic migration in the combined E_L field and the external electric field E_{ex} is also expected.

EXPERIMENTAL

Irradiation was performed at room temperature. The crystal temperature was maintained below 473 K. Thermal annealing at such temperatures in similar conditions produced no change in the bulk properties of the treated materials. The laser power density was chosen below the detectable damage threshold and varied within 5 W/cm$^2 \lesssim W \lesssim$ 35 W/cm^2. The lower limit of
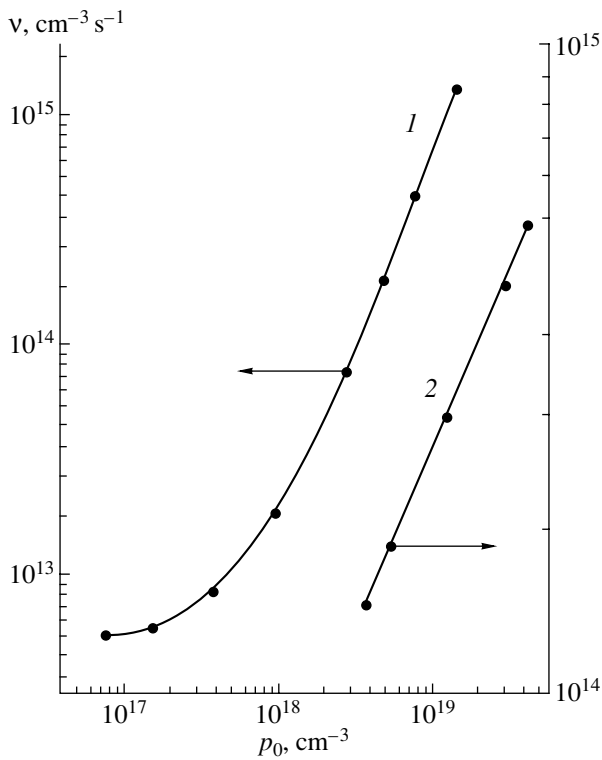
Fig. 1. The rate of production of defects ν in the laser-irradiated (curve *1*) PbTe and (curve *2*) PbSnSe crystals versus the free carrier concentration p_0. Laser power density $W =$ (*1*) 20 and (*2*) 7.5 W/cm^2; all measured at $T = 77$ K.

W corresponds to the power density that leaves the crystal structure unchanged over a considerable exposure time. The external electric field was constant and did not exceed $E_{ex} \lesssim 1$ V/cm. The source of radiation was a CO laser with $\lambda = 5–6$ μm or a CO$_2$ laser with $\lambda = 10.6$ μm.

For experimental samples, we used IV–VI semiconductor crystals, which were grown by the Czochralski and Bridgman–Stockbarger methods and by planar crystallization from the melt or vapor phase. The samples were doped directly during growth. Doping impurities of Na, Tl, Ga, and In were introduced to vary the concentration of the charge carriers, while the paramagnetic impurities of the transition metal (Mn) and the rare-earth (Eu) groups served as indicators of impurity localization in the lattice. The charge carrier concentration and the conductivity type were controlled by the dopant concentration and the deviation from stoichiometry in the range of 2×10^{16} cm$^{-3} \lesssim p, n \lesssim 10^{20}$ cm^{-3}. Small amounts of manganese and europium were introduced into the crystal ($N_{imp} \approx 10^{18}$ cm^{-3}) when the line of exchange interaction had yet to appear in the electron spin resonance (ESR) spectra. When Mn occupies the sites or interstices, the half-width of the lines and the g factor of Mn ions are different and well known [8], which allows the use of ESR to determine the position of ions in the lattice.

The impurity distribution along the crystal was derived from the Hall effect measurements and also from the dependences of the ESR line integrated intensities on the time of interaction, the laser power density, and the E_{ex} and E_L mutual orientation.

RESULTS

The main contribution to the absorption of laser radiation in the 5- to 10-μm range comes from the absorption in free carriers; therefore, when only the direct absorption by the inclusions occurs, the rate of the production of defects $\nu = dN/dt$ should be higher in the crystals with low charge carrier concentrations. However, our experiment demonstrated an increase in ν with the carrier concentration p_0 (Fig. 1). Laser-induced transformations studied in the crystals with different concentrations of free carriers suggest that, in order to obtain the same fraction of annealed defects $\Phi(t) = [N_0 - N(t)]/N_0$ in crystals with initially lower carrier concentration, laser annealing with a higher power density is required.

For nearly all of the crystals studied, a certain lower limit of free-carrier concentration exists; at this limit, the effect can still be detected at the maximum allowable laser power densities. For example, in Si:P and GaAs:Te(Sn) crystals with a carrier concentration $n \lesssim 10^{15}$ cm^{-3} and at the laser power density $W \lesssim 10^2$ W/cm^2, redistribution of the intrinsic and impurity point defects was not observed. For IV–VI compounds, we failed to reveal the lower limit of concentration because of the special features of the phase diagram, which preclude the obtaining of crystals with a carrier concentration close to the intrinsic value (~10^{16} cm^{-3}) without special doping or heat treatment. Moreover, lowering the carrier concentration in the narrow-gap semiconductors loses its efficiency, since the laser irradiation with the power densities used in the experiment heats the crystal so that the carrier concentration differs from what it was initially at room temperature, and, in the crystals with low carrier concentrations, it will be close to the intrinsic value.

The rate of change in the concentration of the laser-induced defects ν also depends on the laser power density W. Figures 2a and 2b present the dependences of ν on the power density W at the sample surface and on the electric field E_L in the laser wave propagating in the IV–VI crystal samples. Each dot in the curve corresponds to the same initial carrier concentration. It can be seen that all the dependences $\nu(W, E_L)$ are not linear, and the curves for the crystals with different initial concentrations of free carriers display a qualitative similarity. However, the values of the electric field E_c and the power density W_c corresponding to the kink in the $\nu(W, E_L)$ curves (a change in their slope) are different.

Concentrations of electrically active defects along the p-PbSnTe crystal under the combined effect of the laser wave field E_L and the external constant electric
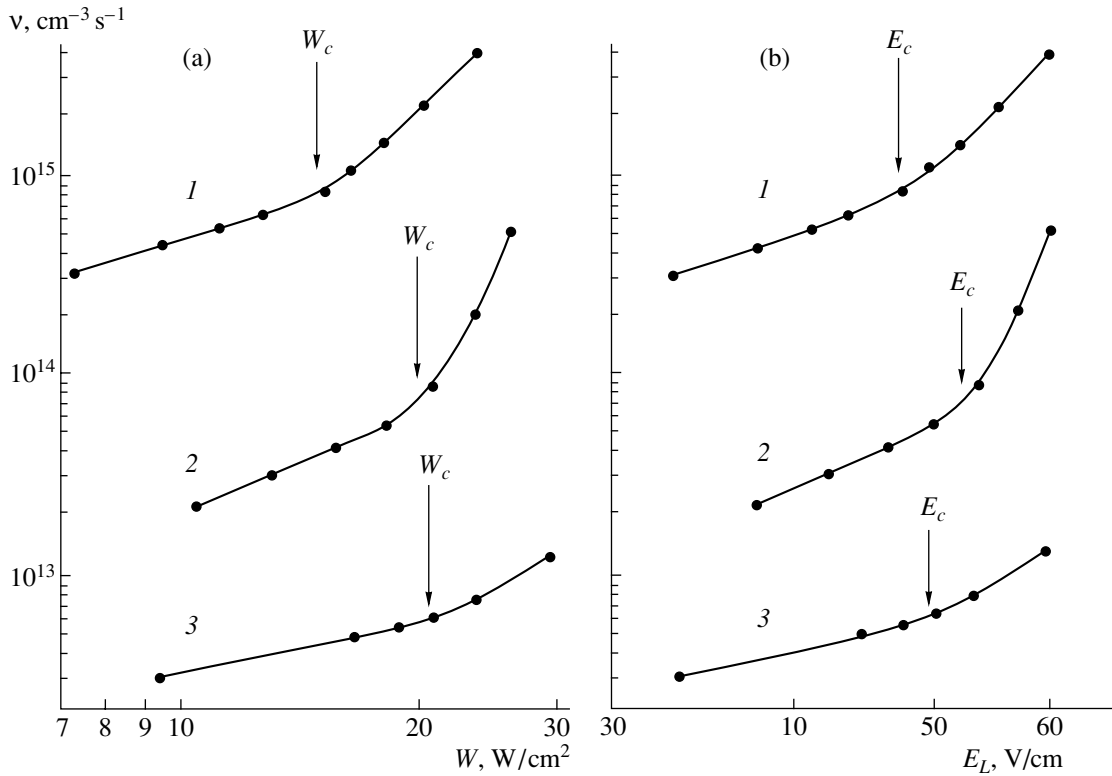
Fig. 2. The rate of the laser production of the intrinsic defects ν versus (a) the laser power density W at the sample surface and (b) the electric field E_L in the laser wave for (*1*) p-PbSnSe, (*2*) p-PbTe, and (*3*) p-PbSnTe. The initial concentration of carriers at $T = 77$ K $p =$ (*1*) 20×10^{18}, (*2*) 2.8×10^{18}, and (*3*) 0.51×10^{18} cm^{-3}.

field E_{ex} are depicted in Fig. 3. The direction of the E_{ex} field lies in the polarization plane of the laser wave $E_{ex} \parallel E_L$. The value of E_{ex} is lower by more than an order of magnitude than the maximum of $E_L \lesssim 70$ V/cm in the material. The first effect to appear in the crystal during the action of the E_{ex} and E_L fields was the conductivity-type conversion (it takes a time which is shorter by an order of magnitude than that required in the absence of E_{ex}); the next effect that occurred was the redistribution of the intrinsic defects along the sample in the direction of the external field E_{ex}. The distribution of the carrier concentration established after 10–14 h of irradiation at $W = $ const is shown in Fig. 3. The carrier concentration in crystal is controlled by electrically active intrinsic point defects; therefore, the resulting distribution of the carrier concentration may be uniquely related to the redistribution of the intrinsic defects along the crystal. The distribution can be almost inverted by changing the direction of the external electric field E_{ex} for some time in the vicinity of the moment of conductivity conversion. ESR spectra of Mn and Eu ions measured in PbTe:Mn(Eu) single crystals after irradiation under similar conditions gave a similar distribution of ions of the paramagnetic impurities (Fig. 4, curves *1*, *2*) in the case where the impurity concentration does not affect the carrier concentration. A significant growth in the concentration of Mn and Eu ions is
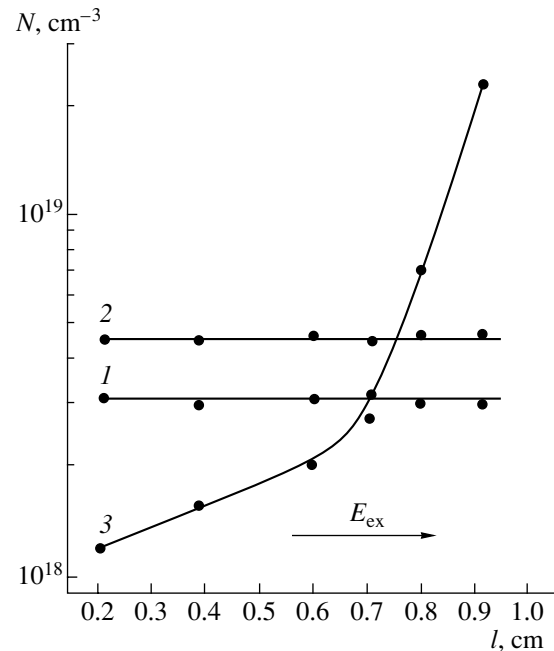

Fig. 3. Distribution of the free carrier concentration in PbTe crystal under the combined effect of laser radiation and a constant external electric field: (*1*) as-prepared sample, (*2*, *3*) after the conversion of the conductivity type as a result of irradiation for (*2*) 90 and (*3*) 1.08×10^3 min.
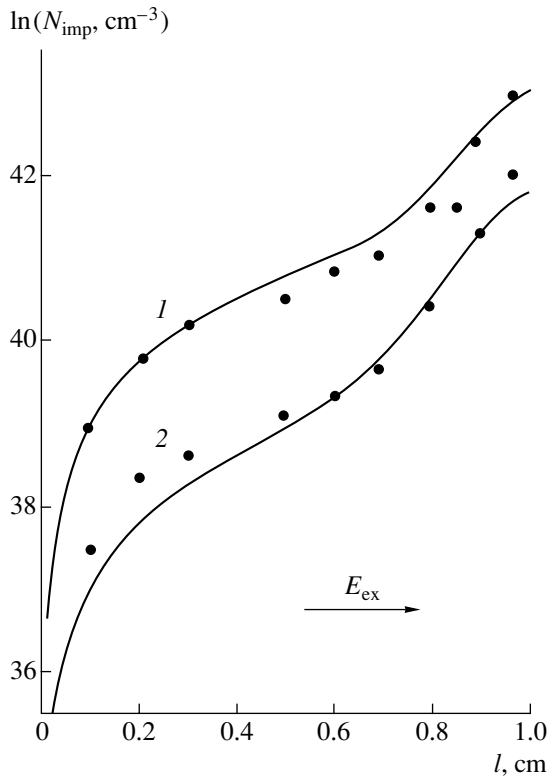
Fig. 4. Distributions of Eu and Mn impurities in (*1*) PbTe:Eu and (*2*) PbTe:Mn crystals under the combined effect of laser radiation and constant external electric fields for (*1*) 840 and (*2*) 960 min.

observed in the near-cathode region of the sample, which correlates with the variation in the carrier concentration along the sample (Fig. 3). For the distributions shown in Fig. 4, it is also possible to obtain mirror images but not reverse conversion of the conductivity type.

The fraction of annealed defects depends on the E_{ex} and E_L mutual orientation as $\Phi(\theta) = \Phi_0 + \Phi_{max}\cos^2\theta$, where θ is the angle between the directions of E_{ex} and E_L. The Φ_0 and Φ_{max} values denote the values of Φ at $\theta = n\pi/2$ and $\theta = n\pi$, respectively.

It is possible to find a laser power density W at which, in the absence of the external field E_{ex}, a change in Φ can not be detected within experimental accuracy, while the application of E_{ex} makes such a change in Φ evident. Moreover, it is impossible to observe the anisotropy of Φ without an external electric field. An alternating external field also suits this purpose; however, one fails to obtain the directed motion of ions in this case.

DISCUSSION

All the changes that take place in a crystal exposed to laser radiation are due to the following two factors: a high concentration of electrically active vacancies ($N_V \approx$

10^{19} cm^{-3}) in both the metal and chalcogenide sublattices, and the presence of neutral regions (inclusions) enriched with intrinsic or, for the doped crystals, with impurity components, as well as with their compounds. The inclusions are represented in the host in a variety of shapes and with a considerable scatter in their sizes: from 100 Å to 100 μm [9–11]. Though these studies do not give the concentrations of the inclusions in an explicit form, they can be readily obtained from the results presented there. Thus, the concentration of Pb inclusions with a size of $R_{inc} \approx 1300$ Å in PbTe was estimated as $N_{inc} \approx 1.4 \times 10^{16}$ cm^{-3}, which, after the conversion to the Pb atoms per unit volume, yields ~(1–5) × 10^{18} cm^{-3}. In fact, this value of the concentration of inclusions in the PbTe matrix is inconsistent with the data obtained from the measurement of the optical absorption in the same crystals, which is by 3–4 orders of magnitude lower than the $\alpha_{inc} \approx S_{inc}N_{inc}$ value calculated from the attenuation of radiation by the inclusions of size d. Hence, it follows that the actual concentration of the inclusions of size d in the matrix should either be lower than 10^{12} cm^{-3} or increase slightly with a decrease in the absorption cross section S_{inc}. Laser-induced conversion of the conductivity type attained in the undoped IV–VI crystals with an initial concentration of free holes ~2×10^{19} cm^{-3} gives strong evidence that the concentration of Pb atoms in the inclusions should be at least of the same order of magnitude but not lower. This yields the average distance d between the inclusions ($N_{inc} \approx 1/d^3$) as $d \approx 10^3$–10^4 Å.

In the previously chosen model of laser-induced point defect production, the isolated impurity centers are assumed to arise from the inclusions of the intrinsic or impurity components heated from the direct absorption of the laser radiation, which leads to a temperature gradient at the inclusion/host interface and to the mass transfer induced by thermal and diffusion processes [5–6]. In the host, the temperature gradient drops rapidly; therefore, the mechanism described above may only provide a source of separate activated atoms in the vicinity of an inclusion. The estimations made within this model show that the temperature of inclusions whose radii are in the range of 10^{-1} μm $\lesssim R \lesssim 1$ μm changes by 10^{-4}–10^{-3} K with respect to the initial value. Even the assumption that the temperature of inclusion is shape-dependent and grows by a factor of 7 and 30, respectively, in the cylinder- and plate-like inclusions gives no grounds to expect noticeable thermal diffusion of the inclusion components into the host. However, because of the nonuniform distribution of inclusions, there always exist regions where a large number of inclusions can be found within the laser wavelength: $(R_{inc} + d) \ll \lambda_L$. These regions are characterized by a different absorption mechanism, and a situation is possible where the absorption cross section is ~10^2 times as large as the transverse size of an inclusion. Under certain conditions, with allowance made for the field of the

dipole moments induced in the inclusions by the external wave, the electric field in the inclusions E_{inc} is of the same order of magnitude as the electric field in the laser wave E_L [12]:

$$E_{\text{inc}} = \frac{E_L}{1 + (\varepsilon - 1)(\delta - \beta V/d^3)}. \quad (1)$$

Here, δ is the depolarization factor equal to 1/3, 1/2, and 1 for a sphere, cylinder, and plate, respectively; β is a coefficient that depends on the inclusion configuration with respect to the local field and is close to 1/3; $\varepsilon(\omega)$ is the permittivity of the inclusion; V is the inclusion volume; and $d \approx N_{\text{inc}}^{-1/3}$ is the average distance between the inclusions.

It is important to note that, if a crystal contains regions where $\delta \approx \beta V/d^3$, then the local electric field in an inclusion is ε-independent. According to the experiments with optical absorption of laser radiation, the probability that some regions in the crystal contain a large number of inclusions within the laser-wavelength distance is rather high. For inclusions the size of which satisfies $l \approx 10^{-6}$–10^{-5} cm $\gtrsim R_{\text{inc}}$ (where l is the electron mean free path), the absorption cross section can be expressed as [13]

$$\sigma_{\text{inc}} = (64/411)(\mu/\hbar\omega)^2 S_{\text{inc}}. \quad (2)$$

The Fermi energy μ for the metal inclusions is about several electron volts. Assuming for definiteness that $\mu = 5$ eV and taking the photon energy $\hbar\omega = 0.117$ or 0.248 eV, we have $\sigma_{\text{inc}}/S_{\text{inc}} \approx 63$ or 3×10^2, respectively. In this case, the temperature of an inclusion will be significantly higher than that of an isolated inclusion:

$$\Delta T_{\text{inc}} = \sigma_{\text{inc}} W/3KR_{\text{inc}}. \quad (3)$$

Here, W is the laser power density and K is the thermal conductivity of a semiconductor crystal. Our estimations at $R_{\text{inc}} = 650$ Å and $W = 25$ W/cm² showed that the temperature in the inclusions exceeds the initial value by $\Delta T_{\text{inc}} \approx 2.6$ K. Cylinder- and plate-shaped inclusions of equal volume may feature the same ΔT_{inc} if the distance between the inclusions is sufficiently small. Otherwise, the condition $\delta \approx \beta V/d^3$ is not satisfied and we return to the case of isolated inclusions, where the near-ΔT_{inc} temperatures can only be attained for the inclusions whose size is several times larger than the laser wavelength in the crystal. This only extends the range of sizes that an inclusion has to interact with the laser wave and presents an additional (rather than a competitive) mechanism which implies a certain dependence on the parameters of the laser wave, crystal history, and the nature of inclusions. Both the absorption cross section σ_{inc} and the field E_{inc} may differ considerably for crystal intrinsic defects and impurities. This is apparently a prerequisite for the donor character of the laser-induced defects in IV–VI compounds.

The above discussion leads one to conclude that laser irradiation with $\hbar\omega \lesssim E_g$ necessarily gives rise to a temperature gradient at the inclusion/host interface of crystals. Mass transfer of the inclusion components into the surrounding area causes the local excitation of the system and produces a considerable deviation of the lattice from the former equilibrium state. A new equilibrium state is established via the reconstruction of a lattice with the relaxation of the local oscillations of atoms surrounding the defect. The amplitude of the atom displacement is defined by the relaxation properties of the lattice, i.e., by the fraction of ionic bonds in the crystal. Such a short-time appearance and disappearance of the intense local oscillations accompanying the introduction of an atom from the inclusion into a practically cold host not only essentially enhances the probability of the transport of defects (which does not require the thermal activation energy) but also considerably facilitates the new point-defect formation. In this case, the concentration of laser-induced defects will be primarily a function of the laser power density and the wavelength. This model, however, fails to account for the dependence of the defect production rate (i.e., the flux of the inclusion components) on the initial carrier concentration; moreover, the model predicts an increase in the production rate with a decrease in the carrier concentration. We would like to note that it is the concentration of free carriers rather than that of electrically active vacancies that is implied here. It is exactly for this purpose that we used the crystals grown at the same temperature, while the carrier concentration was varied by the introduction of impurities with concentrations no higher than $N_i \lesssim 10^{19}$ cm^{-3}. Because of this, we may consider the concentration of vacancies as constant. Alternatively, we should not entirely disregard the contribution of vacancies to the laser-induced mass transfer because of their direct participation in the relaxation of the activated defects.

The dependence of ν on the carrier concentration, as well as the directional migration of atoms and the dependence of the mass-transfer direction and efficiency on the mutual orientation of E_{ex} and E_L fields, may be explained under the assumption that the electric field causes not only the drift of ions but also the interaction of diffusing particles with free charge carriers, which drag the ions. Two slopes displayed by the dependences $\nu(p_0)$ in Fig. 1 indicate a change in the mechanism of laser-induced mass transfer. Thus, the mechanisms that prevail at low carrier concentrations are the entrainment of a substance from the inclusions due to thermal diffusion and the drift of ions in the field E_L, with both of them only slightly affecting the concentration of defects within the allowed range of W. This gives evidence to the effect that thermal diffusion and drift in the E_L field can only be a source of activated centers (atoms, ions) in the lattice rather than play the main role in mass transfer. At the same time, the activated states may be the centers of the effective scattering of free carriers. For a normal host atom interacting

with the external field and the free charge carriers, the effective charge of drag Z_{eff} is zero, while, for an activated host or dopant atom, $Z_{eff} \neq 0$. A noticeable entirely ionic transfer in the electric fields $E < 70$ V/cm is hardly possible in solid crystals even for the activated atoms at near-room temperature.

Theoretical aspects of the drag in metals and semiconductors are presented in [14]. In certain cases, experimental evidence for this effect was obtained when studying the diffusion of impurities in metals and semiconductors [15]. The transfer of momentum to the scattering centers was considered with allowance made for the effect of the crystal lattice, which allows one to attribute the diffusion in the external electric field to the drag of ions by the charge carriers. The electron drag of ions also manifests itself in semiconductors despite a significant (several orders of magnitude) difference in carrier concentrations. The effect can be observed in semiconductors because of the lower (thermal) velocities of the charge carriers and, consequently, the considerable scattering cross section of the activated atoms in these materials. Another special feature of semiconductor crystals is that the ions may be dragged by either holes or electrons, which induces the migration of ions along the external electric field E_{ex} or in the opposite direction, respectively. Moreover, the drag of normal lattice-site ions in p-type semiconductors is also possible when the balance of forces from the external field and the charge carriers is upset. However, the small-amplitude oscillations of ions about their equilibrium sites would hardly allow them to take part in the migration processes, even if the total force acting on them is nonzero.

The drag of impurity ions by charge carriers can be evaluated using the scattering cross sections for the normal ions. Then, the effective dragged charge of entrainment is expressed as

$$Z_{eff} = nl\langle \sigma_n \rangle, \qquad (4)$$

where l is the mean free path, $\langle \sigma_n \rangle$ is the scattering cross section, and n is the carrier concentration.

Since the cross section $\langle \sigma_n \rangle$ of normal ions is directly proportional to $1/\varepsilon_0^2$, one may expect the effective charge of entrainment to be close to unity in the semiconductors with a low permittivity, high mobility, and a comparatively narrow band gap (Ge, Si, InSb, and InAs). In reality, it should be taken into account that the absorption cross section of the activated atoms σ_{ac} may be significantly greater than σ_n; this situation may result in quite a noticeable drag even in the semiconductors with high ε_0.

Neutral activated particles and even complexes can also contribute to drag. When slow electrons are scattered by neutral atoms, the energy-relaxation time depends neither on the carrier energy nor on the temperature. The latter circumstance enables the drag effect to be related to conductivity. Then, the total drag

charge of the neutral atoms can be determined from expression [14]

$$Z_{n,\,p} = \frac{20\hbar^3 \varepsilon_0}{em_0}\left(\frac{p\langle \tau_l \rangle_p}{k_p^2} - \frac{n\langle \tau_l \rangle_n}{k_n^2}\right), \qquad (5)$$

where $k_{n,\,p} = m_{n,\,p}/m_0$; p and n are the hole and electron concentrations, respectively; m_0 is the free electron mass; and $\langle \tau_l \rangle$ is the total relaxation time.

The special feature of the electric drift of neutral atoms is that it is only the drag by carriers that defines the direction of motion. In order to obtain large effective charges, one should choose materials with a high permittivity, such as the IV–VI semiconductors, for which $\varepsilon_0 \gtrsim 10^2$. Another advantage of these elements is that, because of the low enthalpy of vacancy formation $\Delta H_V^{M,\,X}$ [8, 16], they are characterized by a high concentration of electrically active intrinsic point defects $N, P \approx 10^{19}$ cm^{-3}. In other semiconductors, including silicon, germanium, and III–V compounds, the effective charge of entrainment may also far exceed unity.

The effective charge of drag Z_{eff} may be determined from the data of the experiment on the directional mass transfer (Fig. 4) of manganese and europium ions by considering the mass transfer in terms of the stimulated diffusion of ions in a uniformly doped crystal. For a sufficiently large time t, the dopant distribution along the crystal of the length l can be written in the form [15]

$$N(x, t) = A(t)\exp(\nu x/2D)\sin(\pi x/l). \qquad (6)$$

This expression makes it possible to directly determine the diffusion coefficient D from the dependence $N_{imp}(l) \equiv N_{Eu,\,Mn}(x)$, the drift velocity ν, and the effective charges of drag Z_{eff}. The two slopes displayed by the curves in Fig. 4 correspond to a twofold difference in D values, which are 7.7×10^{-7} and 1.5×10^{-6} cm^2/s, respectively. This result may be explained if we assume that the defects that take part in the migration are characterized by equal migration-activation energies for the corresponding effective charges. The effective charges Z_{eff} [16] were estimated for the electric field equal to E_{ex} (which is reasonable because it is just this field which "pulls") at $Z_{1eff} \approx 1.2$ and $Z_{2eff} \approx 3.1$, respectively. These values are in close correlation with trustworthy experimental values of europium and manganese charge states in IV–VI compounds. Solid curves in Fig. 4 show the dopant distributions along the crystal, which were calculated according to (6) with allowance made for the two mechanisms of migration of impurities in the presence of a constant external electric field.

Substituting the effective charges obtained above into (4) and taking the carrier concentration of ~$(2-10) \times 10^{18}$ cm^{-3} and the mean free path $l = (1-10) \times 10^{-7}$ cm, we arrive at quite a reasonable order-of-magnitude estimate for the cross section: $\sigma_{ac} \approx 10^{-12}$ cm^2.

The laser-induced diffusion of defects in two charge states also explains the dependences $\nu(W, E_L)$ shown in

Fig. 2 (in the absence of the external field E_{ex}). As evident from Fig. 2, the W_c and E_c values are slightly different for PbSnSe, PbSnTe, and PbTe; this may be caused by different activation energies for defect migration in these compounds. A significant increase in ν under the conditions $E > E_c$ and $W > W_c$ also implies that the concentrations of the activated centers in the two charge states are different, and the difference may be as large as 1–2 orders of magnitude.

The last point to be noted is the possibility of the reverse conversion of the conductivity type by reversing the direction of the external field E_{ex}. By adhering to the notion that the donor defects in IV–VI compounds are represented by chalcogen vacancies and interstitial lead, then one finds that the conversion of the conductivity type is controlled by interstitial lead in an activated state [3], while the lead vacancies are not filled up yet. In contrast, the fact that conversion is impossible in crystals that have acquired a distribution similar to that in Fig. 3 points to the complete filling of the lead vacancies even though the concentration of interstitial lead is still considerable. ESR studies of irradiated undoped crystals or crystals doped with ESR-inactive impurities suggest that the charge state of the interstitial lead is Pb^{+1}; however, judging by the intensity of the line, the concentration of these centers is considerably lower than that of the charge carriers, which is controlled by the chalcogen vacancies.

CONCLUSION

The experimental results presented above provide firm ground for one to conclude that the steady-state interaction of the laser radiation ($\hbar\omega < E_g$ with the power density below the thermal damage threshold) with IV–VI semiconductor compounds gives rise to donor point defects of both intrinsic and impurity-related origin. The production rate and the fraction of annealed defects are governed by the free-carrier concentration, the electric field of the laser wave E_L, and the external constant field E_{ex}, as well as by their configuration. In the narrow-gap compounds, of which PbSnTe(Se) is an example, the laser-induced defects may be encountered in two charge states with different concentrations and different migration activation energies.

We argue that the laser-induced intrinsic defects originate from the regions of accumulation of submicron inclusions with sizes $R_{inc} + d \ll \lambda_L$ and a density

that would suffice for the local electric field in the inclusion to become comparable with the E_L field. The transportation and directional migration of induced defects in the crystal lattice are due to the appearance of activated atoms and their drag by free charge carriers in the field of the laser wave E_L under the combined action of E_L and the external electric field E_{ex}.

REFERENCES

1. S. V. Plyatsko, Yu. S. Gromovoĭ, and F. F. Sizov, Kvantovaya Élektron. (Kiev) **29**, 93 (1985).

2. S. V. Plyatsko and V. P. Klad'ko, Fiz. Tekh. Poluprovodn. (St. Petersburg) **31** (10), 1206 (1997) [Semiconductors **31**, 1037 (1997)].

3. S. V. Plyatsko, Fiz. Tekh. Poluprovodn. (St. Petersburg) **34** (9), 1046 (2000) [Semiconductors **34**, 1004 (2000)].

4. Yu. S. Gromovoĭ, L. A. Korovina, S. V. Plyatsko, *et al.*, Fiz. Tekh. Poluprovodn. (Leningrad) **24** (2), 250 (1990) [Sov. Phys. Semicond. **24**, 152 (1990)].

5. N. N. Grigor'ev, T. A. Kudykina, S. V. Plyatsko, and F. F. Sizov, Semicond. Sci. Technol. **3**, 951 (1988).

6. N. N. Grigor'ev, T. A. Kudykina, S. V. Plyatsko, and F. F. Sizov, Infrared Phys. **28**, 307 (1988).

7. Yu. S. Gromovoj, S. V. Plyatsko, and F. F. Sizov, Mater. Lett. **8**, 495 (1989).

8. Yu. S. Gromovoj, S. V. Plyatsko, and F. F. Sizov, J. Phys.: Condens. Matter **2**, 10 391 (1990).

9. S. D. Darchuk, G. N. Panin, S. V. Plyatsko, *et al.*, J. Phys. Chem. Solids **51**, 1333 (1990).

10. S. D. Darchuk, T. Dietl, L. A. Korovina, *et al.*, Fiz. Tekh. Poluprovodn. (St. Petersburg) **32**, 786 (1998) [Semiconductors **32**, 700 (1998)].

11. R. Breshi, A. Camanzi, and V. Fano, J. Cryst. Growth **58**, 399 (1982).

12. A. Wocaun, J. G. Bergman, J. P. Heritage, *et al.*, Phys. Rev. B **24** (2), 849 (1981).

13. A. A. Benditskiĭ, L. V. Viduta, V. I. Konov, *et al.*, Preprint No. 291, IOF AN SSSR (General Physics Institute, Academy of Sciences of USSR, Moscow, 1987).

14. V. B. Fiks, *Ionic Conduction in Metals and Semiconductors* (Nauka, Moscow, 1969).

15. B. I. Boltaks, *Diffusion in Semiconductors* (Fizmatgiz, Moscow, 1961; Academic, New York, 1963).

16. J. P. Stark, *Solid State Diffusion* (Wiley, New York, 1976; Énergiya, Moscow, 1980).

Translated by A. Sidorova-Biryukova

ELECTRONIC
AND OPTICAL PROPERTIES
OF SEMICONDUCTORS

Physical Properties of Semi-Insulating CdTe:Cl Single Crystals Grown from the Vapor Phase

V. D. Popovich*, G. M. Grigorovich*, P. M. Peleshchak*, and P. N. Tkachuk**

* Ivan Franko State Pedagogical University, Drogobych, 82100 Ukraine
e-mail: vpopovych@yahoo.com
** Fed'kovich National University, 58012 Chernovtsy, Ukraine
Submitted November 8, 2001; accepted for publication November 28, 2001

Abstract—A vapor phase method for the growth of high-resistivity CdTe:Cl single crystals is described. The photoluminescence spectra of these crystals are studied as a function of the dopant content. The energy level position which determines the conductivity of these single crystals was determined from electric and photoelectric investigations. © 2002 MAIK "Nauka/Interperiodica".

1. INTRODUCTION

In recent years demand has arisen for structurally perfect semi-insulating CdTe single crystals for producing γ- and X-ray uncooled detectors. One of the methods for growing high-resistivity CdTe crystals is by compensating doping during the growth. As a rule, chlorine is the dopant. As a result of the self-compensation effect [1, 2], equilibrium between concentrations of the donor and acceptor levels is achieved. Due to this fact, the material becomes semi-insulating.

Liquid-phase growth which is a modification of the Bridgman [3, 4] and floating-zone methods [5, 6] is extensively used for growing high-resistivity, large-size CdTe:Cl crystals. These methods make it possible to obtain a semi-insulating material with the resistivity $\rho > 10^8$ Ω cm and with transport parameters which are suitable for application (the product of mobility by lifetime is equal to 10^{-4}–2×10^{-3} cm^2/V for electrons and 10^{-5}–10^{-4} cm^2/V for holes). Nevertheless, the homogeneity and structural perfection of such crystals are insufficient (there are twins, microcracks, and pipes). These circumstances reduce the efficiency of the detector material. From this standpoint, vapor phase growth is more acceptable, because it enables one to grow crystals at lower temperatures and with an insignificant deviation from the stoichiometric composition. Recently, attempts to grow semi-insulating CdTe:Cl by chemical transport reactions [7] and the modified Markov method [8] were carried out.

In this paper, the sublimation method of growth in vacuum of large homogeneous high-resistivity CdTe:Cl single crystals is described. We also report the results of studying the local energy levels in the band gap of these crystals.

2. CRYSTAL GROWTH

The crystal growth procedure consists of two stages: synthesis of the chemical compound and single-crystal growth. At the first stage, conditions are selected for producing a charge homogeneous in its chemical composition. At the second stage, we focussed on the formation of structurally perfect single crystals of a required size.

The charge synthesis was performed in quartz ampoules pumped out to the residual pressure of $p = 10^{-5}$ Torr. Cadmium and tellurium of "Ekstra" grade and preliminarily dehydrated CdCl$_2$ salt were used as the starting materials. We calculated appropriate weights assuming that Cl atoms substitute Te atoms in the CdTe matrix. A sealed cell was placed in a horizontal two-zone furnace in which it was gradually heated to 5–10°C above the CdTe melting temperature in the absence of a temperature gradient. At the same time, the furnace was rotated at a velocity of 10 min^{-1}. The ampoule was heat-treated for 12 h. During this time, the total synthesis of the chemical compound was completed. After this stage, the furnace temperature was lowered by approximately 50°C, and a 20–30°C temperature gradient was established along the ampoule. This regime is conducive to intense material transport into a cold zone through the vapor phase. Then, the gradient sign was reversed. Because the convective streams in the vapor phase are significant at such temperature conditions and Cl is a volatile element, an approximately uniform distribution of the dopant (Cl) is attained in the charge volume after 2–3 complete transports.

The quality of the synthesized charge ingot was tested by contactless resistivity measurements using an

E9-4 Q-meter. The resistivity was calculated according to the formula [9]

$$\rho = k\frac{Q_1 Q_2}{Q_1 - Q_2}\frac{f n^2 R^4 l}{L}, \qquad (1)$$

where ρ is the charge resistivity (Ω cm), f is the frequency (MHz), L is the coil inductance without the ingot (μH), n is the number of turns per cm (cm^{-1}) of the coil, R is the ingot radius (cm), l is the ingot length (cm), Q_1 is the coil quality factor without the ingot at the frequency f, Q_2 is the coil quality factor at the same frequency with the ingot inside the coil, and $k = 1.945 \times 10^{-4}$.

The second stage of CdTe:Cl growth consists in single crystal formation from a preliminarily mechanically ground charge using sublimation in a special cell pumped out to the pressure of $p = 10^{-5}$ Torr. The temperature gradient in the vertical furnace for single-crystal growth was selected in such a manner so as to provide preliminary cleaning of the nucleation and growth sites of the finest particles of the charge which could be found there during the pumping. In addition, the crystal growth rate at these temperature conditions was equal to the cell pulling speed.

This procedure was used to grow CdTe:Cl single crystals up to 40 mm in length and 18 mm in diameter without microcracks and cavities. The crystals were grown with three different Cl concentrations: $N_{Cl} = 10^{17}$, 10^{18}, and 10^{19} cm^{-3}.

3. THE PHOTOLUMINESCENCE STUDY

To determine the location of the energy levels and assess the homogeneity and perfection of the obtained single crystals, we studied the photoluminescence of the CdTe:Cl single crystals in the wavelength range $\lambda = 750$–1000 nm (the photon energy $h\nu = 1.25$–1.65 eV) at $T = 77.3$ K. The photoluminescence spectra from freshly cleaved surfaces taken from different parts of the crystals containing each of the three Cl concentrations were measured. For excitation, we used the light (632.8 nm) of a He–Ne laser with a radiation power of $P = 40$ mW and a beam diameter of 0.1 mm. Photoluminescence emission was analyzed using an MDR-24 monochromator with 600 grooves/mm diffraction grating.

Typical spectra of the steady-state photoluminescence of the CdTe:Cl single crystals are shown in Fig. 1. The photoluminescence spectrum of the crystals with Cl concentrations of $N_{Cl} = 10^{18}$ and 10^{19} cm^{-3} consists of a narrow line with the peak at $h\nu_{max} = 1.582$ eV and a broad structureless band near 1.4 eV. One can see that the photoluminescence spectra of the crystals with $N_{Cl} = 10^{17}$ cm^{-3} have an additional band of a much lower intensity with the peak at $h\nu_{max} = 1.545$ eV.

The dominant band at 1.582 eV is due to the radiative recombination of excitons in CdTe [10, 11]. The significant width of the structureless asymmetric band in the 1.4 eV region shows that this radiative process is
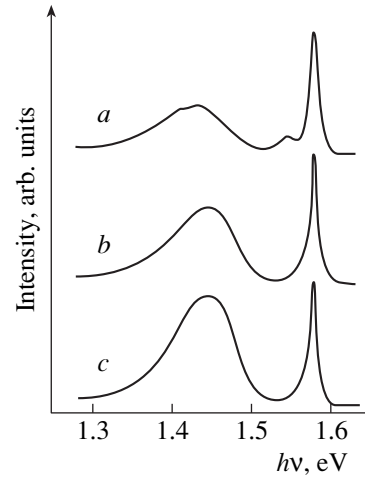

Fig. 1. Steady-state photoluminescence spectra of the CdTe:Cl single crystals, grown from the vapor phase, at $T = 77.3$ K. Cl concentration in the weight $N_{Cl} =$ (a) 10^{17}, (b) 10^{18}, and (c) 10^{19} cm^{-3}.

nonelementary. This band is due to so-called acceptor A centers, which consist of substitutional Cl atoms at the Te site and a nearest vacancy in the Cd sublattice $(V_{Cd}Cl_{Te})^-$. Their level is located at 0.14 eV above the valence-band top [12]. Radiative transitions from the conduction band to the acceptor level (short-wavelength component) and from the donor levels located within the donor–acceptor pair (long-wavelength component) to the acceptor level are not resolved at liquid nitrogen temperature [13]. The band maximum corresponds to $h\nu_{max} = 1.447$ eV for crystals with Cl concentrations $N_{Cl} = 10^{18}$ and 10^{19} cm^{-3}, whereas the band maximum for the samples with $N_{Cl} = 10^{17}$ cm^{-3} is shifted to longer wavelengths, and it corresponds to $h\nu_{max} = 1.432$ eV.

A similar shift was previously observed in [14]. This fact can probably be explained by the decrease in the distance between the components of the donor–acceptor pair with increased doping. This circumstance leads to an increase in the Coulomb interaction between them and to a shift to a high-energy region according to the relation [13]

$$h\nu = E_g - (E_A - E_D) + \frac{e^2}{\varepsilon R} + J(R), \qquad (2)$$

where E_D and E_A are the energies of the donor and acceptor levels relative to the corresponding band edges; ε is the dielectric constant of the crystal; R is the distance between the components of the pair; $J(R)$ is the exchange-interaction component which decreases rapidly with R; and E_g is the band gap.

It is possible that the band at 1.545 eV, typical of the crystals with a Cl concentration of $N_{Cl} = 10^{17}$ cm^{-3}, corresponds to the (conduction band)–(acceptor level) transition dominant in this region at the liquid-nitrogen temperature [15, 16]. We estimated the acceptor ioniza-
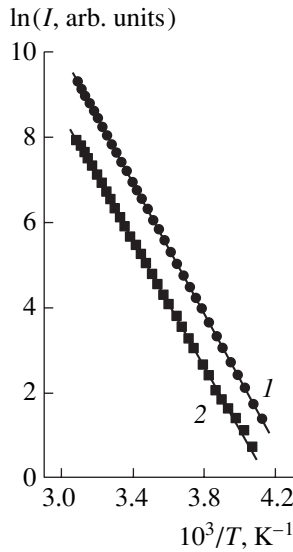
ln(I, arb. units)

Fig. 2. Dark-current temperature dependence of the CdTe:Cl single crystals grown from the vapor phase. Cl concentration in the weight $N_{Cl} = $ (*1*) 10^{18} and (*2*) 10^{19} cm^{-3}.

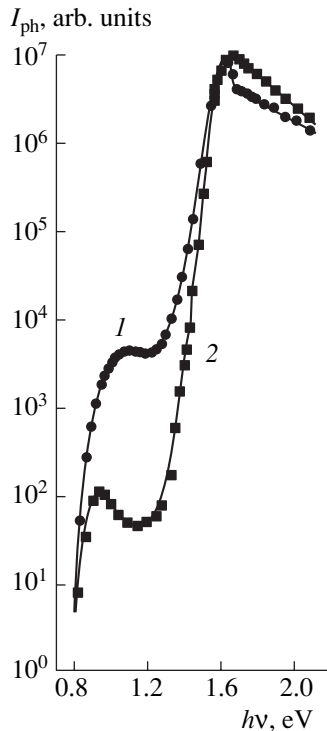**Fig. 3.** The photoconductivity spectrum (recalculated for the equal number of quanta) grown from the vapor phase at $T = 80$ K. Cl concentration in the weight $N_{Cl} = $ (*1*) 10^{18} and (*2*) 10^{19} cm^{-3}.

tion energy E_A from the peak position of this band [17]; i.e.,

$$h\nu_{max} = E_g - E_A + \frac{1}{2}k_B T_e, \qquad (3)$$

where $E_g = 1.602$ is the band gap of CdTe at $T = 77.3$ K, T_e is the electron temperature (which coincides with the lattice temperature at a low excitation level), and k_B is the Boltzmann constant. The obtained value of $E_A = 0.062$ eV is in good agreement with the energy position of the centers corresponding to singly ionized cadmium vacancies V_{Cd}^- of a fairly high concentration for the Cl doping under consideration [12].

It should be noted that the intensity of the photoluminescence bands for samples from different parts of the crystal was similar. This fact indicates that the homogeneity of the grown CdTe:Cl single crystals is very high.

4. ELECTRICAL AND PHOTOELECTRIC PROPERTIES

Hall effect measurements showed that the resistivity of the CdTe:Cl single crystals of *n*-type conductivity for a Cl concentration of $N_{Cl} = 10^{18}$ and 10^{19} cm^{-3} is equal to $\rho = (3–4) \times 10^8$ Ω cm at room temperature. The concentration of the majority carriers (electrons) is equal to $n = (5–7) \times 10^7$ cm^{-3}, and their Hall mobility $\mu_n = 300–400$ cm^2 V^{-1} s^{-1}. The Fermi level was calculated from the following relation for a compensated nondegenerate semiconductor [18]:

$$F = E_c + k_B T \ln \frac{N_D - N_A}{N_c}. \qquad (4)$$

Here, $N_c = 2(2\pi m_e^* k_B T/h^2)^{3/2} \approx 9.17 \times 10^{17}$ cm^{-3} is the effective density of states in the CdTe conduction band; the difference between the donor and acceptor concentrations $N_D - N_A = n$ at $T = 300$ K. We find from (4) that $F = E_c - (0.599–0.608)$ eV.

Crystals with $N_{Cl} = 10^{17}$ cm^{-3} are mostly of the *p*-type, and their resistivity is two orders of magnitude lower. These results correlate with the photoluminescence measurements and are due to a fairly high concentration of shallow acceptor centers V_{Cd} in the crystals with $N_{Cl} = 10^{17}$ cm^{-3}.

We studied the dark-current temperature dependences in semi-insulating CdTe:Cl single crystals to establish the positions of the deep levels, which have a dominant role in the electrical properties and transport phenomena. To produce electrical contacts for these (and photoelectric) measurements, we alloyed metallic indium on a freshly cleaved surface. Before the measurements, all samples were heated to $T = 330$ K and kept for a long time in the dark at room temperature to avoid the possible influence of thermally stimulated currents.

Typical temperature dependences of the dark current (*1*) of the crystals with $N_{Cl} = 10^{18}$ and 10^{19} cm^{-3} are shown in Fig. 2. One can see that the conductivity activation energy is the same for both concentrations (0.66 eV) in the temperature range $T = 250–330$ K.

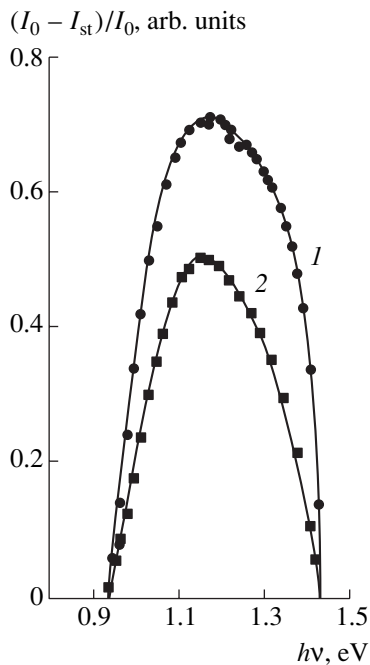$(I_0 - I_{st})/I_0$, arb. units

Fig. 4. Spectral distribution of the photocurrent optical quenching in the CdTe:Cl single crystals grown from the vapor phase at $T = 80$ K. I_0 is a background current, I_{st} is the steady-state photocurrent after quenching. The Cl concentration in the weight $N_{Cl} = (1)$ 10^{18} and (2) 10^{19} cm^{-3}.

Because these crystals are of the *n*-type, this ionization energy corresponds to the level located at 0.66 eV below the conduction band edge, i.e., near the Fermi level.

The CdTe:Cl single crystals with $N_{Cl} = 10^{18}$ and 10^{19} cm^{-3} have a high photosensitivity in the fundamental-absorption range both at liquid nitrogen and room temperatures. The photocurrent (I_{ph}) spectra for these crystals at $T = 80$ K are displayed in Fig. 3. The energies of the photosensitivity peaks are very close to the CdTe band gap at this temperature. The impurity photoconductivity region clearly appears at $h\nu < 1.3$ eV in the spectra of both samples. The energy position of a corresponding center can be determined from the onset of an abrupt increase in photosensitivity. The level of this center is located at 0.8 eV below the bottom of the conduction band.

Additional information about the localization of the sensitivity centers of the crystals with $N_{Cl} = 10^{18}$ and 10^{19} cm^{-3} was obtained from the study of photocurrent optical quenching under steady-state illumination in the fundamental-absorption region. The spectral distribution of the optical quenching at $T = 80$ K is shown in Fig. 4. The energy position of these centers relative to the valence band top was determined to be $E_v + 0.94$ eV from the long-wavelength edge of the quenching band. If we set the CdTe band gap at 1.602 eV at liquid nitrogen temperature [19], we obtain the energy of the center relative to the bottom of the conduction band, which

is equal to $E_c - 0.662$ eV. This value actually coincides with the energy level obtained from the dark-current temperature dependence.

It is most probable that this center manifests itself in the impurity photoconductivity of the semi-insulating CdTe:Cl single crystals as well. Levels with similar ionization energies are often related to the doubly ionized cadmium vacancy V_{Cd}^{2-} [13, 20]. The significant difference between the thermal and optical ionization energies can be attributed, in such a case, to penetration through the Coulomb barrier related to the center $E_c -$ 0.66 eV. However, recent studies have shown that the energy level corresponding to the Cd vacancies cannot be located at 0.47 eV above the valence band top of CdTe [14]. Therefore, more detailed studies are necessary in order to elucidate the nature of these centers.

5. CONCLUSION

Large homogeneous CdTe:Cl single crystals were grown by sublimation from the vapor phase. Semi-insulating crystals of the *n*-type with the resistivity $\rho = (3–4) \times 10^8$ Ω cm were obtained for the Cl concentration $N_{Cl} \geq 10^{18}$ cm^{-3} in the starting material. This was the result of a decrease in the concentration of the shallow acceptor level $E_v + 0.062$ eV with an increase in the level of doping. It was found that the conductivity of the CdTe:Cl single crystals obtained by the method mentioned above in the temperature range of 250–330 K is governed by the level located at 0.66 eV below the bottom of the conduction band.

REFERENCES

1. F. A. Kroger and J. Vink, Phys. Status Solidi **3**, 310 (1956).
2. G. Mandel, Phys. Rev. A **134**, 1073 (1964).
3. T. I. Milenov and M. M. Gospodinov, Nucl. Instrum. Methods Phys. Res. A **322**, 368 (1992).
4. P. Hoshl, P. Polivka, M. Vanecek, and M. Skrivankova, Rev. Phys. Appl. **12**, 229 (1977).
5. R. Triboulet, Prog. Cryst. Growth Charact. Mater. **85**, 128 (1994).
6. T. Shoji, H. Onabe, and Y. Hiratate, Nucl. Instrum. Methods Phys. Res. A **322**, 324 (1992).
7. N. A. Ukrainets, Author's Abstract of Candidate's Dissertation (NU "L'vovskaya Politekhnika", L'vov, 2000).
8. M. Fiederle, T. Feltgen, M. Rogalla, *et al.*, Nucl. Instrum. Methods Phys. Res. A **434**, 152 (1999).
9. A. L. Grokhol'skiĭ, *Quality-factor Meters – Q-meters* (Nauka, Novosibirsk, 1966).
10. Zh. R. Panosyan, Tr. Fiz. Inst. Akad. Nauk SSSR **68**, 147 (1973).
11. N. V. Agrinskaya, N. N. Zinov'ev, O. A. Matveev, and I. D. Yaroshetskiĭ, Fiz. Tekh. Poluprovodn. (Leningrad) **14**, 172 (1980) [Sov. Phys. Semicond. **14**, 100 (1980)].
12. Hage-Ali and P. Siffert, Nucl. Instrum. Methods Phys. Res. A **322**, 313 (1992).

13. D. V. Korbutyak, S. V. Mel'nichuk, É. V. Korbut, and M. M. Borisyuk, *Cadmium Telluride: Impurity–Defect States and Detector Properties* (Izd. "Ivan Fedorov", Kiev, 2000).

14. B. K. Meyer and W. Stadler, J. Cryst. Growth **161**, 119 (1996).

15. N. V. Agrinskaya, E. N. Arkad'eva, and O. A. Matveev, Fiz. Tekh. Poluprovodn. (Leningrad) **5**, 869 (1971) [Sov. Phys. Semicond. **5**, 767 (1971)].

16. N. V. Agrinskaya, O. A. Matveev, A. V. Nikitin, and V. A. Sladkova, Fiz. Tekh. Poluprovodn. (Leningrad) **21**, 676 (1987) [Sov. Phys. Semicond. **21**, 414 (1987)].

17. J. Saraie, H. Shinohara, H. Edanatzu, and T. Tanaka, J. Lumin. **21**, 337 (1980).

18. K. V. Shalimova, *Physics of Semiconductors* (Énergiya, Moscow, 1976).

19. A. V. Lyubchenko, E. A. Sal'kov, and F. F. Sizov, *Physical Foundations of Semiconductor Quantum Photoelectronics* (Naukova Dumka, Kiev, 1984),

20. N. V. Agrinskaya, E. N. Arkad'eva, O. A. Matveev, and Yu. V. Rud', Fiz. Tekh. Poluprovodn. (Leningrad) **2**, 932 (1968) [Sov. Phys. Semicond. **2**, 776 (1969)].

Translated by I. Kucherenko

ELECTRONIC
AND OPTICAL PROPERTIES
OF SEMICONDUCTORS

Low-Temperature Time-Resolved Photoluminescence in InGaN/GaN Quantum Wells

A. V. Andrianov, V. Yu. Nekrasov, N. M. Shmidt, E. E. Zavarin, A. S. Usikov, N. N. Zinov'ev, and M. N. Tkachuk

Ioffe Physicotechnical Institute, Russian Academy of Sciences,
Politekhnicheskaya ul. 26, St. Petersburg, 194021 Russia
Submitted December 6, 2001; accepted for publication December 18, 2001

Abstract—The results of the investigation of low-temperature time-resolved photoluminescence in undoped and Si-doped $In_{0.2}Ga_{0.8}N$/GaN structures, which contain 12 quantum wells of width 60 Å separated by barriers of width 60 Å, are reported. The structures were grown by the MOCVD technique on sapphire substrates. The photoluminescence properties observed are explained by the manifestation of two-dimensional donor–acceptor recombination. These properties are the high-energy shift of the peak upon increasing the pumping intensity, a low-energy shift with increasing delay time, and a power law of luminescence decay of the $t^{-\gamma}$ type. The estimates of the total binding energy for donor and acceptor centers are given. This energy is 340 and 250 meV for Si-doped and undoped quantum wells, respectively. The role of the mosaic structure, which is typical for Group III hexagonal nitrides, is discussed as a factor favorable for the formation of donor–acceptor pairs. © 2002 MAIK "Nauka/Interperiodica".

1. INTRODUCTION

At present, heterostructures and structures with quantum wells (QWs) based on InGaN/GaN systems are being intensively investigated. This is associated with the necessity of increasing the operating life of ultraviolet lasers and of extending the spectral range of semiconductor lasers [1, 2]. This is also associated with the application of these structures in the new generation of semiconductor electronic devices, which can operate at high temperatures [3].

Optical properties and, specifically, photoluminescence (PL) and electroluminescence of the structures with $In_xGa_{1-x}N$/GaN QWs have been investigated in many studies [4–16]. In some publications [8, 10], the luminescence in InGaN/GaN QWs was attributed to recombination of dimensionally quantized electrons and holes, which are strongly affected by the built-in piezoelectric field. This field emerges due to the distortion of the QW material. On the other hand, it was also reported that a piezoelectric field really exists in the structures with single QWs and is actually absent in the structures with multiple QWs, due to the stress relaxation [11, 12]. The model of recombination of excitons localized on the fluctuations of the solid solution is also used to explain the effective luminescence of the InGaN/GaN QWs [13–16]. According to this model, the fluctuations of In content give rise to potential wells for excitons or even quantum dots in the QW plane. These objects trap the excitons and act as the effective centers of radiative recombination. However, the entire set of known experimental data on the luminescence properties in the InGaN/GaN QWs cannot be explained

completely in the context of any of these models. Moreover, it is possible in some cases to encounter contradictions within one or another model used for the discussion even of a small group of experimental data. By virtue of this fact, further investigations and the establishment of the mechanisms responsible for spontaneous emission in actual device structures are urgently needed.

In this paper, we present the results of the investigation of time-resolved PL in structures with multiple InGaN/GaN QWs, both Si-doped and without special doping, which were formed by the MOCVD method on sapphire substrates.

2. EXPERIMENTAL

The structures were formed by the low-pressure MOCVD method on $Al_2O_3(0001)$ substrates and contained a GaN layer 2.5 μm thick; an $In_{0.1}Ga_{0.9}N$ layer 250 Å thick; 12 $In_{0.2}Ga_{0.8}N$/GaN QWs 60 Å thick, with barrier widths being also 60 Å thick; and then a GaN layer 0.1 μm thick. The results of the transmission electron microscopy investigation of the structures obtained are indicative of the high quality of the InGaN/GaN interfaces. The details associated with producing the structures were described previously [17]. Two types of structures were investigated, namely, Si doped to the level of $\approx 10^{18}$ cm^{-3} and nominally undoped Si.

Photoluminescence was excited by the radiation of a pulsed nitrogen laser ($\lambda_{exc} = 337$ nm), which operated at a frequency of 400 Hz with a pulse duration of 6 ns. The level of optical excitation varied within the range
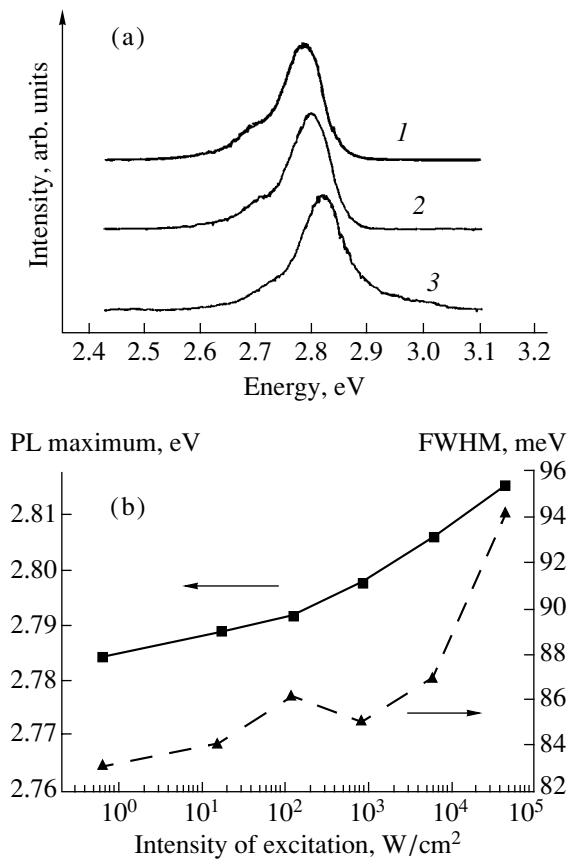
Fig. 1. Dependence of photoluminescence for Si-doped InGaN/GaN QWs on the excitation intensity. $T = 4.2$ K, zero delay. Photoluminescence is normalized to the largest signal, and the spectra, corresponding to various pumping intensities, are shifted along the vertical axis. (a) PL spectra normalized to the largest signal for various pumping intensities: (*1*) 0.6, (*2*) 120, and (*3*) 4×10^4 W/cm^2. (b) Position of the PL band peak and its half-width as a function of the excitation intensity.

from 0.6 to 4×10^4 W/cm^2, which was achieved using calibrated neutral filters. The photoluminescence was measured using a DFS-24 double diffraction monochromator and a FEU-100 photomultiplier, which possesses a high sensitivity and a relatively uniform spectral sensitivity in violet and ultraviolet spectral regions. The time-resolved PL spectra and kinetics of the emission decay were obtained using a measuring system based on a BCI-290 boxcar integrator linked to a computer. The total time resolution of the recording system was approximately 10 ns. The experiments were carried out mainly at the liquid-helium temperature (4.2 K). However, certain reference experiments were also carried out at $T = 78$ and 300 K.

3. RESULTS AND DISCUSSION

With low-intensity pumping (0.6 W/cm^2), the QW emission spectrum measured at the peak of the laser pulse (Fig. 1a) is represented by a band with a peak at 2.784 eV and a half-width of ≈ 83 meV. The low-frequency shoulder in the emission spectrum is probably determined by the phonon replica of the fundamental line at 2.784 eV. A small shift (no larger than 30 meV in the pumping range from 0.6 to 4×10^4 W/cm^2) of the PL band peak to the short-wavelength region can be seen with increasing photoexcitation intensity. A certain broadening of the PL band is also observed with an increase in the pumping intensity. This pattern, with variations of the PL spectrum with increasing excitation intensity, is illustrated in Fig. 1b.

The "violet" shift of the luminescence spectrum of InGaN/GaN QWs with an increase in the pumping intensity was observed in a large number of studies. One of the possible causes of this behavior is the screening of the built-in piezoelectric field by nonequilibrium charge carriers, which are generated as a result of optical excitation [8, 9, 18]. Actually, such screening should lead to the suppression of the dimensional Stark effect in the QW, which should cause a shift of the PL band to higher energies and a narrowing of this band as observed, e.g., in the case of isolated GaAs/AlGaAs QWs [19]. In the experiment with the structures which contain numerous InGaN/GaN QWs, the emission band is broadened with increasing excitation intensity (Fig. 1). Another explanation of the high-energy shift of the emission spectrum with an increase in pumping intensity is based on the effect of filling the localized tail states with nonequilibrium charge carriers [20, 21]. The recombination of excitons localized at compositional fluctuations of the solid solution was considered as the cause of the effective PL in the InGaN/GaN QWs [13, 14]. However, in the context of this model, it is rather difficult to explain the variations observed in the emission spectra at relatively low photoexcitation intensities ($\approx 10^2$ W/cm^2). The model of localized excitons is believed to be validated by the characteristic dependence of PL decay on the emission energy [14, 22]. This dependence is qualitatively similar to the dependence observed in the case of recombination of localized excitons in II–VI solid solutions [23]. The approach for the analysis of transient PL properties, which is similar to that used in studies [14, 22], for the InGaN/GaN QWs investigated in this study yields a radiative lifetime of localized excitons of about 60–70 ns, which seems to be unrealistic. These factors give no way of assigning the PL observed to the recombination of localized excitons. On the other hand, the shift of the PL peak to higher energies with an increase in pumping intensity can be associated with the manifestation of the recombination of donor–acceptor pairs. Two causes of the shift of emission bands of donor–acceptor pairs to higher energies with increasing photoexcitation intensity are possible. First, in the case of steady-state photoexcitation, the role of close pairs in the donor–acceptor recombination increases with an increase in the pumping intensity (see, e.g., [24, 25]). Second, nonequilibrium charge carriers can smooth the random potential relief, which, in its turn, is caused by a high

density of impurity centers. This was observed, for example, for the band of the donor–acceptor recombination in highly compensated GaAs [26]. The latter effect should also take place for nonsteady photoexcitation.

The curves of PL decay measured at various energies are shown in Fig. 2. It can be seen that the decay kinetics is distinctly nonexponential. The decay law is more likely close to the power law, specifically, $I_{PL}(t) \propto t^{-\gamma}$. This law is observed over the entire PL spectrum, although the parameter γ depends on energy. The parameter γ is close to 2 for emission energies below 2.78 eV, i.e., for the region where the major fraction of the PL of QWs is concentrated. It should be noted that the power law of PL decay of the t^{-2} type is a characteristic property of donor–acceptor recombination in semiconductors [27]. The time-resolved PL spectra (Fig. 3) also demonstrate behavior characteristic of donor–acceptor recombination. The shift of the PL spectrum to lower energies with increasing delay time between the peak of the laser pulse and the instant of detecting the PL is observed.

It is our opinion that the PL properties observed can be attributed to the manifestation of donor–acceptor recombination in the InGaN/GaN QWs under investigation. Such donor–acceptor pairs can be formed from donor and acceptor centers localized within a single QW and distributed in the QW plane. This recombination can be attributed to the two-dimensional (2D) donor–acceptor recombination. The participation of centers which belong to different QWs is also possible. In the latter case, the donor–acceptor recombination should be similar to three-dimensional donor–acceptor recombination.

The energy of photons emitted as a result of donor–acceptor recombination can be given in the following form [27]:

$$\hbar\omega = E_g - (E_a + E_d) + e^2/\varepsilon R. \qquad (1)$$

Here, E_g is the band gap; E_a and E_d are the binding energies of the acceptor and donor centers, respectively; ε is the static dielectric constant; and R is the distance between the centers. In the case of 2D donor–acceptor recombination, the E_g magnitude should be modified with allowance made for the dimensional quantization of electrons and holes; i.e.,

$$E_g = E_g(0) + \varepsilon^c_{n=1} + \varepsilon^v_{n=1}, \qquad (2)$$

where $E_g(0)$ is the band gap of the $In_xGa_{1-x}N$ solid solution; and $\varepsilon^c_{n=1}$ and $\varepsilon^v_{n=1}$ are the energies of dimensional quantization at the first level for electrons and holes, respectively. The data of study [28] permit us to set $E_g(0) = 3.07$ eV for the $In_{0.2}Ga_{0.8}N$ solid solution. The energies of dimensional quantization for electrons and holes in the QW of width 60 Å can be calculated using the method described, for example, in publication [29]. Let us accept discontinuities in the valence band and the conduction band to be equal to 120 and 380 meV,
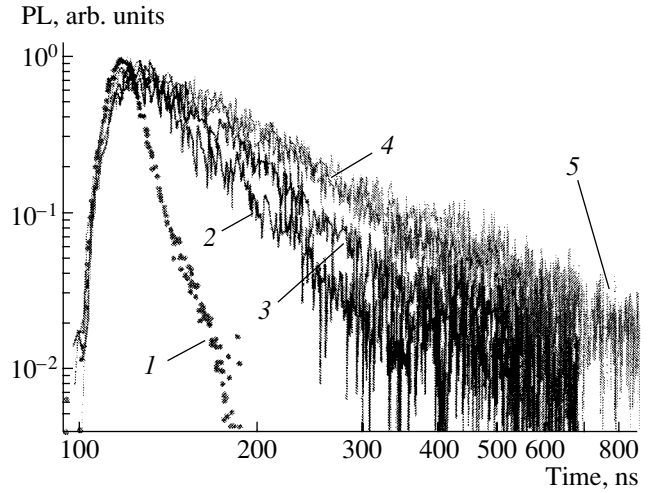

Fig. 2. Decay curves of photoluminescence for Si-doped InGaN/GaN QWs. Photoluminescence is normalized to the largest signal. $T = 4.2$ K; $I_{exc} = 0.6$ W/cm^2. (*1*) laser pulse, (*2*) PL at 2.83 eV, (*3*) PL at 2.81 eV, (*4*) PL at 2.77 eV, and (*5*) PL at 2.70 eV.
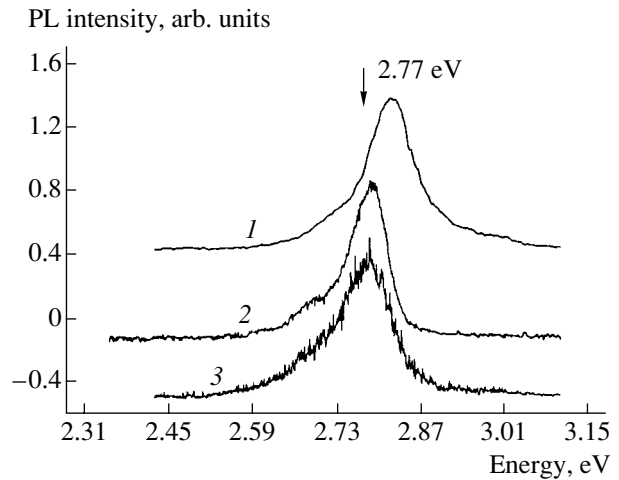

Fig. 3. Time-resolved PL spectra of Si-doped InGaN/GaN QWs for various delay times t_D. The spectra are normalized to the largest signal. $T = 4.2$ K; $I_{exc} \approx 10^4$ W/cm^2. $t_D =$ (*1*) 0, (*2*) 100, and (*3*) 450 ns.

respectively [28, 30], and neglect coupling of the electron and hole states in neighboring QWs. This is apparently an adequate approximation, since many parameters including effective masses are unknown. As a result, we obtain the value of 39 meV for $\varepsilon^c_{n=1} + \varepsilon^v_{n=1}$ and, correspondingly, 3.11 eV for the parameter E_g.

The time-resolved PL spectra, which were measured for considerable delay times, make it possible to determine $E_g - (E_a + E_d)$ and, consequently, the energies of centers, which contribute to donor–acceptor recombination. Under these conditions, the PL is determined mainly by widely separated pairs, and the Cou-
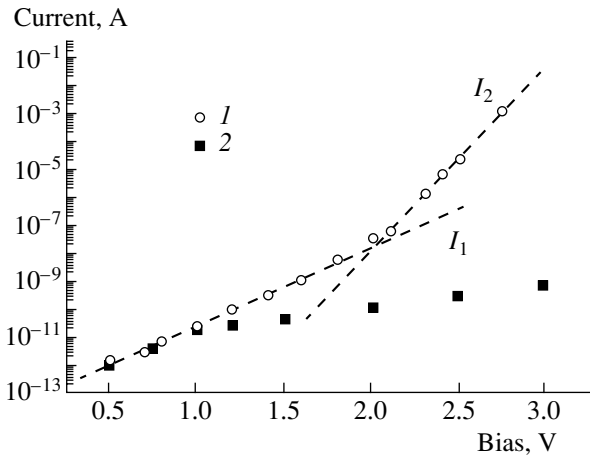
Current, A

Fig. 4. Current–voltage characteristics of light-emitting diode structures with the InGaN/GaN QWs. (*1*) The forward portion of the current–voltage characteristic and (*2*) the reverse portion. Graphic symbols represent experimental data, and dashed lines are the calculated exponential components of the tunnel current: $I_1 = I_{01} \exp(eV/E_1)$ and $I_2 = I_{02} \exp(eV/E_2)$, where the parameters E_1 and E_2 are temperature-independent and are equal to 180 and 58 meV, respectively.

lomb term in expression (1) is small. Such a method for determining the quantity $E_a + E_d$ was recently demonstrated for GaN [31]. It can be seen from Fig. 3 that the time-resolved PL spectra are noticeably shifted to lower energies only if the delay times are shorter than 100 ns. A further increase in the delay time leads to virtually no shift in the PL band. For this reason, from the peak of the PL spectrum, which corresponds to a large delay time and is measured at an acceptable signal-to-noise ratio (450 ns, as can be seen from Fig. 3), we obtain $E_g - (E_a + E_d) \simeq 2.77$ eV for Si-doped InGaN/GaN QWs. Consequently, the total energy of the donor and acceptor centers is ≈ 340 meV. This energy does not seem unusual since similar impurity centers are observed in GaN [31, 32]. A pronounced Stokes shift between the spectrum of the edge absorption and the PL spectrum has been reported for the InGaN/GaN QWs by many authors (see, for example, [33, 34]). In the context of donor–acceptor recombination, this shift finds a natural explanation.

Donor and acceptor centers responsible for the donor–acceptor recombination in the InGaN/GaN QWs, which were investigated in this study, can be associated both with impurities and with defects of the crystal lattice. It also seems that donor–acceptor recombination in the InGaN/GaN QWs is possible due to the mosaic or columnar structure, which is typical of hexagonal Group III nitrides. It is well known that all light-emitting devices with a high quantum efficiency are obtained based on hexagonal Group III nitrides with a high dislocation density. Dislocations form the mosaic or columnar structure with a characteristic domain size from 100 to 600 nm [35, 36]. The mosaic structure is

formed as a result of the interaction between the misfit and threading dislocations during the growth with expanding nuclei, which are formed on the surface during the low-temperature stage of epitaxial growth [37]. This interaction between dislocations is accompanied by the trapping of impurities such as oxygen and carbon. According to the SIMS data of many authors, the typical concentration of oxygen and carbon in the MOCVD-grown layers and structures is $\approx 10^{18}$–10^{19} cm^{-3} [38]. According to the electron microscopy data, some of the dislocation walls are formed by Ga vacancies, which are deep-level acceptors according to evaluations [39]. The complexes which contain oxygen and carbon, according to the data [32, 40], can be deep-level donors.

Thus, the mosaic structure can be favorable for the formation of donor–acceptor pairs. This supposition is also corroborated by the tunnel character of the current in light-emitting structures fabricated based on the investigated InGaN/GaN QWs (Fig. 4). It should be noted that the current–voltage characteristics of our structures, similarly to study [20], can be described by expressions of the type $I = I_0 \exp(eV/E_0)$ with the parameter E_0 independent of the temperature. Authors of publication [41] believe that the tunnel character of the current in the structures with the InGaN/GaN QWs is caused by the donor–acceptor mechanism of recombination.

The recombination via the tails of the conduction and valence bands, which is used by some authors to explain the luminescence properties of the InGaN/GaN QWs [20, 21], is a peculiar analogue of donor–acceptor recombination. In the course of such recombination, similarly to donor–acceptor recombination, tunnel transitions between the localized states of electrons and holes take place. Such tail states in the vicinity of the conduction band bottom and the valence band top could be caused by defects of the crystal lattice, fluctuations of the composition of the solid solution, and, in addition, the mosaic structure of Group III nitrides. It should be noted that, along with a series of common features between recombination via tail states of bands and donor–acceptor recombination, a distinction exists. This is related primarily to the form of the density function for localized states. In the case of tail states, such a function, whose form is not known in the general case, should decrease steadily with increasing localization energy. In contrast with this, in the case of donor and acceptor centers, the density of states will have the form of the δ function for energies of donors and acceptors. This distinction in the density-of-states functions should lead to a distinction in the PL kinetics between donor–acceptor recombination and recombination via the tail states of bands. As far as we know, theoretical calculations which permit the correlation of these two mechanisms of recombination are absent. A qualitative consideration demonstrates that recombination via the tail states should lead to a wide variation in the decay kinetics over the PL spectrum. In contrast with this,
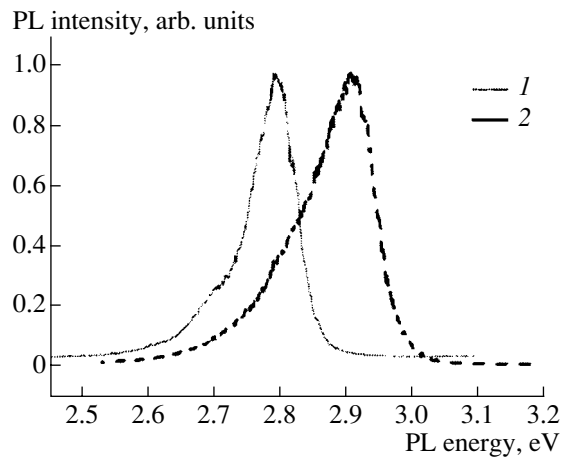
PL intensity, arb. units

Fig. 5. (*1*) Photoluminescence spectrum for Si-doped QWs, and (*2*) photoluminescence spectrum for undoped QWs. $T = 4.2$ K; $I_{exc} \approx 10^2$ W/cm^2, zero delay. Photoluminescence spectra are normalized to the largest signal.

conventional donor–acceptor recombination [27] comprises a process of gradual transition in preferential recombination from close pairs to distant ones, which is responsible for the power law of decay.

The photoluminescence of undoped InGaN/GaN QWs demonstrates similar spectral and temporal behavior, which allows us to also attribute this PL to donor–acceptor recombination. However, certain distinctions take place. Specifically, the PL spectrum with zero delay for undoped QWs is shifted to the high-energy region by about 120 meV and has a spectral width that is larger than that of the PL spectrum for Si-doped QWs by a factor of 1.5 (Fig. 5). The time-resolved spectra measured for long delay times yield the value of ≈ 250 meV for the total energy of the donor and acceptor centers. The photoluminescence decay for undoped QWs is more rapid. The decay kinetics also follows the power law of the $t^{-\gamma}$ type. In this case, the parameter γ varies over the spectrum from 3 to 6. It is possible that these distinctions in the PL behavior between Si-doped and undoped QWs are associated with various types of centers, which contribute to recombination, as well as with variations in the degree of compensation of the samples.

It is necessary to add to the aforesaid that our previous investigations of charge-carrier transport in individual epilayers of both undoped and lightly Si-doped GaN also demonstrated considerable distinctions [42]. It was found that carrier transport is profoundly affected by chaotically distributed charge, which is associated with the mosaic structure. For undoped GaN epilayers, low mobilities and pronounced scattering by charged centers are observed, whereas the carrier transport mechanism is similar to that for low-dimensional structures. In this case, the introduction of Si considerably lowers the potential barriers and actually eliminates the influence of these barriers for epilayers with

the pronounced mosaic structure, whereas the mechanism of carrier transport is the same as for elemental semiconductors. It was also found that frozen photoconductivity for lightly Si-doped layers, in contrast with undoped layers, was not observed at room temperature at all; at low temperatures, this quantity is smaller by an order of magnitude [43]. It seems likely that the introduction of Si in the QW structure of InGaN/GaN diminishes both the effect of random electric fields on the recombination of nonequilibrium carriers and the contribution of nonradiative channels to recombination.

4. CONCLUSION

The low-temperature time-resolved PL in In$_{0.2}$Ga$_{0.8}$N/GaN quantum wells was investigated. The structures were grown by the low-pressure MOCVD method on sapphire and contained 12 QWs of width 60 Å, which were separated by barriers of width 60 Å. We observed the following PL properties: a high-energy shift of the peak with an increase in the pumping intensity, a low-energy shift with a prolongation of the delay time, and a power law of PL decay of the $t^{-\gamma}$ type. These properties allow us to attribute this PL to donor–acceptor recombination in QWs. Such recombination, which can be assigned to the 2D donor–acceptor recombination, can proceed in a QW plane between the centers localized at various sites. Recombination between the centers localized in various QWs, which is a peculiar analogue of three-dimensional donor–acceptor recombination, is also possible. For Si-doped InGaN/GaN QWs, the total binding energy of the donor and acceptor centers is ≈ 340 meV. In the case of undoped QWs, this total energy is ≈ 250 meV. The experimental results obtained allow one to assume that the mosaic structure, which is typical of Group III nitrides, is favorable for the formation of donor–acceptor pairs.

REFERENCES

1. S. Nakamura, M. Senoh, S. Nagahama, *et al.*, Appl. Phys. Lett. **68**, 3269 (1996).
2. L. Akasaki, S. Sota, H. Sakai, *et al.*, Electron. Lett. **32**, 1105 (1996).
3. S. K. Islam, F. C. Jain, G. Zhao, and E. Heller, Int. J. Infrared Millim. Waves **19**, 1633 (1998).
4. S. Nakamura, T. Mukai, M. Senoh, and S. Nagahama, J. Appl. Phys. **74**, 3911 (1993).
5. R. Singh, D. Doppalapudi, and T. D. Moustakas, Appl. Phys. Lett. **69**, 2388 (1996).
6. W. D. Herzog, R. Singh, T. D. Moustakas, *et al.*, Appl. Phys. Lett. **70**, 133 (1997).
7. J. Dalfors, J. P. Bergman, P. O. Holtz, *et al.,* Appl. Phys. Lett. **74**, 3299 (1999).
8. T. Takeuchi, C. Wetzel, S. Yamaguchi, *et al.,* Appl. Phys. Lett. **73**, 1691 (1998).
9. A. Hangleiter, J. S. Im, H. Kollmer, *et al.*, MRS Internet J. Nitride Semicond. Res. **3**, 15 (1998).

10. L. H. Peng, C. W. Chuang, and L. H. Lou, Appl. Phys. Lett. **74**, 795 (1999).

11. T. Wang, D. Nakagawa, J. Wang, *et al.*, Appl. Phys. Lett. **73**, 3571 (1998).

12. T. Wang, T. Sugahara, S. Sakai, and J. Orton, Appl. Phys. Lett. **74**, 1376 (1999).

13. Y. Narukawa, Y. Kawakami, M. Funato, *et al.*, Appl. Phys. Lett. **70**, 981 (1997).

14. Y. Narukawa, Y. Kawakami, Shizou Fujita, *et al.*, Phys. Rev. B **55**, R1938 (1997).

15. X. Zhang, D. R. Rich, J. T. Kobayashi, *et al.*, Appl. Phys. Lett. **73**, 1430 (1998).

16. K. P. O'Donnell, R. M. Martin, and P. G. Middleton, Phys. Rev. Lett. **82**, 237 (1999).

17. A. V. Sakharov, V. V. Lundin, V. A. Semenov, *et al.*, Pis'ma Zh. Tekh. Fiz. **25** (12), 1 (1999) [Tech. Phys. Lett. **25**, 462 (1999)].

18. F. D. Salla, A. D. Carlo, P. Lugli, *et al.*, Appl. Phys. Lett. **74**, 2002 (1999).

19. S. Schmidtt-Rink, D. S. Chemla, and D. A. B. Miller, Adv. Phys. **38**, 89 (1989).

20. P. G. Eliseev, P. Perlin, J. Lee, and M. Osinski, Appl. Phys. Lett. **71**, 569 (1997).

21. T. Wang, H. Saeki, J. Bai, *et al.*, Appl. Phys. Lett. **76**, 1737 (2000).

22. S. F. Chichibu, T. Sota, K. Wada, *et al.*, MRS Internet J. Nitride Semicond. Res. **4S1**, G2.7 (1999).

23. C. Gourdon and P. Lavallard, Phys. Status Solidi B **153**, 641 (1989).

24. P. J. Dean and J. L. Merz, Phys. Rev. **178**, 1310 (1969).

25. E. Zacks and A. Halperin, Phys. Rev. B **6**, 3072 (1972).

26. V. P. Dobrego and I. S. Shlimak, Phys. Status Solidi **38**, 805 (1969); D. Redfield, J. P. Wittke, and J. I. Pankov, Phys. Rev. B **2**, 1830 (1970); H. P. Gislason, B. Y. Yang, and M. Linnarson, Phys. Rev. B **47**, 9418 (1993).

27. D. G. Thomas, J. J. Hopfield, and W. M. Augustyniak, Phys. Rev. **140**, A202 (1965).

28. H. Morkoc, F. Hfmdani, and A. Salvador, Semicond. Semimet. **50**, 193 (1998).

29. C. Weisbuch and B. Vinter, *Quantum Semiconductor Structures: Fundamentals and Applications* (Academic, Boston, 1991).

30. S. F. Chichibu, A. C. Abre, M. S. Minsky, *et al.,* Appl. Phys. Lett. **73**, 2006 (1998).

31. V. Yu. Nekrasov, L. V. Belyakov, O. M. Sreseli, and N. N. Zinov'ev, Fiz. Tekh. Poluprovodn. (St. Petersburg) **33**, 1428 (1999) [Semiconductors **33**, 1284 (1999)].

32. *Properties of Advanced Semiconductor Materials: GaN, AlN, InN, BN, SiC, SiGe*, Ed. by M. E. Levinshtein, S. L. Rumyantsev, and M. S. Shur (Wiley, New York, 2001), p. 1.

33. S. Chuhubu, T. Azuhata, T. Sota, and S. Nakamura, Appl. Phys. Lett. **69**, 4188 (1996).

34. P. Riblet, H. Hirayama, A. Kinoshita, *et al.*, Appl. Phys. Lett. **75**, 2241 (1999).

35. E. G. Brazel, M. A. Chin, and V. Narayanamutri, Appl. Phys. Lett. **74**, 2367 (1999).

36. X. Du, Y. Z. Wang, L. L. Cheng, *et al.*, Mater. Sci. Eng., B **75**, 228 (2000).

37. F. A. Ponce, MRS Bull. **22**, 51 (1997).

38. M. Razeghi, A. Saxler, P. Kung, D. Walker, X. Zhang, K. S. Kim, H. R. Vydyanath, J. Solomon, M. Ahoujja, and W. C. Mitchel, in *Physics of Semiconductor Devices*, Ed. by V. Kumar and S. K. Agarwal (Narosa Publishing House, New Dehli, 1998), Vol. 1, p. 277.

39. C. G. van de Walle, Phys. Rev. B **56**, R10020 (1997).

40. T. A. Kennedy, E. R. Glaser, J. A. Freitas, Jr., *et al.*, J. Electron. Mater. **24**, 219 (1995).

41. H. C. Casey, J. Muth, S. Krishnankutty, and J. M. Zavada, Appl. Phys. Lett. **68**, 2867 (1996).

42. N. M. Shmidt, V. V. Emtsev, A. S. Kryzhanovsky, *et al.*, Phys. Status Solidi B **216**, 581 (1999).

43. N. M. Shmidt, W. V. Lundin, A. V. Sakharov, *et al.,* Proc. SPIE **4340**, 92 (2000).

Translated by N. Korovin

SEMICONDUCTOR STRUCTURES, INTERFACES, AND SURFACES

Silicon Nanocrystal Formation upon Annealing of SiO$_2$ Layers Implanted with Si Ions

G. A. Kachurin*, S. G. Yanovskaya*, V. A. Volodin*, V. G. Kesler*, A. F. Leier*, and M.-O. Ruault**

* Institute of Semiconductor Physics, Siberian Division, Russian Academy of Sciences,
pr. Akademika Lavrent'eva 13, Novosibirsk, 630090 Russia
e-mail: kachurin@isp.nsc.ru
** CSNSM–CNRS/IN2P3, 91045 Orsay, France

Abstract—The formation of silicon nanocrystals in SiO$_2$ layers implanted with Si ions was investigated by Raman scattering, X-ray photoelectron spectroscopy, and photoluminescence. The excess Si concentration was varied between 3 and 14 at. %. It was found that Si clusters are formed immediately after implantation. As the temperature of the subsequent annealing was raised, the segregation of Si accompanied by the formation of Si–Si$_4$ bonds was enhanced but the scattering by clusters was reduced. This effect is attributed to the transformation of loosely packed clusters into compact, separate-phase nanoscale Si precipitates, with the Raman peak observed at 490 cm^{-1} being related to surface scattering. The process of Si segregation was completed at 1000°C. Nevertheless, characteristic nanocrystal photoluminescence was observed only after annealing at 1100°C. Simultaneously, scattering in the range 495–520 cm^{-1}, typical of nanocrystals, appeared; however, the "surface-related" peak at 490 cm^{-1} persisted. It is argued that nanocrystals are composed of an inside region and a surface layer, which is responsible for their increased formation temperature. © 2002 MAIK "Nauka/Interperiodica".

1. INTRODUCTION

Currently, considerable attention is being given to the investigation of nanometer-size silicon crystals. This is related, on the one hand, to a steady reduction in the dimensions of microelectronic elements and, on the other hand, to the observation of intense visible-light emission from nanocrystalline Si (nc-Si). Usually, nc-Si is obtained upon decomposition of the supersaturated solid solution that takes place under the annealing of SiO$_2$ layers containing a certain amount of excess Si [1–4]. Strong photoluminescence (PL) in the red–near-IR spectral range is only observed when the concentration of excess Si is higher than ~10^{21} cm^{-3} (~2 at. %) and the annealing temperature is as high as 1100°C [5–7]. In this context, a number of questions about the mechanism of nc-Si formation arise. For instance, one can argue that, in the case of diffusion-controlled growth of Si nanoprecipitates, the growth should proceed at lower Si concentrations, and lower annealing temperatures would be sufficient (although at the expense of a longer annealing duration). To reveal the mechanism of the nc-Si formation, one apparently needs to use techniques that can probe the effect of annealing on excess Si at earlier stages of the process, preceding the formation of light-emitting crystallites.

In this paper, we report the results of studying the behavior of excess Si in SiO$_2$ in a wide range of annealing temperatures. In addition to the PL, we use Raman scattering and X-ray photoelectron spectroscopy (XPS)

methods, which satisfy the above-mentioned requirements.

2. EXPERIMENTAL

Two types of samples were investigated: SiO$_2$ layers of ~ 80 nm thickness thermally grown on Si(100) and plates of silica glass polished on both sides. The advantage of the latter type of sample is the absence of strong scattering from the crystalline Si substrate that hinders the Raman measurements. The SiO$_2$ plates were implanted with 150-keV Si ions at a dose of 5×10^{16}, 10^{17}, or 2×10^{17} cm^{-2}; this corresponds to the mean excess Si concentration of about 3, 6, and 12 at. %, respectively. To examine the role of defects in the scattering, SiO$_2$ plates implanted with 150-keV Ar ions to a dose of 2×10^{17} cm^{-2} were also studied. The samples with thermally grown SiO$_2$ layers were implanted with Si ions to yield an excess Si concentration of about 14 at. %. The Raman spectra were recorded in the quasi-backscattering configuration with an Ar laser (λ = 514.5 nm) as the pump source; polarization was disregarded. The PL was excited by a nitrogen laser operating at 337 nm. Both the PL and the Raman spectra were measured at 20°C. To prepare the samples for the XPS measurements, the upper half of the implanted layer was removed by etching in a 1 : 8 aqueous solution of HF. A photoelectron escape depth of about 2–3 nm ensures that the most important region of the layer is
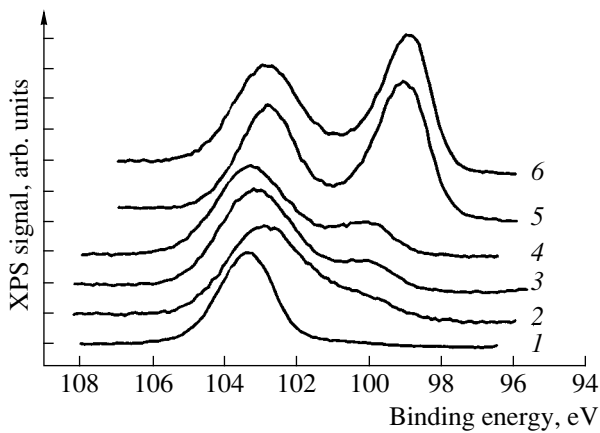
Fig. 1. The XPS spectra of thermal SiO_2 on Si: (*1*) as-grown layer; (*2*) layer implanted with Si ions; and implanted layer after annealing at (*3*) 500, (*4*) 650, (*5*) 1000, and (*6*) 1150°C, respectively.

probed. The XPS measurements were carried out using a Riber MAC-2 spectrometer with 0.5-eV resolution. We employed a nonmonochromatic Mg K_α X-ray source; the line energy is 1253.6 eV. Anneals were carried out in a nitrogen atmosphere or in a vacuum, with their duration being up to 1 h.

3. RESULTS

The XPS spectra of thermally grown SiO_2 layers contain a single line at ~ 103 eV, which corresponds to

a Si atom bonded to four O atoms. After Si-ion implantation, this band broadens and a tail appears on its low-energy side, where the bands corresponding to $Si–Si_1$ (102.3 eV), $Si–Si_2$ (101.3 eV), $Si–Si_3$ (99.9 eV), and $Si–Si_4$ (99.4 eV) are known to be located. This indicates that Si atoms with various degrees of oxidation are present in the implanted layers. The effect of subsequent annealing was the following: as the temperature increases, the width of the $Si–O_4$ band returns to its initial value and the band of 4-coordinated Si at 99.4 eV (whose intensity may be considered as a measure of Si-phase precipitation) becomes more pronounced (Fig. 1). One can see from Fig. 1 that Si precipitation is nearly completed at 1000°C, and raising the annealing temperature to 1150°C does not lead to any changes in this respect.

The Raman spectra of SiO_2 plates after implantation with Si and Ar ions are shown in Fig. 2. Si implantation results in the appearance of new spectral features whose intensity depends on the dose; they do not appear upon Ar implantation. The spectra of all Si-implanted samples contain a peak at ~ 490 cm^{-1} and a weaker, very broad band at ~ 510–450 cm^{-1} peaked around 480 cm^{-1}. The scattering intensity increases as the Si dose is raised, with the increase being more rapid in the low-frequency portion of the broad-band feature.

The effect of annealing at 800°C is illustrated in Fig. 3. In spite of the fact that, according to the XPS data (Fig. 1), the Si segregation increases with the annealing temperature, we observed a weakening of the broad band in the Raman spectra of all samples. In the samples with a low implantation dose, the scattering
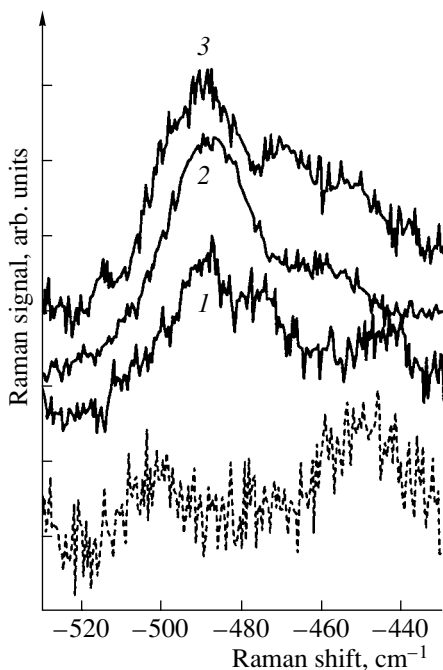

Fig. 2. The Raman spectra of SiO_2 plates implanted with Ar ions (dashed line) and Si ions (solid lines); the doses are (*1*) 5×10^{16}, (*2*) 1×10^{17}, and (*3*) 2×10^{17} cm^{-2}.
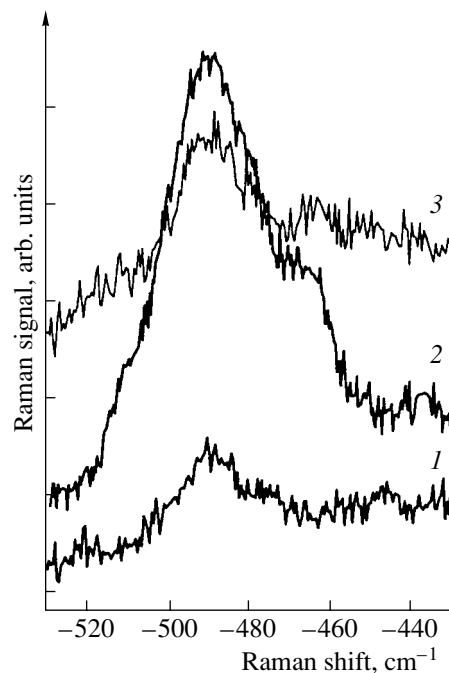

Fig. 3. The Raman spectra of Si-implanted SiO_2 plates annealed for 30 min at 800°C; the implantation doses are (*1*) 5×10^{16}, (*2*) 1×10^{17}, and (*3*) 2×10^{17} cm^{-2}.

intensity in the region above ~500 cm⁻¹ and below ~470 cm⁻¹ virtually dropped to the background level. Simultaneously, in the samples with low and medium doses, a step formed near 480 cm⁻¹, where scattering by the amorphous-Si phase takes place. The peak at 490 cm⁻¹ persisted in all spectra; in the medium-dose sample, its intensity even increased, with the spectral position unchanged. In the samples with an implanted dose of 2×10^{17} cm⁻², the scattering against both low- and high-frequency regions of the spectrum remained considerable and the peak at 490 cm⁻¹ was less pronounced against the background of the broad band.

Figure 4 represents the spectra of the samples annealed at 1100°C. The most important feature of these spectra is that the peak at 490 cm⁻1 is still present, but the scattering at its low-frequency side disappeared and steps appeared on the high-frequency side, where scattering by nanocrystals is expected to occur. In the samples with implanted doses of 5×10^{16} and 10^{17} cm⁻², the steps can be seen at 495 and 500 cm⁻¹, respectively; the scattering around 520 cm⁻¹ is at the background level in both cases. The high-frequency scattering was observed (a broad line at about (515 ± 10) cm⁻¹) only in the samples with an implanted dose of 2×10^{17} cm⁻². Recall that bulk crystalline Si exhibits a line at 520 cm⁻¹ with a width of ~ 3.6 cm⁻¹.

An intense PL band in the long-wavelength region of the visible spectrum, which is commonly attributed to the emission from nanometer-sized Si crystals, appeared after annealing at 1100°C (see Fig. 5). As the Si concentration is raised, the PL peak shifts to longer wavelengths (from ~ 750 to ~ 850 nm). It should also be noted that an increase in the mean Si concentration from 3 to 14 at. % leads to a decrease in the luminescence intensity. Anneals at 1100°C did not result in the appearance of emission bands at shorter wavelengths (in the spectral region to 450 nm).

4. DISCUSSION

The data obtained give insight into the process of nc-Si formation under annealing and allow an understanding of its special features in relation to the Si concentration and the annealing temperature. The XPS spectra in Fig. 1 indicate that variously coordinated atoms of excess Si (from Si–Si₁ to Si–Si₄) can be found in implanted layers. Thus, in as-implanted material, the excess Si already forms clusters. The wide Raman band between 510 and 450 cm⁻¹ (see Fig. 2) most probably originates from the Si clusters. The following are arguments in favor of this assignment. This band is not related to radiation defects in SiO₂, since it does not appear upon implantation with heavier Ar⁺ ions, in which case the defect production rate is much higher. Next, the band intensity increases as the Si dose is raised, and it is centered around 480 cm⁻¹, where scattering by Si–Si bonds in amorphous silicon takes place. Experimental data [8, 9] and calculations of the possi-
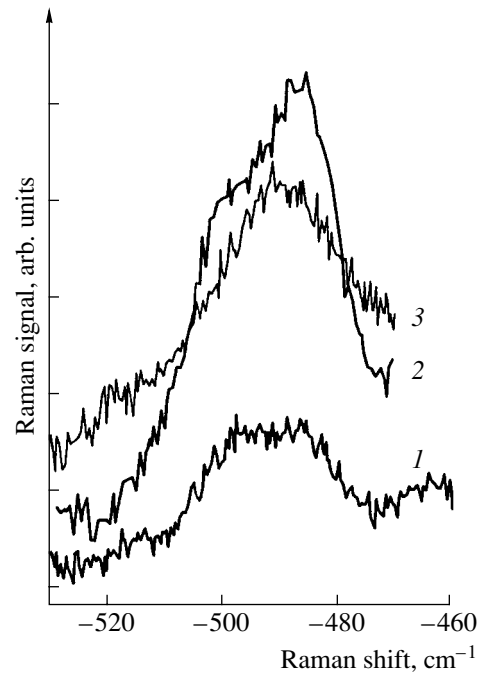

Fig. 4. The Raman spectra of Si-implanted SiO₂ plates annealed for 30 min at 1100°C; the implantation doses are (*1*) 5×10^{16}, (*2*) 1×10^{17}, and (*3*) 2×10^{17} cm⁻².
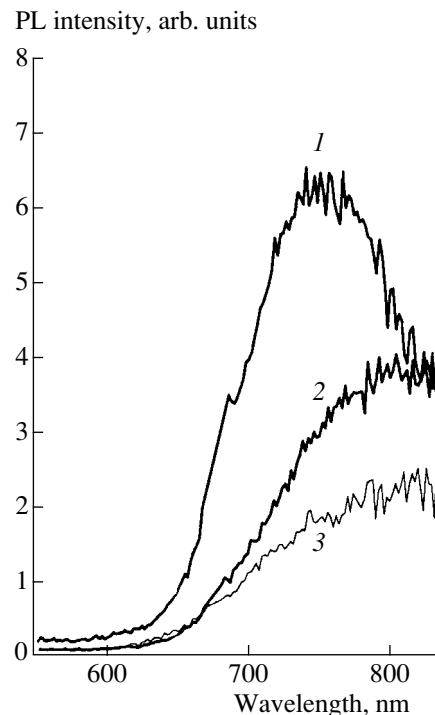

Fig. 5. The photoluminescence spectra of SiO₂ plates (curves *1*, *2*) and a thermal SiO₂ layer (curve *3*) implanted with Si ions and annealed at 1100°C. The mean Si concentrations are (*1*) 3, (*2*) 12, and (*3*) 14 at. %.

ble Raman lines corresponding to different types of clusters [10] agree with the assumption on the cluster origin of this band. Comparing the samples with different Si implantation doses, we note that nc-Si formation is possible in the material with an excess Si concentration on the order of 10^{21} cm^{-3}. When the average distance between the excess Si atoms becomes ~ 1 nm, the probability of the fluctuation-assisted formation of Si clusters in as-implanted layers (prior to any annealing) is greatly enhanced. We believe that the presence of such clusters, acting as nucleation centers, is a necessary condition for the homogeneous decomposition of the solid solution under annealing and for the subsequent formation of nc-Si. In the opposite case, heterogeneous decomposition takes place and the excess Si atoms simply diffuse to random sinks.

Sample annealing results in rather unusual behavior. On the one hand, the XPS data indicate that the segregation of excess Si from the oxide is enhanced as the annealing temperature is raised (see Fig. 1). On the other hand, annealing at 800°C leads to a weakening of the cluster-related Raman scattering (see Fig. 3). This means that segregating Si appears in some new state. Those clusters where Si atoms have both Si and O as their neighbors are chainlike or fractal Si inclusions in SiO$_2$, which, in fact, do not have distinct boundaries. One can see from Fig. 1 that, as the annealing temperature increases, 4-coordinated atoms (which form Si–Si$_4$ bonds) become the most abundant. Apparently, loosely packed clusters transform into more compact Si precipitates possessing a phase boundary. It is reasonable to attribute the peak at 490 cm^{-1} to the scattering by the surface of nanoscale Si inclusions. The nature of this peak has not been discussed previously, although some indications of its existence can be found in the literature [3, 11, 12]. Our assumption relies on the following argumentation. The position of the peak is close to that of the line corresponding to Si–Si bonds in amorphous silicon. At the surface, the interatomic bonds are slightly stretched in comparison with those in the bulk [13–15]. In nanoparticles, the fraction of atoms that belong to the surface layer is high [16] and the surface scattering itself is fairly intense [17, 18]. Our observation that, in the samples with an implantation dose of 10^{17} cm^{-2}, annealing at 800°C leads to an enhancement of the peak at 490 cm^{-1} is explained by the transformation of the clusters into nanoscale precipitates with a distinct phase boundary. When the implantation dose is lower, the number and the size of the clusters decrease. When the dose is higher, the transformation of the clusters into separate-phase nanoscale precipitates is hindered by the rapid growth of the size of clusters and by their partial linking. The sharp dependence on the dose and the behavior of the clusters under annealing agree well with the results of computer simulation [19], in which percolation-type cluster formation was considered and Si diffusion in SiO$_2$ was taken into account [20]. It should be noted that the surface-related peak is present even in the spectra of unannealed samples (see Fig. 2). Probably, some of the Si inclusions in the as-implanted material either already have a boundary (which participates in light scattering) or are two-dimensional.

The XPS data indicate that the segregation of Si from SiO$_2$ with the formation of separate-phase precipitates is largely completed at 1000°C; however, intense PL is observed only if the annealing temperature is raised to 1100°C (cf. Figs. 1, 5). According to [1, 4–6], intense red PL appears due to the formation of nc-Si. Obviously, it is crystallization that brings about a drop in the scattering on the lower-frequency side of the 490-cm^{-1} peak and a rise of scattering in the high-frequency region, which is characteristic of nc-Si (see Fig. 4). Thus, nanoscale separate-phase Si precipitates crystallize at considerably higher temperatures than the 500–600°C needed for amorphous silicon crystallization. A similar observation was reported previously [21]: after the amorphization of Si nanocrystals was induced by radiation, their recrystallization took place only upon annealing at temperatures higher than ~1000°C. Thus, there is one more reason as to why high-temperature annealing of the samples is needed for nc-Si formation (another one is the requirement for the conditions of diffusion-controlled growth of the crystal size). The thermodynamics of small particles is governed by the balance between the gain in the bulk energy and the expenditure of energy related to overcoming the surface tension. We believe that it is the counteraction of the surface that causes the high crystallization temperatures of nc-Si. On the one hand, the fact that the peak at 490 cm^{-1} persisted even after annealing at 1100°C provides an additional argument in favor of its surface-related nature, and, on the other hand, it indicates that the physical properties of the surface layer are not identical to those of the bulk. It follows from the shift of the PL peak position (Fig. 5) that the average crystallite size in the sample grows from ~ 3 to ~ 5–6 nm with an increase in the Si concentration. At the same time, calculations of the Raman shift [22–24] indicate that peaks at 495 and 500 cm^{-1} (Fig. 4) correspond to a crystallite size of about 2 nm. Evidently, the discrepancy between these two estimates is related to some difference between the properties of the inside region of the crystallite and the surface layer. Finally, it should be noted that, previously, studies of the formation of light-emitting nc-Si by Raman spectroscopy encountered certain difficulties [1–3, 8, 14, 25, 26]. On the one hand, only in samples with small amounts of excess Si did annealing result in the appearance of luminescence; however, the Raman scattering did not correspond to nc-Si. On the other hand, with an increase in the Si concentration and in the precipitate sizes, the expected Raman signal appeared but the PL vanished. These problems are, apparently, related to the existence of two different scattering regions in the crystallites, the core and the surface region.

5. CONCLUSION

Thus, analysis of the XPS and Raman spectra of SiO$_2$ layers implanted with Si to concentrations of several atomic percent indicates that silicon clusters are formed even in the as-implanted material and grow as the implantation dose is increased. Upon subsequent thermal treatments, two concurrent processes take place: segregation of excess Si from SiO$_2$, which brings about the dominance of Si–Si$_4$ bonds, and weakening of the broad scattering band that originates from Si clusters. The latter effect is attributed to the transformation of loosely packed non-separate-phase Si precipitates into more compact separate-phase ones, which have a distinct boundary with SiO$_2$. This boundary is responsible for the observed peak at 490 cm^{-1} in the Raman spectra. The segregation of excess Si is almost complete at 1000°C, but intense photoluminescence that is characteristic of nanometer-sized silicon crystallites appears only after annealing at 1100°C. Under these conditions, the surface-related peak at 490 cm^{-1} persists, while the peak related to scattering by amorphous Si precipitates around 480 cm^{-1} is replaced by a high-frequency peak in the range between 495 and 520 cm^{-1}, where scattering by Si nanocrystals occurs. Estimates of the nanocrystal size based on the luminescence and Raman-scattering data indicate that the crystallites are composed of a core and a surface layer, whose thickness is about one nanometer. Apparently, it is the surface-layer counteraction that is responsible for the high values of the crystallization temperature of Si nanoprecipitates.

REFERENCES

1. T. Shimizu-Iwayama, K. Fujita, S. Nakao, *et al.*, J. Appl. Phys. **75** (12), 7779 (1994).

2. U. Herrmann, H. H. Dunken, E. Wendler, and W. Wesch, J. Non-Cryst. Solids **204**, 237 (1996).

3. E. Wendler, U. Herrmann, W. Wesch, and H. H. Dunken, Nucl. Instrum. Methods Phys. Res. B **116**, 332 (1996).

4. G. A. Kachurin, I. E. Tyschenko, K. S. Zhuravlev, *et al.*, Nucl. Instrum. Methods Phys. Res. B **112**, 571 (1997).

5. P. Mutti, G. Ghislotti, S. Bertoni, *et al.*, Appl. Phys. Lett. **66**, 851 (1995).

6. G. A. Kachurin, A. F. Leier, K. S. Zhuravlev, *et al.*, Fiz. Tekh. Poluprovodn. (St. Petersburg) **32**, 1371 (1998) [Semiconductors **32**, 1222 (1998)].

7. S. P. Withrow, C. W. White, A. Meldrum, *et al.*, J. Appl. Phys. **86**, 396 (1999).

8. S. Hayashi, T. Nagareda, Y. Kanazawa, and K. Yamamoto, Jpn. J. Appl. Phys. **32**, 3840 (1993).

9. T. Ehara and S. Machida, Thin Solid Films **346**, 275 (1999).

10. K. Jackson, M. R. Pederson, D. Porezag, *et al.*, Phys. Rev. B **55**, 2549 (1997).

11. Y. Guyot, B. Champagnon, M. Boudeulle, *et al.*, Thin Solid Films **297**, 188 (1997).

12. V. G. Baru, M. I. Elinson, V. A. Zhitov, *et al.*, Mikroélektronika **27**, 456 (1998).

13. S. Veprek, F.-A. Sarrot, and Z. Iqbal, Phys. Rev. B **36**, 3344 (1987).

14. Ch. Ossadnik, S. Veprek, and I. Gregora, Thin Solid Films **337**, 148 (1999).

15. R. Z. Valiev and I. V. Aleksandrov, *Nanostructural Materials Produced by Severe Plastic Deformation* (Logos, Moscow, 2000).

16. H. H. Andersen and E. Johnson, Nucl. Instrum. Methods Phys. Res. B **106**, 480 (1995).

17. Yu. I. Petrov, *Clusters and Small Particles* (Nauka, Moscow, 1986).

18. S. Hayashi and H. Kanamori, Phys. Rev. B **26**, 7079 (1982).

19. A. F. Leier, L. N. Safronov, and G. A. Kachurin, Fiz. Tekh. Poluprovodn. (St. Petersburg) **33**, 389 (1999) [Semiconductors **33**, 380 (1999)].

20. L. A. Nesbit, Appl. Phys. Lett. **46**, 38 (1985).

21. G. A. Kachurin, S. G. Yanovskaya, M.-O. Ruault, *et al.*, Fiz. Tekh. Poluprovodn. (St. Petersburg) **34**, 1004 (2000) [Semiconductors **34**, 965 (2000)].

22. T. R. Guilinger, M. J. Kelly, D. R. Tallant, *et al.*, Mater. Res. Soc. Symp. Proc. **283**, 115 (1993).

23. J. Zi, H. Buscher, C. Falter, *et al.*, Appl. Phys. Lett. **69**, 200 (1996).

24. P. Mishra and K. P. Jain, Phys. Rev. B **62**, 14790 (2000).

25. T. Okada, T. Iwaki, K. Yamamoto, *et al.*, Solid State Commun. **49**, 809 (1984).

26. T. Inokuma, Y. Wakayama, T. Muramoto, *et al.*, J. Appl. Phys. **83**, 2228 (1998).

Translated by M. Skorikov

SEMICONDUCTOR STRUCTURES, INTERFACES, AND SURFACES

Role of Silicon Vacancies in Formation of Schottky Barriers at Ag and Au Contacts to 3*C*- and 6*H*-SiC

S. Yu. Davydov*, A. A. Lebedev*, O. V. Posrednik**, and Yu. M. Tairov**

* Ioffe Physicotechnical Institute, Russian Academy of Sciences, St. Petersburg, 194021 Russia
** St. Petersburg State University of Electrical Engineering (LETI), St. Petersburg, 197376 Russia
Submitted November 13, 2001; accepted for publication December 2, 2001

Abstract—A modified Ludeke model assuming that interfacial defect states are responsible for the formation of the Schottky barrier is applied to calculate the barrier heights Φ_b^n in the systems ⟨Ag, Au⟩–⟨3*C*-, 6*H*-SiC⟩. Excellent agreement with experimental data is obtained. The calculation also shows that the concentration of silicon vacancies determining the Φ_b^n value depends only slightly on the nature of the metal constituent of the contact. © *2002 MAIK "Nauka/Interperiodica".*

The effect of changes in polytypes on Schottky barrier formation was convincingly demonstrated in a number of experiments [1–5]. In [6], the dependence of the Schottky barrier height Φ_b^n at the Cr–SiC contact on the polytype of silicon carbide was accounted for, in terms of the modified Ludeke model [7–9], by the influence of vacancies in the silicon sublattice. Indeed, it is well known that the concentration of silicon vacancies, N_{Si}, gradually decreases in going from 4*H* to the 3*C* polytype [10], i.e., with an increasing share of the cubic structure. Φ_b^n [1] grows in the same order. These two facts could be related by assuming that the Fermi level E_F at the Cr–SiC contact coincides with the defect level E_d, which is the key parameter of the Ludeke model, and by calculating, on the basis of this assumption (and experimental Φ_b^n values), the surface concentration of these defects, N_d [6]. It was found that the ratios N_{Si}^S/N_d (where N_{Si}^S is the concentration of silicon vacancies, N_{Si}, recalculated to the 2D case) and Φ_b^n/N_d are approximately the same for the 8*H*, 6*H*, 15*R*, 27*R*, and 4*H* polytypes. It is this fact which enables one to state that silicon vacancies exert a dominant influence on the Φ_b^n value at the contact of various SiC polytypes with one and the same metal.

The condition $E_F = E_d$, which significantly simplifies the evaluation, is rather arbitrary. In the present study, we calculate, in terms of the model [9] and without relying upon such a simplification, the barriers appearing at the interface between silver or gold and 3*C*- and 6*H*-SiC polytypes with *n*-type conduction. These four systems were chosen, first, on the basis of

the fact that the experimental Φ_b^n values were obtained for these systems by the same group of researchers using different experimental techniques [2, 3]. Second, the barrier heights at the contacts of Ag or Au to 3*C*-SiC differ by more than a factor of 2, being very close at the interface with 6*H*-SiC (see [2, 3] and table).

Let the level E_d correspond to the unoccupied state of the silicon vacancy. Such a state was indeed found in 3*C*-SiC [11]. If the electron affinity χ is taken to be 4.4 eV for all the polytypes, as was done in [6], then the vacancy level E_d, reckoned from the valence band top (henceforth $E_V = 0$), is approximately 1.5 eV for the cubic polytype (see Appendix). We assume that $E_d = 1.5$ eV also in 6*H*-SiC. In accordance with [9], the Φ_b^n

Input parameters and results of calculation

Semiconductor	3*C*-SiC $N_d = 2 \times 10^{13}$ cm^{-2}, $E_d = 1.5$ eV, $\Gamma = 0.5$ eV		6*H*-SiC $N_d = 4 \times 10^{13}$ cm^{-2}, $E_d = 1.5$ eV, $\Gamma = 0.5$ eV	
Metal	Ag	Au	Ag	Au
n_d	0.43	0.35	0.77	0.31
Theory	0.40	0.95	0.97	1.15
Φ_b^n, eV				
Experiment	0.40	0.87	0.97	1.14
	(XPS)	(*C–V*)	(*C–V*)	(XPS)

Note: Experimental data were taken from [2, 3]; the bottom row gives in parentheses the experimental techniques used to obtain these data.

value can be found from the following self-consistent equations:

$$\Phi_b^n = \phi_m - \chi + 4\pi e^2 \lambda N_d n_d,$$

$$n_d = \frac{1}{\pi}\operatorname{arccot}[(E_d - E_g + \Phi_b^n)/\Gamma].$$

(1)

Here, ϕ_m is the work function of the metal and is equal to 4.26 and 5.1 eV for Ag and Au, respectively [2]; E_g is the energy gap constituting, respectively, 2.4 [12] and 3.02 eV [1] for the $3C$ and $6H$ polytypes; 2λ is the thickness of the double layer at the contact, taken to be 4 Å;[1] e is the elementary charge; Γ is the halfwidth of the vacancy quasi-level (with broadening resulting from the interaction with metal); and n_d is the occupancy of the vacancy quasi-level. Equation (1) takes into account the fact that the vacancy level is empty prior to interaction with the metal [6, 9].

We find the concentration N_d for the cubic polytype $3C$-SiC by recalculating N_{Si} to N_{Si}^S with the use of the mean value of the ratio $N_{\mathrm{Si}}^S/N_d \approx 1.71$, thus obtaining $N_d \approx 2 \times 10^{13}$ cm^{-2}. For $6H$-SiC, we take the value $N_d \approx 4 \times 10^{13}$ cm^{-2}, rounding off the result obtained in [6] for the contact of chromium to various polytypes of silicon carbide. As is known, the parameter which is most difficult to evaluate in the Anderson–Newns theory of adsorption [14], on which the Ludeke model of the contact is based [7–9], is the width of the 2Γ quasi-level. In what follows, we take the value $\Gamma = 0.5$ eV for all cases.[2]

Problem parameters, results of calculations, and experimental data[3] are listed in the table. It is seen that the agreement between theory and experiment is excellent, even though no fitting procedures were carried out and all the parameters were determined (with some degree of reliability) from experimental data or were taken equal to their most probable values. Comparison of the results obtained in this study with the data of [6] led us to conclude that N_d is the concentration of *intrinsic defects in silicon carbide*, which is only slightly dependent on the nature of the metal contact.

Thus, it has been established once again that the vacancy-related defectiveness of silicon carbide not only governs its polytype, but also determines the Schottky barrier height at the metal–SiC interface.

---

[1] The 2λ value is assumed to be approximately equal to the lattice constants of silver (4.09 Å) and gold (4.08 Å) [13].

[2] Fortunately, variation of the parameter Γ does not affect the results of our calculations in any significant way. For example, if we set $\Gamma = 0.1$ eV for the Au/$3C$-SiC contact, we obtain $n_d = 0.35$ and $\Phi_b^n = 0.95$ eV, which is in close agreement with the data presented in the table.

[3] We emphasize that the experimental data obtained in [2, 3] by different experimental techniques are represented in the table by Φ_b^n values best corresponding to our theoretical results.

APPENDIX

It is known that those models of Schottky barrier formation which are based on the key role of interfacial defects (see, e.g., [15]) commonly place, beginning with Bardin and Shokley's works, the "defect band" more or less close to the midgap of a semiconductor. The validity of such an approximation can be demonstrated in the following simple way without performing any labor-consuming calculations.

Let E_d^0 be the "seed" position of the silicon vacancy level, which can be taken equal to the energy of dangling $|sp^3\rangle$ orbitals of carbon [16]. Using Harrison's method of bonding orbitals [17–19], we obtain $E_d^0 = -13.15$ eV relative to the vacuum level. Let us take into account the interaction of dangling orbitals with the rest of the crystal by representing the states in the conduction and valence bands in a simplified way by two local levels E_C and E_V. Then, the following Dyson equations can be written

$$G_{dd} = g_{dd} + g_{dd}(V_{dc}G_{cd} + V_{dv}G_{vd}),$$

$$G_{cd} = g_{cc}V_{cd}G_{dd}, \quad G_{vd} = g_{vv}V_{vd}G_{dd}.$$

(A.1)

Here, $g_{dd}^{-1} = \omega - E_d^0$, $g_{cc}^{-1} = \omega - E_C$, and $g_{vv}^{-1} = \omega - E_V$ are the seed Green functions of, respectively, the defect, conduction, and valence "bands"; $V_{di}(i = c, v)$ are the matrix elements of interaction between the defect level and the bands; and ω is the energy variable. Assuming for simplicity $|V_{cd}|^2 \approx |V_{vd}|^2 \equiv V^2$, we obtain an equation from which the position of the vacancy level E_d can be found:

$$(\omega - E_d^0)(\omega - E_C)(\omega - E_V) - (2\omega - E_C - E_V)V^2 = 0.$$

(A.2)

Let us further set $E_V = 0$, then $E_C = E_g$. From Eq. (A.2), it immediately follows that the difference $(E_d - E_d^0)$, i.e., the shift of the defect level via interaction with the bands, is small if $E_d \approx E_g/2$. Moreover, it can be readily shown that the interaction V drags the E_d^0 level to the midgap, wherever the original position of this level may be. Let, e.g., $E_d^0 < 0$ and $|E_d^0| \gg E_g$, which exactly corresponds to the case of a silicon vacancy. Assuming $V \gg E_g$, we obtain $E_d \approx (E_g/2)(1 + E_g^2/4V^2)$.[4] Naturally, the conclusion made in this study that the seed level E_d^0 is shifted to the midgap is largely due to the assumption

---

[4] There are two more solutions of Eq. (2) corresponding to levels in the conduction and valence bands, but these are of no importance for the problem at hand.

that the seed elements of the interaction between this level and the band states are equal, but, on the other hand, there is no reason to cast doubt on the equality $|V_{cd}|^2 \approx |V_{vd}|^2 \equiv V^2$.

There also exists another aspect of the problem under consideration. It can be shown, in the framework of the Anderson–Newns Hamiltonian [14] and using the model of an infinitely wide metallic band, that hybridization with metal states results in no shift of the vacancy level E_d; this, of course, is only an approximation. This approximation is, however, quite satisfactory if E_d lies close to the midgap [20].

REFERENCES

1. R. G. Verenchikova, V. I. Sankin, and E. I. Radovanova, Fiz. Tekh. Poluprovodn. (Leningrad) **17**, 1757 (1983) [Sov. Phys. Semicond. **17**, 1123 (1983)].

2. J. R. Waldrop and R. W. Grant, Appl. Phys. Lett. **56**, 557 (1990).

3. J. R. Waldrop, R. W. Grant, Y. C. Wang, and R. F. Davis, J. Appl. Phys. **72**, 4757 (1992).

4. J. R. Waldrop and R. W. Grant, Appl. Phys. Lett. **62**, 2685 (1993).

5. J. R. Waldrop, J. Appl. Phys. **75**, 4548 (1994).

6. S. Yu. Davydov, A. A. Lebedev, O. V. Posrednik, and Yu. M. Tairov, Fiz. Tekh. Poluprovodn. (St. Petersburg) **35**, 1437 (2001) [Semiconductors **35**, 1375 (2001)].

7. R. Ludeke, G. Jezequel, and A. Tabel-Ibrahimi, Phys. Rev. Lett. **61**, 601 (1988).

8. R. Ludeke, Phys. Rev. B **40**, 1947 (1989).

9. S. Yu. Davydov, A. A. Lebedev, and S. K. Tikhonov, Fiz. Tekh. Poluprovodn. (St. Petersburg) **31**, 597 (1997) [Semiconductors **31**, 506 (1997)].

10. A. A. Lebedev, Fiz. Tekh. Poluprovodn. (St. Petersburg) **33**, 769 (1999) [Semiconductors **33**, 707 (1999)].

11. P. Deak, A. Gali, J. Miro, *et al.*, Mater. Sci. Forum **264–268**, 279 (1998).

12. V. I. Gavrilenko, A. M. Grekhov, D. V. Korbutyak, and V. G. Litovchenko, *Optical Properties of Semiconductors: Handbook* (Naukova Dumka, Kiev, 1987).

13. C. Kittel, *Introduction to Solid State Physics* (Wiley, New York, 1976; Nauka, Moscow, 1978).

14. D. M. Newns, Phys. Rev. **178**, 1123 (1969).

15. W. Mönch, Rep. Prog. Phys. **53**, 221 (1990).

16. M. M. Lanno and J. Bourgoin, *Point Defects in Semiconductors I* (Springer-Verlag, New York, 1981; Mir, Moscow, 1984).

17. W. A. Harrison, Phys. Rev. B **27**, 3592 (1983).

18. W. Mönch, Europhys. Lett. **7**, 275 (1988).

19. S. Yu. Davydov and S. K. Tikhonov, Fiz. Tverd. Tela (St. Petersburg) **37**, 2749 (1995) [Phys. Solid State **37**, 1514 (1995)].

20. S. Yu. Davydov, Zh. Tekh. Fiz. **68** (4), 15 (1998) [Tech. Phys. **43**, 361 (1998)].

Translated by M. Tagirdzhanov

SEMICONDUCTOR STRUCTURES,
INTERFACES, AND SURFACES

Measurements of Deep Trap Concentration in Diodes with a High Schottky Barrier by Deep-Level Transient Spectroscopy

E. N. Agafonov, A. N. Georgobiani*, and L. S. Lepnev

Lebedev Institute of Physics, Russian Academy of Sciences, Leninskiĭ pr. 53, Moscow, 117924 Russia
*e-mail: georg@sci.lebedev.ru

Abstract—The effect of the Schottky barrier height, energy position of deep traps, deep and shallow defect concentrations, temperature, and voltages applied to samples in the expression defining the deep center concentration in diodes with high Schottky barriers was studied by deep-level transient spectroscopy. Based on the results of the analysis, a method is suggested for determining the deep center concentration; this method is appropriate for both "normal" and "anomalous" deep traps. © 2002 MAIK "Nauka/Interperiodica".

Anomalous peaks are often observed when studying diodes with a high Schottky barrier by deep-level transient spectroscopy (DLTS). These peaks are related to deep levels which are located near the band of minority carriers and cross the Fermi level in the near-contact zone [1]. A feature of the energy-band diagram of such samples is that the regions of deep-center recharging and depletion do not coincide. Depending on the relation of the Schottky barrier height, energy position of a deep level, and the distribution of shallow- and deep-center concentrations, this noncoincidence can have a significant impact on the method for the calculation of the deep center concentration in a material.

The relation between the capacitance relaxation amplitude ΔC and the deep center concentration N_T is given by

$$\frac{\Delta C}{C} = \frac{C|_0 - C|_\infty}{C|_\infty} \approx \frac{N_T}{2N_0}\left(\frac{x_1'^2}{W^2} - \frac{x_1^2}{W^2}\right), \qquad (1)$$

where $N_T \ll N_0$, N_0 is the shallow center concentration, $C = \varepsilon/4\pi w$ is the capacitance of a structure unit area, ε is the material dielectric constant, w is the depletion region width, x_1' and x_1 are the boundaries of deep trap filling during the course of the filling pulse and in the steady state, $W = \sqrt{(2\varepsilon/qN_0)V_w}$, q is the elementary charge, and V_w is the potential difference between the contact and the depletion region boundary.

The deep-center concentration is conventionally estimated in the complementary approximation $V_B \ll V$, where V_B is the Schottky barrier height and V is the applied bias voltage. This approximation is considered in [2]. It is in fact assumed that the boundary of deep center filling in the steady state coincides with the depletion region boundary and, during the course of the filling pulse, with the contact. This yields the simplified formula for determining the deep-center concentration

$$\frac{\Delta C}{C} = \frac{N_T}{2N_0}. \qquad (2)$$

In [3], one of the parenthetical terms in (1) was retained; however, estimates of both terms were not presented. Hence, substantiation of this approximation and corresponding errors were not considered.

This paper is aimed at analyzing the impact of the Schottky barrier height, energy position of deep levels, concentrations of deep and shallow defects, as well as voltages applied to a sample and the temperature of DLTS signal observation, on the contribution of the terms $x_1'^2/W^2$ and x_1^2/W^2 (related to the boundaries of deep center filling) to the formula for the determination of the deep–level impurity concentration.

The relative deviation of the term x_1^2/W^2 from x_1^2/w^2 does not exceed N_T/N_0. The consideration of this term in (1) should yield nothing more than the terms of higher order smallness. Hence, this deviation may be neglected within the approximation $N_T \ll N_0$. In the subsequent analysis, we shall not distinguish between the values x_1^2/W^2 and x_1^2/w^2.

Let us calculate the deep center concentration within the model of the diode with a high Schottky barrier with a uniform distribution of shallow and deep impurities for the cases of normal and anomalous DLTS peaks.

We consider an n-type semiconductor with a deep level in the upper or lower half of the band gap, which brings into existence the normal and anomalous DLTS
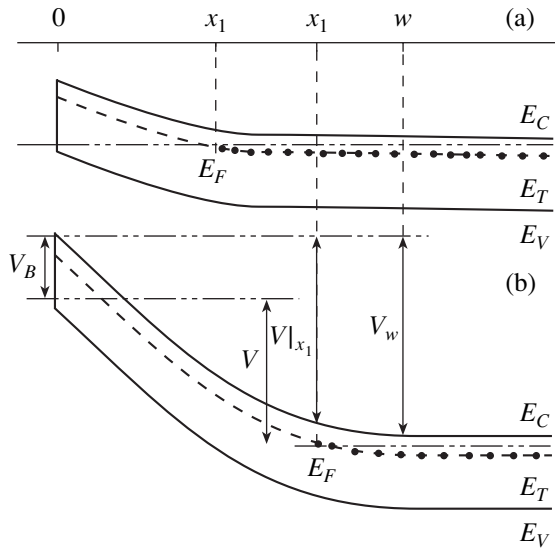
Fig. 1. Energy-band diagram of the diode with a high Schottky barrier with the deep level E_T in the upper half of the band gap, giving rise to the "normal" DLTS peak in the case of an *n*-type semiconductor (a) during the filling pulse and (b) at the steady state.
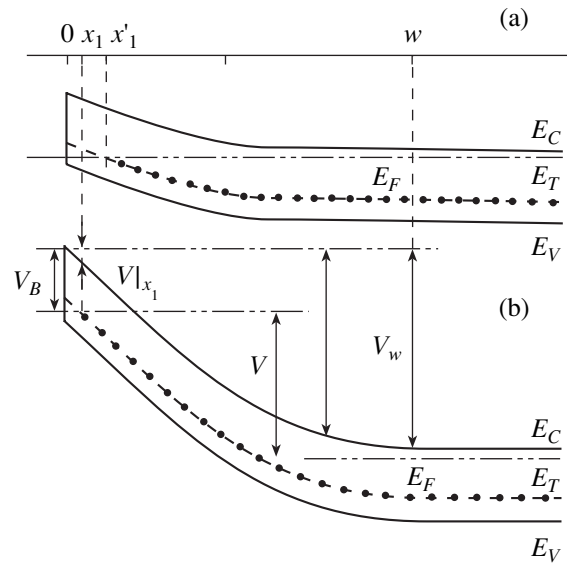

Fig. 2. Energy-band diagram of the diode with a high Schottky barrier with the deep level E_T in the lower half of the band gap, giving rise to the "anomalous" DLTS peak in the case of an *n*-type semiconductor (a) during the filling pulse and (b) at the steady state.

peaks, respectively (see Figs. 1, 2). The *p*-type semiconductor is studied in a similar way.

The Poisson equation for a steady state is written as

$$\frac{\partial^2 V}{\partial x^2} = -\frac{q}{\varepsilon} N(x), \quad N(x) = \begin{cases} N_0 + N_T, & 0 < x < x_1 \\ N_0, & x_1 < x < w \end{cases}. \quad (3)$$

Its solution with the boundary conditions

$$V|_{x=0} = 0, \quad V|_{x=w} = V_w, \quad \frac{\partial V}{\partial x}\bigg|_{x=w} = 0 \quad (4)$$

is given by

$$\begin{cases} 1 + \dfrac{N_T x_1^2}{N_0 w^2} = \dfrac{2\varepsilon}{q N_0 w^2} V_w \\ \left(1 - \dfrac{x_1}{w}\right)^2 = \dfrac{2\varepsilon}{q N_0 w^2}(V_w - V|_{x_1}) \end{cases}, \quad (5)$$

$$V_w = -V_B + V + \frac{1}{q} E_F.$$

The quantity x_1^2/w^2 can be expressed from (5) as

$$\frac{x_1^2}{w^2} = \left\{ \left[1 - \left(a + \frac{N_T}{N_0}a - \frac{N_T}{N_0}a^2\right)^{1/2}\right] \Big/ \left[1 - \frac{N_T}{N_0}a\right] \right\},$$

$$a = \frac{V_w - V|_{x_1}}{V_w}. \quad (6)$$

Let us consider the "normal" case, when the deep level E_T is in the upper half of the band gap (Fig. 1). Then, $q(V_w - V|_{x_1}) = E_F - E_T$, where the energy positions of the deep level E_T and the Fermi level E_F are measured from the conduction band edge E_C. Thus, we have

$$a \equiv a_N = \frac{E_T - E_F}{-qV + qV_B - E_F}. \quad (7)$$

We note that, after transformations that take into account (6) and (7), expression (1) can be reduced to the form found in [2] for the "normal" case. However, the special feature of this study is that the anomalous case is considered along with the normal case. Furthermore, the chosen method makes it possible to conveniently analyze the effect of important experimental parameters on the formulas for the determination of the deep center concentration, which is very important in practice.

In the anomalous case, when the deep level E_T is in the lower half of the band gap (see Fig. 2), $V|_{x_1} = -V_B + (1/q)E_T$ and

$$a \equiv a_A = \frac{qV - E_T + E_F}{-qV + qV_B - E_F}. \quad (8)$$

It is noteworthy that the energy positions of the deep level and the Fermi level are also measured from the conduction band edge.

Figure 3 shows the dependence of x_1^2/w^2 on the parameter a. This dependence is monotonic with $x_1^2/w^2 = 1$ at $a = 0$ and $x_1^2/w^2 = 0$ at $a = 1$. The range of the parameter a from 0 to 1 contains virtually all the used voltages V for the cases of normal and anomalous DLTS peaks. A characteristic feature of (6) is the very weak dependence of x_1^2/w^2 on N_T/N_0 when the latter varies from 0 to 0.2, which spans all the values N_T/N_0 used in the experiment (Fig. 4). This weak dependence enables one, without knowing the exact value of N_T/N_0, to employ (6) to determine the values of x_1^2/w^2 by substituting one of the numbers from the aforementioned range, e.g. 0.1, instead of the factual N_T/N_0. Then, the obtained parameters x_1^2/w^2 and x_1^2/w^2 can be used to determine the deep center concentrations by formula (1).

Let us analyze the dependences of x_1^2/w^2 on the voltage, Schottky barrier height, and energy position of the deep level in the band gap for the normal and anomalous deep centers. To this end, it is convenient to consider the above dependence of the parameter a and to invoke (6) or Fig. 3.

First, we consider the case of the normal deep center. In (7), the minus sign in $-qV$ with a bias corresponding to the steady state coincides with the sign of $qV_B - E_F$. Therefore, at a high negative bias, we have $|-qV + qV_B - E_F| \gg |E_T - E_F|$ and $a_N \approx 0$. The lower the semiconductor doping level and the shallower the level E_T, the lower the steady bias voltages at which the above relation is valid.

Since the deep level energy E_T controls the temperature of DLTS peak observation, while the Fermi level E_F position is governed by shallow centers, the difference $E_T - E_F$ for low-temperature peaks is smaller, and the relation $a_N \approx 0$ holds at lower bias voltages. Under these conditions, the corresponding term $x_1^2/w^2 \approx 1$ in (1) is close to unity. This means that the boundary of deep-level filling under the steady state differs only slightly from the depletion region boundary. The relation $a_N = 1$ is valid at $qV = qV_B - E_T$, which corresponds to a positive bias. In the case of $V = 0$, which is widely encountered in practice, the closer the Schottky barrier height E_T to the trap depth E_T, the smaller the difference of a_N from unity during the filling pulse. The case $a_N = 1$ corresponds to the vanishing of the term $x_1'^2/w^2$ in (1); i.e., it corresponds to the filling of the deep center with majority carriers during the filling pulse over the entire depletion region, as well as to the coincidence of its filling boundary with the contact.

For the "anomalous" deep center, we have $|qV_B - E_F| > |E_T - E_F|$ and, at a high negative bias, $|V| \gg |V_B|$, the relation $a_A \approx 1$ is valid. In this situation, x_1^2/w^2 is close to
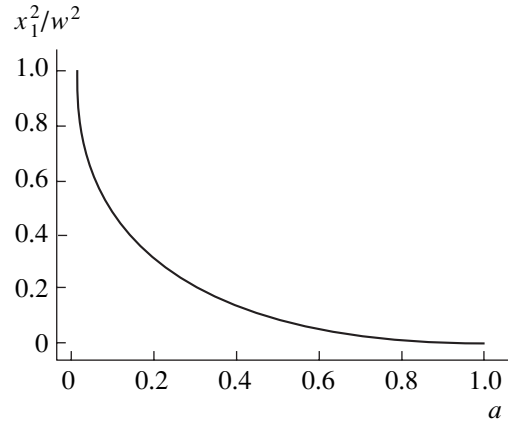

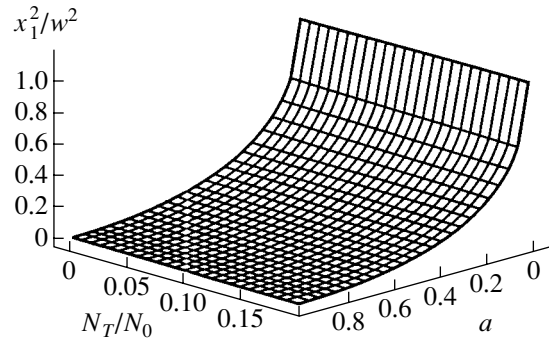**Fig. 3.** Dependence of the ratio x_1^2/w^2 on the parameter a.

Fig. 4. Dependence of the ratio x_1^2/w^2 on the parameters a and N_T/N_0.

zero. The case $a_A \approx 0$, which formally follows from (8) at a positive bias $qV = E_F - E_T$, corresponds to a significant forward current. In the widely encountered case, where $V = 0$ during the filling pulse, the equality $a_A = (E_T - E_F)/(qV_B - E_F)$ is valid. For the anomalous center, the energy E_T is comparable to qV_B. The quantity a_A decreases as the deep level recedes from the valence band E_V (E_T is lowered), as the barrier height V_B grows, and as the temperature increases, which causes an increase in the absolute value of E_F. All these factors lead to the growing role of the term $x_1'^2/w^2$ in (1), which always exceeds x_1^2/w^2 in the case of the anomalous peak. Thus, if, in case of the anomalous peak, the term x_1^2/w^2 becomes small at high reverse biases, the term $x_1'^2/w^2$ should always be taken into account when determining the deep center concentration in diodes with a high Schottky barrier.

As an illustration, we consider an anomalous Au donor center in Si described in [3]: $E_T = E_C - 0.76$ eV,

$V_B = 0.9$ V, $N_0 = 2 \times 10^{15}$ cm^{-3}, $N_T \approx 10^{13}$ cm^{-3}, $N_C = 2.8 \times 10^{19}$ cm^{-3} is the density of states in the conduction band, $T \approx 200$ K is the temperature of DLTS peak observation, $V = -4$ V is the bias under steady state, and $V = 0$ V is the bias during the filling pulse. Substituting these values into (8), we obtain $a_A = 0.79$ and 0.97 and $x_1'^2/w^2 = 0.012$ and 0.0002 at $V = 0$ and -4 V, respectively. Thus, the use of expression (2) instead of (1) in this example would result in error. The quantity $x_1'^2/w^2$ should be taken into account when determining the deep center concentration, while the value x_1^2/w^2 can be neglected in comparison with $x_1'^2/w^2$.

ACKNOWLEDGMENTS

We thank E.A. Bobrova and N.M. Omel'yanovskaya for their participation in discussions of the results.

REFERENCES

1. E. N. Agafonov, U. A. Aminov, A. N. Georgobiani, and L. S. Lepnev, Fiz. Tekh. Poluprovodn. (St. Petersburg) **35**, 48 (2001) [Semiconductors **35**, 48 (2001)].

2. L. S. Berman and A. A. Lebedev, *Deep-Level Transient Spectroscopy of Semiconductors* (Nauka, Leningrad, 1981).

3. L. Stolt and K. Bohlin, Solid-State Electron. **28**, 1215 (1985).

Translated by A. Kazantsev

Simulation of the Energy Spectrum of Surface States in an MIS Structure Taking Current Leakage through the Insulator into Account

L. S. Berman

*Ioffe Physicotechnical Institute, Russian Academy of Sciences,
St. Petersburg, Politekhnicheskaya ul. 26, 194021 Russia*

Abstract—In metal–insulator–semiconductor (MIS) structures with a thin dielectric layer, account must be taken of the effect of current through the insulator on the charge of surface states. The capture of carriers to surface states suppresses the thermal emission from these states. This latter process decelerates the increase of the surface state charge when the surface potential increases (in absolute value). The high-frequency capacitance technique yields an underestimated (down to zero in the limiting case) density of surface states. An anomalous dependence of the surface state density on the surface potential may indicate uniform distribution of the current density over the insulator area. © 2002 MAIK "Nauka/Interperiodica".

1. INTRODUCTION AND FORMULATION OF THE PROBLEM

The energy spectrum of surface states strongly affects the parameters of semiconductor devices, including metal–insulator–semiconductor (MIS) structures, such as FETs, charge-coupled devices, MIS varactors, and others. To date, several methods have been developed for studying the energy spectrum of surface states at the semiconductor/insulator interface [1, 2], but these methods disregard the leakage current through the insulator. However, the modern tendency of MIS structure miniaturization requires, in particular, that the insulator thickness be decreased. For thin (~100 Å) insulators, due consideration of the leakage current's effect on the MIS structure parameters is crucial.

The effect of leakage current on the deep level transient spectroscopy (DLTS) signal has been discussed in [3–5]. It was shown that the DLTS signal can be distorted even at the current density $j > 10^{-8}$ A cm^{-2}, thus leading to considerable errors in the defined parameters of surface states. The influence of leakage current on the parameters of the MIS structure InP–⟨anode oxide⟩–metal (Au, Al) was studied in [6]. The current–voltage characteristics, capacitance–voltage (C–V) characteristics, conductance, and DLTS were discussed. These methods become inefficient for the determination of the surface state parameters at elevated leaks.

It is noteworthy that the filling of deep level centers in the base of a p–n diode in the forward current mode can also distort the DLTS signal measured under reverse bias [7].

In this report, we present the simulation of the influence of leakage current on the determination of the energy spectrum of surface states. We consider the effect of leakage current on the filling and charge of surface states. For definiteness, we consider a MIS structure with an n-type semiconductor and assume that the surface states are donors. We also assume that only shallow donors with a density N_d are present and that they are completely ionized. The high-frequency capacitance method [1, 2] is applied. This method is valid if the semiconductor surface potential ψ_s is below some critical value ψ_{scr} defined from the relation $2\pi f \tau_n = 1$ [8], where τ_n is the time constant of electron thermal emission from surface states and f is the frequency of the capacitance measurement. The dependence of τ_n on ψ_s is determined by standard methods [1, 2]. Typical ψ_{scr} values lie in the range of –(0.1–0.25) V.

2. SIMULATION RESULTS AND ANALYSIS

Integrating the Poisson equation and differentiating the result with respect to the surface potential ψ_s, we obtain

$$\frac{dV}{d\psi_s} - 1 - \frac{C_{sc}}{C_i} = -\frac{1}{C_i}\left(\frac{dQ_{ss}}{d\psi_s} + \frac{dQ_i}{d\psi_s}\right), \qquad (1)$$

where V is the voltage between the metal and the ohmic contact to the semiconductor, C_{sc} is the capacitance of the space charge region in the semiconductor, C_i is the capacitance of the insulator, Q_{ss} is the charge of surface states, and Q_i is the charge in the insulator. At $Q_i = 0$, relation (1) is similar to relation (37) in Chapter 7 of [1]. The charge Q_i includes the charge of ions, and the charge Q_j, of free carriers in the insulator. The first component becomes zero under differentiation. Numerical evaluation shows that, at the current density $j < 10^{-5}$ A cm^{-2} and the insulator thickness $d < 0.1$ μm, the charge Q_j and its
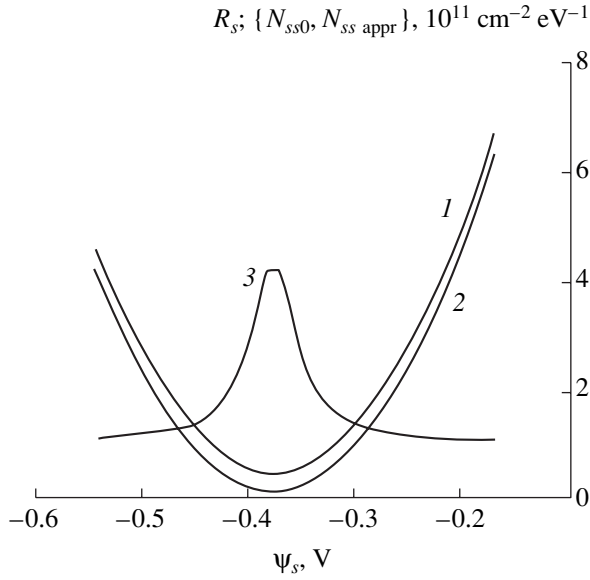
Fig. 1. (*1*) N_{ss0}, (*2*) $N_{ss\,appr}$, and (*3*) R_s vs. the surface potential ψ_s.

derivative with respect to ψ_s are several orders of magnitude less than the charge Q_{sc} in the semiconductor space charge region and its derivative with respect to ψ_s. Therefore, the term $dQ_j/d\psi_s$ in Eq. (1) can be disregarded. Nevertheless, under current flow, electrons are captured by surface states and their charge is modified. The charge of surface states is defined by the relation

$$Q_{ss} = q \int_0^{E_g} N_{ss}(E)[1 - f(E)]dE, \qquad (2)$$

where q is the elementary charge, E_g is the band gap, $N_{ss}(E)$ is the density of states with energy E, and $f(E)$ is the electron filling probability for a level with energy E (all the energies are counted off from the valence band top at the interface). The $1 - f(E)$ value is defined by the relation

$$1 - f(E) = \frac{n_1}{n_1 + n}, \qquad (3)$$

where

$$n_1(E) = N_c \exp\left[-\left(\frac{E_g - E}{kT}\right)\right], \qquad (4)$$

N_c is the effective density of states in the conduction band, n is the electron density in the semiconductor at the interface, k is the Boltzmann constant, T is the temperature,

$$n = n_0 + n_j, \qquad (5)$$

n_0 is the electron density at the interface with zero current across the insulator, and n_j is the additional density due to the current flow.

The following relations for n_0 and n_j are valid:

$$n_0 = N_d \exp\left(\frac{q\psi_s}{kT}\right), \quad n_j = \frac{j}{q v_{dr}}, \qquad (6)$$

where v_{dr} is the electron drift velocity. The drift velocity levels off in a strong electric field; therefore, it will be considered as a constant.

For definiteness, we specify the energy spectrum of surface states as

$$N_{ss}(E) = N_{ss\,min}\left[1 + D\left(\frac{E - E_0}{kT}\right)^2\right], \qquad (7)$$

where $N_{ss\,min}$ is the minimal value of N_{ss} and D is the coefficient.

The rearrangement of Eqs. (2)–(7) yields

$$Q_{ss} = qN_{ss\,min}\int_0^{E_g}\left\{\left[1 + D\left(\frac{E - E_0}{kT}\right)^2\right]\right.$$

$$\left. \times \exp\left(\frac{E - F}{kT}\right)\middle/\left[\exp\left(\frac{E - F}{kT}\right) + 1 + \frac{n_j}{n_0}\right]\right\}dE, \qquad (8)$$

where F is the Fermi level.

We select the following parameters: $E_g = 1.4$ eV, $E_0 = 0.7$ eV, $T = 300$ K, $N_d = 10^{14}$ cm^{-3}, $N_c = 5.5 \times 10^{16}T^{3/2}$ cm^{-3}, $N_{ss\,min} = 10^{10}$ cm^{-2} eV^{-1}, $D = 1$, and $v_{dr} = 10^7$ cm s^{-1}. At first, we consider the zero-current case ($n_j = 0$). Differentiating (8) with respect to ψ_s, we obtain the relation for the density of surface states

$$N_{ss0} = -\frac{1}{q}\frac{dQ_{ss}}{d\psi_s} = N_{ss\,min}\int_0^{E_g}\left[1 + D\left(\frac{E - E_0}{kT}\right)^2\right]$$

$$\times \left\{\frac{q}{kT}\exp\left(\frac{E - F}{kT}\right)\middle/\left[\exp\left(\frac{E - F}{kT}\right) + 1\right]^2\right\}dE. \qquad (9)$$

It is generally assumed that the surface states are empty at $E > F$ and at $E < F$ they are completely filled with electrons. In terms of this stepwise approximation, the surface state density $N_{ss\,appr}(E)$ equals the N_{ss} value at $E = F$. If the surface state energy spectrum is described by Eq. (7), we obtain

$$N_{ss\,appr} = N_{ss\,min}\left[1 + D\left(\frac{F - E_0}{kT}\right)^2\right]. \qquad (10)$$

The value of the Q_{ss} derivative with respect to ψ_s is determined from the experimental values of the parameters on the left-hand side of Eq. (1). In the stepwise approximation of the $N_{ss}(E)$ dependence, it is assumed that the differentiation of Q_{ss} with respect to ψ_s does not yield the N_{ss0} value (Eq. 9), but $N_{ss\,appr}$ (Eq. 10). Figure 1 shows the dependences N_{ss0}, $N_{ss\,appr}$, and their ratio $R_s = N_{ss0}/N_{ss\,appr}$ as functions of ψ_s; R_s is maximal in the
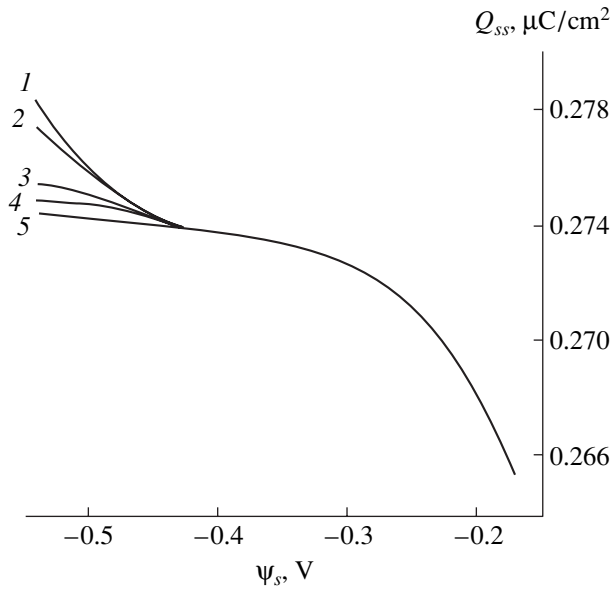
Fig. 2. Charge of surface states Q_{ss} vs. the surface potential ψ_s at different current densities, j: (*1*) 0, (*2*) 10^{-7}, (*3*) 10^{-6}, (*4*) 2×10^{-6}, and (*5*) 5×10^{-6} A cm^{-2}.

Fig. 3. Simulated density of surface states N_{ssj} vs. the surface potential ψ_s at different current densities. The j values are the same as in Fig. 2.

vicinity of the minimal density of surface states, its value is on the order of several units, and it tends to unity at varied ψ_s.

Further, we consider the effect of leakage current on the charge of surface states. For definiteness, we assume that the current is defined by the Schottky emission. For the negative values of the surface potential defined above and the relevant negative voltage applied to the metal, the current is governed by the electron flow from metal to semiconductor. The image force is disregarded. In this case, the potential barrier for the electron flow from metal to semiconductor and, consequently, the current are independent of voltage (see, e.g., [1], Chapter 6). Substituting (6) into (8), we obtain

$$Q_{ss} = q N_{ss\,min} \int_0^{E_g} \left[1 + D\left(\frac{E - E_0}{kT}\right)^2 \right]$$

$$\times \left\{ \exp\left(\frac{E - F}{kT}\right) \middle/ \left[\exp\left(\frac{E - F}{kT}\right) \right. \right. \tag{11}$$

$$\left. \left. + 1 + \frac{j}{q v_{dr} N_d \exp(q\psi_s/kT)} \right] \right\} dE.$$

The Q_{ss} dependence on ψ_s is defined from (11). Further, the surface state density is calculated by numeric differentiation of Q_{ss} with respect to ψ_s.

The calculation results are as follows. Figure 2 presents a family of $Q_{ss}(\psi_s)$ dependences for different val-
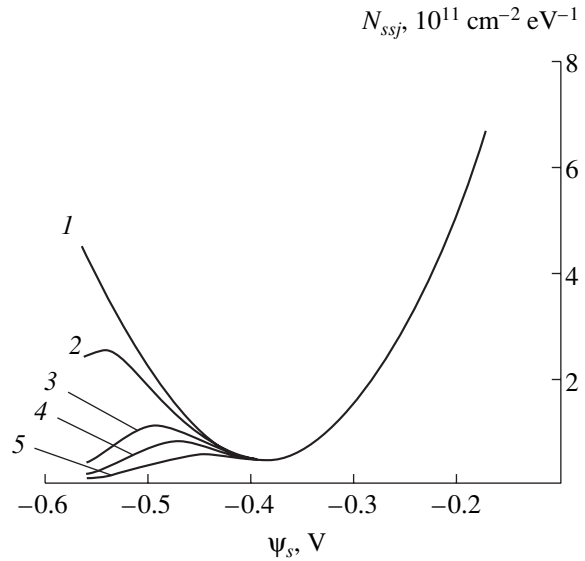
ues of j. The ratio n_j/n_0 increases with a rise in $|\psi_s|$, which means that the electron capture by surface states suppresses the thermal emission of electrons from these states, and the surface-state charge increases more slowly. Naturally, this effect is stronger for higher current values.

Figure 3 shows a family of $N_{ssj}(\psi_s)$ dependences for different j values. At $j = 0$, $N_{ssj} = N_{ss0}$. The difference between the real and calculated surface-state densities, that is, between N_{ssj} and N_{ss0}, increases with an increase in $|\psi_s|$. For example, N_{ssj} is significantly less than N_{ss0} at $\psi_s = -0.5$ V and $j = 10^{-7}$ A cm^{-2} (compare curves *1* and *2*). The rise of Q_{ss} terminates at a current density of $\sim 10^{-5}$ A cm^{-2}, with N_{ssj} almost falling to zero (Fig. 3, curve *5*). This anomalous $N_{ssj}(\psi_s)$ dependence may indicate the uniform distribution of current over the insulator area.

3. CONCLUSION

At a high absolute value of surface potential in a MIS structure, the electron capture by surface states suppresses the thermal emission of electrons from these states, which moderates the growth of the surface state charge. An analysis of the surface-state spectrum by the high-frequency capacitance method yields an underestimated (down to zero in the limiting case) value of the surface-state density in a specific range of the surface potential. The anomalous dependence of the surface-state density on the surface potential may indicate the uniform distribution of current over the insulator area.

ACKNOWLEDGMENTS

I am grateful to I.V. Grekhov and L.S. Kostina for the formulation of the problem and helpful discussions.

REFERENCES

1. S. Sze, *Physics of Semiconductor Devices* (Wiley, New York, 1981; Mir, Moscow, 1984), Vol. 1.

2. E. H. Nicollian and J. R. Brews, *MOS (Metal-Oxide-Semiconductor) Physics and Technology* (Wiley, New York, 1983).

3. M. C. Chen, D. V. Lang, W. C. Dautremont-Smith, *et al.*, Appl. Phys. Lett. **44**, 790 (1984).

4. E. K. Kim, H. Y. Cho, and S. K. Min, J. Appl. Phys. **67**, 1380 (1990).

5. K. Dmowski, B. Lepley, E. Losson, and M. El. Bouabdellati, J. Appl. Phys. **74**, 3936 (1993).

6. S. V. Tikhov, A. P. Kasatkin, and S. I. Karpovich, Fiz. Tekh. Poluprovodn. (Leningrad) **25**, 434 (1991) [Sov. Phys. Semicond. **25**, 263 (1991)].

7. A. A. Lebedev, Fiz. Tekh. Poluprovodn. (St. Petersburg) **28**, 1980 (1994) [Semiconductors **28**, 1092 (1994)].

8. L. S. Berman, I. V. Grekhov, I. N. Karimov, and E. V. Ostroumova, Fiz. Tekh. Poluprovodn. (St. Petersburg) **27**, 917 (1993) [Semiconductors **27**, 497 (1993)].

Translated by D. Mashovets

Mixed Vibrational Modes of PbTe Nanocrystallites

A. I. Belogorokhov*, L. I. Belogorokhova**, D. R. Khokhlov**, and S. V. Lemeshko***

* Institute of Rare Metals, Moscow, 109017 Russia
** Moscow State University, Vorob'evy gory, Moscow, 119899 Russia
e-mail: belog@mig.phys.msu.su
*** Lukin Scientific Research Institute of Physical Problems, Zelenograd, Moscow, Russia
Submitted October 4, 2001; accepted for publication October 17, 2001

Abstract—Far-infrared reflectance (20–700 cm^{-1}) and Raman spectra of porous PbTe were studied. The spectral dependences found significantly differ from those observed in the case of bulk single-crystal PbTe. Aside from the transverse (TO) and longitudinal (LO) optical phonon modes, additional vibrational modes were detected in the spectra, whose frequencies are close to those in a bulk material. Their number and spectral positions are in satisfactory agreement with the results of calculations carried out to determine the vibrational mode frequencies for nanocrystallites taking into account boundary conditions at their surface. The macroscopic continuum model allows calculation of the frequencies of the mixed phonon modes in quantum dots by the simultaneous consideration of atomic displacements and the accompanying change in the electrostatic potential. It was found experimentally that the detected modes are mixed (LO–TO), as was predicted by theory. The data of atomic-force microscopy allowed us to estimate the average radius of quantum dots, which form the nanorelief of the porous PbTe layer. © 2002 MAIK "Nauka/Interperiodica".

INTRODUCTION

Currently, optical and electron properties of semiconductor nanocrystallites (NC), often referred to as quantum dots (QDs), are being actively studied. Nevertheless, the vibrational properties of such objects have not yet been studied adequately. Interest in the influence of size quantization effects on optical properties of NCs forming a porous semiconductor layer has already for quite some time extended beyond the context of silicon structures [1]. This is caused both by pure fundamental problems [2] and by the practical need for such materials [3]. The use of porous layers of various semiconductors as intermediate layers allows for the design of new heterojunction types. Recently, successful attempts in this line of inquiry were undertaken [3]. Porous semiconductor layers are employed more and more often as substrates to produce materials with improved structural properties [4]. Further advancement in this direction requires detailed studies of the vibrational properties of the crystallites composing a porous structure, in particular, the behavior of optical phonons when there is a significant decrease in the average radius of these crystallites (10 nm and smaller). In turn, this will yield additional data in studies of the electron–phonon interaction in nanostructures when the effect of size quantization on the properties of porous semiconductor materials becomes important.

Pore formation in a single-crystal material during the electrochemical etching reaction begins in the surface area where an excess carrier, i.e., a hole, is localized. As a rule, this takes place near the lattice defect or impurity atom. It is expedient to assume that the crystalline skeleton formed in the course of this reaction will have a structure with fewer stacking faults.

The volume of NCs, whose average radius is 10 nm, is formed by the lattice of an initial semiconductor material. In this case, electron and hole wave functions become significantly localized. The size quantization of phonon modes is often neglected, and NC vibrational properties are approximated using bulk phonon frequencies. Attempts to calculate the phonon vibrations restricted to the QD volume were undertaken in [5]. If the QD shape is close to spherical, the longitudinal phonon frequency is shifted and surface vibrational modes arise. The correct description of the NC phonon subsystem dynamics requires consideration of boundary conditions when calculating the field of displacements of lattice atoms and the electrostatic potential caused by these displacements. As was shown in [6], this gives rise to mixed modes formed by longitudinal optical (LO) and transverse optical (TO) phonons. Such modes appeared in the optical spectra of the PbS NCs observed in [7]. Porous PbS is a convenient, unique nanostructurized material. Studies of its optical properties can validate calculations of the vibrational modes in low-dimensional semiconductor crystals.

The Raman scattering (RS) and Fourier transform infrared (FTIR) spectroscopy techniques are the most sensitive to variations in the vibrational properties of crystal. Therefore, we will employ the data found by these methods to compare calculated and experimental data.

BELOGOROKHOV *et al.*

EXPERIMENTAL

Porous lead telluride layers were produced by electrochemical etching [8] on wafers of initially single-crystal PbTe (111) undoped and doped with 0.4 at. % of gallium. The etching time was 10, 15, and 25 min, and the current density was 15 mA/cm^2. The porous layer thickness was 1–3 μm.

The reflectance spectra $R(\omega)$ were measured with a Bruker IFS-113v Fourier spectrometer at room temperature in the frequency range $\omega = 10$–700 cm^{-1}, with the spectral resolution no worse than 0.2 cm^{-1}. The measured spectral dependences $R(\omega)$ were processed using a combined approach that involved the Kramers–Kronig relation and analysis of variance [9].

The NC microstructure and surface morphology were studied using a JEOL 840A electron scanning microscope with a LINK system of element analysis, as well as with atomic-force microscopy (AFM).

Raman spectra were measured in the backscattering mode using irradiation with an Ar$^+$-laser at the wavelengths of 488 and 514.5 nm. The setup incorporated a Jobin-Yvon T64000 double monochromator and a GaAs photomultiplier cooled to 78 K. To study the microstructure, an Olympus metallographic microscope was used. In this case, the laser beam was focused onto a spot 0.7 mm in diameter. To avoid irreversible thermal effects on a sample or its degradation, the laser pumping power was varied from 3 to 100 mW. A CCD camera combined with the microscope allowed visual observation of the surface state of the object in the course of Raman spectra measurements.

DISCUSSION

Lead telluride belongs to a class of semiconductor materials that exhibit significant dispersion of optical phonon modes [10]. When considering the problem of the influence of size quantization effects on PbTe vibrational properties, one should take into account the boundary conditions in the equations describing lattice atom displacements and the change of its local polarizability at the crystallite boundary. A similar problem was solved in [6] where, besides the calculation of frequencies of optical phonons in QDs, mixed vibrational modes consisting of longitudinal and transverse phonon modes of a bulk material were considered. These modes are caused by the simultaneous solution of the equations describing displacements of atoms from equilibrium sites and a change in the lattice electrostatic potential. According to [6], this makes these modes optically active. It was shown for CdS that the mixed modes consisting of frequencies of optical phonons of a bulk material begin to prevail as the crystallite radius decreases to $R_0 \lesssim 1.5$ nm (where R_0 is the QD radius). The authors of [6] have assumed that the semiconductor electron states are described by the two-

band model, which in the strict sense is inapplicable to the case of CdS, whose valence band is degenerate. The optical properties of PbS QDs about 2 nm in size were studied in [7]. It was shown that the adequate simulation of the dispersion dependences of phonon modes within the PbS Brillouin zone requires linear terms $\omega \propto q$ along with the quadratic terms $\omega \propto q^2$ in the relations of [6]. Nevertheless, the condition for zero amplitude of phonon vibrations at the QD–environment interface remains unchanged. If the crystallite shape is close to spherical, this approach is quite justified. The phonon modes calculated on the assumption that their angular momentum is zero were shown in [6] to be pure radial and longitudinal; moreover, they converge to the frequencies of bulk LO phonons of the Brillouin zone center as the sphere radius grows. When the angular momentum is unity, both the TO and LO modes are active with the same asymptotics at $R_0 \longrightarrow \infty$.

The frequencies of polar optical phonons were calculated in [6] within the macroscopic model of an isotropic medium taking into account the effect of displacements of atoms from equilibrium sites on the crystallite electrostatic potential. It was shown that the frequencies of mixed LO–TO phonon modes (ω_1 and ω_2) arranged between the longitudinal and transverse optical phonons of bulk PbTe can be found by solving the secular equation

$$[2z\cos z + (z^2 - 2)\sin z]$$

$$\times \left\{ \left[-\frac{\gamma}{x^2}\left(\frac{3}{x^2} - 1\right) + \left(1 + \frac{2}{\varepsilon_\infty}\right)\left(1 - \frac{1}{x^2}\right) \right]\sin x \right.$$

$$\left. + \left[-\frac{3\gamma}{x^3} + \frac{1}{x}\left(1 + \frac{2}{\varepsilon_\infty}\right) \right]\cos x \right\} \qquad (1)$$

$$= [\sin z - z\cos z]\left\{ \frac{1}{x}\left[-1 - \frac{2}{\varepsilon_\infty} + \frac{3\gamma}{x^2\varepsilon_\infty} \right]\cos x \right.$$

$$\left. + \frac{1}{x^2}\left[\frac{\gamma}{\varepsilon_\infty}\left(1 - \frac{3}{x^2}\right) + \left(1 + \frac{1}{\varepsilon_\infty}\right) \right]\sin x \right\},$$

where

$$\gamma = \frac{\omega_{LO}^2 - \omega_{TO}^2}{\beta_T^2}R_0^2, \qquad (2)$$

$$\omega_1^2 = \omega_{LO}^2 - \beta_L^2\left(\frac{z}{R_0}\right)^2, \qquad (3)$$

$$\omega_2^2 = \omega_{TO}^2 + \beta_T^2\left(\frac{x}{R_0}\right)^2. \qquad (4)$$

SEMICONDUCTORS   Vol. 36   No. 6   2002

Here, R_0 is the QD radius; ε_∞, ω_{TO}, and ω_{LO} are the high-frequency dielectric constant and frequencies of transverse and longitudinal optical phonons of bulk PbTe crystal, respectively; β_T and β_L are the parameters related to the dispersion of TO and LO phonon modes in bulk PbTe; and x and z are the dimensionless variables, which, being known for a given R_0, allow determination of the frequencies of coupled phonon vibrations, arranged lower (in energy) than LO and higher than TO phonons of PbTe. It is noteworthy that Eq. (1) is written for the case of PbTe QDs surrounded with free space.

The results calculated according to Eq. (1)–(4) for the frequencies of mixed lattice vibrations with an angular momentum of unity at PbTe QDs are shown in Fig. 1. One can see that the frequencies of mixed modes tend towards those of corresponding optical phonons in the bulk PbTe crystal as the crystallite radius grows.
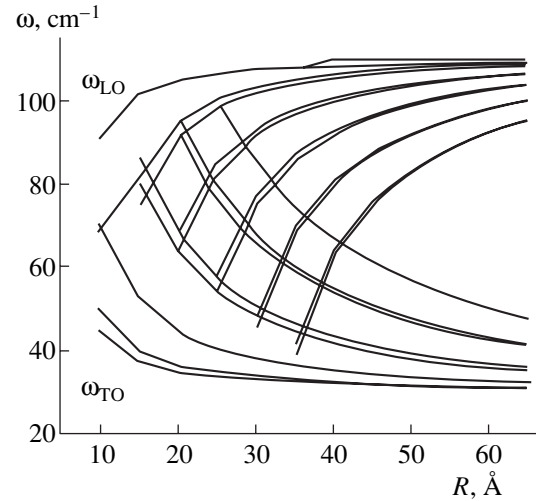

Fig. 1. Frequencies of combined phonon vibrations: $\omega_1(R_0)$ calculated according to (3) (upper curves) and $\omega_2(R_0)$ calculated according to (4) (lower curves).

INFRARED SPECTROSCOPY

The experimental reflectance spectra $R(\omega)$ of three porous PbTe (*por*-PbTe) samples prepared at various etching times (10, 15, and 25 min) are displayed in Fig. 2, together with $R(\omega)$ of bulk single-crystal PbTe, whose surface was used to produce porous layers. Comparing these curves, one can see that the *por*-PbTe spectrum $R(\omega)$ exhibits a variety of additional features, which are absent in the initial substrate spectrum. However, the single reflection minimum in the dependence $R(\omega)$ of crystalline PbTe is virtually flattened. This minimum corresponds to the frequency of the mixed plasmon–phonon mode ($\omega_+ \approx 183$ cm^{-1}). Its shape and width are defined by the damping parameter of such vibrations [11]. The *por*-PbTe spectra exhibit additional deep minima at frequencies of 50–70 cm^{-1}, which are absent in the reflectance spectrum of bulk PbTe. These minima correspond to the frequencies 55.3, 61.1, and 53.6 cm^{-1} for samples 1, 2, and 3, respectively. Their mutual shift is caused by different average NC radii. The frequencies of bounded LO phonons in the aforementioned *por*-PbTe samples, found from the dependences $R(\omega)$ of Fig. 2, are 103.4, 101.9, and 102.7 cm^{-1}, respectively. In bulk PbTe crystals, $\omega_{TO} = 31$ cm^{-1} and $\omega_{LO} \approx 105$ cm^{-1} [10]. The shift of LO modes in the por-PbTe samples to lower frequencies is caused by the effect of dimensional quantization as the average PbTe NC radius decreases [2].

The reflectance minimum at the frequency $\omega_+ \approx$ 183 cm^{-1} in the bulk PbTe spectrum (substrate) (Fig. 2), caused by mixed plasmon–phonon vibrations ($\omega_\pm$), shifts to longer wavelengths in the case of *por*-PbTe. This shift is caused by a decrease in the LO phonon fre-
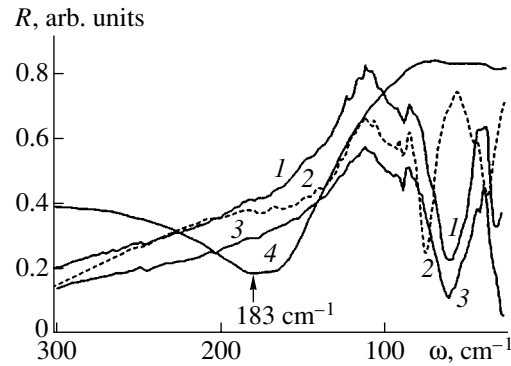
Fig. 2. Reflectance spectra measured at room temperature for por-PbTe samples 1–3 (curves *1–3*) and the initial bulk single-crystal PbTe wafer (substrate).

quency in porous films. The expression for $\omega_\pm$ includes the frequencies ω_{LO} and ω_{TO} [12]; i.e.,

$$\omega_\pm^2 = \frac{1}{2}(\omega_{LO}^2 + \omega_P^2) \pm \frac{1}{2}[(\omega_{LO}^2 - \omega_p^2)^2 + 16C^2\omega_{LO}\omega_p]^{1/2}, \quad (5)$$

$$C = \frac{1}{2}[\omega_{LO}\omega_p(1 - \omega_{TO}^2/\omega_{LO}^2)]^{1/2}, \quad (6)$$

where ω_p is the plasma frequency [10, 12]. It follows from (5) and (6) that ω_+ increases with ω_{LO}; in the case of ω_{TO}, the pattern is reversed. In the spectra $R(\omega)$ in Fig. 2, one can see the shift of the long-wavelength edge of the ω_+ minimum ($\omega \approx 140$–180 cm^{-1}) to the right by 4–5 cm^{-1} in the case of sample 2 in comparison with samples 1 and 3. This is explained by the difference in the average radii of NCs composing the porous
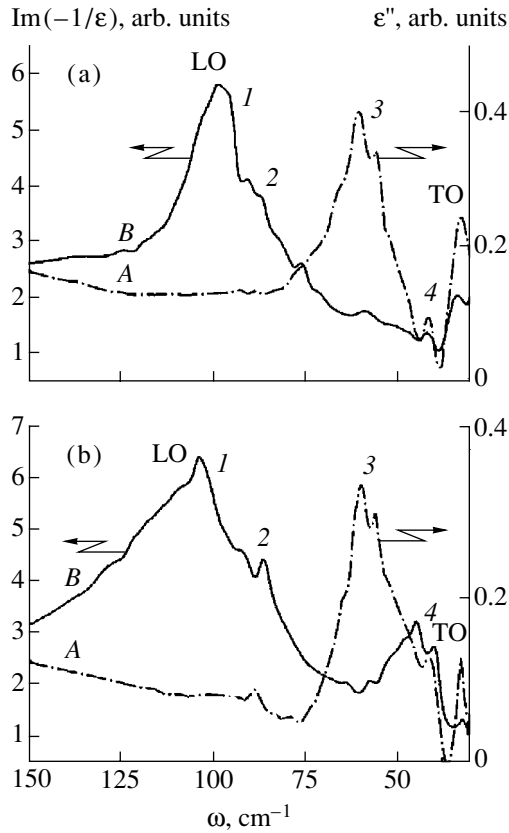
Fig. 3. Spectral dependences ε''(ω) and Im(–1/ε) for *por*-PbTe samples 2 (a) and 3 (b) with the main extrema (*1–4*).
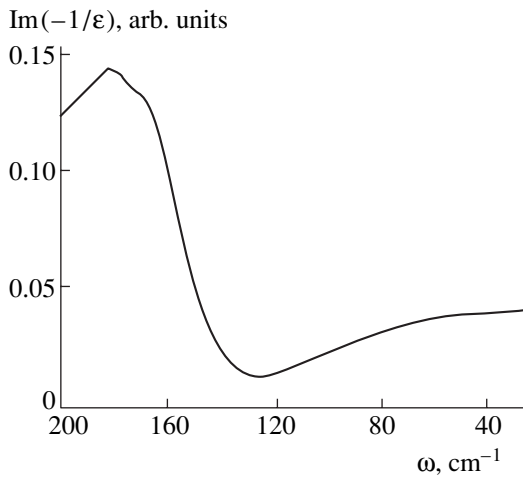

Fig. 4. Spectral dependence Im(–1/ε) for the initial wafer of bulk single-crystal PbTe (substrate).

layer. The ω_+ minimum is wider in samples 1 and 3 and narrower in sample 2, which is caused by different numbers of mixed phonon modes participating in $\omega_\pm$ formation. It is noteworthy that a few ω_+-type modes should formally exist in porous layers due to the fact that they are formed by a variety of mixed LO–TO

vibrations. Here, it should be mentioned that the aforesaid is valid if the plasma frequency remains unchanged when a bulk semiconductor is transformed into its porous modification, which is not quite obvious. As the frequency of combined vibrations grows from the side of ω_{TO}, the ω_--minimum, also caused by mixed plasmon–phonon vibrations, should shift to shorter wavelengths. Indeed, the spectra $R(\omega)$ of *por*-PbTe samples exhibit such pronounced deep, long-wavelength minima in the submillimeter range ($\omega \approx 30$–36 cm^{-1}), which correspond to the ω_--modes. In the case of sample 2, the ω_- position is shifted to the left by 4.5 cm^{-1} in comparison with samples 1 and 3, which conforms to the ω_+ spectral shift.

Fröhlich-type modes with a zero angular momentum can manifest themselves in optical FTIR spectra. These modes are not mixed and consist of longitudinal vibrations confined within the crystallite volume. Such vibrations in pure form should be active in the Raman spectra and should not participate in optical absorption in the infrared range [7]. This is valid in the case of total passivation of all the dangling surface bonds, e.g., if all the tellurium surface atoms participate in the formation of chemical bonds with oxygen atoms. In practice, it is not always possible to form NCs, whose surface is ideal in this sense. In all likelihood, this can explain the IR activity of the aforementioned modes, although, in the strict sense, we are dealing here with surface phonons. They should manifest themselves at frequencies $\omega_F \approx 74$–76 cm^{-1}. The experimental optical spectra exhibit additional features in this frequency range.

Figure 3a displays the spectral dependences of the imaginary part of ε''(ω) of the effective dielectric constant $\varepsilon(\omega) = \varepsilon'(\omega) + i\varepsilon''(\omega)$ and the function Im(–1/ε) of *por*-PbTe sample 2. Figure 3b shows similar spectra for sample 3. The frequencies corresponding to the spectral dependence extrema correspond to the frequencies of the main optical phonons participating in the formation of the reflectance spectrum of the *por*-PbTe sample. In the limit of dimensional quantization, it is impossible to separate the contribution of the LO and TO phonons to the considered dependences, since (as was indicated above) mixed-type lattice vibrations should be taken into account. Such phonon modes are mostly arranged at the wavelengths indicated in Fig. 3 as *1–4*. One can see additional extrema in the spectral dependences ε''(ω) and Im(–1/ε); these extrema are absent in the case of bulk single-crystal PbTe (Fig. 4), where a single peak, caused by the mixed plasmon–phonon mode ω_+, is observed. The first peak in Im(–1/ε) (see Figs. 3a, 3b) is caused by the confined LO phonon in *por*-PbTe. In turn, there is a maximum in the dependence ε''(ω) at the lowest energies (at frequencies $\omega \approx 30$–32 cm^{-1}), which is caused by TO phonon modes. The fact that the spectral dependence $R(\omega)$ partially retains its shape is

Spectral positions of main extrema in the experimental dependences $\varepsilon''(\omega)$ and $Im(-1/\varepsilon)$ for *por*-PbTe samples 2 and 3, as well as the calculated frequencies of mixed phonon vibrations for PbTe nanocrystals with $\overline{R_0}$ = 2.6 and 4.1 nm

Sample 2			Sample 3		
$Im(-1/\varepsilon)$	$\varepsilon''(\omega)$	Calculation, $\overline{R_0}$ = 2.6 nm	$Im(-1/\varepsilon)$	$\varepsilon''(\omega)$	Calculation, $\overline{R_0}$ = 4.1 nm
31.0	32.8	32.7–33.0	33.4	32.7	31.6–34.9
40.1	41.9	37.4–39.7	42.3	40.7	41.4–42.7
45.0	47.4	47.9	59.1	54.6	52.2–54.1
57.6	56.1	53.4–57.8	76.6	58.5	65.2
64.1	60.3	65.8	87.5	63.8	82.1
No extremum	65.7	68.5	91.0	No extremum	93.1–93.4
86.5	88.7	84.0–86.6	99.3	No extremum	100.6–100.8
92.9	No extremum	97.8–100.6	No extremum	No extremum	No extremum

Note: The frequencies are given in cm^{-1}.

caused by the por-PbTe layer structure: NCs are arranged against the background of a microcrystalline (large-scale) relief. As a rule, the variance of the average NC radius ($\overline{R_0}$) in porous semiconductor layers is rather significant. This fact is caused by a negative porosity gradient over the layer depth. A similar pattern is also observed in the case of porous silicon. The variance can be decreased by changing (in a certain way) the ion exchange kinetics directly at the boundary of the region of the electrochemical etching reaction [13] or by using other technological approaches to produce NC semiconductor structures [14]. In the case under consideration, the extension of peak *1* to shorter wavelengths in the experimental dependence $Im(-1/\varepsilon)$ for sample 3 can be explained by the contribution of a larger NC to $R(\omega)$.

The table lists the spectral positions of the main extrema in the dependences $\varepsilon''(\omega)$ and $Im(-1/\varepsilon)$ for *por*-PbTe samples 2 and 3. Comparing these results with the calculated data of Fig. 1, we can try to estimate the average radius of NCs forming the small-scale relief of the porous layer. Reasonable agreement for samples 2 and 3 can be achieved assuming that the average radius of NCs forming the nanoscale relief of the porous layer is $\overline{R_0} \approx 2.6$ and 4.1 nm, respectively.

Applying the combined approach involving the Kramers–Kronig relations and the method of dispersion oscillators to the spectrum $R(\omega)$, we can find formal values γ_j of the damping parameter and oscillator strengths of mixed phonon vibrations. The calculation for *por*-PbTe samples 2 and 3 shows that the values of γ_j range from 5 to 11 for lattice modes. In the frequency range where the $R(\omega)$-shape dependence is caused by the ω_{+j}-type modes ($\omega \approx 180$ cm^{-1}), i.e., by mixed plasmon–phonon vibrations, the parameter γ_j is equal to

22–47, which can indicate significant anharmonicity (intense electron–phonon interaction). At the same time, such parameters as the oscillator strength of the indicated vibrations are almost the same (in magnitude) for virtually all the mixed LO–TO modes.

The accuracy of the values found can be assessed from the data of Fig. 5, which shows both the experimental and calculated dependences $R(\omega)$- for por-PbTe sample 2. One can see that there is good agreement between experiment and theory.

RAMAN SCATTERING

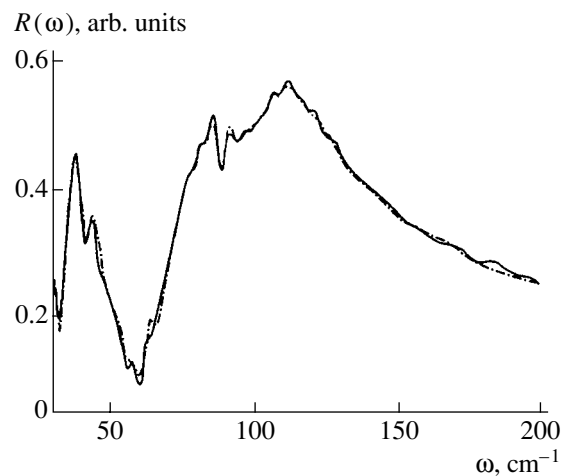The first-order Raman modes in materials with an NaCl-type crystal structure (related to the space sym-

$R(\omega)$, arb. units

Fig. 5. Experimental spectrum $R(\omega)$ and the spectrum reconstructed using the dispersion approach for *por*-PbTe sample 2.
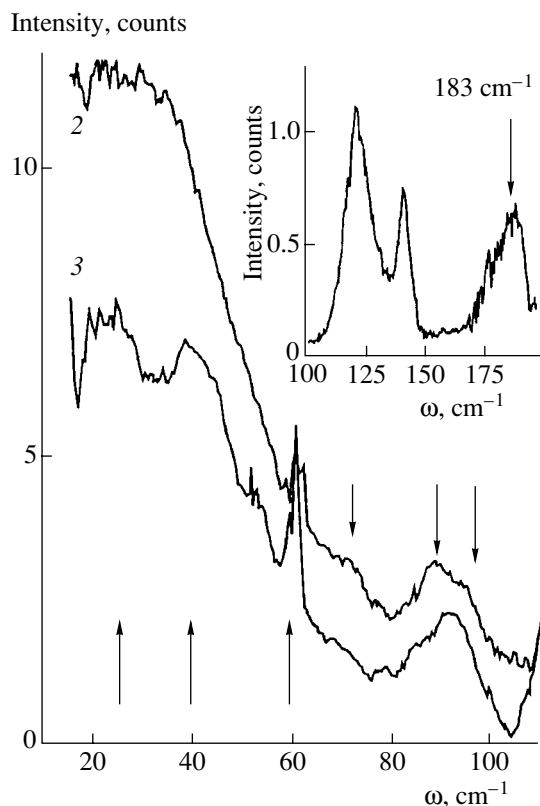
Intensity, counts

Fig. 6. Raman spectra for *por*-PbTe samples 2 (curve *2*) and 3 (*3*). The inset shows a portion of the Raman spectrum for bulk PbTe crystal.
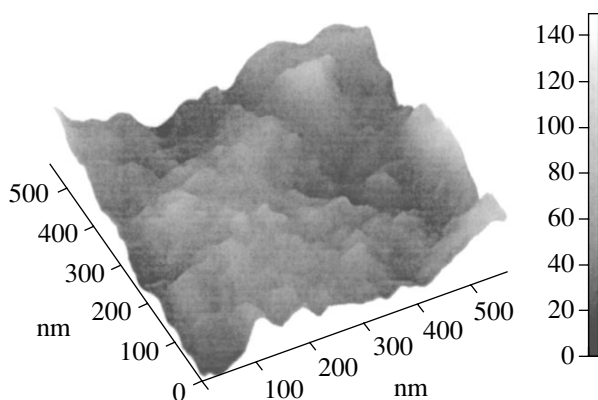

Fig. 7. Three-dimensional atomic-force microscopy image of the surface area of *por*-PbTe sample 2.

metry group O_h) are not active, i.e., do not manifest themselves in the Raman spectra. Nevertheless, under certain conditions (Jahn–Teller instability of the lattice, local symmetry violations, photon scattering by longitudinal optical phonons with a nonzero quasi-wave vector ($q \neq 0$), internal electric fields related to built-in semiconductor junctions, etc.), active resonance modes,

including those corresponding to optical phonons, can appear in the Raman spectra.

Peaks at frequencies 68, 126, and 143 cm^{-1} are observed, among others, in unpolarized Raman spectra of *por*-PbTe samples, measured at room temperature, as well as in RS spectra of single-crystal samples. These peaks are related to the vibrational modes of a thin TeO_2 layer at the PbTe surface [15]. The Raman spectra of samples 2 and 3 are displayed in Fig. 6, where the positions of the modes corresponding to the main resonance vibrations are indicated. The inset shows the spectral region of bulk PbTe. Along with the two peaks ($\omega = 120–145$ cm^{-1}) caused by photon scattering in the TeO_2 surface layer, one can see a pronounced peak, which is caused by plasma vibrations, at a frequency of about 183 cm^{-1}. Earlier, when discussing the FTIR spectra, we mentioned the deep minimum in the dependence $R(\omega)$ of bulk PbTe, which, as in the case of RS, is caused by mixed plasmon–phonon modes. It is noteworthy that the peak at the frequency $\omega \approx 183$ cm^{-1} in the Raman spectra of *por*-PbTe becomes lower than that for initial bulk PbTe. This can be explained by the decreased oscillator strength for pure LO vibrations in the porous layer.

Figure 6 exhibits a variety of peaks (indicated by arrows) which are absent in the Raman spectra of the initial bulk PbTe. The fact that they become active modes during scattering of light can be explained by taking into account the fact that they represent mixed LO–TO phonon vibrations in the NC bulk in the case of *por*-PbTe. This, in turn, leads to a change in their selection rules. The spectral positions of these peaks turn out to be close to the frequencies of FTIR-active modes, which are listed in the table. Such a coincidence can be considered as proof of the fact that the nature of the discussed vibrational modes has indeed changed. From purely longitudinal or transverse, they have become (to one extent or another) mixed, which predetermined their activity in both Raman and FTIR spectra.

ATOMIC-FORCE MICROSCOPY

The surface structure of the *por*-PbTe samples was studied by atomic-force microscopy methods. The results for *por*-PbTe sample 2 are shown in Figs. 7 and 8. The right-hand part of Fig. 7 displays the scale allowing estimation of the average size of NCs composing one or another surface area. Against the background of rather large (from the viewpoint of the manifestation of dimensional quantization effects) microcrystallites forming the surface microrelief, one can see prominent extended regions, whose nanorelief forms crystallites with average radii from 2.0 to 3.0 nm. The analysis of a two-dimensional pattern of the surface of the
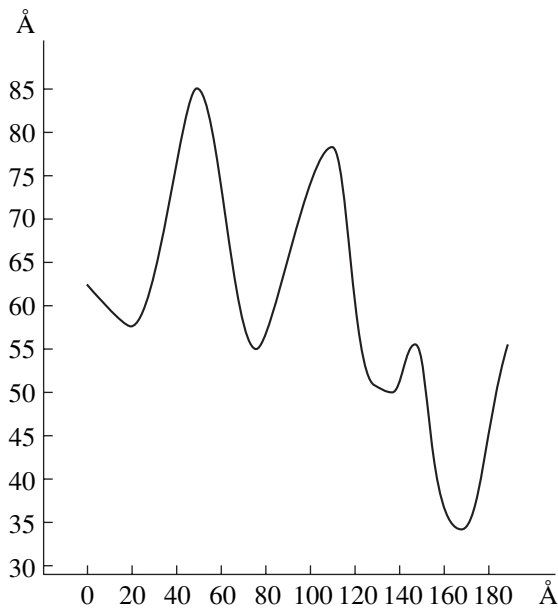
Fig. 8. Two-dimensional pattern of the surface relief of *por*-PbTe sample 2.

por-PbTe sample 2 (see Fig. 8) allows similar conclusions on the average NC size: $\overline{R_0} \approx 2.1$–2.2 nm. Comparing the FTIR (see table) and AFM data, one sees that they are in satisfactory agreement.

CONCLUSION

Additional vibrational modes were detected in the reflectance spectra in the far infrared range (20–700 cm^{-1}) and in the Raman spectra of porous lead telluride; these modes were not observed in the optical spectra of bulk PbTe. The spectral dependences found significantly differ from those observed in the case of bulk single-crystal PbTe. The number and spectral positions of the additional vibrational modes are consistent with the data calculated within the macroscopic model of an insulator medium taking into account boundary conditions at the nanocrystallite surface. This model allows the calculation of the frequencies of mixed phonon modes in quantum dots with the simultaneous consideration of atomic displacements and the accompanying change of the electrostatic potential [6]. The experimental data allow us to conclude that the additional detected modes are related to LO–TO mixed vibrations. In particular, this follows from the fact that these modes are active in both FTIR and Raman spectra. Atomic-force microscopy was used to estimate the average radius of quantum dots forming the porous PbTe film nanorelief. Satisfactory agreement between the FTIR, RS, and AFM experimental data was found.

Taking into account that the model calculations in [6] were carried out within certain approximations of the macroscopic model, as well as the fact that the crystallites composing the porous PbTe layer are not strictly spherical, it should be concluded that the calculated data fit well the experimental results.

REFERENCES

1. A. I. Belogorokhov, V. A. Karavanskiĭ, A. N. Obraztsov, and V. Yu. Timoshenko, Pis'ma Zh. Éksp. Teor. Fiz. **60**, 262 (1994) [JETP Lett. **60**, 274 (1994)].
2. H. Fu, V. Ozoliņš, and A. Zunger, Phys. Rev. B **59**, 2881 (1999).
3. V. V. Mamutin, V. P. Ulin, V. V. Tret'yakov, *et al.*, Pis'ma Zh. Tekh. Fiz. **25** (1), 3 (1999) [Tech. Phys. Lett. **25**, 1 (1999)].
4. A. D. Akhsakhalyan, Yu. N. Buzynin, N. V. Vostokov, *et al.*, in *Proceedings of the IX National Conference on Crystal Growth, Moscow, 2000*.
5. S. Nomura and T. Kobayashi, Phys. Rev. B **45**, 1305 (1992).
6. E. Roca, C. Trallero-Giner, and M. Cardona, Phys. Rev. B **51**, 1680 (1995).
7. T. D. Krauss, F. W. Wise, and D. B. Tanner, Phys. Rev. Lett. **76**, 1376 (1996).
8. M. K. Norr, J. Electrochem. Soc. **109**, 433 (1962).
9. E. A. Vinogradov and I. I. Khammadov, *Spectroscopy of Bulk and Surface Phonons in Crystals* (Fan, Tashkent, 1989).
10. Yu. I. Ravich, B. A. Efimova, and I. A. Smirnov, *Semiconducting Lead Chalcogenides* (Nauka, Moscow, 1968; Plenum, New York, 1970).
11. N. Romcevic, M. Romcevic, D. R. Khokhlov, *et al.*, Infrared Phys. Technol. **40**, 453 (1999).
12. J. I. Pankove, *Optical Processes in Semiconductors* (Prentice-Hall, Englewood Cliffs, 1971; Mir, Moscow, 1973).
13. A. I. Belogorokhov, R. Enderlein, A. Tabata, *et al.,* Phys. Rev. B **56**, 10276 (1997).
14. V. I. Klimov, A. A. Mikhailovsky, Su Xu, *et al.*, Science **290**, 314 (2000).
15. A. P. Mirgorodsky, T. Merle-Me'jean, J.-C. Champarnaud, *et al.*, J. Phys. Chem. Solids **61**, 501 (2000).

Translated by A. Kazantsev

LOW-DIMENSIONAL SYSTEMS

Electron States in $(AlAs)_M(Al_xGa_{1-x}As)_N$ Superlattices

G. F. Karavaev^, V. N. Chernyshov, and R. M. Egunov

Siberian Physicotechnical institute, Tomsk State University, Tomsk, 634050 Russia
^ e-mail: karavaev@elefot.tsu.ru
Submitted September 10, 2001; accepted for publication November 12, 2001

Abstract—Electronic states have been studied for energies within the conduction band of $(AlAs)_M(Al_xGa_{1-x}As)_N$ (111) superlattices. Calculations were carried out in terms of the model of the matching of envelope functions at heterointerfaces, generalized to the case of the structures under consideration. Miniband spectra, symmetry and localization of wave functions, and the probabilities of interband IR absorption were analyzed. The probabilities are shown to be substantial not only for light polarized along the superlattice growth axis, but also for normal incidence on the structure surface. The superlattices studied are shown to be promising materials for IR photodetectors. © 2002 MAIK "Nauka/Interperiodica".

1. INTRODUCTION

Electronic properties of $(AlAs)_M(Al_xGa_{1-x}As)_N$ (111) superlattices (where x is the content of Al atoms in $Al_xGa_{1-x}As$ solid solutions) are known to be mainly determined by electrons of X, Γ, and L valleys in materials of the layers. It is noteworthy that ΓL and XL mixing of electron states at the (111) orientation of the heterointerfaces occurs at different points of the Brillouin zone for superlattices (see Fig. 1 in [1]). The ΓL interaction is essential along the ΓA line if the number $N + M$ is divisible by 3, or along the ΓZ line otherwise. In this case, the X states exert no influence on the miniband formation and there is no XL mixing. The XL mixing occurs along the $M\bar{L}$ (or DA) line, with the contribution of Γ states to the electron spectrum, which is absent in this case. The contribution of Γ, X, and L valleys to forming the lower part of the miniband spectrum depends on the relative arrangement of the Γ level in the $Al_xGa_{1-x}As$ well and the X level in AlAs. This arrangement is obviously determined by the number of monolayers M, N and by the content x. In [1], we considered the miniband electron energy spectra for the $(AlAs)_M(GaAs)_N$ (111) superlattices, where electron states in the X and L valley play a major part. We restricted our consideration to the case of sufficiently thin GaAs layers in order to exclude the effect of Γ electrons. In this study, we generalize the previous analysis to the case of superlattices, where $(GaAs)_N$ layers are replaced by layers of the $(Al_xGa_{1-x}As)_N$ solid solution. In this case, the effect of Γ electrons can be excluded by the choice of x, which characterizes the composition of the solid solution, and, therefore, the restriction on the thickness of the GaAs layers can be lifted.

2. CALCULATION TECHNIQUE

A study of the electron energy spectra of $(AlAs)_M(Al_xGa_{1-x}As)_N$ superlattices was carried out using the technique presented in [1] for $(AlAs)_M(GaAs)_N$ structures. Let us briefly formulate the basic ideas of this technique. We use the scattering matrix method [2–4] for calculation of the electron structure. It is known that the scattering matrix contains the entire body of information about the system; after it is calculated, various quantum mechanical problems can be solved and, in particular, electron states in the superlattices can be studied. We use the envelope function approximation [1, 2] to simplify calculations. An analysis made in [1] and in the present study shows that the three-valley description of the electron scattering at heterointerfaces is sufficient for our system. They are X_1, X_3, and L_1 conduction band valleys related to, e.g., the $\mathbf{k}_x = (00\bar{1})2\pi/a$ and $\mathbf{k}_L = (11\bar{1})\pi/a$ points in the Brillouin zone of the bulk crystal (a is the lattice constant). These points are projected on the same point of the 2D (surface) Brillouin zone, and, therefore, X–L scattering is possible at the heterointerface. The mixing matrix for envelope functions within this approximation is a 6×6 matrix. Its elements were found, as in [1, 2], using pseudopotential calculations. Our study has shown that the elements of the mixing matrix linearly depend on the composition parameter x. The energies at the X and L points of the Brillouin zone and the matrix elements of the momentum operator for $Al_xGa_{1-x}As$ at various values of x, necessary for calculations, were also determined using the pseudopotential method. The concentration dependences of the energies of the Γ_1, X_1, and L_1 levels in the conduction band of $Al_xGa_{1-x}As$ are presented in Fig. 1. It is seen that the energy of the Γ_1 and L_1 levels rapidly increases with increasing concentration x. Therefore, their contribu-

tion will decrease with increasing x, and the X levels will play the main part in forming the lower minibands. The matrix elements of the momentum operator, essential for our model, linearly and rather weakly depend on the parameter x.

3. ANALYSIS OF SPECTRUM AND WAVE FUNCTIONS

Similarly to [1], here we calculated the electron spectrum for the (AlAs)$_M$(Al$_x$Ga$_{1-x}$As)$_N$ superlattices (denoted below as (M, N), where $N = 7–9$; $M = 7–14$) at eight values of x within the range from 0 to 0.7. Insignificant modifications were introduced into the calculation procedure. It is noteworthy that at $x = 0$ the calculation completely coincides with that carried out in [1] for (AlAs)$_M$(GaAs)$_N$ structures. Let us consider the results obtained with $(7, 7)$, $(9, 9)$, and $(9, 14)$ superlattices. A basic difference between the energy spectra of these structures is observed only at $x = 0$, since only in this case the main contribution to the formation of the second miniband for the $(9, 14)$ structure comes from the L_1 level in GaAs. At $x > 0.1$, X_1 levels provide the main contribution to forming the first and second minibands, and, therefore, no drastic difference in the behavior of the spectral lines is observed for the structures at these values of x. It is also noteworthy that, when x tends toward unity, the spectral lines of all the structures take on a configuration characteristic of the AlAs conduction band in the Brillouin zone of the superlattice. A distinction in the slope of the third miniband, related to the even number of monolayers [1], is observed only for structures with $x = 0$ and $x = 0.1$, in which the third miniband is formed mainly due to the L_1 valley contribution in the Al$_x$Ga$_{1-x}$As solid solution. The main contribution to the energy of the third miniband at $x > 0.1 - 0.3$ comes from the X_1 valley of Al$_x$Ga$_{1-x}$As, and, therefore, the slope of the third miniband is already independent of the parity of the number of layers $M + N$. The dependence of the positions of the miniband level on the parameter x for the $(9, 9)$ and $(9, 14)$ structures at $Q = 0$ (solid lines) and $Q = \pi/d$ (dotted lines) is presented in Figs. 2a and 2b, respectively. Here, Q is the component of the superlattice wave vector in the (111) direction (along the lines $M\bar{L}$ or DA) reckoned from the point M (or D) on which the point $X = (00\bar{1})2\pi/a$ is projected. The value $Q = 0$ corresponds to the points M and D of the Brillouin zone for the $(9, 9)$ and $(9, 14)$ superlattices, respectively; and $Q = \pi/d$ corresponds to the L and A points, respectively [1]. Figures 2a and 2b also show the origin of the corresponding levels. It is seen from the figures that the lower miniband for the $(9, 9)$ and $(9, 14)$ superlattices is related to the X_1 states in the AlAs layers. The second miniband is of a more complicated origin. For the $(9, 9)$ structure, it is due to X_1 states in AlAs layers with an
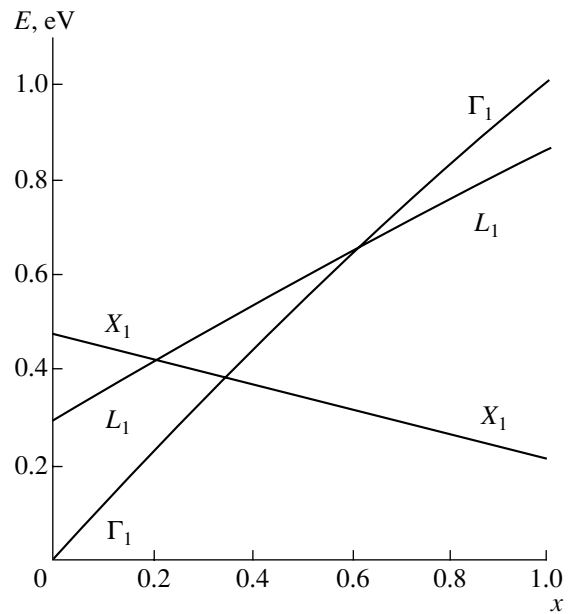

Fig. 1. Dependence of the Γ_1, X_1 and L_1 level positions on the aluminum concentration x in the Al$_x$Ga$_{1-x}$As solid solution.

arbitrary solid solution composition at the point $Q = 0$, and to X_1 states in AlAs layers when $x < 0.3$ and X_1 states in Al$_x$Ga$_{1-x}$As at $x > 0.3$ when the point $Q = \pi/d$. For the $(9, 14)$ structure, the second miniband is due to the L_1 states of Al$_x$Ga$_{1-x}$As when x is close to zero, and to X_1 states in AlAs layers when $0.1 < x < 0.3$. Beginning with $x = 0.3$, the origin of states at different points of the Brillouin zone is different for this miniband. For example, these states are due to X_1 states in Al$_x$Ga$_{1-x}$As at the point $Q = \pi/d$ and to X_1 states in AlAs layers (before $x = 0.6$) or in the solid solution layers (after $x = 0.6$) at the point $Q = 0$.

The total electronic density of a unit cell averaged over the bulk crystal (i.e. the electronic density calculated with the help of envelope functions) for the $(9, 9)$ structure is presented in Fig. 3 for $x = 0.3$ at $Q = \pi/d$ for the two lowest levels. A small discontinuity, observed at the interface between layers, does not contradict the current continuity through the heterointerface, since the current (certainly satisfying the continuity equation) is determined by exact wave functions, rather than by the constituent envelope functions. The discontinuity of the envelope wave functions is due to the difference of the Bloch wave functions in AlAs and Al$_x$Ga$_{1-x}$As. It is seen that the electronic density is mainly located in the AlAs layer for the first miniband and in the AlAs (49%) and Al$_x$Ga$_{1-x}$As (51%) layers for the second one. The electronic density distribution for the first and second minibands at $Q = \pi/d$ in the $(7, 7)$ and $(9, 14)$ structures is similar to that presented in Fig. 3.

At $Q = 0$ for x close to zero, the electronic density of the first level is localized in the AlAs layer, and that of
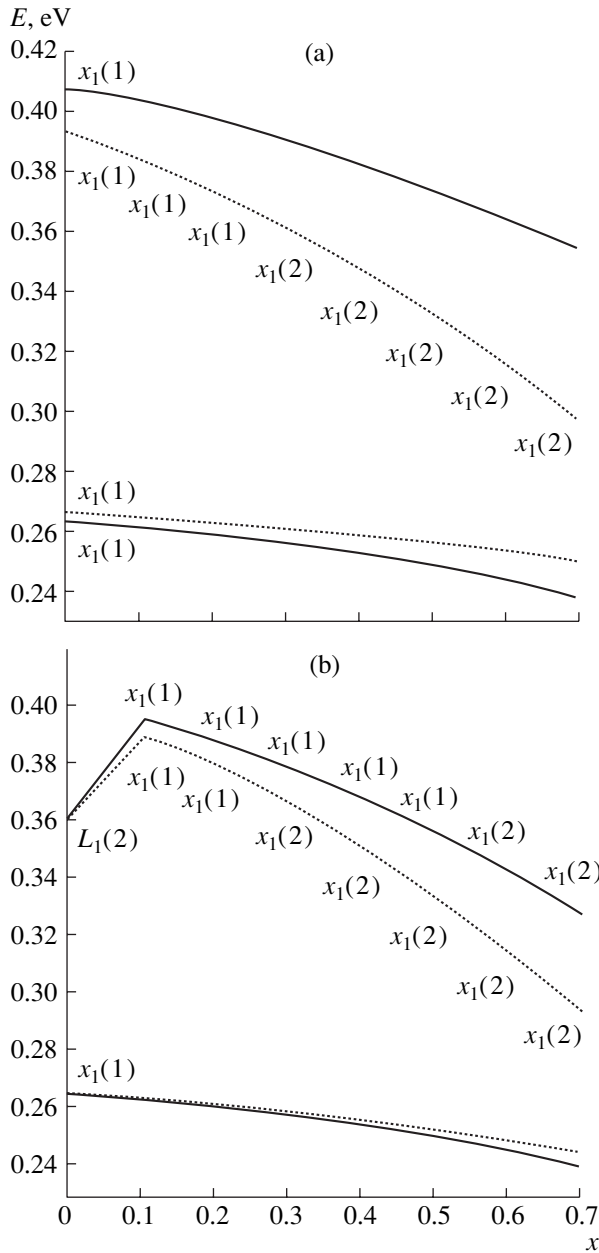
E, eV

(a)

$x_1(1)$
$x_1(1)$
$x_1(1)$
$x_1(1)$
$x_1(2)$
$x_1(2)$
$x_1(2)$
$x_1(2)$
$x_1(2)$
$x_1(1)$
$x_1(1)$

(b)

$x_1(1)$
$x_1(1)$
$x_1(1)$
$x_1(1)$
$x_1(1)$
$x_1(1)$
$x_1(1)$
$x_1(2)$
$x_1(2)$
$L_1(2)$
$x_1(2)$
$x_1(2)$
$x_1(2)$
$x_1(2)$
$x_1(1)$

x

Fig. 2. Dependence of the two lowest miniband level positions on the Al concentration x in the $Al_xGa_{1-x}As$ solid solution: (a) (9, 9) superlattice and (b) (9, 14) superlattice. Solid lines correspond to levels at the point $Q = 0$, and dotted lines, to levels at the point $Q = \pi/d$. The designations $X_1(i)$ and $L_1(i)$ indicate the origin of the states: $i = 1$ corresponds to the AlAs layer, and $i = 2$, to the $Al_xGa_{1-x}As$ layer.

the second level, in the $Al_xGa_{1-x}As$ layer in the (7, 7) and (9, 14) structures. This is so since the dominant contribution into the second miniband energy is due to the L_1 valley in $Al_xGa_{1-x}As$ for these structures at $x = 0$. Electronic densities are located mainly in the AlAs layer for both minibands at $x > 0.1$.

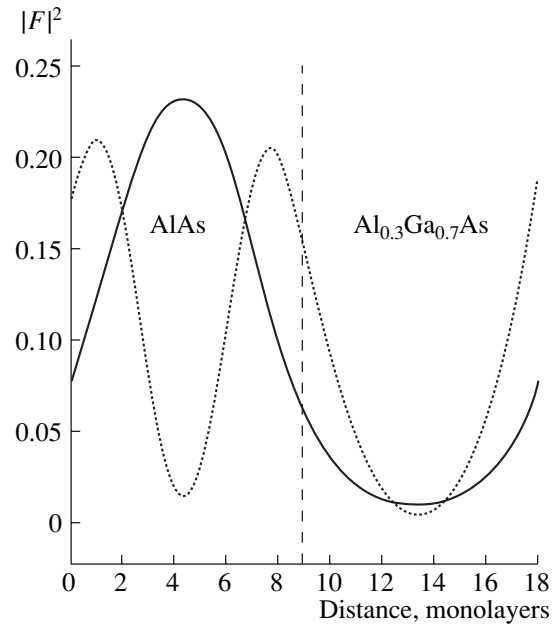A similar behavior is observed for most of the other studied structures.

$|F|^2$

AlAs

$Al_{0.3}Ga_{0.7}As$

Distance, monolayers

Fig. 3. Averaged over the bulk crystal unit cell electronic density for the first (solid line) and second (dotted line) minibands at the point $Q = \pi/d$ within a period of the (9, 9) superlattice at $x = 0.3$.

Similarly to [1], we calculated the quantity

$$\Sigma = \left|\mathbf{e} \cdot \mathbf{P}_{12}\right|^2_{(1)} + \left|\mathbf{e} \cdot \mathbf{P}_{12}\right|^2_{(2)} + \left|\mathbf{e} \cdot \mathbf{P}_{12}\right|^2_{(3)}$$

for all of the above-mentioned superlattices. Here, $\mathbf{P}_{12} = \langle\Psi_1(\mathbf{r})|\mathbf{P}|\Psi_2(\mathbf{r})\rangle$ is the matrix element of momentum between the first and second miniband wave functions divided by the dimensional value $\hbar/a$ (where $\hbar$ is Planck's constant); and $\mathbf{e}$ is the polarization vector of the light wave, which is chosen so that the value Σ is maximum. The subscripts in parentheses enumerate one of the three possible choices of the $\mathbf{k}_x$ and $\mathbf{k}_L$ points, which can be obtained from those initially chosen by 120° rotations about the (111) axis. This quantity characterizes the IR light absorption ability of a superlattice. The calculation shows that the $(AlAs)_M(Al_xGa_{1-x}As)_N$ (111) structures can effectively absorb the light of normal incidence (see table). It is seen from the results obtained that the magnitude of Σ for normal light incidence is about 3 times less than for lateral incidence. However, since in the case of normal light incidence the irradiated surface is several orders of magnitude larger than that for lateral incidence, the results obtained are quite acceptable. The conclusion made above is interesting and calls for a qualitative explanation. Similarly to [1], we have shown that taking minor corrections related to the X_5 states of the wave functions into consideration is important. We have analyzed their contribution to the total electronic density for states of the two lowest minibands. The contribution of the X_1 states for the first miniband at $Q = 0$ is found to rapidly decrease with increasing x in both layers of the superlattice, while, for

Quantity Σ characterizing the light absorption ability for various superlattices (M, N) at different points of the Brillouin zone Q for three different values of x and two variants of radiation incidence on the structure

(M, N)	x	$Q = 0$		$Q = \pi/2d$		$Q = \pi/d$	
		normal	lateral	normal	lateral	normal	lateral
(7, 7)	0.0	0.012	0.035	0.333	0.902	0.630	1.569
(7, 7)	0.3	0.153	0.503	0.296	0.780	0.621	1.570
(7, 7)	0.6	0.065	0.216	0.152	0.414	0.590	1.556
(9, 9)	0.0	0.221	0.649	0.322	0.895	0.409	1.094
(9, 9)	0.3	0.210	0.625	0.293	0.794	0.410	1.075
(9, 9)	0.6	0.109	0.329	0.187	0.509	0.381	1.014
(9, 14)	0.0	0.005	0.014	0.004	0.013	0.002	0.014
(9, 14)	0.3	0.284	0.799	0.305	0.825	0.337	0.894
(9, 14)	0.6	0.171	0.469	0.196	0.527	0.272	0.723

the second miniband, it increases insignificantly in the solid solution layer and changes only very weakly in the AlAs layer. On the whole, the contribution of these states to the electronic density is small. This contribution is two orders of magnitude smaller in comparison with the total electronic density, and the amplitude of the corresponding wave function is one order of magnitude lower. When the light wave polarization vector $\mathbf{e}$ is perpendicular to the (111) axis, the main contribution to the momentum matrix element comes from terms like $\langle F_{X5x}(z')|F_{X1}(z')\rangle\langle X_{5x}|\mathbf{e}\cdot\mathbf{P}|X_1\rangle$. These contributions are essential due to the large magnitude of the matrix elements $\langle X_5|\mathbf{P}|X_1\rangle$ and $\langle X_5|\mathbf{P}|X_3\rangle$. The quantity $\langle F_{X5x}(z')|F_{X1}(z')\rangle$ is estimated to be about 0.1, and the matrix element $\langle X_{5x}|\mathbf{e}\cdot\mathbf{P}|X_1\rangle$, about 6 (in dimensionless units). This is why the magnitude of Σ is so large for the normal incidence. Comparatively small values of Σ in the (7, 7) and (9, 14) structures $(x = 0)$ at $Q = 0$ can be accounted for by the fact that the first and the second energy levels are formed in this superlattice due to the contribution of different valleys. Some increase of Σ at $Q = \pi/2d$ and $Q = \pi/d$ in comparison with the case of $Q = 0$ is mainly because of the increase of the X_5-states contribution in the solid solution layer for the first miniband and the increase of the X_1-state contribution in this

layer for the second miniband. It is noteworthy that, at $Q = 0$, Σ, characterizing the light absorption ability, decreases with increasing x: it drops by a factor of 3 with an increase of x from 0 to 0.7. The decrease of Σ with an increase of x from 0 to 0.7 at $Q = \pi/d$ is insignificant, but its abrupt fall to zero is observed for the x value within the range from 0.9 to 1.0.

4. CONCLUSION

The miniband spectra and optical characteristics of the $(AlAs)_M(Al_xGa_{1-x}As)_N$ (111) superlattices considered in this study show that structures absorbing IR radiation via interminiband transitions can be constructed on the basis of such superlattices. A distinctive feature of such structures is the possibility of the absorption of normally incident light. Using $Al_xGa_{1-x}As$ solid solution layers instead of pure GaAs allows us to increase the thickness of these layers, which must lead to the lowering of the dark current. For this reason, such superlattices are promising materials for IR photodetectors. The model developed in this study provides a possibility for analyzing various complex structures based on AlAs and $Al_xGa_{1-x}As$ with sufficient accuracy and minimal consumption of computer resources.

REFERENCES

1. G. F. Karavaev, V. N. Chernyshov, and R. M. Egunov, Fiz. Tekh. Poluprovodn. (St. Petersburg) **36** (5), 558 (2002) [Semiconductors **36**, 527 (2002)].
2. D. Y. Ko and J. S. Inkson, Phys. Rev. B **38**, 9945 (1988).
3. S. N. Grinyaev and V. N. Chernyshov, Fiz. Tekh. Poluprovodn. (St. Petersburg) **26**, 2057 (1992) [Sov. Phys. Semicond. **26**, 1157 (1992)].
4. G. F. Karavaev and V. N. Chernyshov, Fiz. Tekh. Poluprovodn. (St. Petersburg) **35**, 105 (2001) [Semiconductors **35**, 106 (2001)].

Translated by S. Ktitorov

Electron Mobility in a AlGaAs/GaAs/AlGaAs Quantum Well

V. G. Mokerov*, G. B. Galiev*, J. Pozela**, K. Pozela**, and V. Juciene**

* Institute of Radio Engineering and Electronics, Russian Academy of Sciences, Moscow, 103907 Russia
** Semiconductor Physics Institute, Vilnius, 2600 Lithuania
Submitted November 19, 2001; accepted for publication November 21, 2001

Abstract—An oscillatory dependence of the electron mobility on the quantum well (QW) thickness in a AlGaAs/GaAs/AlGaAs heterostructure with double-sided modulation doping has been observed experimentally. A steep decrease in mobility with increasing electron concentration in the QW is established. The conditions for an increase in mobility on introducing a thin barrier into the QW are determined. The first experimental observation of an increase in mobility by a factor of 1.3 in a QW of thickness $L = 26$ nm upon introducing a thin (1–1.5 nm) AlAs barrier is reported. © 2002 MAIK "Nauka/Interperiodica".

1. INTRODUCTION

The electron scattering in quantum well (QW) AlGaAs/GaAs/AlGaAs modulation-doped heterostructures at temperatures above 77 K is due to polar optical (PO) phonons. The suppression of this scattering in the channel of field-effect transistors leads to a further increase in the electron mobility and improves the speed of modulation-doped field-effect transistors (MODFET). Electron scattering on PO phonons is inelastic and depends on the occupancy of quantum states. Calculations in [1, 2] demonstrated that PO scattering of electrons in QWs can be controlled by modifying the electron spectrum and the occupancy of states in QWs. Such control can make the electron mobility either higher or lower, with the transistor speed modified and improved. The possibility of mobility modulation by introducing a thin AlAs barrier into a QW has been extensively discussed [3–5].

The present study is concerned with the possibility of the experimental implementation of this method of control in an AlGaAs/GaAs/AlGaAs QW. For this purpose, we studied the dependences of electron mobility on the width and doping level of a QW, and also the possibility of raising the electron mobility by the introduction of a thin AlAs barrier at the center of a QW.

2. MBE-GROWN AlGaAs/GaAs/AlGaAs STRUCTURES

Samples were grown in a TsNA-24 molecular beam epitaxy (MBE) machine (Ryazan, Russia). The growth temperature was 600 and 640°C for GaAs and AlGaAs layers, respectively. Double-sided doping was used for AlGaAs layers, so that the QW in GaAs had a nearly rectangular shape. Figures 1a and 1b show the structures of the samples under study.

To determine the dependence of mobility on the QW thickness and doping, two sets of samples were grown: with relatively low and strong doping ($n_s \lesssim 10^{16}$ m^{-2}, $n_s > 10^{16}$ m^{-2}) and different QW thicknesses. The GaAs QW thicknesses were $L = 13, 18, 26, 30,$ and 35 nm for the lightly doped set (Fig. 1a), and $L = 13, 26,$ and 35 nm for the heavily doped set (Fig. 1b). Two types of samples were fabricated in the second set: with (Fig. 1b) and without a thin AlAs barrier introduced at the QW center. The AlAs barrier was 10 Å thick. The electron mobility and concentration in a QW were found from Hall effect measurements.

Table 1. Electron mobility and density in the lightly doped set of n-AlGaAs/GaAs/n-AlGaAs structures (Fig. 1a) with a QW of varied thickness

GaAs QW thickness L, nm	n_{2D}, 10^{15} m^{-2}		μ, m^2 V^{-1} s^{-1}		n_{2D}, 10^{15} m^{-2}, in the dark		μ, m^2 V^{-1} s^{-1}, in the dark	
	300 K	77 K	300 K	77 K	300 K	77 K	300 K	77 K
13	1.9	2.2	0.4836	3.9479	2.6	1.6	0.2669	4.6022
18	3.3	1.2	0.3069	3.8051	3.1	0.99	0.2577	3.5832
26	8.6	4.4	0.2920	2.6565	9.6	3.2	0.2181	3.0774
30	5.6	4.5	0.2661	1.3323	6.8	3.5	0.1907	1.2545
35	6.1	1.7	0.2168	4.6476	6.7	1.3	0.1483	4.5885

3. DEPENDENCE OF ELECTRON MOBILITY ON QW THICKNESS

Table 1 presents the measured electron mobilities and concentrations in samples of the lightly doped set with different thicknesses.

Figure 2 shows the experimentally determined electron mobilities in relation to the QW thickness in comparison with the mobilities calculated under the assumption of predominant electron scattering on PO phonons.

The scattering on PO phonons in GaAs is inelastic [1], and, therefore, the electron mobility μ is considered proportional to the inverse frequency of electron scattering on PO phonons, W:

$$\mu \propto \frac{1}{W}. \tag{1}$$

This approximation allows for the evaluation of changes in mobility on the basis of the relative change in the scattering frequency.

In terms of the dielectric continuum model, the electron scattering on PO phonons is described as follows. The frequency of transitions of electrons captured in a QW from the initial state with momentum $\mathbf{k}_i$ in the E_{si} subband to any final state with momentum $\mathbf{k}_f$ in the E_{sf} subband for the ν mode of the PO phonon is given by

$$W_{if\nu}^{\pm}(k_i, E_{si}) = \sum_{\mathbf{k}_f} \frac{4\pi m e^2}{\hbar^3} |G_\nu(z)|^2 F_{q\nu}^2$$
$$\times \left(N_{q\nu} + \frac{1}{2} \pm \frac{1}{2}\right) \delta(k_f^2 - k_i^2 + \beta_\pm), \tag{2}$$

$$G_\nu(z) = \int_L \varphi_{e1}(z)\varphi_{e2}(z)\varphi_{q\nu}(z)dz. \tag{3}$$

Here, z is the direction perpendicular to QW walls; L is the QW thickness; $\varphi_{ei}(z)$ and $\varphi_{e\nu}(z)$ are the z components of the electron and phonon wave functions, respectively; $N_{q\nu}$ is the number of phonons in the ν mode; and

$$\beta_\pm = \frac{2m}{\hbar^2}(E_{sf} - E_{si} \pm \hbar\omega_\nu). \tag{4}$$

Here, the positive and negative signs correspond to phonon emission and absorption, respectively. $F_{q\nu}$ is the normalized coefficient of electron–phonon coupling.

The electron mobility in a QW is given by

$$\mu \propto \frac{e}{m} \sum_i \frac{n_i}{W_i n_s}, \tag{5}$$

where n_i and W_i are the concentration and scattering frequency of electrons in the i-th subband, and n_s is the total electron concentration in the QW. The calculated dependences of mobility on the QW thickness for dif-

(a)

n-GaAs	$d_1 \approx 80$ Å
n-Al$_{0.22}$Ga$_{0.78}$As	$d_2 = 145$ Å
i-Al$_{0.22}$Ga$_{0.78}$As	$d_3 = 180$ Å
i-GaAs	$L = 13; 18; 26; 30; 35$ nm
i-Al$_{0.22}$Ga$_{0.78}$As	$d_4 = 180$ Å
n-Al$_{0.22}$Ga$_{0.78}$As	$d_5 = 145$ Å
i-Al$_{0.22}$Ga$_{0.78}$As	$d_6 = 800$ Å
i-GaAs	$d_7 = 0.5$ μm
GaAs (substrate)	

(b)

n-GaAs	$d_1 \approx 80$ Å
n-Al$_{0.22}$Ga$_{0.78}$As	$d_2 = 165$ Å
i-Al$_{0.22}$Ga$_{0.78}$As	$d_3 = 165$ Å
i-GaAs	$L = 65; 130; 175$ Å
AlAs barrier, $d_{AlAs} \approx 10$ Å	
i-GaAs	$L = 65; 130; 175$ Å
i-Al$_{0.22}$Ga$_{0.78}$As	$d_4 = 165$ Å
n-Al$_{0.22}$Ga$_{0.78}$As	$d_5 = 165$ Å
i-GaAs	$d_6 = 0.5$ μm
GaAs (substrate)	

Fig. 1. Sample structure: (a) lightly doped structures ($n_s < 10^{16}$ m^{-2}) and (b) heavily doped structures ($n_s > 10^{16}$ m^{-2}).

ferent levels of structure doping are presented in Fig. 2. The calculated mobility is reduced to its experimental value $\mu = 4.9$ m^2 V^{-1} s^{-1} at $L = 35$ nm and $n_s = 1.5 \times 10^{15}$ m^{-2}. The mobility in a QW with $L = 35$ nm is close to its value in the bulk sample [6]. It can be seen that the calculated curves have an oscillatory nature with two
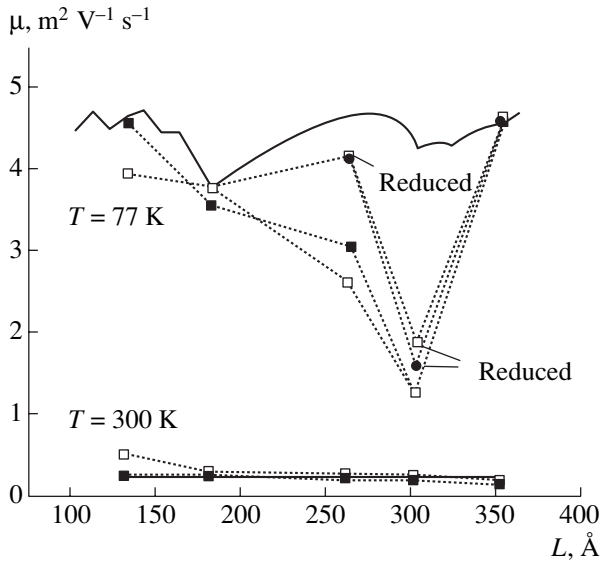
μ, m² V⁻¹ s⁻¹

Fig. 2. Mobility vs. QW width. Solid lines: calculation. Squares: experimental data. The μ values at $L = 26$ and 30 nm reduced to $n_s = 1.5 \times 10^{15}$ m⁻² are indicated by arrows.

dips at $L \approx 18$ and 30 nm. In a rectangular GaAs QW, the energy gap between the first and second subbands (for $L \approx 18$ nm), or between the first and third subbands (for $L = 30$ nm), is close to the PO phonon energy. At these QW thicknesses, resonant enhancement of the intersubband scattering of electrons with absorption of phonons occurs [1, 7, 8], which is responsible for the oscillatory variation of the electron mobility in a QW. As seen in Fig. 2, the experimental dependences of the electron mobility on the QW width confirm the occurrence of dips in the electron mobility at L in the range of 13–18 nm and also at $L \approx 30$ nm.

The experimentally observed additional decrease in mobility in structures with a QW width of 26 and 30 nm is due to the high electron density in these QWs. Using the calculated concentration dependence of mobility (Fig. 3), we reduced the experimental mobilities to the same electron density ($n_s = 1.5 \times 10^{15}$ m⁻²), which

allowed evaluation of the change in mobility in QWs with $L = 26$ and 30 nm at this density. With this estimate taken into account, we obtain an oscillatory dependence of mobility on the QW thickness with two dips, which is in good agreement with the theoretical estimation obtained assuming the predominance of electron scattering on PO phonons (Fig. 2).

The experimentally observed dip in the mobility at $L = 30$ nm far exceeds the calculated value, which, along with the scattering on PO phonons, indicates the existence of an additional electron scattering mechanism in this structure.

As calculations show, only a single dip in the mobility at $L \approx 18$ nm, associated with resonant scattering of electrons on PO phonons between the first and second subbands [9], should be observed at $T = 300$ K. The experiment confirms this feature in the dependence of the mobility on the QW thickness (Fig. 2).

Thus, the oscillatory behavior of the electron mobility with the QW thickness, associated with inelastic electron scattering on PO phonons in a GaAs QW, was confirmed experimentally for the first time. The lowest electron mobility is observed at a QW thickness in the range of 15–20 nm. This fact should be taken into account in designing high-speed MODFETs.

4. ELECTRON MOBILITY IN AlGaAs/GaAs/AlGaAs QWS IN THE CASE OF DEGENERATE ELECTRON GAS

Table 2 lists the measured mobilities and electron densities in heavily doped samples with and without an introduced AlAs barrier. The increased level of modulation doping of a QW strongly suppresses the electron mobility in the QW. Figure 3 shows the mobilities measured at 77 K. The dependences of mobility on the concentration n_s for QWs of thicknesses $L = 13$, 26, and 35 nm are compared with the calculated values of the change in mobility with respect to its experimental value at $L = 35$ nm and $n_s = 1.5 \times 10^{15}$ m⁻², which corresponds to the electron mobility in the bulk. As seen,

Table 2. Electron mobility and density in the heavily doped set of *n*-AlGaAs/GaAs/*n*-AlGaAs structures (Fig. 1b) with GaAs QWs with or without AlAs barrier

| QW thickness L, nm	AlAs barrier in GaAs QW		n_{2D}, 10¹⁶ m⁻²		μ, m² V⁻¹ s⁻¹		n^{2D}, 10¹⁶ m⁻², in the dark		μ m² V⁻¹ s⁻¹, in the dark	
			300 K	77 K	300 K	77 K	300 K	77 K	300 K	77 K
13		Absent	1.88	1.6	0.4578	1.3775	1.89	1.55	0.4239	1.2977
	Present		1.85	1.6	0.4141	1.2519	1.9	1.6	0.3854	1.1667
26		Absent	1.89	1.5	0.5173	2.3250	1.96	1.4	0.4738	2.0978
	Present		2.14	1.1	0.4486	3.0363	2.1	1.1	0.4423	2.7108
35		Absent	2.1	1.4	0.5845	3.3740	2.13	1.4	0.5410	3.1515
	Present		2.04	1.1	0.4746	3.7212	2.1	1.1	0.4473	3.1440
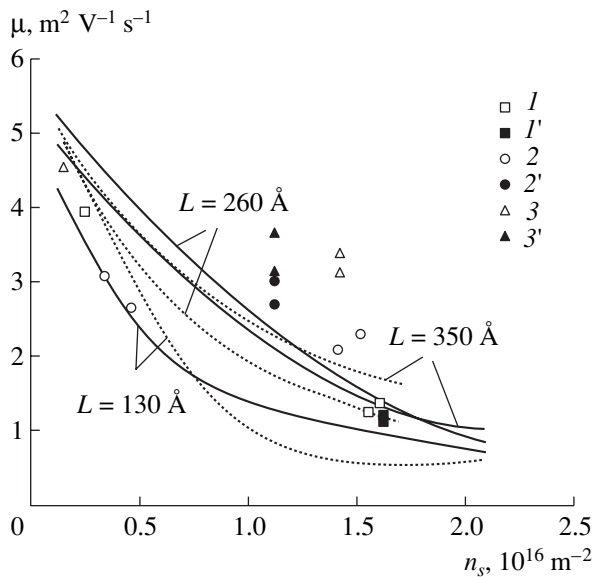
Fig. 3. Electron mobility in GaAs QWs vs. the electron density n_s, $T = 77$ K. Lines: calculation; points *1–3* and *1'–3'*, experiment. Calculation for QWs: solid lines, with AlAs barrier ($d_{AlAs} \approx 10$ Å); dashed lines, without a barrier. Experiment: (*1–3*) QWs without barrier; (*1'–3'*) with a barrier. QW thickness L: (*1, 1'*) 130, (*2, 2'*) 260, and (*3, 3'*) 350 Å.

the increased electron scattering on PO phonons, resulting from enhanced scattering with the absorption of a phonon in the case of a degenerate electron gas in QWs [6], correlates with the experimentally observed decrease in mobility with increasing n_s. However, the substantial rise in mobility with increasing QW thickness, observed experimentally at $n_s > 10^{16}$ m^{-2}, cannot be accounted for solely by the suppression of electron scattering on PO phonons, although the contribution of this factor is significant. Naturally, the scattering on heterogeneities and interfacial defects must decrease with increasing QW thickness, and this is the case in the structures under study (Fig. 3).

The introduction of an AlAs barrier into a QW modifies the intersubband energy gaps, and this suppresses the electron scattering on PO phonons in the lower subband and, correspondingly, raises the electron mobility in the QW. The calculated curves of mobility variation with electron density in QWs upon the introduction of a thin ($d \approx 10$ Å) AlAs barrier demonstrate that the mobility increases in a 13-nm-thick QW at $8 \times 10^{15} < n_s < 2.1 \times 10^{16}$ m^{-2}, and in a 26-nm-thick QW at $2 \times 10^{15} < n_s < 1.7 \times 10^{16}$ m^{-2} (Fig. 3). In a thick (35 nm) QW, the introduction of a barrier does not lead to any increase in the mobility. By contrast, the introduction of a barrier into a 35-nm-thick QW makes the electron mobility lower at $n_s > 10^{16}$ m^{-2}.

Experimentally, an increase in mobility is observed at 77 K upon introducing an AlAs barrier into a 26-nm-thick

QW. In a narrow (13 nm) QW, the predicted increase in mobility upon barrier introduction is not observed. This must be due to the predominance of scattering on hetero-interface heterogeneities in thin QWs. In a wide (35 nm) QW, the observed small increase in mobility can be attributed to a decrease in the electron density upon introducing a barrier.

A 26-nm-thick QW demonstrates a considerable (by a factor of 1.3) increase in mobility upon barrier introduction (see Table 2). Calculations predict an increase in mobility by a factor of 1.3 at $n_s < 1.1 \times 10^{16}$ m^{-2} owing to depression of electron scattering on PO phonons upon the introduction of an AlAs barrier into a QW (see Fig. 3). Therefore, the experimentally observed increase in mobility upon barrier introduction should be related to electron scattering on PO phonons in a QW.

5. CONCLUSION

Thus, the experimental data on the dependence of electron mobility on the electron density, GaAs QW thickness, and presence of a barrier in a QW confirm the theoretical conclusions about the key role played by inelastic electron scattering on PO phonons, which heavily depends on the energy spectrum and degree of degeneracy of the electron gas.

(1) The possibility of controlling the mobility in QWs was confirmed experimentally. The mobility in QWs decreases, compared with the bulk mobility, by 30% when the QW thickness $L = 18$ and 30 nm, whereupon resonant intersubband electron scattering on PO phonons occurs. A certain increase in mobility in QWs, compared with the bulk value, occurs at QW thicknesses of about 13 and 25 nm. The oscillatory dependence of mobility on the QW thickness and dips in the mobility in the range of resonant electron scattering on PO phonons were observed experimentally for the first time.

(2) The electron mobility in a QW decreases sharply when there is degeneracy of the electron gas in a QW ($n_s > 5 \times 10^{15}$ m^{-2}). The conditions were determined under which the introduction of a thin barrier into a QW raises the electron mobility. An increase in mobility by a factor of 1.3 upon the introduction of a thin (1–1.5 nm) AlAs barrier at the center of a 26-nm-thick AlGaAs/GaAs/AlGaAs QW was established experimentally for the first time.

REFERENCES

1. J. Pozela, V. Jucienë, A. Namajûnas, and K. Pozela, Physica E (Amsterdam) **5**, 108 (1999).

2. I. Lee, S. M. Goodnick, M. Gulia, *et al.*, Phys. Rev. B **51**, 7046 (1995).

3. C. R. Bennet, M. A. Amato, N. A. Zakhleniuk, *et al.*, J. Appl. Phys. **83**, 1499 (1998).

4. Q. X. Zhao, S. Wongmanerod, M. Willander, *et al.*, Phys. Rev. B **62**, 10984 (2000).

5. K. W. Kim, A. R. Bhatt, M. A. Stroscio, *et al.*, J. Appl. Phys. **72**, 2282 (1992).

6. J. Pozela, K. Pozela, and V. Jucienë, Fiz. Tekh. Poluprovodn. (St. Petersburg) **34**, 1053 (2000) [Semiconductors **34**, 1011 (2000)].

7. T. Tsuchiya and T. Ando, Phys. Rev. B **47**, 7240 (1993); Phys. Rev. B **48**, 4599 (1993).

8. W. Xu, F. M. Peeters, and J. T. Devreese, Phys. Rev. B **48**, 1562 (1993).

9. J. Pozela, V. Jucienë, A. Namajûnas, and K. Pozela, J. Appl. Phys. **81**, 1775 (1997).

Translated by D. Mashovets

LOW-DIMENSIONAL SYSTEMS

Resonance Transfer of Charge Carriers in Si/CaF$_2$ Periodic Nanostructures via Trap States in Insulator Layers

Yu. A. Berashevich*, A. L. Danilyuk, and V. E. Borisenko

Belarussian State University of Informatics and Radioelectronics, Minsk, 220013 Belarus
* e-mail: julia@nano.bsuir.edu.by

Abstract—A model of the resonance-tunneling transport of charge carriers via discrete-level traps in insulator layers in Si/CaF$_2$ periodic low-dimensional structures is proposed. Upon application of the external bias voltage to the structure, the resonance-tunneling transport occurs in the cases when the energy of the charge carriers in Si wells coincides with the energy of the trap level in CaF$_2$ layers. It is shown that filling of the traps and violation of the conditions for the resonance-tunneling transport of charge carriers via the trap level, which take place when the energy of the carriers in the wells exceeds the energy of the trap state in the insulator, result in a drop in the current through the structure; thus, a region of negative differential resistance is formed in the current–voltage characteristics of Si/CaF$_2$ periodic structures. Simulation of this effect shows that devices based on these structures may operate in a wide range of temperatures from 77 to 300 K. Another advantage is their compatibility with silicon integrated-circuit technology. © *2002 MAIK "Nauka/Interperiodica".*

1. INTRODUCTION

Nanoscale structures with quantum wells (QWs) are attracting the ever-increasing interest of scientists and engineers. This is related to the prospects for the development of solid-state devices based on the effects of quantum confinement [1]. Since the 1970s, attention has mostly been focussed on periodic structures made from III–V semiconductors [1–3]. In these structures, the resonance tunneling effect was predicted theoretically [3] and was later observed experimentally [4] for the first time. This effect is responsible for the appearance of a negative differential resistance (NDR) portion in the current–voltage (*I–V*) characteristics due to the energy-level quantization in a potential well formed by a semiconductor with a narrower band gap. On this basis, it became possible to design fast logic devices whose speed is limited only by the time of resonance tunneling of the charge carriers through the barrier. Nevertheless, these resonance-tunneling structures have certain drawbacks, such as low operating temperatures (which are needed to ensure the conditions for the formation of quantum energy levels in the well) and incompatibility with the technology of III–V semiconductors possessing well-developed silicon integrated-circuit technology.

The observation of a NDR portion in the room-temperature *I–V* characteristics of periodic Si/CaF$_2$ structures [5] provided a possibility for the development of logic devices based on silicon technology, which initiated the intensive investigation of Si-based quantum-confinement structures [6]. A thorough study of the discovered effect demonstrated that, in this case, the NDR portion appears due to charge accumulation in insulator layers upon the transfer of charge carriers via discrete-level traps and vanishes as the temperature is slightly lowered. However, another group of researchers studying the same structures observed behavior typical of the resonance tunneling of charge carriers through the structure both at room and liquid-nitrogen temperatures (77 K) [7, 8]. Nevertheless, an adequate explanation accounting for the experimental conditions under which the electrical characteristics of the structures were measured and making these characteristics consistent with the mechanism of charge-carrier resonance transfer has not been suggested.

In this study, we develop a model for the transport of charge carriers in periodic Si/CaF$_2$ nanostructures; this model describes the conditions for resonance transfer and the appearance of the NDR.

2. THE MODEL

A thin Si layer clad from both sides by layers of a wide-gap CaF$_2$ insulator forms a quantum well (QW), with the insulator layers acting as potential barriers. In silicon/insulator structures, the formation of the quantized energy levels in a potential well is obstructed by the presence of defects at the interfaces, with the defect density being as high as 10^{26} m^{-3} [9]. However, in a number of experimental studies of Si/CaF$_2$ structures, a resonance peak was observed in their *I–V* characteristics. In these studies, the thickness of the semiconductor layers varied in the range of 2.8–3.4 nm. Resonance was observed both at room and liquid-nitrogen temperatures, and raising the temperature did not lead to any
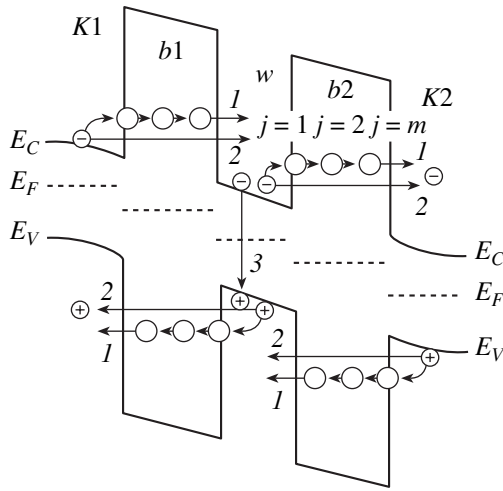
Fig. 1. The energy diagram of a two-period silicon/insulator structure. The transport and recombination processes taking place in the structure are outlined schematically: (*1*) transport via trap states in the insulator, (*2*) elastic tunneling through the potential barrier, and (*3*) interband recombination.

reduction in the peak-to-valley current ratio in the NDR portion of the *I–V* curve (which does occur in resonance-tunneling structures based on III–V compounds because of the broadening of the resonance level in the QW [4]). Taking into account the conditions under which these results were obtained (room temperature, fairly large potential-well widths, and considerable charge carrier scattering at the interfaces), one can exclude the resonance-tunneling mechanism of the charge carrier transport with the participation of resonance levels in the QW.

At the same time, as we noticed in previous publications devoted to charge-carrier transport in periodic Si/CaF$_2$ structures [10], carrier transport via trap states in insulator layers plays a major role in systems of this type. Experimental data give evidence that the trap involved, presumably related to certain lattice defects, forms a discrete level [9]; the trap density N_t is about 10^{25} m^{-3}. Studies of the mechanisms of radiation-assisted ionization of deep-level trap states in different materials [11] indicate that, in the case where the probability of the activation ionization is much lower than the probability of the escape of charge-carrier tunneling from the trap, the latter mechanism is dominant. In periodic Si/CaF$_2$ structures, the electron traps in the insulator form a deep level located close to the conduction-band edge of silicon [9]. Thus, the probability of the activation-assisted capture of charge carriers from Si layers by these traps is high. The trap ionization energy is around 3 eV even for electrons, and the probability of the activation-assisted transport of the carriers between the traps is insignificant in comparison with the probability of tunneling of the captured carriers through the

barrier, whose thickness is comparable to the lattice constant of the crystal. Consequently, we assume that the dominant mechanism of charge carrier transport in periodic silicon/insulator structures under an external electric field consists in the activation capture of charge carriers from the Si conduction band by the traps in the insulator that are located at the interface ($j = 1$ states, see Fig. 1), followed by the tunneling-assisted charge carrier transport between the traps. Since the trap levels in the insulator are identical, the energy and momentum of the carriers transferred in this way are conserved. This ensures the resonance character of the transport process.

In Fig. 1, we show the energy diagram of a two-period Si/CaF$_2$ structure under external bias; also, the electron and hole transport mechanisms considered in this paper are illustrated schematically. In addition to the charge-carrier transport via traps in insulator layers, the model takes into account elastic tunneling, which inevitably occurs in periodic structures with alternating potential barriers and wells. Its probability was calculated in the context of the Wentzel–Kramers–Brillouin (WKB) approximation [12]. It is assumed that, in the absence of external bias, the potential barriers have a rectangular shape. The potential distribution across the structure was calculated using the Poisson equation [10].

If, under external applied bias, the energy of the charge carriers in the conduction band of Si is lower than the trap energy level in the insulator E_t, the rate of their capture by the traps with $j = 1$ (which is proportional to the concentration of empty traps) can be expressed in the following form [12]:

$$g_t = S v_T n N_t \frac{D(\varphi_S)}{1 + D(\varphi_S)}. \quad (1)$$

Here, S is the cross section of the charge carrier capture by the trap; v_T and n are the thermal velocity and the density of the charge carriers in the Si conduction band, respectively; $q\varphi_S$ is the energy of a charge carrier in the well, which depends on the potential distribution in the structure; and $D(\varphi_S)$ is the occupancy of the traps for the case of their uniform spatial distribution, which is equal to [12]

$$D(\varphi_S) = g \exp\left(-\frac{E_t - q\varphi_S}{k_B T}\right), \quad (2)$$

where g is the degeneracy multiplicity of the trap level, k_B is the Boltzmann constant, and T is the temperature.

If, under external applied bias, the energy of the charge carriers is comparable to the energy of the trap level in the insulator, almost all of the traps are occu-

pied and the electrons from the Si conduction band are captured by the traps at a rate given by

$$g_t = Sv_T nN_t\left(1 - \frac{D(\varphi_S)}{1 + D(\varphi_S)}\right). \qquad (3)$$

After being captured by the first discrete-level trap ($j = 1$) in the insulator, charge carriers travel between the traps by resonance-tunneling transitions. The calculation of the transition probability is described in detail elsewhere [13].

Speed is one of the important characteristics of electronic devices. In the case we are concerned with, the charge-carrier transit through the potential barrier is a multistep process. To determine the speed of the devices based on periodic silicon/insulator structures, one needs to consider the kinetics of the activation-assisted capture of charge carriers, their tunneling-assisted transport via traps, interband recombination, and elastic tunneling. This is described by the following set of kinetic equations:

for the Si layer,

$$\frac{dn_{k1}}{dt} = G_n - \frac{n_{k1}}{\tau_a} - \frac{n_{k1}p_{k1}/p_{k2}}{\tau_{R0}} - \frac{n_{k1}}{\tau_{WKB}},$$

$$\frac{dn_w}{dt} = \frac{n_{j=m,b1}}{\tau_t} + \frac{n_{k1}}{\tau_{WKB}} - \frac{n_w}{\tau_a} - \frac{n_w p_w/p_{k2}}{\tau_{R0}} - \frac{n_w}{\tau_{WKB}},$$

$$\frac{dn_{k2}}{dt} = \frac{n_{j=m,b2}}{\tau_t} + \frac{n_w}{\tau_{WKB}} - \frac{n_{k2}p_{k2}/n_{k1}}{\tau_{R0}};$$

for traps with $j \neq 1$ in the first and the second layers of the insulator,

$$\frac{dn_{j+1,b1(2)}}{dt} = \frac{n_{j,b1(2)}}{\tau_t} - \frac{n_{j+1,b1(2)}}{\tau_t}; \qquad (4)$$

for traps with $j = 1$ in the first and the second layers of the insulator,

$$\frac{dn_{1,b1(2)}}{dt} = \frac{n_{k1(w)}}{\tau_a} - \frac{n_{1,b1(2)}}{\tau_t}.$$

Here, $j = 1 \dots m$ is the number of a trap along the path of charge-carrier motion; G_n is the rate of electron generation at the n-type contact k_1; n_{b1} and n_{b2} are the concentrations of the charge carriers captured by traps in the first and second insulator layers, respectively; $\tau_a = n/g_t$ is the time of the carrier capture by traps; $\tau_t = (\omega_0 D_{tun})^{-1}$ is the time of the carrier tunneling between the traps, which is characterized by the probability D_{tun}; ω_0 is the frequency of local charge-carrier oscillations ($\approx 10^{12}$ s^{-1} [11]); $\tau_{WKB} = (\omega_0 D_{WKB})^{-1}$ is the time of the carrier elastic tunneling through the barrier, characterized by the probability D_{WKB} [11]; and τ_{R0} is the radiative recombination time. For $j = 1$, in the first (the second) barrier

$$\frac{n_{j,b1(b2)}}{\tau_t} = \frac{n_{k1(w)}}{\tau_a}.$$

We obtained a time-dependent solution for the set of kinetic equations (4) in the following form (external bias is taken into account):

$$n_{k2}(t) = n_{k2}(0) + n_{b2}(t)$$
$$+ n_w(t)\frac{\tau_1}{\tau_{WKB}}[1 - \exp(-t/\tau_{WKB})], \qquad (5)$$

where

$$n_{b2}(t) = \sum_{j=1}^{m} n_{j,b2}(0)[1 - \exp(-t/\tau_t)]^{j-1}\exp(-t/\tau_t)$$
$$+ n_w(t)\frac{\tau_1}{\tau_a}[1 - \exp(-t/\tau_a)][1 - \exp(-t/\tau_t)]^m, \qquad (6)$$

$$n_w(t) = n_w(0)[1 - \exp(-t/\tau_1)] + n_{b1}(t)$$
$$+ n_{k1}\frac{\tau_1}{\tau_{WKB}}[1 - \exp(-t/\tau_{WKB})], \qquad (7)$$

$$\tau_1 = \left[\frac{\tau_R\tau_a + \tau_R\tau_{tun} + \tau_{tun}\tau_a}{\tau_R\tau_a\tau_{tun}}\right]^{-1}, \qquad (8)$$

$$\tau_R = \tau_{R0}\frac{p_{k2}}{p_w}. \qquad (9)$$

The expression for the concentration of charge carriers at the mth trap in the first barrier layer $n_{m(b1)}(t)$ is similar to (6).

Calculating the probabilities of capture of the charge carriers from the Si conduction band by traps and their tunneling between the traps, one needs to take into account the density of empty traps. Upon a stepwise increase of the external bias, an accumulation of captured charge carriers takes place and the density of empty traps decreases. In the pulsed mode, the charge accumulates during the time interval Δt when the pulse is applied; when the pulse is switched off, the occupied traps discharge under the conditions of a zero charge-carrier injection rate. Hole transport through the structure is described by a similar set of kinetic equations.

The current through the structure is determined by the density of electrons that reach the second contact n_{k2} and the density of holes that reach the first contact p_{k1}, with the potential distribution across the structure taken into account [10]. We assume that the energy E_t of the electron-trap level with respect to the bottom of the Si conduction band and the energy of the hole-trap level with respect to the top of the Si valence band equal 0.1 eV and that the insulator thickness is 1.5 nm. The charge carrier density at the electron and hole contacts is assumed to be $n_{k1} = p_{k2} = 5 \times 10^{23}$ m^{-3}.

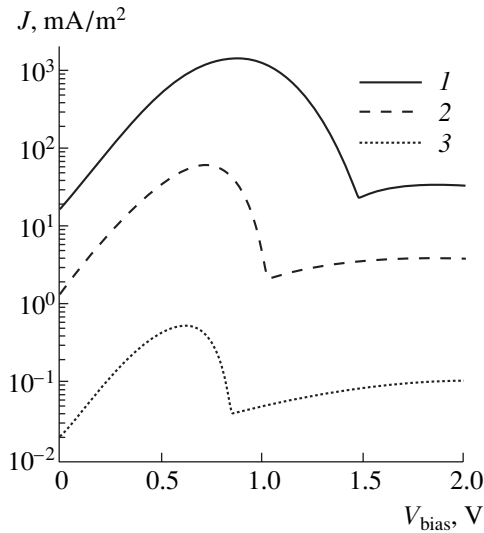**Fig. 2.** Effect of the trap density N_t on the *I–V* characteristics of a two-period Si/CaF$_2$ structure. $T = 300$ K, $\Delta t = 5 \times 10^{-8}$ s, $V_{step} = 0.1$ V, and $N_t = $ (*1*) 3×10^{24}, (*2*) 5×10^{23}, and (*3*) 10^{23} m^{-3}.
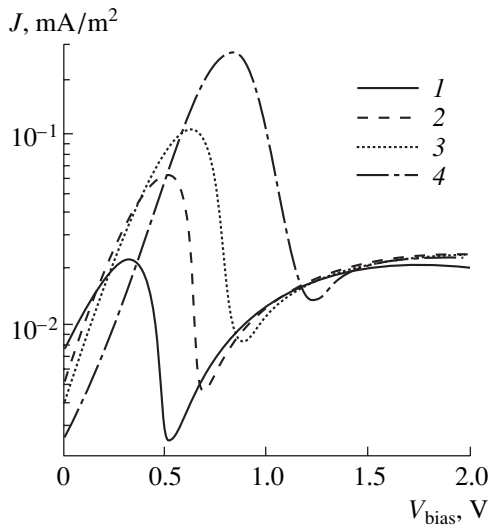

Fig. 3. Effect of the external-bias step height V_{step} on the NDR in a two-period Si/CaF$_2$ structure. $T = 300$ K, $\Delta t = 5 \times 10^{-8}$ s, and $V_{step} = $ (*1*) 0.02, (*2*) 0.05, (*3*) 0.1, and (*4*) 0.2 V.

3. RESULTS OF CALCULATIONS

The transport of charge carriers via discrete-level traps in Si/CaF$_2$ structures is primarily governed by the ratio of the charge carrier concentrations at the contacts and the trap density, as well as by the law describing the variation of the external bias and the ratio of the capture probability to the probability of a tunneling transition of a charge carrier from a trap to a well. Thus, due consideration was given to all of these factors in the numer-

ical calculation of the *I–V* characteristics of the structures under study.

An increase in the external bias applied to the silicon/insulator structure leads to an increase in the rate of charge carrier transport via discrete-level traps in the insulator, with the rate of carrier transit through the barrier by elastic tunneling (determined in the WKB approximation) being insignificant. As soon as all of the traps become occupied, the rate of the activation-assisted capture of the charge carriers by traps decreases, along with the rate of the resonance-tunneling transitions between the traps; both are determined by the rate of charge carrier release from the traps. At the same time, a reduction in the rate of carrier capture from the conduction band of silicon results in the increased importance of other processes, e.g., recombination and elastic tunneling [see equation set (4)].

In Fig. 2, the *I–V* curves of a two-period Si/CaF$_2$ structure calculated for different trap densities are plotted. An increase in the trap density, with the charge-carrier concentration at the contacts kept constant and the structure parameters unchanged, leads to a rise in the current density through the structure. This brings about an increase in the peak current and peak-to-valley ratio J_{max}/J_{min} in the NDR portion. The current peak shifts to higher external biases and broadens. This is caused by an increase in the concentration of the charge carriers at which all traps become occupied.

When the external bias is applied in a stepwise mode, the charge accumulation also depends on the height V_{step} of the bias step (of width Δt). In Fig. 3, the *I–V* curves of a two-period Si/CaF$_2$ structure calculated for different values of the V_{step} are shown. A reduction in V_{step} leads to a shift of the resonance conditions to higher biases, which results in an increased peak current and peak-to-valley ratio J_{max}/J_{min}.

It follows from the calculation that the times of charging and discharging of the trap states are no longer than 10^{-10}–10^{-8} s. With the bias-step temporal width varying in the range $\Delta t = 10^{-6}$–1.0 s, the *I–V* curve of the structure under consideration virtually does not change and there is a pronounced NDR portion in it. As Δt is reduced, the carrier transport through the traps falls off exponentially and the NDR portion disappears at $\Delta t = 5 \times 10^{-6}$ s.

When external bias is applied in the pulsed mode, the shape of the *I–V* curves in the NDR region depends on the two parameters characterizing the pulse train: the pulse duration t_I (which determines the degree of trap charging) and the delay t_D (the time interval between the pulses during which the traps discharge). In Fig. 4, the peak-to-valley ratio J_{max}/J_{min} in the NDR portion for two- and three-barrier Si/CaF$_2$ structures is plotted as a function of t_D and t_I. Calculations have shown that, with an increase in the number of periods
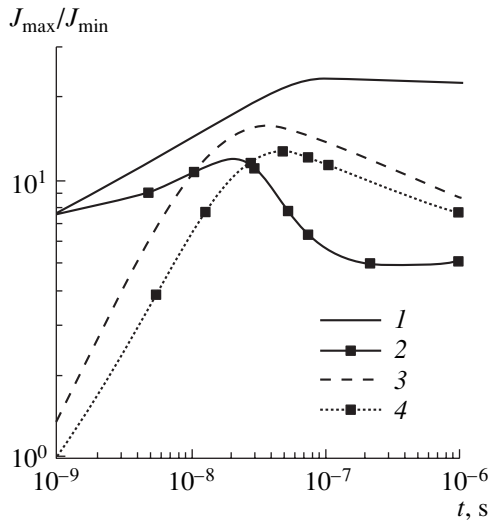
Fig. 4. Effect of the delay time t_D and the pulse duration t_I on the peak-to-valley current ratio in the pulsed mode in two- and three-period Si/CaF$_2$ structures; $T = 300$ K and $N_t = 10^{24}$ m^{-3}. Curves *1* and *2* show J_{max}/J_{min} as a function of t_D at $t_I = 10^{-6}$ s for a two- and a three-period structure, respectively; curves 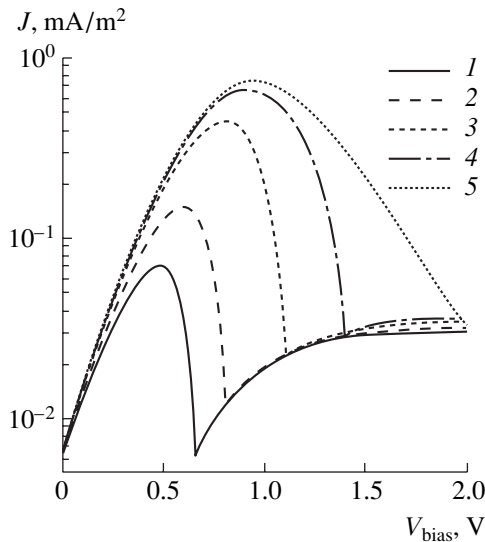*3* and *4* show J_{max}/J_{min} as a function of t_I at $t_D = 10^{-9}$ s for a two- and a three-period structure, respectively.

Fig. 5. Effect of the pulse delay time t_D on the *I–V* characteristics of a two-period Si/CaF$_2$ structure. $T = 300$ K, $N_t = 10^{24}$ m^{-3}, $t_I = 10^{-6}$ s, and $t_D = $ (*1*) 10^{-9}, (*2*) 10^{-8}, (*3*) 3×10^{-8}, (*4*) 5×10^{-8}, and (*5*) 10^{-7} s.

N, the resonance broadens and the NDR portion smears out and disappears for $N = 14$.

In Fig. 5, the *I–V* curves of a two-period Si/CaF$_2$ structure are plotted for different delay times t_D. It can be seen that an increase in the trap discharge duration

leads to an increase in the peak current and to the broadening of the resonance due to a reduction in the rate of charge accumulation at the traps.

At lowered temperatures, the probability of charge carrier capture by traps is reduced. This brings about a decrease in the current in the ascending portion of the *I–V* curve and an increase in the contribution of the elastic tunneling to the transport of charge carriers through the structure. However, in so far as the trap levels in the insulator are located near the Si conduction band, the ratio J_{max}/J_{min} virtually does not change with temperature down to 77 K. Below 77 K, the peak-to-valley ratio decreases since the elastic tunneling, which depends only slightly on temperature, becomes dominant.

4. CONCLUSION

To describe the mechanism leading to resonance conditions in periodic silicon/insulator nanostructures, we considered a model that takes into account the resonance transport of charge carriers via discrete-level traps in insulator layers along with carrier elastic tunneling through the potential barriers.

We demonstrated that, in the case when the concentration of charge carriers at the contacts is close to the density of traps in the insulator, the transport via trap states is governed by the latter quantity and its rate is highest when the energy of the charge carriers in the well coincides with the trap level in the insulator. As the carrier energy is increased still further, the probability of carrier transfer through the trap level is reduced due to a decrease in the concentration of empty traps. Then, the onset of resonance conditions in the structure is primarily affected by the rate of trap filling upon application of the external bias, which is determined by the bias step height and the bias pulse duration.

The devices based on such structures have the advantages of a wide temperature-of-operation range (from 77 to 300 K) and their compatibility with silicon integrated-circuit technology.

REFERENCES

1. C. G. Smith, Rep. Prog. Phys. **59**, 235 (1996).
2. L. L. Chang, P. J. Stiles, and L. Esaki, J. Appl. Phys. **38**, 4440 (1967).
3. L. Esaki, Phys. Rev. **109**, 63 (1958).
4. R. Tsu and L. Esaki, Appl. Phys. Lett. **22**, 562 (1973).

5. S. Ménard, A. N. Kholod, M. Liniger, *et al.*, Phys. Status Solidi A **181**, 561 (2000).

6. L. Vervoort, F. Bassani, I. Michalcescu, *et al.*, Phys. Status Solidi B **190**, 123 (1995).

7. M. Watanabe, T. Funayama, T. Teraji, and N. Sakamaki, Jpn. J. Appl. Phys., Part 2 **39**, L716 (2000).

8. M. Watanabe, I. Iketani, and M. Asada, Jpn. J. Appl. Phys., Part 2 **39**, L964 (2000).

9. V. Ioannou-Sougleridis, V. Tsakiri, and A. G. Nassiopoulou, in *Silicon Modules for Integrated Light Engineering*, Report on the ESPRIT Project No. 28741 (Marseilles, France, 2000), p. 133.

10. Yu. A. Berashevich, A. L. Danilyuk, A. N. Kholod, and V. E. Borisenko, Fiz. Tekh. Poluprovodn. (St. Petersburg) **35**, 110 (2001) [Semiconductors **35**, 112 (2001)].

11. S. D. Ganichev, I. N. Yassievich, and W. Prettl, Fiz. Tverd. Tela (St. Petersburg) **39**, 1905 (1997) [Phys. Solid State **39**, 1703 (1997)].

12. K. C. Kao and W. Hwang, *Electrical Transport in Solids* (Pergamon, New York, 1981; Mir, Moscow, 1984), Vol. 1.

13. V. Ya. Kirpichenkov, Zh. Éksp. Teor. Fiz. **116**, 1048 (1999) [JETP **89**, 559 (1999)].

Translated by M. Skorikov

<center>LOW-DIMENSIONAL
SYSTEMS</center>

Inversion of the Electron Population in Subbands of Dimensional Quantization with Longitudinal Transport in Tunnel-Coupled Quantum Wells

V. Ya. Aleshkin and A. A. Dubinov

Institute of Physics of Microstructures, Russian Academy of Sciences, Nizhni Novgorod, 603600 Russia

Abstract—The scheme of a laser which can operate in the far-infrared range ($\lambda \sim 150$ μm) is suggested. In order to attain the inversion of the subband population it was suggested that electron transport in three tunnel-coupled quantum wells in a strong electric field, which lies in the plane of quantum wells, be used. An important specific feature of the structure suggested is the presence of a single rough heterointerface. The electron transport was simulated by the Monte Carlo method for the $Al_xGa_{1-x}As/GaAs$ ($x = 0.2$–0.3) heterostructure. The simulation demonstrated that the population inversion in the first and second subbands of dimensional quantization is realized in the field above 1.2 kV/cm at $T = 4.2$ and 77 K. © 2002 MAIK "Nauka/Interperiodica".

1. INTRODUCTION

At present, the physics of unipolar semiconductor lasers based on quantum wells is being vigorously developed. Cascade [1] and fountain [2] lasers operating in the mid-infrared (IR) region have already been developed. However, the advance of cascade lasers to the far-IR range is highly problematic. Indeed, the absorption of light by free carriers increases proportionally to the squared wavelength. For this reason, this absorption in passive regions of cascades and contacts should substantially decrease the laser gain for the far-IR region. The fountain laser is free of this disadvantage. However, optical pumping by the external laser makes it very inconvenient for practical applications.

In the mid-1980s, pulsed unipolar semiconductor lasers based on bulk, lightly doped p-Ge, which operate at the liquid helium temperature in crossed E and H fields (the wavelength 300 μm $< \lambda <$ 70 μm), were developed [3]. A semiconductor laser which is based on bulk strained p-Ge ($\lambda \sim 100$ μm) also exists [4]. The characteristic size of the crystal for these lasers is about 1 cm, and the characteristic electric fields are about 1 kV/cm. For this reason, a high-voltage pulse supply is necessary for the operation of these lasers. This, of course, complicates their use. Note that continuous stimulated far-IR radiation was observed for strained p-Ge in conditions of the impurity breakdown of acceptors [5].

In this study, another possible scheme of a laser which can operate in the far-IR region ($\lambda \sim 150$ μm) is considered. In order to attain the population inversion, we suggest using electron transport in three tunnel-coupled quantum wells (QWs) in a strong (below the onset of the Gunn effect) electric field, which lies in the plane of QWs. An important specific feature of the structure

suggested is the presence of a single rough heterointerface. The Monte Carlo simulation of the electron transport carried out demonstrated that, in the fields above 1.2 kV/cm at liquid helium and liquid nitrogen temperatures, population inversion in the first and second subbands of dimensional quantization is attained. In contrast with the cascade laser, the contact regions in such a laser can be positioned outside the active region, which makes it possible to substantially reduce the losses due to free carriers.

The method suggested for the attainment of population inversion is one of the possibilities for realizing a general idea suggested previously [6]. Let us recall this idea. Assume that there are two groups of charge carriers which differ widely in their mobility. Upon applying a strong electric field, the average kinetic energy of carriers in a high-mobility group will be significantly higher relative to that in a low-mobility group. If the probability of carrier transition from one group to another increases with increasing kinetic energy, the accumulation of particles in the group with a low mobility and low kinetic energy takes place. A similar idea of particle transport from a hot group to a cold one has long been in use in stills and, specifically, in home-brewed brandy equipment, which are well known in Russia. Using this idea, a scheme of a laser based on Γ–X valleys in QWs, which can operate in the mid-IR region, was suggested [7].

2. MODEL OF ELECTRON TRANSPORT IN THREE TUNNEL-COUPLED QUANTUM WELLS

Let us consider current flow in three tunnel-coupled QWs, which are shown in Fig. 1. The electric field lies
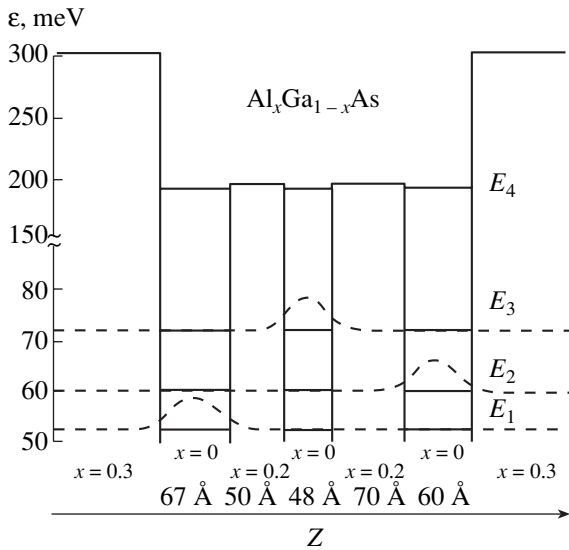
Fig. 1. Energy-band diagram and electron wave functions in the system of three tunnel-coupled quantum wells. The conduction band bottom of GaAs is selected as the origin of energy scale.

in the plane of QWs so that the current flows along the structure. Each of the electron wave functions on three lower subbands of dimensional quantization is localized mainly in its own QW. Note that overlap of the wave functions in the first and third subbands is substantially larger relative to their overlap in the first and second subbands (see Fig. 1). The parameters of the structure are selected so that the scattering by polar optical phonons represents the mechanism of the main electron exchange between the subbands (wells) in the fields lower than the onset of the Gunn effect. To provide the difference in mobilities between the electrons of the first two wells and a second one, it is suggested that a rough internal boundary of the third well (farthest to the right) be grown. Since the amplitudes of electron wave functions in the first and third subbands of dimensional quantization on this heterointerface are small, scattering at its roughness is weak. Alternatively, the electron wave function of the second subband at its rough heterointerface is not small. For this reason, scattering of these electrons on the roughness is rather strong. Thus, due to the high sensitivity of scattering at the roughness to the wave-function value at the heterointerface, it is possible to provide the difference in mobilities for electrons whose wave functions are localized in different wells. This should lead to a considerable difference between the average kinetic energy of electrons in the second subband and average kinetic energies of electrons in the first and second subbands in strong electric fields. In other words, the high-energy tail of the electron distribution function in the first and third subbands is extended by energy considerably farther when compared with that in the second subband. Some electrons possess an energy high enough to trans-

fer to the second subband with the emission of polar optical phonons. For this reason, the fraction of such electrons in the first and third subbands is sufficiently larger compared with the fraction of electrons which can transfer into other subbands in the second subband. This circumstance is favorable to the accumulation of electrons in the second subband and to the emergence of population inversion between the second and first subbands in electric fields that are sufficiently strong.

In order to find the spectrum and wave functions of the electron in three tunnel-coupled QWs of the $Al_xGa_{1-x}As$ heterostructure, the time-independent Schrödinger equation with the Hamiltonian $\hat{H} = \frac{1}{2}\hat{\mathbf{p}}\frac{1}{m^*(z)}\hat{\mathbf{p}} + E_c(z)$ was solved in the approximation of a simple conduction band (Γ valley). Here, $\hat{\mathbf{p}}$ is the momentum operator; $E_c(z)$ is the location of the bottom of the Γ valley, which is shown in Fig. 1; and $m^*(z)$ is the effective electron mass at the bottom of the Γ valley. Assuming that the motion in the XY plane is infinite, we represent the wave functions describing the electron as

$$\Psi(\mathbf{r}) = \frac{1}{\sqrt{S}}\exp(i\mathbf{k}\mathbf{r})\Phi(z). \tag{1}$$

Here, $\mathbf{r}$ and $\mathbf{k}$ are the radius vector and wave vector of the electron in the plane of the quantum well, respectively; and S is the structure area in this plane. For the dependences of the effective electron mass and position of the conduction band bottom on the Al fraction, we used the data of study [8]. The results of calculating the wave functions and energies of dimensional quantization (they are denoted by letters E_i) are shown in Fig. 1. We are interested only in the three lower subbands of dimensional quantization. Other subbands, which possess high energies (E_4 in Fig. 1), are not considered in our study. The reason is that no electron population of these subbands for the parameters we selected (the temperature and electric field) is actually observed.

Note that the electron masses in the plane of QWs for three of the first subbands of dimensional quantization are close to the effective electron mass at the bottom of the Γ valley for GaAs, which we denote by the letter m. This is the consequence of two factors. First, the energy of dimensional quantization is low relative to the band gap. Due to this, it is possible to neglect the effects of nonparabolicity of the bands. Second, the probability of an electron being located in the $Al_xGa_{1-x}As$ solid solution is low compared with the probability of it being located in GaAs (see Fig. 1). For this reason, we further assume that the electron energy in the ith subband with the wave vector k is equal to $E_i + \frac{\hbar^2 k^2}{2m}$.

3. SCATTERING

In strong electric fields at low temperatures, scattering mechanisms for our structure are scattering by optical phonons and scattering at the roughness of the heterointerface. For this reason, we neglect scattering by acoustic phonons and electron–electron scattering, as well as scattering by the charged impurity, assuming that the electron density is sufficiently low.

Considering electron scattering by polar optical phonons, we assumed the law of phonon dispersion to be the same as for bulk GaAs. In addition, the phonon gas was assumed to be in equilibrium with the temperature corresponding to the crystal temperature. In order to calculate the probability of electron scattering from the *i*th subband to the *j*th subband by polar optical phonons, we used the standard approach [9], in which this probability can be written as

$$W_{ij}^{\pm}(\mathbf{k}_i, \mathbf{k}_j) = \frac{2\pi}{\hbar}|V_{ij}(\mathbf{k}_i, \mathbf{k}_j)|^2 \left(N_q + \frac{1}{2} \pm \frac{1}{2}\right)$$

$$\times \delta\left(E_i - E_j + \frac{\hbar^2(k_i^2 - k_j^2)}{2m} \mp \hbar\omega_0\right). \quad (2)$$

Here, $\mathbf{k}_j$ is the electron wave vector in the *i*th subband; q is the wave vector of the optical phonon, with the superscript and subscript being related to the emission and absorption of the phonon, respectively; $\hbar\omega_0$ is the energy of the longitudinal optical phonon; $N_q = \dfrac{1}{\exp(\hbar\omega_0/k_\mathrm{B}T) - 1}$ is the number of longitudinal optical phonons with the wave vector $\mathbf{q}$; k_B is the Boltzmann constant; and T is the temperature of the crystal. The squared modulus of the matrix element for the operator of the electron–phonon interaction can be written as

$$|V_{ij}(\mathbf{k}_i, \mathbf{k}_j)|^2 = \frac{\pi e^2 \hbar \omega_0}{S\bar{\varepsilon}|\mathbf{k}_i - \mathbf{k}_j|} \iint dz dz_1 \Phi_i(z) \Phi_i^*(z_1)$$

$$\times \Phi_j(z) \Phi_j^*(z_1) \exp\{-|z - z_1||\mathbf{k}_i - \mathbf{k}_j|\}. \quad (3)$$

Here, $\bar{\varepsilon} = (1/\varepsilon_\infty - 1/\varepsilon_0)^{-1}$; ε_∞ and ε_0 are the high-frequency and low-frequency dielectric constants for GaAs, respectively.

Figure 2 demonstrates angular dependences of the scattering probability for transitions between the states of the first and second subbands of dimensional quantization due to the optical phonon emission for two values of the kinetic energy of the electron motion along QWs. It can be seen from Fig. 2 that high-energy electron scattering is of the small-angle type. The reason is that, at sufficiently high electron energies, the wave vector q of the phonon emitted by the electron increases as the scattering angle increases. In this case, the scattering-matrix element is inversely proportional to q: $V_{ij} \propto 1/q$ [9]. On the contrary, low-energy electron scat-
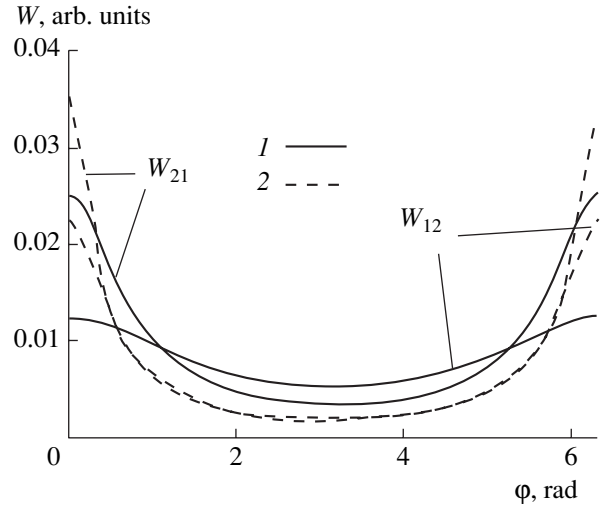
Fig. 2. Angular dependences of probability of electron scattering between the states of the first and second subbands of dimensional quantization with the emission of an optical phonon for two values of the kinetic energy of motion along the quantum wells ε = (*1*) 50 and (*2*) 90 meV.
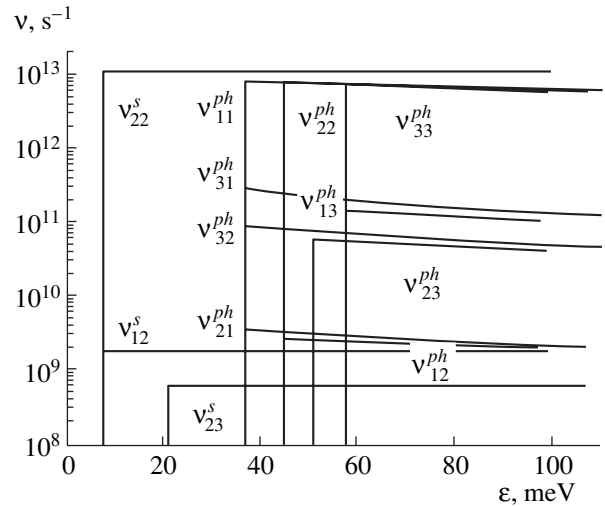

Fig. 3. Dependence of frequencies of scattering of the electron by an optical phonon (lines with the superscript p_h) and at the heterointerface roughness (lines with the superscript s) on the total electron energy for various transitions at liquid helium temperature.

tering is almost isotropic, since q is actually independent of the electron scattering angle in this case.

The electron-energy dependences of frequency of scattering by an optical phonon at liquid helium temperature (lines with the superscript ph) are given in Fig. 3 and can be represented as

$$\nu_{ij}(\varepsilon) = \sum_{\mathbf{k}_{ij}} (W_{ij}^+, (\mathbf{k}_i, \mathbf{k}_j) + W_{ij}^-(\mathbf{k}_i, \mathbf{k}_j)),$$

$$\varepsilon = E_1 + \frac{\hbar^2 k_i^2}{2m}. \quad (4)$$

Since spontaneous phonon emission prevails in scattering at this temperature, scattering frequencies depend on the electron energy in a threshold manner. Note that the scattering frequency decreases with increasing electron energy, since the average wave vector of the phonon emitted increases as the electron energy increases. Let us also note that the frequencies of intrasubband scattering considerably exceed the frequencies of intersubband scattering.

In order to calculate the probability of scattering at the roughness of the heterointerface, we used the following expression:

$$W_{ij}(\mathbf{k}_i, \mathbf{k}_j) = \frac{2\pi}{\hbar}|U_{ij}(\mathbf{k}_i - \mathbf{k}_j)|^2$$

$$\times \delta\left(E_i - E_j - \frac{\hbar^2(k_i^2 - k_j^2)}{2m}\right). \quad (5)$$

Here, $U_{ij}(\mathbf{k}_i - \mathbf{k}_j)$ is the matrix element of the scattering operator $\hat{U}(\mathbf{r}, z)$, which is associated with the surface roughness of the heterointerface and differs from zero only in the following regions:

$$\hat{U}(\mathbf{r}, z) = \begin{array}{ll} -\Delta E_c & z_h(\mathbf{r}) < z < \bar{z}_h, \quad z_h(\mathbf{r}) < \bar{z}_h, \\ \Delta E_c & \bar{z}_h < z < z_h(\mathbf{r}), \quad z_h(\mathbf{r}) < \bar{z}_h. \end{array} \quad (6)$$

Here, $z_h(\mathbf{r})$ is the z coordinate of the heterointerface with a given radius vector in the plane of the QW $\mathbf{r}$, $\bar{z}_h$ is the z coordinate of a smooth heterointerface, and ΔE_c is the energy discontinuity of the conduction band bottom at the heterointerface. Subsequently, we assume that the characteristic scale of the roughness in the z direction is much smaller than the characteristic scale on which the wave functions $\Phi_i(z)$ vary. In this approximation, the squared matrix element of the scattering operator can be written as

$$|U_{ij}(\mathbf{k}_i - \mathbf{k}_j)|^2 = \Delta E_c^2 |\Phi_i(\bar{z}_h)\Phi_j(\bar{z}_h)|^2$$

$$\times \frac{1}{S}\int d^2r \exp\{-i(\mathbf{k}_i - \mathbf{k}_j)\mathbf{r}\}\langle\Delta(\mathbf{R})\Delta(\mathbf{R} + \mathbf{r})\rangle. \quad (7)$$

Here, $\langle\Delta(\mathbf{R})\Delta(\mathbf{R} + \mathbf{r})\rangle$ is the correlation function of the surface roughness [10]:

$$\langle\Delta(\mathbf{R})\Delta(\mathbf{R} + \mathbf{r})\rangle$$

$$= \frac{1}{S}\int d^2R[z_h(\mathbf{R}) - \bar{z}_h][z_h(\mathbf{R} + \mathbf{r}) - \bar{z}_h]. \quad (8)$$

Conventionally, the correlation function of the surface roughness is considered as the Gaussian function [10]:

$$\langle\Delta(\mathbf{R})\Delta(\mathbf{R} + \mathbf{r})\rangle = \Delta_z^2 \exp(=r^2/\Lambda^2). \quad (9)$$

Here, Δ_z is the rms shift of the heterointerface, and Λ is the characteristic magnitude of the roughness on the heterojunction plane. In the approximation $|\mathbf{k}_i - \mathbf{k}_j|\Lambda \ll 1$,

the frequency of electron scattering at the heterointerface roughness can be written as

$$\nu_{ij} = \pi m(|\Phi_i(\bar{z}_h)||\Phi_j(\bar{z}_h)|\Delta E_c \Delta_z \Lambda)^2/\hbar^3. \quad (10)$$

In this approximation, the scattering probability is independent of the electron kinetic energy and the scattering angle. The results of calculating the frequencies of electron scattering at the roughness of the heterointerface for various transitions are given in Fig. 3 (lines with the superscript s). We accepted the following values for Δ_z and Λ: $\Delta_z = 10$ Å and $\Lambda = 38$ Å.

4. RESULTS OF SIMULATION OF THE ELECTRON TRANSPORT

It can be seen from Fig. 3 that the frequencies of scattering between the states of the second subband and the states of the first and third subbands are several orders of magnitude lower than other scattering frequencies. For this reason, we used an approximation in which it was assumed that the form of the electron distribution in energy in the second subband is governed by electron scattering inside this subband only. Scattering between the second and other subbands determines only the total number of electrons in this subband. On the contrary, the forms of the distribution functions in the first and third subbands affect each other and, for this reason, they were calculated jointly. The absolute values of the electron distribution functions over the subbands were found from the time-independent equation of the particle balance,

$$\frac{dn_2}{dt} = \int\nu_{12}(\varepsilon)f_1(\varepsilon)d\varepsilon + \int\nu_{32}(\varepsilon)f_3(\varepsilon)d\varepsilon$$

$$- \int(\nu_{21}(\varepsilon) + \nu_{23}(\varepsilon))f_2(\varepsilon)d\varepsilon, \quad (11)$$

and the conservation law for the number of particles,

$$n_1 + n_2 + n_3 = n. \quad (12)$$

Here, n_i is the electron density in the ith subband, n is the total electron density for the system, ν_{ij} is the total frequency of scattering from the ith subband to the jth subband, $f_i(\varepsilon)$ is the electron distribution function by the energy in the ith subband, and $n_i = \int f_i(\varepsilon)d\varepsilon$.

The dependences of electron distribution functions on the total energy for all three subbands and the other two values of the electric field are shown in Fig. 4. It can be seen from Fig. 4 that each distribution function has two characteristic portions. The boundary between them lies in the energy region from which intrasubband scattering with the emission of a polar optical phonon is possible. The distribution function decreases gradually to this boundary and decreases more sharply beyond it. Such behavior of the distribution function can be explained by the electron scattering by a polar optical phonon. Indeed, an electron that gained a kinetic energy larger than the energy of the optical

phonon rapidly releases it and enters the low-energy domain. In this domain, the electron resides for a long time until it gains energy due to heating by the electric field. As was already noted above, electrons located in the second subband of dimensional quantization are strongly scattered at the heterointerface roughness. Due to this, their distribution function decreases more sharply and has a weakly pronounced high-energy tail in the field of 2 kV/cm. For this reason, the average kinetic energy of electrons located in this subband is lower than that of electrons in the first and third subbands. The electron transitions between the subbands proceed mainly owing to scattering by optical phonons; in this case, $\nu_{12}, \nu_{21} < \nu_{23}$, and $\nu_{32} < \nu_{13}, \nu_{31}$ (see Fig. 3). This leads to a considerable electron drain from the third subband to the second one. The third subband is actively occupied by electrons from the first subband, since the electron transitions due to scattering by phonons often occur between them. By virtue of the above reasons, the electrons in a strong electric field experience scattering by phonons and transfer from the first subband to the third one and from the third subband to the second one, where they accumulate. This leads to inverse electron distribution in the first and second subbands.

The electric field dependences of the ratio and the difference of electron densities in the second and first subbands at liquid helium temperature are shown in Fig. 5a. It can be seen from Fig. 5a that the population for inversion of the first and second subbands of dimensional quantization is attained in the fields stronger than 1.2 kV/cm. Since electrons accumulate in the subband with a low mobility as the electric field becomes stronger, the drift velocity falls simultaneously. The electric field dependence of the average drift velocity of electrons in our structure is also shown in Fig. 5a. It can be seen from Fig. 5a that the electron drift velocity begins to fall as the electric field becomes stronger, beginning at fields of ~50 V/cm.

The results of calculating the same quantities as in Fig. 5a for the liquid nitrogen temperature are given in Fig. 5b. It can be seen from a comparison between Figs. 5a and 5b that a decrease in the inversion is small with such an increase in the temperature. Only the electric field dependence of the electron drift velocity undergoes noticeable variations. In addition to the fact that the magnitude of the drift velocity noticeably decreases, its fall as the electric field increases already begins from the fields of about 500 V/cm.

Let us now estimate the possible gain in such a structure. The approximate expression for the gain at a frequency ω which corresponds to the difference in energies $E_2 - E_1$ can be written as

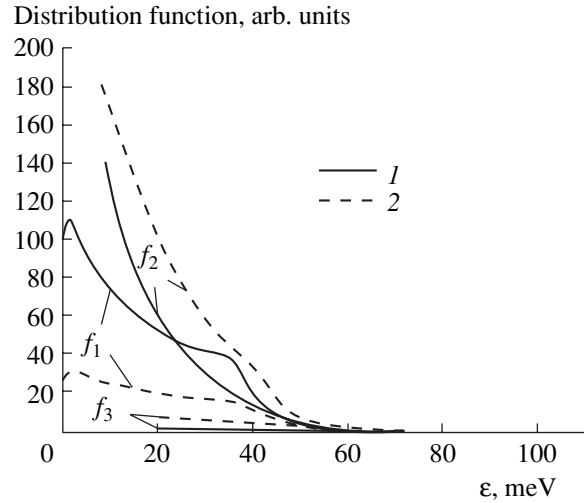$$\beta = \alpha \frac{4\pi|z_{12}|^2(n_2 - n_1)\omega\tau}{\sqrt{\varepsilon_0}L_z}. \qquad (13)$$

Fig. 4. Dependences of electron distribution functions in three subbands on the total energy for two values of the electric field at $T = 4.2$ K; electron transport was simulated using the Monte Carlo method. $E = (1)$ 1 and (2) 2 kV/cm.
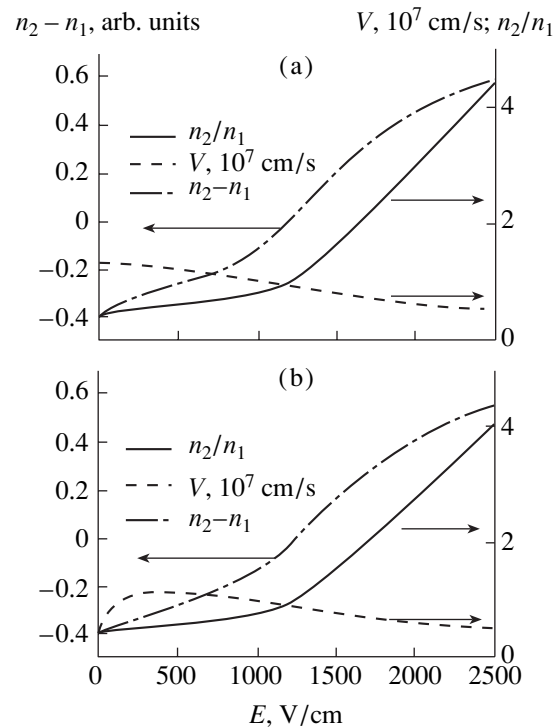

Fig. 5. Dependences of the n_2/n_1 ratio, the $n_2 - n_1$ difference of electron densities in the second and first subbands, and the average drift velocity of electrons V in the structure considered on the electric field E for the temperature (a) 4.2 K and (b) 77 K calculated by the Monte Carlo method.

Here, $\alpha = e^2/\hbar c$ is the fine-structure constant, z_{12} is the matrix element of the operator **z**, τ is the time characterizing the spectral width of the transition between the second and first subbands (relaxation time of the phase), and L_z is the characteristic size of wave localiza-

tion in the z direction. If the system is periodic in the z direction, i.e., contains many triads of QWs, the period can be accepted as L_z. Let $\omega\tau \approx 10$, $\varepsilon_0 \approx 13$, $(n_2 - n_1) \approx 10^{11}$ cm^{-2}, $L_z \approx 5 \times 10^{-6}$ cm (the periodic system is kept in mind), and $z_{12} \approx 2.9 \times 10^{-8}$ cm, which corresponds to our system. In this case, from expression (12) we obtain $\beta \approx 4.3$ cm^{-1}. Note that the lattice absorption in GaAs for radiation with a wavelength of 150 μm is less than 1 cm^{-1} at $T = 4.2$ K [11].

ACKNOWLEDGMENTS

REFERENCES

1. J. Faist, F. Capasso, D. L. Sivko, *et al.*, Science **264**, 533 (1994).
2. O. Gauthier-Lafaye, P. Boucaud, F. H. Julien, *et al.*, Appl. Phys. Lett. **71**, 3619 (1997).
3. A. Andronov and E. Gornik, Opt. Quantum Electron. **23** (2), S205 (1991).
4. I. V. Altukhov, M. S. Kagan, K. A. Korolev, *et al.*, Zh. Éksp. Teor. Fiz. **101**, 756 (1992) [Sov. Phys. JETP **74**, 404 (1992)].
5. I. V. Altukhov, M. S. Kagan, K. A. Korolev, *et al.*, Zh. Éksp. Teor. Fiz. **115**, 89 (1999) [JETP **88**, 51 (1999)].
6. V. Ya. Aleshkin, A. A. Andronov, A. V. Antonov, *et al.*, Phys. Status Solidi B **204**, 563 (1997).
7. V. Ya. Aleshkin and A. A. Andronov, Pis'ma Zh. Éksp. Teor. Fiz. **68**, 73 (1998) [JETP Lett. **68**, 78 (1998)].
8. E. H. Li, *Physica E* (Amsterdam) **5**, 215 (2000).
9. V. F. Gantmakher and Y. B. Levinson, *Carrier Scattering in Metals and Semiconductors* (Nauka, Moscow, 1984; North-Hooland, New York, 1987).
10. T. Ando, A. B. Fowler, and F. Stern, Rev. Mod. Phys. **54**, 437 (1982).
11. P. D. Coleman, G. Sherman, D. Parsons, and D. Akitt, in *Proceedings of Symposium on Submillimeter Waves, New York, 1970*, p. 694.

Translated by N. Korovin

<center>AMORPHOUS, VITREOUS,
AND POROUS SEMICONDUCTORS</center>

Photoconductivity of Nanostructured Hydrogenated Silicon Films

O. A. Golikova

Ioffe Physicotechnical Institute, Russian Academy of Sciences,
Politekhnicheskaya ul. 26, St. Petersburg, 194021 Russia
Submitted November 1, 2001; accepted for publication November 21, 2001

Abstract—The photoconductivity of nanostructured hydrogenated silicon films prepared by different techniques was studied in relation to the Fermi level position, the density of defects, and the type of Si–H bonding. The influence of Si$^+$ ion implantation on the photoconductivity and other parameters of a-Si:H films was determined. © 2002 MAIK "Nauka/Interperiodica".

1. INTRODUCTION

Nanostructured hydrogenated Si (ns-Si:H) can be considered as an amorphous matrix containing small (~2–3 nm) Si crystals and/or clusters. This newly developed material is of interest because its photoconductivity (σ_{ph}) exceeds the photoconductivity of conventional a-Si:H by orders of magnitude [1, 2]. Since the product of the mobility and the electron lifetime for ns-Si:H is radically increased, this material is of interest from the point of view of practical application. At the same time, ns-Si:H films are an interesting object of investigation in the physics of thin semiconductor films. Indeed, in accordance with generally accepted ideas, one should expect the photoconductivity of this heterogeneous material to decrease rather than increase.

As is known [1], silicon films with increased values of σ_{ph} can be prepared by deposition from silane glow-discharge plasma in special conditions that make it possible to simultaneously deposit Si–H radicals and nano-sized Si particles. The aim of this study was to carry out a comparative analysis of the data on the photoconductivity of nanostructured hydrogenated silicon films prepared by different techniques. In this study, it was found for the first time that the implantation of Si$^+$ ions with an energy of a few keV into conventional a-Si:H films leads to an increase in their photoconductivity.

2. EXPERIMENTAL

Conventional a-Si:H films were prepared by glow-discharge deposition in a triode reactor with the use of undiluted silane at $T_s = 300°C$ and at a gas pressure $P = 20$ mTorr. The specific discharge power, W, was equal to 0.2 W cm^{-2}. Infrared spectroscopic measurements showed that the deposited films contained mainly monohydride complexes (SiH) with a microstructure parameter $R \approx 0$. The minimum content of hydrogen in the films (C_H) was ~7 at. %. Nonconventional a-Si:H films with radically increased σ_{ph} were deposited at

considerably higher W and P compared with the relevant values given above. Judging from the value of σ_{ph}, these films are nanostructured, although nanocrystalline inclusions could not be identified in them using Raman spectroscopy. This may be related to the very small size and (or) low content of the inclusions.

In addition to glow-discharge deposition, magnetron-assisted silane decomposition (MASD) was used to prepare the films. Two processes are combined in MASD: decomposition of silane mixed with argon and magnetron sputtering of a crystalline Si target with Ar ions. The deposition conditions were as follows: $T_s = 300°C$, $P = 3$ mTorr, anode voltage $V = 500$ V, and magnetic flux density $B = 500$ G. Along with Si–H complexes, the films contained a large number of dihydride complexes (SiH$_2$) with the microstructure parameter $R = 0.65–070$. The value of C_H was equal to 10 at. %. Raman spectroscopy measurements showed that there were no nanocrystalline inclusions in these films.

Along with the films described above, nanostructured a-Si:H films received from École Polytechnique (France) were also investigated. These films were prepared by glow-discharge deposition in a diode reactor with the use of silane that was heavily diluted with hydrogen at $T_s = 150°C$ [3]. In accordance with the data reported in [3], the films contained ~20 at. % of hydrogen, which is characteristic of films containing a large number of dihydride complexes.

The temperature dependence of the dark conductivity (σ) of the films was measured in order to determine the activation energy (ΔE) of conductivity. The value of ΔE was used to determine the position of the Fermi level (ε_F) relative to the edge of the conduction band (ε_c).

The photoconductivity of the films was measured at room temperature. The energy of quanta of incident light and the generation rate of photocarriers were 2 eV and 10^{19} cm^{-3} s^{-1}, respectively.
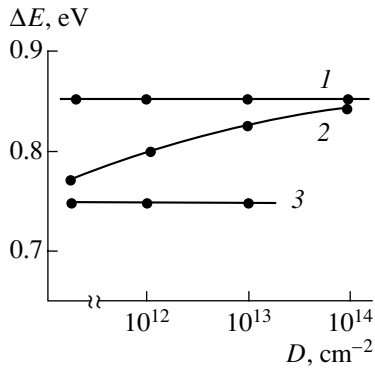
ΔE, eV

Fig. 1. Activation energy of dark conductivity as a function of the Si$^+$ implantation dose (schematic representation) for (*1*) intrinsic films prepared by glow-discharge deposition and pseudodoped films prepared by (*2*) glow-discharge deposition and (*3*) MASD.

The density of defects in the films (N_D) was measured at room temperature by the conventional constant photocurrent method (CPM).

Ions of Si$^+$ were implanted at room temperature into the films prepared by glow-discharge deposition in a triode reactor and by MASD. In order to obtain uniform distribution of implanted ions over the film depth ($d \approx 0.3$ μm), each film was subjected to a three-step implantation of ions with energies 30, 60, and 120 keV at doses varied in such a way so as to add up to a total dose D in the range of 10^{12}–10^{14} cm^{-2}. After the implantation, the films were annealed in a vacuum chamber under a residual pressure of $(3–4)$ 10^{-5} Torr at 200°C for one hour. The values of σ, σ_{ph}, and N_D were measured both before and after the implantation of Si$^+$.

3. RESULTS AND DISCUSSION

Figure 1 shows the dependence of the activation energy ΔE on the ion dose D for two conventional *a*-Si:H films prepared by glow-discharge deposition (curves *1* and *2*) and for a film prepared by MASD (curve *3*). These curves schematically generalize the results presented in [4, 5].

Let us first consider curves *1* and *2* that correspond, respectively, to intrinsic and pseudodoped films prepared by glow-discharge deposition. For the intrinsic *a*-Si:H film, whose conductivity activation energy ΔE before implantation was equal to $E_g/2$ (E_g is the width of the mobility gap), the Fermi level does not shift with an increase in D. At the same time, for the pseudodoped film, which had $\Delta E < E_g/2$ before implantation, ε_F shifts with an increase in D to the middle of the mobility gap. Thus, this phenomenon is analogous to the Staebler–Wronski effect.

In the case of the pseudodoped film prepared by MASD (curve *3*), ΔE does not change with an increase in D; i.e., the Fermi level does not shift. This is in agreement with the fact that the Staebler–Wronski effect

does not manifest itself in films of this type, which was reported previously in [5]. However, one should take into account that the given value of ΔE is determined for temperatures exceeding 300 K, while, for lower temperatures, considerably smaller values of the activation energy of σ were observed after Si$^+$ implantation (for different films, ΔE ranged from 0.2 to 0.5 eV). This can be attributed to the partial crystallization of the films, due to which the other (crystalline) phase with a lower resistivity also contributes to the conductivity at low temperatures. At high temperatures, the conductivity is governed by the dominant high-resistivity amorphous phase.

The assumption that the films prepared by MASD were partially crystallized after Si$^+$ implantation was confirmed by an analysis of ultrasoft X-ray emission Si$L_{2,3}$ spectra [5]. However, the crystallization of this kind results in a decrease, rather than in an increase, in the photoconductivity [6]. Indeed, the Si$L_{2,3}$ spectra measured for films implanted at a dose $D = 10^{13}$ cm^{-2} are rather close to the Si$L_{2,3}$ spectra measured for crystalline Si. This is indicative of the intensive crystallization of the films, rather than the formation of crystalline nanosized inclusions distributed over an amorphous host [5].

Ions with energies possessing an order of magnitude of a few tens of keV can only initiate such an intensive crystallization of the films if the latter initially contain crystallization centers. Otherwise, the ion energy should have an order of magnitude of a few MeV [7]. Therefore, one can conclude that the films prepared by MASD are initially nanostructured, but the content and/or size of the nanoinclusions are so small that they cannot be identified by Raman spectroscopy. Hence, the structure of these films is similar to that of nonconventional films prepared by glow-discharge deposition. However, unlike the latter, the films prepared by MASD do not possess increased photoconductivity compared with conventional *a*-Si:H.

Let us continue our consideration of the effect of Si$^+$ ion implantation on the electrical parameters of conventional *a*-Si:H films. The defect density increases with the implantation dose, reaches the value of $N_D \approx 10^{17}$ cm^{-3} (when $\Delta E = E_g/2$), and does not change with a further increase in the implantation dose, in spite of an increase in the concentration of implanted ions (N_{Si}) [4]. This phenomenon is also similar to the Staebler–Wronski effect.

It is worth noting that for $\Delta E = E_g/2$, i.e., in the intrinsic material, all defects (dangling Si–Si bonds) are in the neutral state D^0 and their density N_D can be determined from electron spin resonance.

The dependence of σ_{ph} of *a*-Si:H on the density of unpaired spins, i.e., on the density of defects in the D^0 state, was determined in [8]. Figure 2 shows the dependence of the ratio $\sigma_{ph}/\sigma_{ph}(0)$ on N_D, which was derived from the data presented in [8] ($\sigma_{ph}(0)$ is the photocon-

ductivity of a film with N_D 5×10^{15} cm^{-3}). One might expect that the values of σ_{ph} of films subjected to Si$^+$ implantation would correspond to the dependence of the ratio $\sigma_{ph}/\sigma_{ph}(0)$ on N_D, which is shown in Fig. 2. However, such a correspondence occurs only for initially pseudodoped films, whereas σ_{ph} of initially intrinsic films increases rather than decreases, after Si$^+$ implantation ($D = 10^{14}$ cm^{-2}). Typical results obtained in this study are shown in Fig. 2.

It is worth noting that the above-mentioned increase in σ_{ph} is observed if $N_D \ll N_{Si}$. Therefore, it is believed that not all implanted Si$^+$ ions contribute to the formation of defects (by analogy with the Staebler–Wronski effect in the breaking of weak Si–Si bonds). Stated differently, implantation leads not only to the formation of defects, but also to the formation of nanocrystalline Si inclusions distributed over the amorphous host. This accounts for the increase in σ_{ph} of nanostructured films obtained in this way.

Indeed, as was shown in [9], intrinsic a-Si:H films have a maximally ordered structure in terms of short-range and medium-range orders. In this case, in accordance with the results obtained in [10], external factors should result in the most rapid formation of crystallization centers. It is worth noting that the increase in σ_{ph} is observed despite the radical increase in N_D after implantation (up to $N_D \approx 10^{17}$ cm^{-3}); i.e., the effect of nanoinclusions on σ_{ph} is dominant.

Let us now consider the dependence of photoconductivity at $T = 300$ K on the value of ΔE, i.e., on the position of the Fermi level in the mobility gap relative to the edge of the conduction band (Fig. 3). The curve for conventional a-Si:H represents the universal dependence $\sigma_{ph} = f(\varepsilon_c - \varepsilon_F)$ for this material. The photoconductivity of nanostructured films prepared by MASD at $T = 300$°C is close to that of conventional a-Si:H (see Fig. 3, crosses 1). At the same time, the values of σ_{ph} of nanostructured films prepared by glow-discharge deposition at $T_s = 300$ [2] and 250°C [11] in reactors of different types are larger by orders of magnitude (Fig. 3, circles 2 and 3, approximated by a dashed line).

Figure 3 shows the values of σ_{ph} for three films prepared by glow-discharge deposition and subjected to Si$^+$ implantation, after which they all had $\Delta E = E_g/2$ (black triangles (4)). These data illustrate the fact that implantation affects the photoconductivity of intrinsic and pseudodoped a-Si:H films differently, which was stated above. It can be seen that the value of σ_{ph} of an intrinsic film subjected to implantation is close to that of nanostructured films prepared by glow-discharge deposition in a diode reactor at $T_s = 150$°C [3] (approximation by a dot line).

An analysis of the results presented in Fig. 3 (the data are numbered to correspond with the film numbers) shows that the photoconductivity of nanostructured films, for which $(\varepsilon_c - \varepsilon_F) = $ const, depends heavily on the technique of their preparation. The preparation
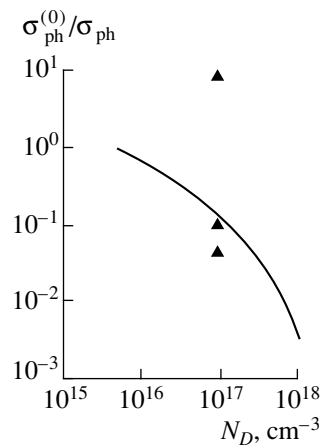

Fig. 2. Relative change in photoconductivity as a function of the density of defects in the D^0 state. The solid line represents the data from [8]; triangles represent the data for films prepared by glow-discharge deposition and subjected to Si$^+$ ion implantation ($D = 10^{14}$ cm^{-2}).
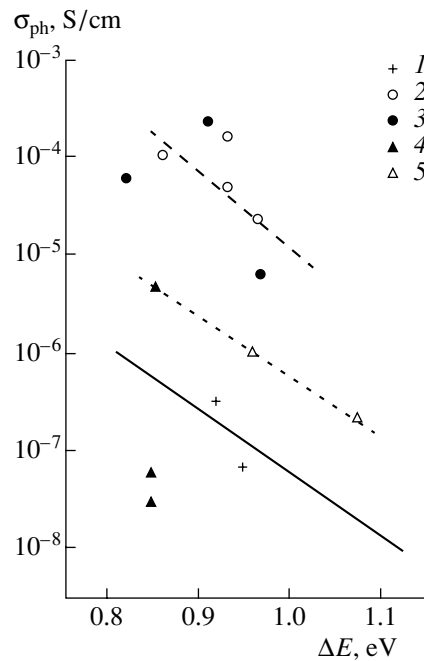

Fig. 3. Photoconductivity at 300 K as a function of dark conductivity activation energy. The solid line represents the data for conventional a-Si:H; (1), for films prepared by MASD at $T_s = 300$°C; (2) and (3), for nanostructured films prepared by glow-discharge deposition at $T_s = 300$ [2] and 250°C [3], respectively; (4), for implanted films; and (5), for nanostructured films prepared by glow-discharge deposition at $T_s = 150$°C [3].

technique governs such structural parameters as the type of Si–H complexes and defect density. The considerable contribution of dihydride complexes leads to a decrease in σ_{ph} at $N_D \approx$ const. Indeed, this can be seen from a comparison of the data for films 2, 3, and 5, which have $\Delta E = 0.95$ eV, $N_D \approx 5 \times 10^{15}$ cm^{-3}, and dif-

ferent structure parameters: $R \approx 0$ for films 2 and 3 and $R \approx 1$ for film 5. At the same time, the effect of N_D on σ_{ph} at $R \approx$ const can be deduced from a comparison of the data for films 2, 3, and 4, which have $\Delta E = 0.85$ eV, $R \approx 0$, and different values of N_D: 5×10^{15} cm^{-3} for films 2 and 3 and 10^{17} cm^{-3} for film 4. Finally, when $\Delta E = 0.95$ eV, film 1 has increased R and N_D ($R \approx 0.70$ and $N_D \approx 10^{16}$ cm^{-3}) compared with films 2 and 3, and increased N_D compared with film 5. As a result, nanostructured film 1 has the lowest value of σ_{ph}.

4. CONCLUSION

In this study, it was experimentally ascertained that the implantation of Si$^+$ ions with an energy of a few keV into a-Si:H films leads to a change in the electrical properties σ, σ_{ph}, and N_D of the films, as well as to film crystallization. It was shown how the initial electrical and structural properties of the films affect these phenomena. The increase in photoconductivity of intrinsic a-Si:H films after ion implantation is of special interest both theoretically and practically. This effect is related to the formation of, along with defects, nanocrystalline Si inclusions distributed over an amorphous host. The influence of the Fermi level position, defect density, and type of Si–H complexes on the value of σ_{ph} of nanostructured films prepared in different conditions was also determined.

REFERENCES

1. P. Roca i Cabarrocas, S. Hamma, P. St'ahel, *et al.*, in *Proceedings of the 14th European Photovoltaic Solar Energy Conference, Barcelona, 1997*, p. 20.

2. O. A. Golikova and M. M. Kazanin, Fiz. Tekh. Poluprovodn. (St. Petersburg) **33**, 110 (1999) [Semiconductors **33**, 97 (1999)].

3. S. Vignoli, R. Butte, R. Meaudre, *et al.*, J. Phys.: Condens. Matter **11**, 8749 (1999).

4. O. A. Golikova, Fiz. Tekh. Poluprovodn. (St. Petersburg) **33**, 464 (1999) [Semiconductors **33**, 447 (1999)].

5. O. A. Golikova, A. N. Kuznetsov, V. Kh. Kudoyarova, *et al.*, Fiz. Tekh. Poluprovodn. (St. Petersburg) **34**, 86 (2000) [Semiconductors **34**, 87 (2000)].

6. O. A. Golikova, M. M. Kazanin, A. N. Kuznetsov, and E. V. Bogdanova, Fiz. Tekh. Poluprovodn. (St. Petersburg) **34**, 1125 (2000) [Semiconductors **34**, 1085 (2000)].

7. L. A. Magrues, M.-J. Caturba, and H. Huang, Mater. Res. Soc. Symp. Proc. **396**, 201 (1996).

8. R. A. Street, Philos. Mag. B **46**, 273 (1982).

9. O. A. Golikova, A. N. Kuznetsov, V. Kh. Kudoyarova, *et al.*, Mater. Res. Soc. Symp. Proc. **467**, 519 (1997).

10. Y. Masai, P. G. LeComber, and A. G. Fitzgerald, J. Appl. Phys. **74**, 129 (1993).

11. R. Butte, R. Meaudre, M. Meaudre, *et al.,* Philos. Mag. B **79**, 1079 (1999).

Translated by Yu. Sin'kov

AMORPHOUS, VITREOUS,
AND POROUS SEMICONDUCTORS

Vibratonal Spectroscopy of *a*-C:H(Co)

T. K. Zvonareva*, E. I. Ivanova*, G. S. Frolova*,
V. M. Lebedev**, and V. I. Ivanov-Omskiĭ*

* Ioffe Physicotechnical Institute, Russian Academy of Sciences,
Politekhnicheskaya ul. 26, St. Petersburg, 194021 Russia
e-mail: ivanov.ivom@pop.ioffe.ru
** Konstantinov Institute of Nuclear Physics, Russian Academy of Sciences,
Gatchina, Leningrad oblast, 188850 Russia
Submitted November 27, 2001; accepted for publication November 28, 2001

Abstract—The interaction between cobalt and a carbon host was investigated for films of amorphous hydrogenated carbon modified by cobalt. Films of amorphous hydrogenated carbon with various concentrations of cobalt, *a*-C:H(Co), were grown by the DC magnetron cosputtering of graphite and cobalt targets in an argon–hydrogen plasma. Rutherford backscattering of protons and the method of nuclear reactions were used to determine the relative atomic content of cobalt and carbon in the films. Infrared absorption was investigated in the region of stretching vibrations of the C–C-bond and bending vibrations of the C–H-bond; Raman scattering was also measured. A giant intensification of absorption by the vibrational C–H modes and the appearance of additional C–C modes induced by cobalt were observed. The intensity of the fundamental vibrational modes were analyzed as functions of cobalt content and annealing temperature. The principal mechanisms of interaction between cobalt and the amorphous carbon host is revealed. Thermal vacuum annealing at ~350°C was shown to suppress the cobalt–carbon interaction, which might favor the formation of cobalt nanoclusters in the amorphous carbon host at these or higher temperatures. © 2002 MAIK "Nauka/Interperiodica".

1. INTRODUCTION

In recent years, the unique ability of carbon atoms to form chemical bonds of various configurations has brought about ever increasing interest in its use for solving the problem of the incapsulation of metal nanoclusters in solid media. The importance of this problem is well illustrated in the case of nanostructures based on magnetic metals [1], because, in this case, the encapsulation is able to play a dual role—the protection of nanoclusters from the aggressive action of its environment and the weakening of the exchange interaction between neighboring particles. This opens up attractive prospects for using such nanocomposites as media for ultrahigh-density magnetic recording. In fact, *a*-C:H can adequately protect a metal surface from degradation in aggressive media, as was shown by the example of Ag, which is extremely sensitive to such action [2].

The problem of encapsulating nanoclusters of metals with large magnetic moments into a carbon host was considered in a number of studies (see, for example, [3–5]). However, the range of methods for the control and characterization of the obtained composites was restricted to electron microscopy, X-ray diffraction, and to measurements of macroscopic magnetic characteristics. At the same time, for optimizing the synthesis and magnetic properties of nanoclusters, it was found to be important to know the nature of the interaction between the nanoclusters and the carbon host. Methods of vibrational spectroscopy, such as infrared (IR) absorption and Raman scattering, are useful sources of information about the properties of the composites.

2. EXPERIMENTAL

The *a*-C:H(Co) films were obtained by DC magnetron cosputtering of graphite and cobalt targets in argon–hydrogen plasma ($80\%\,Ar + 20\%\,H_2$) [6]. The concentration of cobalt introduced in the carbon films was varied by varying the ratio between areas of the cobalt and graphite targets. The films were deposited on substrates of (100) single crystal silicon KDB-20 (*p*-Si:B, $\rho = 20\ \Omega$ cm) heated up to 200°C. In the sputtering chamber, we preliminarily attained a residual-gas pressure at the level of 10^{-6} Torr. The films were deposited in the working-gas flow under a pressure of 10^{-2} Torr and an ion-current density of 10^{-1} A/cm². The film-growth rate in our experiments amounted to 2–5 nm/min. The layers grown were annealed in vacuum for 1 h at temperatures of 190–380°C.

The elemental composition of the *a*-C:H(Co) films, i.e., the relative content of carbon and cobalt, was determined by nuclear-physical methods of element analysis, i.e., Rutherford backscattering (RBS) and nuclear reactions [7, 8]. This study was carried out with an analytic complex for investigating materials developed on
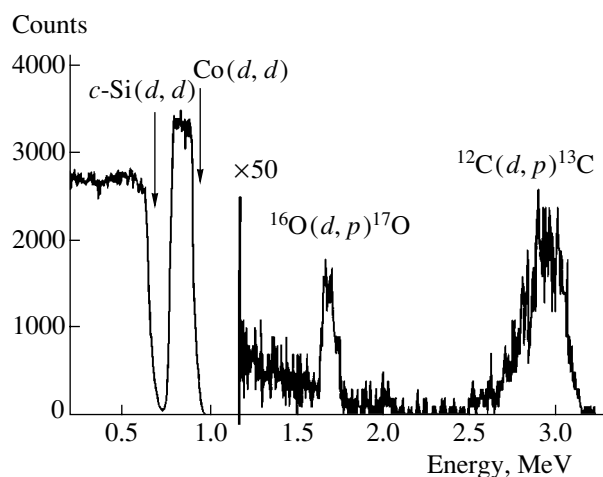
Counts

Fig. 1. Spectrum of protons formed as a result of nuclear reactions $^{12}C(d, p)^{13}C$, $^{16}O(d, p)^{17}O$, and the spectrum of scattered deuterons obtained for deuteron irradiation of the a-C:H(Co) film with [Co]/[C] = 0.73 on the crystalline-silicon substrate. The deuteron energy $E_d = 1$ MeV. The scattering angle is 135°.

the basis of an ÉSU-2 electrostatic accelerator at the Konstantinov Institute of Nuclear Physics in St. Petersburg [7]. We used a modified method of Rutherford backscattering. A sample under investigation was irradiated with a deuteron beam. The deuteron energy in the beam was chosen to be $E_d = 1$ MeV, because the cross section of the $^{12}C(d, p)^{13}C$ nuclear reaction is virtually constant [9] in the region of energies from 0.9 to 1 MeV. The ion detector was positioned at an angle of 135° with respect to the direction of the deuteron beam and had a resolution of ~10 keV at an α-particle energy $E_\alpha = 5.5$ MeV. For determining the content of cobalt with respect to carbon, we measured both the spectrum of scattered deuterons and the spectrum of scattered protons produced as a result of the $^{12}C(d, p)^{13}C$ nuclear reaction. The determination of the atomic ratio [Co]/[C] in films by this method offers a number of advantages over Rutherford backscattering [8], which

Table 1. Parameters of the a-C:H(Co) samples

Sample no.	Film-growth time, h	Thickness, μm	Density, g/cm³	[Co]/C]
1	5.3	1.5	1.8	0.03
2	3	0.45	2.5	0.085
3	3	0.25	3.0	0.5
4	3	0.25	4.0	0.73
5	3	0.15	4.0	0.88
6	3	0.55	4.2	1.4

is traditionally used in these cases.[1] First, in the RBS, the peak from carbon contained in the film is conventionally found on a "pedestal" caused by scattering from the Si substrate. This circumstance hampers the accurate determination of the area under the peak corresponding to C. Second, the scattering cross section for light elements at similar energies is far from the Rutherford one because there is a considerable contribution of the nuclear interaction to the total cross section [8]. The peak of the deuteron scattering related to cobalt atoms contained in the film and observed in the spectrum makes it possible to accurately determine the ratio [Co]/[C], because this peak is located against a zero background, and the scattering cross section of elements with large atomic numbers is known with sufficient accuracy [8]. A typical spectrum obtained for the deuteron irradiation of the a-C:H(Co) film is shown in Fig. 1. In the spectrum, it is possible to observe the peak of the deuteron scattering by cobalt atoms, the step of the deuteron scattering by the silicon substrate, and also the peak of protons produced as a result of the $^{12}C(d, p)^{13}C$ nuclear reaction between deuterons and carbon at an energy of 3 MeV. The deuterons scattered by carbon atoms are virtually invisible against the background of the signal from silicon.

Optical absorption was investigated using a Specord 75 IR two-beam infrared spectrometer with a resolution of 2 cm⁻¹ in the region of vibrational frequencies related to the stretching of carbon–hydrogen bonds in a-C:H(Co). The Raman scattering was investigated using a SPEX Ramalog spectrometer under excitation with the lines of an argon laser at a wavelength of 487.9 nm and with a power of 50 mW. The scattering was measured in the reflection configuration with a spectral slit width of 5.5 cm⁻¹.

3. RESULTS

3.1. Elemental Composition of a-C:H(Co) Films

The relative concentrations of cobalt and carbon in the films were determined from the areas of peaks corresponding to these elements in Fig. 1, with allowance made for the cross section of interaction between the deuterons and atoms under investigation. These cross sections were taken to be equal to 1.29×10^{-24} and 3×10^{-26} cm² for cobalt and carbon, respectively [8–10]. The results of measuring the elemental composition of the a-C:H(Co) films are shown in Table 1. In the RBS experiments, we also determined mass thicknesses of the films (in mg/cm²) from shifts of the high-energy edge of the spectrum corresponding to scattering by the silicon substrate. The spectrum-edge shift is proportional to the film thickness, with the coefficient of pro-

---

[1] We cite only the [Co] concentration related to the [C] concentration in order to facilitate the comparison of our data with those taken from the references, in which Co encapsulation is considered in a nonhydrogenated carbon.

portionality being dependent on the element composition of the film under investigation, the scattering kinematics, and the deuteron bremsstrahlung loss at the entry into the sample and the escape from it. The accuracy in determining the mass thickness amounts to 5% [11]. In combination with known values of linear film thicknesses determined independently, these results enabled us to estimate the mass densities of the films in g/cm^3. In *a*-C:H without cobalt, the density amounted to 1.8 g/cm^3, which is characteristic of amorphous hydrogenated carbon. The values we determined for the films with a cobalt range from 2.5 to 4.2 g/cm^3 can be related to the contribution from cobalt (the mass cobalt density is 8.9 g/cm^3), which explains the film-density increase with the cobalt content in a natural manner.

3.2. Infrared Absorption

In Fig. 2, we show the fragments of absorption spectra for the *a*-C:H and *a*-C:H(Co) films in the frequency region of stretching vibrations of the C–C bonds and the bending vibrations of the C–H bonds for various cobalt content. It can be seen that the introduction of cobalt into the carbon host initially increases considerably the absorption coefficient in the spectral range under consideration. When the ratio [Co]/[C] between the atomic concentrations attains a value of ~0.9, the absorption growth gives way to its decrease. In order to consider the influence of cobalt on the IR absorption by the carbon–hydrogen host more carefully, we analyze the structure of the absorption bands in Fig. 2, decomposing them into Gaussian contours. As an example, in Fig. 3 we show the decomposition of the absorption band under investigation corresponding to the highest absorption for a film with [Co] / [C] = 0.35 after annealing at 320°C. It can be seen that the experimental spectrum can be reasonably well described by the superposition of seven Gaussian contours. It is important that the frequencies of the maxima of these contours are the same within their measurement errors (±10 cm^{-1}) for all the investigated films with various cobalt concentrations. On the one hand, this fact can be considered as the definite confirmation of the reliability of this decomposition; on the other hand, this indicated that there is no marked effect of cobalt on the frequencies of the fundamental vibrational modes, because the peaks of each contour correspond in frequency to the bands characteristic of *a*-C:H [12], with deviations not exceeding their measurement error. An exception is the band with the peak near 1560 cm^{-1}, which was previously observed by us in *a*-C:H(Cu) and studied in detail in [13]. In the case of *a*-C:H(Cu), the band at ~1560 cm^{-1} turned out to be dominant in the spectrum and we interpreted it as a quasi-Raman *G*-band, which owed its origin to dipole moments induced by copper atoms in the graphene rings of the *a*-C:H graphitic fragments [14], i.e., to the activation of a pure Raman band in the optical spectrum. We will return to the discussion of this fact in Subsection 3.3.
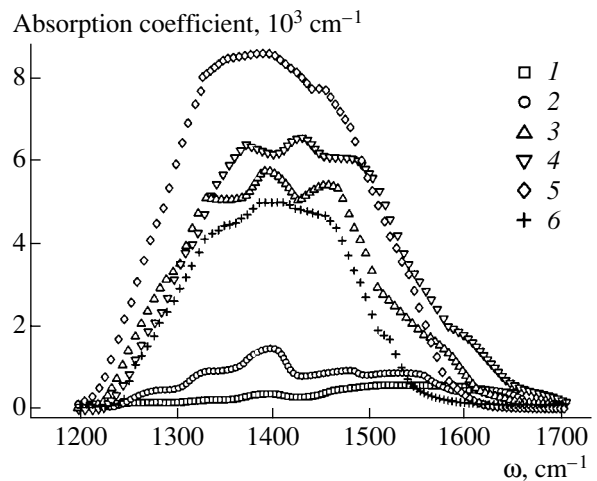

Fig. 2. Spectra of absorption for (*1*) *a*-C:H films and *a*-C:H(Co) films with [Co]/[C] = (*2*) 0.085, (*3*) 0.5, (*4*) 0.73, (*5*) 0.88, and (*6*) 1.4.
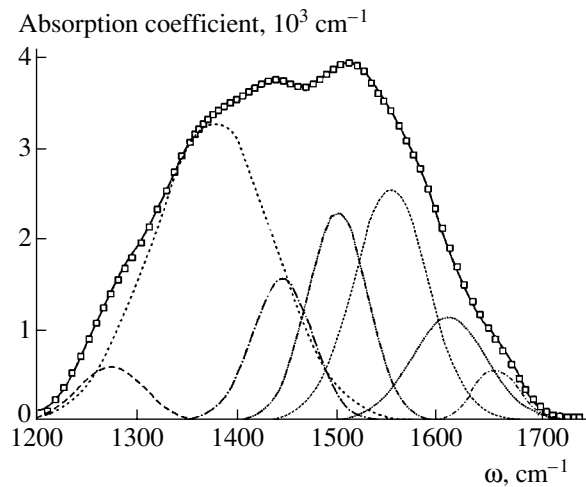

Fig. 3. Spectrum of absorption for the *a*-C:H(Co) film with [Co]/[C] = 0.35 after annealing at 320°C (squares) with the decomposition into the Gaussian components (lines). The frequencies of the Gaussian contours are listed in Table 2. The solid line is the envelope of the Gaussian contours.

A similar decomposition of spectra for the *a*-C:H(Co) films with various Co concentrations was performed for the same set of frequencies; only the amplitude and band width were varied. In Table 2, we list the frequencies of the Gaussian bands of decomposition for the spectra shown in Fig. 2. These sets provide the best agreement with the experiment, and the corresponding dependence of the integrated intensity of the Gaussian contours of decomposition on the concentration of the introduced cobalt is shown in Fig. 4. A striking feature is the fact that (as follows from Table 2) the introduction of cobalt leaves the frequencies of vibrational modes of the hydrogen–carbon host virtually intact, but a drastic intensification of absorp-
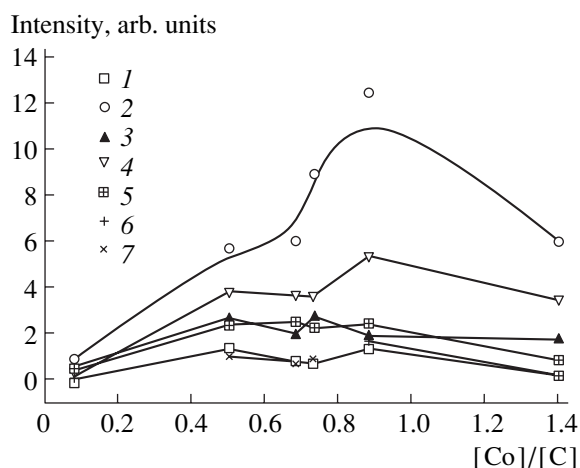
Intensity, arb. units

Fig. 4. Integrated intensity of Gaussian contours as a function of the concentration of cobalt introduced into the film. The frequencies at the peaks are (*1*) 1290, (*2*) 1372, (*3*) 1450, (*4*) 1500, (*5*) 1560, (*6*) 1600, and (*7*) 1650 cm^{-1}.

tion takes place at some of these frequencies, as the comparison of spectra for various concentrations in Fig. 2 shows. Also, it can be seen from Fig. 2 that the integrated intensity first increases with concentration and, then, starts to decrease for high concentrations ([Co]/[C] $\approx$ 0.9). It seems to be natural to associate this fact with the relative decrease in the fraction of carbon in the film as the cobalt concentration increases. In this case, we observe the highest intensification of the band associated with the symmetric vibrational mode sp^3CH_3sym, which can likely be ascribed to the polarizing action of the chemical bond of this group with a cobalt atom belonging to a metal nanocluster or with a cobalt-carbide molecule. The former effect seems to be more probable with allowance made for the fact that the highest intensification corresponds to an approximately equiatomic ratio between carbon and cobalt atoms. The behavior of vibrational modes of the carbon–carbon bonds near the metal surface was considered previously, and it was shown that these are only symmetric modes that prove to be optically active [16], which corresponds to our interpretation of the band at 1372 cm^{-1}

(see, Table 2). Similar behavior is observed for the band at 1500 cm^{-1} corresponding in frequency to the vibrations of a benzene ring presumably connected with cobalt. The appearance of vibrational bands of the benzene ring in the IR spectrum of *a*-C:H(Co) points to a strong interaction between Co atoms and the carbon host, which decomposes the graphene planes of the *a*-C:H(Co) graphitic fragments into isolated benzene rings. A supplementary argument in favor of forming benzene derivatives of cobalt is the appearance of a band at 1600 cm^{-1} in the *a*-C:H(Co) spectrum. In these cases, this band is an unavoidable satellite of the band at 1500 cm^{-1} as a result of the resonance splitting of the absorption band by the vibrations of three double bonds in the benzene ring [15].

In the intermediate case of weaker interaction of the intercalation of the graphene planes of Cu [14], the quasi-Raman band near 1560 cm^{-1} is activated in the IR spectrum. The simultaneous appearance of these three bands indicates that the investigated films both contain Co atoms interacting with the graphene rings [14] and Co atoms combining with carbon and forming benzene derivatives of cobalt carbide. As the results of electron-microscope analysis [3, 4] show, the former type of interaction leads to the formation of graphitic shells around the metal nanoclusters, which increase their stability, whereas the latter type retards the formation of shells and must be suppressed by, for example, after-growth annealing [5].

3.3. Raman Scattering

For a number of samples, we also investigated the Raman scattering in order to compare it with the IR spectra. As an example, in Fig. 5, we show the spectra of Raman scattering (curve *1*) and IR absorption (curve *2*) for the *a*-C:H(Co) sample with [Co]/[C] = 0.5. In the Raman spectrum, we observe two pronounced bands at the frequencies of ~1350 and ~1580 cm^{-1}, which is characteristic of fine-crystalline graphite rather than amorphous carbon in whose spectrum such good resolution of similar bands (*G*- and *D*-bands) is routinely observed only in annealed samples [17]. The position of the *G*-band, which is shifted to the high-fre-

Table 2. Decomposition of spectra (Fig. 2) into the Gaussian contours

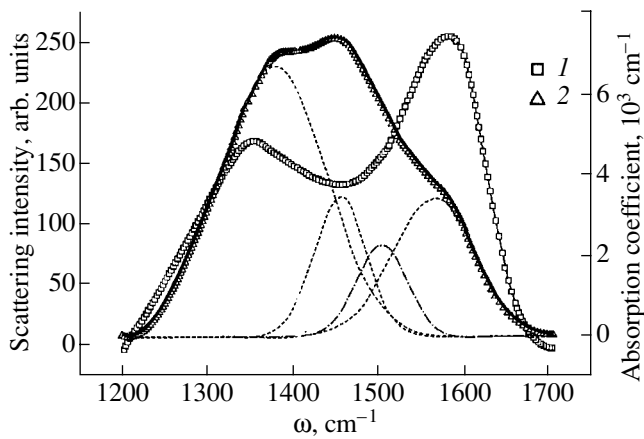| Sample no.	[Co]/C]	Band frequency, cm^{-1}						
2	0.085	1288	1372	1436	1500	1560	1600	
3	0.5	1288	1372	1444	1508	1567		1652
4	0.73	1290	1368	1450	1500	1560		1650
5	0.88	1290	1373	1440	1500	1560	1600	
6	1.4	1290	1372	1440	1500	1560	1598	1650
Band origin		sp^3CH	sp^3CH_3 sym	sp^3CH_2 sp^3CH	Benzene ring [15]	*G* line [13]	C=C aromatic	C=C
		[12]	[12]	[12]			[15]	[12]

Fig. 5. (*1*) Raman spectrum and (*2*) IR absorption spectrum with decomposition into the Gaussian components (lines) for the *a*-C:H(Co) film with [Co]/[C] = 0.5. The solid line is the envelope of the Gaussian components.

Fig. 6. Absorption spectra of the *a*-C:H(Co) film with [Co]/[C] = 0.35 after annealing at a temperature of (*1*) 20, (*2*) 190, (*3*) 260, (*4*) 320, and (*5*) 380° C.

quency region of the spectrum as compared with the position typical of amorphous carbon, only makes this analogy more fitting. It can also be seen that the position of a special feature in the IR spectrum of absorption in the region of 1500–1600 cm^{-1} correlates well with the position of the *G*-band in the Raman spectra, which can be associated with the activation of the quasi-Raman *G*-band in the optical absorption spectrum [13] and justifies consideration of this band in the analysis of the shape of the absorption-spectrum. However, the Gaussian contours of the absorption-spectrum decomposition in Fig. 5 show that the contour with a peak at 1560 cm^{-1}, which we relate to the quasi-Raman *G*-band, is shifted by ~20 cm^{-1} towards the low-frequency region relative to the true Raman *G*-band in the scattering spectrum. Taking into account the considerable ambiguity in the decomposition of the spectrum in this case, it is difficult to assess the accuracy of determining this shift, but the appearance of a quasi-Raman *G*-band in the absorption spectrum seems to be evident. This is not true for the *D*-band, which is probably drastically obscured by the anomalously intensified bands of absorption from vibrations of the C–H bonds in the optical absorption spectra of *a*-C:H(Co), in contrast to *a*-C:H(Cu) [13] noted in Section 3.2.

The analogy of the shift of a true Raman *G*-band to higher frequencies relative to its position in pure amorphous carbon [17] when *a*-C:H is modified by cobalt and thermal annealing confirms, at the atomic level, that the modification by cobalt induces graphitization of the carbon host [3, 4]. Judging from the value of the ratio of intensities of the *D* and *G* bands, which, in this particular case, is equal to ~2.3, and according to the calibration known for graphite [18], the linear dimension of these clusters turns out to be ~2 nm. As for the absolute value of this estimate, we already commented on its arbitrary character [13] and it seems to be of

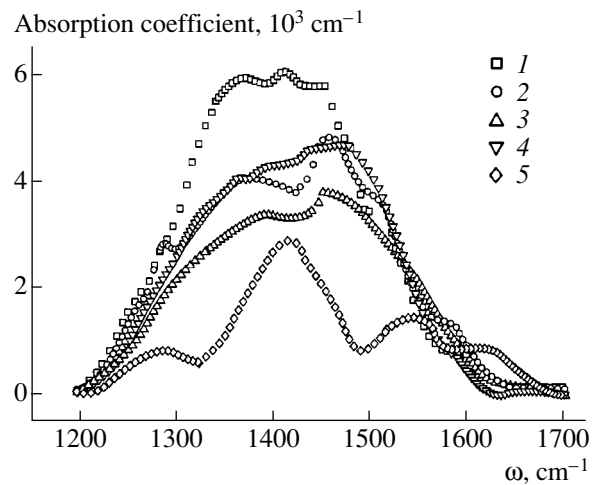interest to compare its value with a similar estimate in the case of the modification of *a*-C:H with copper. According to [13], the graphitic clusters attain such a size only when the concentration of copper is higher than the cobalt concentration by a factor of ~3; i.e., the interaction of cobalt with the carbon host is stronger. Furthermore, in the absorption spectra of *a*-C:H(Co), absorption bands, which are characteristic of the vibrational modes of the benzene rings, appear near 1500 cm^{-1}. Without cobalt, this mode is not observed, as can be seen from Fig. 4.

3.4. Effect of Thermal Annealing

In Fig. 6, we show the absorption spectra for *a*-C:H(Co) films with [Co]/[C] = 0.35 annealed in vacuum at various temperatures. In the range of frequencies of 1400–1600 cm^{-1} assigned to the vibrational modes of the carbon–carbon bonds, the nonmonotone dependence of the absorption on the annealing temperature caught our attention. In Fig. 7, with the aim of gaining deeper insight into this feature, we display the dependence of areas under the Gaussian contours of decomposition of the absorption spectra for this sample on the annealing temperature. Other samples behave in a similar manner during annealing. It can be seen that there are a number of characteristic features in the modification of the spectrum under the effect of thermal annealing. First, we should note a very substantial change in the absorption by the modes which were initially intensified anomalously due to the interaction of cobalt atoms with the carbon host, which was discussed in Section 3.2. A temperature of ~350°C, at which the anomalous intensification of the mode at 1372 cm^{-1} almost completely disappears, coincides with the temperature of the breaking of the Co–C bond in the metastable carbide Co$_2$C [5]. This circumstance corrobo-
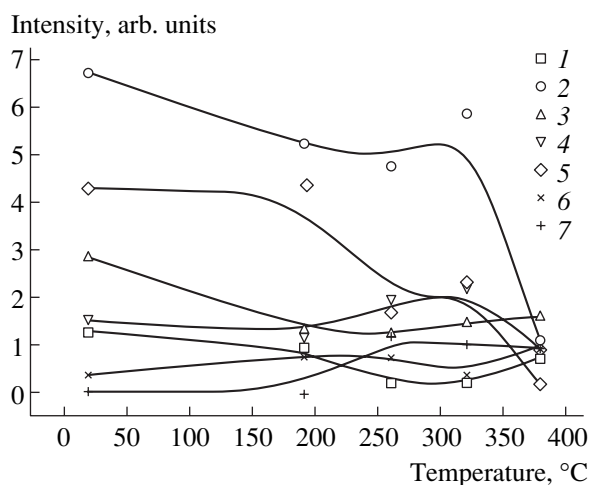
Intensity, arb. units

Fig. 7. Areas under the contours of the absorption-spectra decomposition as functions of the annealing temperature for the *a*-C:H(Co) film with [Co]/[C] = 0.35. The frequencies of the maxima of the peaks are (*1*) 1290, (*2*) 1372, (*3*) 1450, (*4*) 1500, (*5*) 1552, (*6*) 1600, and (*7*) 1665 cm^{-1}.

rates the mechanism proposed above for the intensification of absorption by the bending modes of vibrations of the CH$_3$ group due to the formation of a bond between this group and a cobalt atom. The disappearance of the quasi-Raman band at 1552 cm^{-1} as the annealing temperature is increased also corresponds to weakening of the interaction of cobalt with graphitic fragments of the carbon host, which facilitates the coalescence of the cobalt nanoclusters observed at these temperatures [19]. To some degree, the bond between cobalt and carbon atoms in the benzene rings (bands at 1500 and 1600 cm^{-1}) behaves in a similar manner. The inadequate reliability of the procedure of decomposition of the spectrum makes it senseless to discuss the less pronounced features in Fig. 7; however, an abrupt fall in the absorption coefficient at ~350°C, which can be attributed to the dissociation of cobalt carbide and its derivatives, can apparently be determined with reasonable reliability.

4. CONCLUSION

IR spectroscopy in the region of vibrational frequencies of the carbon–carbon bonds in *a*-C:H(Co), together with Raman spectroscopy, makes it possible to clarify the main mechanisms of interaction between cobalt and the carbon host in relation to the carbon concentration and the annealing temperature. At least three types of interaction are revealed: (a) a strong interaction associated with the formation of a metastable chemical bond in methyl derivatives of cobalt carbide; (b) an interaction destroying the graphitic fragments with the formation of benzene derivatives of carbon; and (c) a weak interaction characteristic of metals that do not form car-

bides, e.g., copper [13]. However, thermal annealing at ~350°C suppresses these interactions favoring, as might be expected, the formation of cobalt nanoclusters in the amorphous carbon host.

REFERENCES

1. T. Hayashi, S. Hirono, M. Tomita, and S. Umemura, Nature **381**, 772 (1996).
2. G. A. Dyuzhev, V. I. Ivanov-Omskii, E. K. Kuznetsova, *et al.*, Mol. Mater. **8**, 103 (1996).
3. J. Jiao and S. Seraphin, J. Appl. Phys. **83** (5), 2442 (1998).
4. T. Cabioc'h, A. Naudon, M. Jaouen, *et al.*, Philos. Mag. B **79** (3), 501 (1999).
5. J.-J. Delaunay, T. Hayashi, M. Tomita, and S. Hirono, J. Appl. Phys. **82** (5), 2200 (1997).
6. T. K. Zvonareva, V. I. Ivanov-Omskiĭ, A. V. Nashchekin, and L. V. Sharonova, Fiz. Tekh. Poluprovodn. (St. Petersburg) **34** (1), 96 (2000) [Semiconductors **34**, 98 (2000)].
7. V. M. Lebedev, Yu. G. Luk'yanov, and V. A. Smolin, in *Proceedings of the XIII International Conference on Electrostatic Accelerators, Obninsk, 2000*, p. 60.
8. *Ion Beam Handbook for Material Analysis*, Ed. by J. W. Mayer and E. Rimini (Academic, New York, 1977).
9. M. Huez, L. Quaglia, and G. Weber, Nucl. Instrum. Methods **105**, 197 (1972).
10. G. Amsel and D. Samuel, Anal. Chem. **39**, 1689 (1967).
11. J. E. Ziegler, J. P. Biersack, and U. Littmark, *The Stopping and Range of Ions in Solids* (Pergamon, New York, 1985).
12. J. Ristein, R. T. Stief, L. Ley, and W. Beyer, J. Appl. Phys. **84** (7), 3836 (1998).
13. V. I. Ivanov-Omskiĭ, T. K. Zvonareva, and G. S. Frolova, Fiz. Tekh. Poluprovodn. (St. Petersburg) **34** (12), 1450 (2000) [Semiconductors **34**, 1391 (2000)].
14. V. I. Ivanov-Omskiĭ and É. A. Smorgonskaya, Fiz. Tverd. Tela (St. Petersburg) **41** (5), 868 (1999) [Phys. Solid State **41**, 786 (1999)].
15. L. J. Bellamy, *The Infrared Spectra of Complex Molecules* (Methuen, London, 1954; Inostrannaya Literatura, Moscow, 1963), p. 59.
16. H. A. Pearce and N. Sheppard, Surf. Sci. **59**, 205 (1976).
17. A. C. Ferrari and J. Robertson, Phys. Rev. B **64**, 075414 (2001).
18. F. Tuinstra and J. L. Koenig, J. Chem. Phys. **53** (3), 1126 (1970).
19. J.-J. Delaunay, T. Hayashi, M. Tomita, and S. Hirono, Jpn. J. Appl. Phys., Part 1 **36** (12B), 7801 (1997).

Translated by V. Bukhanov

Spontaneous and Stimulated Emission from Magnetron-Deposited ZnO–SiO$_2$–Si Thin-Film Nanocavities

A. N. Gruzintsev*, V. T. Volkov*, C. Barthou**, and P. Benalloul**

* Institute of Microelectronic Technology and Ultra-High-Purity Materials,
Russian Academy of Sciences, Chernogolovka, Moscow oblast, 142432 Russia
e-mail: gran@ipmt-hpm.ac.ru
** Université P. and M. Curie, 75252 Paris, France
Submitted November 28, 2001; accepted for publication December 4, 2001

Abstract—The spontaneous and stimulated emission spectra from optically pumped zinc oxide nanolayers on oxidized silicon were studied. Single-mode lasing with a wavelength of 397 nm was observed for a coupled longitudinal mode of the ZnO film at room temperature. For the thin-film nanocavities of ZnO–SiO$_2$–Si, optimal parameters that allow the lowering of the threshold and the attainment of single-mode lasing are determined. © 2002 MAIK "Nauka/Interperiodica".

INTRODUCTION

High-quality ZnO films with the prevailing luminescence in the ultraviolet spectral region are used for the production of high-power semiconductor light-emitting diodes (LEDs) for this region. ZnO is a semiconductor which is characterized by a wide band gap (3.37 eV [1]), direct band-to-band transitions, and low resistivity; all these special features of ZnO make it possible to use this material for manufacturing LEDs [2], transparent contacts, and solar cell windows [3]. Depending on the crystal structure and the defect composition of ZnO films, it is possible to obtain structures with an intense emission band at $\lambda = 375$ nm within the exciton recombination region. Because of the high binding energy of an exciton in ZnO (60 meV), the corresponding luminescence band appears even at room temperature and above up to $T = 550$ K [4, 5]. Lasing was observed in the films produced on sapphire by molecular beam epitaxy and pumped by the third harmonic of a Nd:YAG laser (355 nm) [4, 5].

Stimulated emission from the epitaxial ZnO films was attained for the first time in [6], where it was associated with electron–hole plasma (EHP) recombination. The mechanism behind the stimulated emission of radiation in ZnO requires the effective radiative band-to-band recombination of optically excited photons and holes. This is only possible with a sufficiently high crystal purity and small violations in the stoichiometry of ZnO layers. Crystal defects of any kind, such as point intrinsic and impurity defects, are the competing centers of radiative and nonradiative recombination of excited charge carriers, thus, reducing the population inversion in the layer. Because of this, most of the data mentioned above was obtained for ZnO epitaxial films

grown by molecular beam epitaxy on (0001) crystalline sapphire substrates. Stimulated emission was also detected from the films grown on sapphire by the pulsed laser deposition technique [7]. Both methods yield nearly single-crystal ZnO films with a smooth surface, which essentially favors the onset of the lasing mode in them. However, the use of sapphire substrates prohibits the design of electrically pumped LEDs. The arbitrary choice of the film thickness ranging from 70 to 1000 nm in the studies mentioned above led either to the absence of longitudinal lasing modes or to multimode lasing. Narrow peaks (0.5 nm), which are present in the lasing region [5, 7], suggest the onset of lasing only within a separate single-crystal grain (of size 50–70 nm) of the ZnO film with the Fabry–Perot interference observed at its boundaries.

In this study, we investigate the feasibility of attaining stimulated emission from optically pumped polycrystalline ZnO layers produced on amorphous substrates by the conventional magnetron deposition technique. Using structures of a poorer quality required compensation of the optical losses in specially constructed ZnO–SiO$_2$–Si-type nanocavities with optimal thicknesses of the layers, which allowed an increase in the Q factor by more than an order of magnitude. The ZnO polycrystalline films on amorphous substrates with prevailing band-to-band radiative transitions hold the most promise for practical applications motivated by the search for the optimal conditions of their growth. Along with a low concentration of impurities, such conditions should also imply the effective crystallization of the deposited films as a result of their annealing. The point is that magnetron deposition provides layers with the proper stoichiometry combined with a nearly amorphous structure. Amorphous ZnO features the complete

Minimal thicknesses of the ZnO layer necessary for the existence of the type-III coupled modes

Number of type-III modes, N	1	2	3	4
d_3, μm	0.16	0.31	0.47	0.63

absence of radiative electron–hole recombination. However, annealing in air at 800°C enables one to obtain polycrystalline films with a 50- to 60-nm grain size, a smooth surface, and effective luminescence in the exciton ultraviolet (UV) spectral region.

EXPERIMENTAL

ZnO films 250- to 400-nm-thick were formed at 350°C by magnetron deposition from ZnO tablets using a Z-400 system. Pressed zinc oxide powder was used as the target, and the deposition rate amounted to 1.5–2 Å/s. As substrates, we used polished plates from (111) single-crystal thermally oxidized silicon. The amorphous silicon oxide layer had a thickness of 500 nm. Photoluminescence (PL) was excited by a nitrogen laser ($\lambda = 337.1$ nm, pulse duration 600 ps, peak power $I_0 = 0.23$ MW) within a rectangular light spot 1×3 mm^2 and was detected at room temperature. A computer-controlled MDR-6 double monochromator with an angular aperture of 0.1 was used to analyze the PL spectra at different pump powers and at different angles θ between the film surface and the bundle of optical fibers. The entrance slits used in the experiment ensured a spectral resolution no worse than 1 meV. The resulting film structure and the surface morphology were studied using a Jeol-2000 transmission electron microscope. X-ray analysis of the films was performed using a DRON-2 diffractometer and Cr radiation.

THREE-LAYER CAVITY.
THEORETICAL BACKGROUND

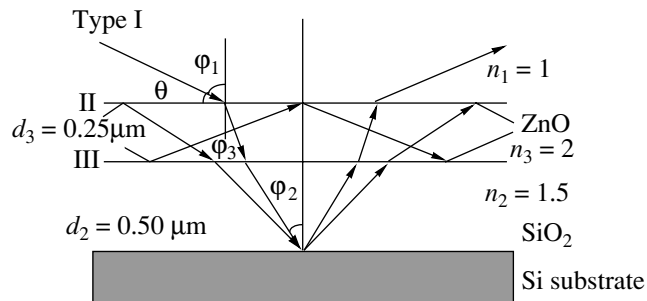The schematic diagram of the optically pumped lasing structure is shown in Fig. 1. Amplification of the

Fig. 1. Lasing in the optically pumped nanostructure. n_1, n_2, and n_3 are the respective refractive indices of the layers; d_2 and d_3 are the respective layer thicknesses.

longitudinal coupled mode in the ZnO layer (the refractive index $n_3 = 2$) was presumed, which requires the presence of insulating (nonabsorbing) layers on both sides of the film. In our case, they were silicon oxide (with the refractive index $n_2 = 1.5$) and air ($n_1 = 1$). In order to promote lasing, it is desirable that only one coupled mode (type III) should be present in the zinc oxide film, while the intensities of the modes coupled in two layers (type II) and the intensity of the radiative modes (type I) should be decreased using Fabry–Perot interference in the three-layer air–ZnO–SiO$_2$ structure. A considerable difference in the refractive indices of the layers (in contrast to the case of deposition on a sapphire substrate) implies effective reflection from the interfaces and interference between the waves that entered the ZnO layer.

We will now consider in more detail the condition for the presence of only one mode (type III) in the lasing layer. Such a condition implies that the phase incursion per one passage of the reflected beam should be a multiple of π,

$$N\pi = (2\pi/\lambda)n_3 d_3 \cos\varphi_3 + \chi_{31} + \chi_{32}, \qquad (1)$$

where d_3 is the zinc layer thickness; and χ_{31} and χ_{32} are the phase shifts, which, because of the total internal reflection from the film boundaries, depend on the refractive indices and the angle of incidence φ_3 [8]. At the same time, the total internal reflection limits the minimal angle of incidence φ_3^0 for a given wavelength λ by the angle of total internal reflection from the ZnO–SiO$_2$ interface, which is defined as $\sin\varphi_3^0 = n_2/n_3 = 3/4$. The minimal ZnO layer thicknesses required for the presence of a certain number of type-III coupled modes were calculated for $\lambda = 400$ nm and are listed in the table. It should be noted that a similar calculation for the air–ZnO interface predicts the presence of two coupled modes in ZnO layers with a thickness of 0.24 μm or greater. In our case, the additional coupled mode (type II) penetrates into the silicon oxide layer (Fig. 1). Since the perpendicular component of the wavevector could not comply with the resonance condition in both the zinc and silicon oxide layers at the same time, its intensity is essentially lower than that of the other mode (type III), which propagates in the ZnO layer only.

The interference quenching of the radiative modes (type I) implies minimization of the interference for the beams with a wavelength of 400 nm (photon energy of 3.12 eV) propagating in the direction perpendicular to the interfaces, i.e., along the Z axis. This condition is satisfied when the doubled sum of the optical path lengths for the zinc and silicon oxide layers is equal to an odd number of half-waves:

$$n_2 d_2 + n_1 d_1 = (2N + 1)\lambda/2. \qquad (2)$$

The correctness of this method for calculations of the quenching of the radiative modes in the structure was verified by measuring the reflection spectra of the incandescent lamp light for the different angles of incidence.

RESULTS

Figure 2 shows the reflection spectra obtained for a ZnO–SiO₂–Si structure with a 0.25-μm-thick ZnO layer for different angles of incidence φ in the range from 10° to 90°. Since we expect lasing on the mode stemming from the radiative recombination of EHP λ = 397 nm ($h\nu$ = 3.12 eV), let us take a closer look at the interference within the corresponding spectral range. The interference in the multilayer structure is distinct. It is important for us that, for the angles of 60°, 70°, 80°, and 90° (i.e., on approaching the normal incidence), the interference pattern displays a minimum with the energy $h\nu$ = 3.12 eV. This fact is indicative of the antiphase summation of the reflected and transmitted signals. In the same manner, the antiphase summation takes place for the reflected and transmitted parts of the radiative mode (type I), which means the fulfillment of quenching condition (2). According to the table, there is only one coupled mode of type III in the 0.25-μm-thick ZnO layer.

The structure was pumped with the nitrogen laser beam (337.1 nm) normal to the surface, and the emitted light was detected at an angle of θ = 0° to the surface (Fig. 3). It is clearly seen that, with an increase in the pump power, the intensity of the 3.12-eV line related to the electron–hole plasma grows considerably. The other peak close to 3.25 eV represents the line of exciton luminescence at room temperature. It is interesting to note that the spectral position of the stimulated luminescence from EHP is practically the same when observed at different angles θ, while the position of the exciton peak in the spectrum of the spontaneous photoluminescence is angle-dependent (Fig. 4a). Another point to be noted is the close correlation between the short-wavelength shifts that the exciton emission peak and the Fabry–Perot interference peaks in the reflection spectra (Fig. 2) exhibit with increasing detection angle. The dependences of the intensities of the exciton and EHP luminescence bands on the optical pump power are also of different character (Fig. 4b). Thus, for the exciton band peaked at $h\nu$ = 3.25 eV (curve *1*), the deviation of the dependence from the linear law is small and can be attributed to the interference effect. In contrast, the enhancement of the EHP line with a peak at $h\nu$ = 3.12 eV (curve *2*) is evidently nonlinear for the power densities exceeding 5.5 MW/cm². The increase in the intensity of the EDP line by nearly two orders of magnitude indicates the onset of stimulated luminescence and optical amplification of light at λ = 397 nm ($h\nu$ = 3.12 eV).
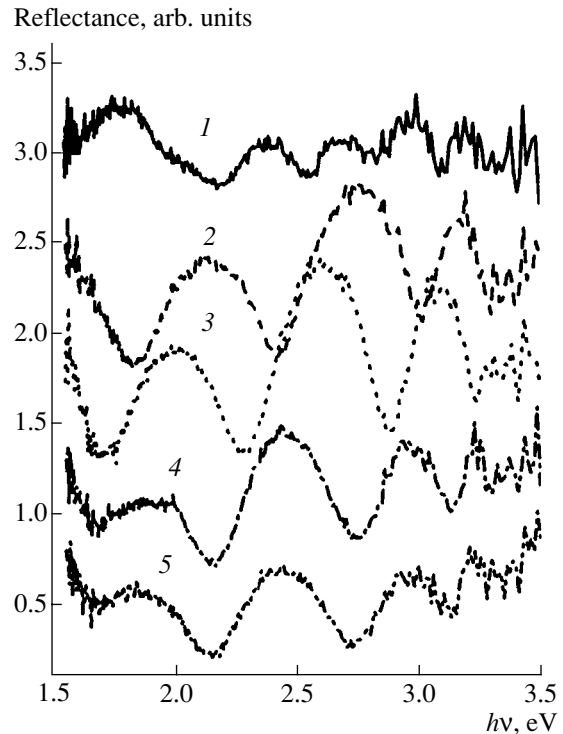

Fig. 2. Reflection spectra for a ZnO–SiO₂–Si structure with a 0.25-μm-thick ZnO layer for different angles of incidence φ to the film surface: (*1*) 10°, (*2*) 30°, (*3*) 50°, (*4*) 70°, and (*5*) 90°. *T* = 300 K.
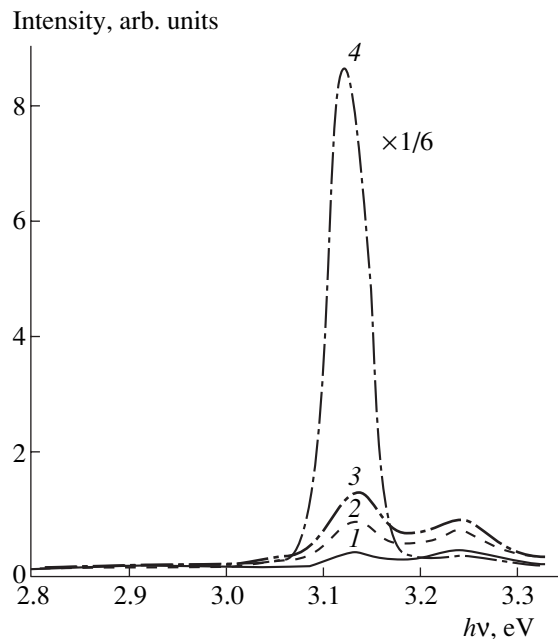

Fig. 3. Photoluminescence spectra detected at the angle θ = 0° to the surface for different pump powers: (*1*) 0.4I_0, (*2*) 0.6I_0, (*3*) 0.71I_0, and (*4*) I_0. *T* = 300 K.
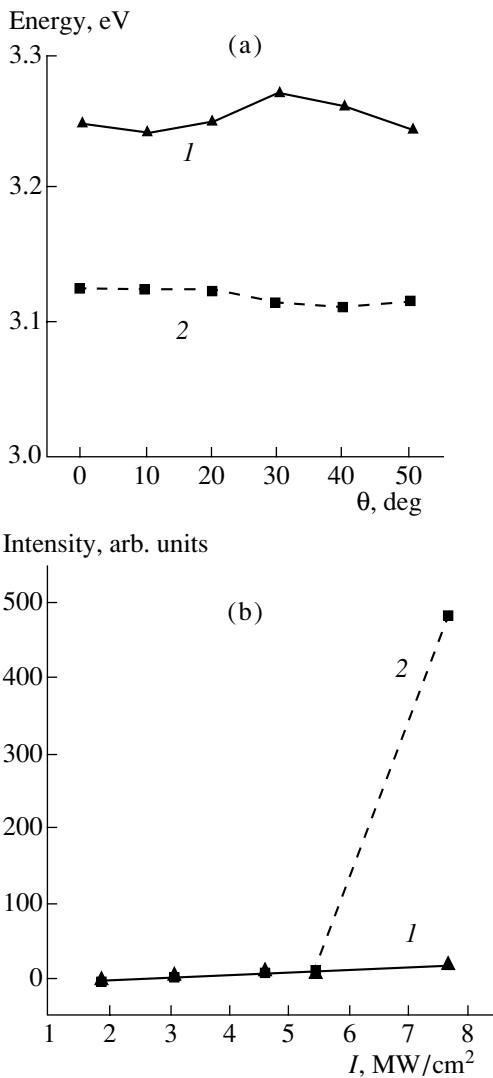
Energy, eV

(a)

Fig. 4. (a) Spectral positions of (*1*) the exciton lumines-
cence lines and (*2*) EHP luminescence versus the detection
angle θ and (b) the intensity of (*1*) exciton luminescence
lines and (*2*) EHP luminescence versus the average pump
power (*I*) of the nitrogen laser at *T* = 300 K.

DISCUSSION

According to the experimental results presented
above, a laser line with a peak at 3.12 eV and a half-
width of 45 meV is stimulated in a ZnO–SiO$_2$–Si struc-
ture by optical pumping with a power of 5.5 MW/cm^2
or higher. Because of the small thickness of the ZnO
film (0.25 μm), there is only one coupling mode (type
III) that exists in the film. It is exactly this mode that
turns out to be amplified. The possibility of a single-
pass amplification at the interfaces in the Fabry–Perot
interferometer should be ruled out, since the reflection
spectrum measured at normal incidence (Fig. 2) dis-
plays a minimum at *hν* = 3.12 eV, whereas there should
be a peak in the case of this amplification. Moreover, no
lasing was observed in a similar structure with a

0.4-μm-thick ZnO layer, in which there was a maxi-
mum of the Fabry–Perot interference for the EHP line.
The reason for this is that the radiative modes of type I,
which enhance the losses, were not suppressed. An
increase in the layer thickness gave rise to another cou-
pled mode of type III (see table), thus, leading to an
increase in the lasing threshold. The possibility of
observing the stimulated luminescence at different
angles to the film may be explained by both an intensive
scattering of light by polycrystals in the zinc-oxide film
and a large diffraction angle (λ/d_s = 1.6 rad or 100°) of
the light leaving the faces of the structure. Transmission
microscopy and X-ray diffraction revealed 100- to
150-nm-large polycrystals in the films. The interfaces
were found to be optically smooth with a roughness
smaller than 10 nm.

In the case under consideration, the small thickness
of the ZnO film is favorable for the onset of lasing due
to the presence of only one coupled mode and the
absence of spread of the excited carriers from the
region where the optical pump radiation is absorbed
(0.1–0.2 μm). The use of the surrounding layers (air
and silicon oxide) with low absorption coefficients not
only allowed a decrease in the thickness of the lasing
layer but also resulted in a considerable decrease in the
angle of total internal reflection, which, in turn, reduced
the spatial angle of the output of the radiative modes
and the related optical losses. Another consequence of
the considerable difference in the refractive indices of
the lasing and the surrounding layers is the significant
enhancement of interference between the radiative
modes (Fig. 2), which enables one to lower their inten-
sity still further by varying the layer thicknesses. As a
result, most of the radiation from EHP is forced into a
single coupled mode in ZnO, thus, giving rise to optical
amplification.

CONCLUSION

For the first time, lasing was obtained from nonepi-
taxial ZnO layers produced by magnetron deposition
onto an amorphous substrate. Choosing the parameters
of a three-layer ZnO–SiO$_2$–Si nanocavity, we managed
to compensate for the moderate crystal quality of the
luminescent layer used in experiment. It is demon-
strated that the use of similar structures consisting of
layers with widely different refractive indices is benefi-
cial for the production of population inversion and opti-
cal amplification. Fundamental differences in the opti-
cal properties of these structures should be noted in
comparison with those of LED conventional hetero-
structures, which are based on solid solutions with
almost the same optical properties.

REFERENCES

1. Y. Chen, D. M. Bagnall, Z. Zhu, *et al.*, J. Cryst. Growth **181**, 165 (1997).

2. Y. R. Ray, W. J. Kim, and H. W. White, J. Cryst. Growth **219**, 419 (2000).

3. J. R. Tuttle, M. A. Contreras, T. J. Gillespie, *et al.*, Prog. Photovoltaics Res. Appl. **3**, 235 (1995).

4. D. M. Bagnall, Y. F. Chen, Z. Zhu, and T. Yao, Appl. Phys. Lett. **73**, 1038 (1998).

5. D. M. Bagnall, Y. F. Chen, M. Y. Shen, *et al.*, J. Cryst. Growth **184–185**, 605 (1998).

6. P. Zu, G. K. Tang, K. L. Wong, *et al.*, Solid State Commun. **103**, 459 (1997).

7. P. Yu, K. Tang, K. L. Wong, *et al.*, J. Cryst. Growth **184–185**, 601 (1998).

8. *Integrated Optics*, Ed. by T. Tamir (Springer-Verlag, Berlin, 1975), p. 344.

Translated by A. Sidorova-Biryukova

PHYSICS
OF SEMICONDUCTOR DEVICES

Photoelectric Properties of p^+–n Junctions Based on 4H-SiC Ion-Implanted with Aluminum

G. N. Violina*, E. V. Kalinina**, G. F. Kholujanov**, G. A. Onushkin**, V. G. Kossov***,
R. R. Yafaev***, A. Hallén****, and A. O. Konstantinov*****

* St. Petersburg State University of Electrical Engineering, St. Petersburg, 197376 Russia
** Ioffe Physicotechnical Institute, Russian Academy of Sciences,
Politekhnicheskaya ul. 26, St. Petersburg, 194021 Russia
e-mail: evk@pop.ioffe.rssi.ru
*** Elektron Optronik, St. Petersburg, 194223 Russia
**** Royal Institute of Technology, Department of Electronics, Electrum 229, SE 164 40 Kista, Sweden
***** ACREO AB, Electrum 236, SE 164 40 Kista, Sweden

Abstract—The photoelectric properties of p^+–n junctions that were based on 4H-SiC ion-implanted with aluminum and were formed in lightly doped n-type epitaxial layers grown by chemical vapor deposition were studied. It is shown that such photodetectors combine in full measure the advantages of photostructures formed on the basis of Schottky barriers and epitaxial p–n junctions. The results of the theoretical calculation of spectral characteristics of ion-implanted photodetectors are in good agreement with experimental data. The structures feature an efficiency of collection of nonequilibrium charge carriers close to 100% in the spectral range of the photon energies of 3.5–4.25 eV. © 2002 MAIK "Nauka/Interperiodica".

1. INTRODUCTION

The fact that SiC has a wide band gap makes this material promising for the development of SiC-based photodetectors for the ultraviolet region of the spectrum. In addition, special features of this material such as high thermal and radiation resistance enhance the dependability of operation of such devices even in extreme conditions. In earlier studies, the photodetector structures involving Schottky barriers or p–n junctions were formed on the basis of 6H-SiC crystals grown by the Lely method [1–3] or on the basis of sublimation-epitaxy layers grown on these crystals [4]. High doping levels and a large number of defects were responsible for the short lifetimes of nonequilibrium charge carriers in the structures under consideration and for the inevitably small areas of these structures, which brought about a decrease in detector efficiency. Detectors based on p–n junctions can operate under the most severe conditions and are, thus, of particular interest. However, if the p-type regions are formed by conventional methods (diffusion, epitaxy, and doping in the course of growth), layers with high acceptor concentrations cannot be obtained owing to the limited solubility of acceptors in SiC. This brings about an increase in the resistance of the detector structures and a decrease in the efficiency of detection. However, it is well known that a nonequilibrium method for doping (ion implantation) makes it possible to obtain p^+-type layers with an acceptor concentration exceeding the solubility limit of the corresponding impurities in SiC; these layers do not

introduce additional resistance in the structures with p–n junctions [5].

Progress made recently in the technology of producing high-quality single-crystal SiC makes it possible to obtain high-purity epitaxial SiC layers with low concentrations of deep-level centers and with diffusion lengths of minority charge carriers of about 5 μm, which enables one to study the photodetector properties of SiC structures at a much higher level. In this paper, we report the results of studying the photoelectric characteristics of p^+–n structures produced using the ion implantation of Al into 4H-SiC epitaxial layers obtained by chemical-vapor deposition (CVD).

2. EXPERIMENTAL

The 25-μm-thick n-4H-SiC epitaxial CVD films with a concentration of uncompensated donors $N_d - N_a = (3–5) \times 10^{15}$ cm^{-3} were grown on commercial n-4H-SiC substrates with $N_d - N_a = 10^{19}$ cm^{-3}. The p^+–n structures were formed using the implantation of Al ions with an energy of $E_{Al} = 150$ keV and at a dose of $Q_{Al} = 5 \times 10^{16}$ cm^{-2}. After implantation, the samples were subjected to thermal-activation annealing for 15 s at $T = 1700°C$ [6]. Ohmic contacts to the n- and p-SiC layers were formed by vacuum deposition of Cr and transparent Al films, respectively. Aluminum served as a mask in the course of forming a mesa structure 300 μm in diameter using ion-plasma etching.

The depth of the Al location in the p^+–n junctions formed by ion implantation was determined using a scanning electron microscope (SEM) with the electron beam being scanned over the cleaved surface of a structure with the p^+–n junction. The diffusion length of minority charge carriers, i.e., of holes in the n-type region (L_p), was determined using a SEM and conventional processing of the signal of the electron-beam-induced current (EBIC). These data were compared with those obtained from the dependence of the photocurrent on reverse voltage; this dependence was measured under the conditions of the quasi-uniform irradiation of the sample. The concentration profile for electrically active impurities in the p^+–n-junction region was determined from the capacitance–voltage (C–V) characteristics. The current–voltage (I–V) characteristics of the p^+–n structure were measured at the forward (in the region of low current density < 200 A/cm^2) and reverse biases in the temperature range $T = 20$–500°C.

The spectral characteristic of photosensitivity was studied in the photon-energy range $h\nu = 2.8$–5.6 eV at room temperature using an MDR-3 monochromator. A DKsSh-200 xenon lamp was used as the excitation source. Luminous flux modulated by a mechanical chopper was focused onto the entrance slit of the monochromator. The signal was measured using a V6-9 narrow-band voltmeter.

3. RESULTS

According to the results of the SEM measurements, the p^+–n-junction depth was about $x_{pn} = 0.6$ μm. Conventional processing of the EBIC signal made it possible to determine the diffusion length of holes ($L_p = 4$–5 μm) in the n-type region adjoining the p^+–n junction [6]. The diffusion length of holes in the starting n-4H-SiC layers was determined from the dependence of the photocurrent for the Schottky barriers on the width of the space-charge region (SCR) using the method outlined in [7]; we obtained $L_p = 2$ μm, which was in good agreement with data reported in [6]. As can be seen, the values of L_p that we obtained are no smaller (in fact, are even somewhat larger) than L_p in the starting material. This experimental fact is indicative of an improvement in the structural quality of the starting epitaxial material in the vicinity of the p^+–n junction formed using implantation of Al ions with subsequent high-temperature heat treatment [8].

Experimental results of studying the dependence of photocurrent on reverse voltage are shown in Fig. 1 in the form of a plot of photocurrent (I_{ph}) versus the SCR width (δ_{SCR}). As can be seen, this dependence is linear, which is consistent with the following expression derived in [7] for the case of quasi-uniform irradiation of the sample:

$$I_{ph} \propto \alpha F(L_p + L_n + \delta_{SCR}). \qquad (1)$$

Here, α is the absorption coefficient; F is the number of photons incident on the unit surface area per unit time;
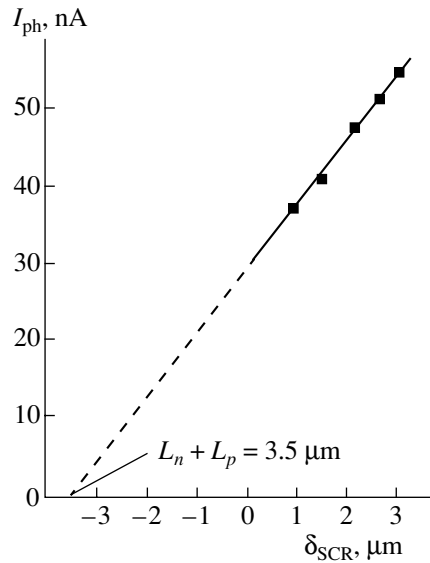

Fig. 1. Photocurrent (I_{ph}) in p^+–n junctions ion-implanted with Al as a function of the width of the space-charge region (δ_{SCR}).

and L_p and L_n are the diffusion lengths of holes and electrons, respectively. Extrapolation of the experimental straight line to the zero value of photocurrent yields $L_p + L_n = 3.5$ μm, which is close to the value of L_p determined previously using the conventional processing of the EBIC signal; this can be attributed to the relatively small contribution of the carriers collected from the thin p^+-type layer to the photocurrent.

The C–V characteristics of p–n junctions under investigation obeyed the $(1/C_{br})^n \propto U_{rev}$ law, where C_{br} is the barrier capacitance and U_{rev} is the reverse voltage. For voltages with an absolute value smaller than 10 V, we had $n = 3$; i.e., the distribution of the electrically active impurity in the region of p^+–n junction was almost smooth (Fig. 2, region 1). For larger absolute values of reverse voltage, the form of the dependence of the barrier capacitance on reverse voltage changed ($n < 3$) (Fig. 2, region 2). This is probably related to special features of the redistribution of implanted Al in 4H-SiC as a result of high-temperature annealing. The use of a model of the gradient p^+–n junction made it possible to estimate the strength of the built-in electric field (ε_{pn}) in the regions adjoining the junction; we use this estimate in the calculations below.

The I–V characteristics of the studied p^+–n junctions were measured under forward biases for current densities as high as 10 A/cm^2 in the temperature range of 20–500°C. In a wide range of voltages, these characteristics obeyed the classical law $J \approx J_0 \exp(qU/\beta kT)$, where q is the elementary charge and β is a coefficient characterizing the mechanism of the current flow. The value of β varied in the range of 1.2–2, which is related to the contribution of thermally stimulated recombination currents to the total current [9].

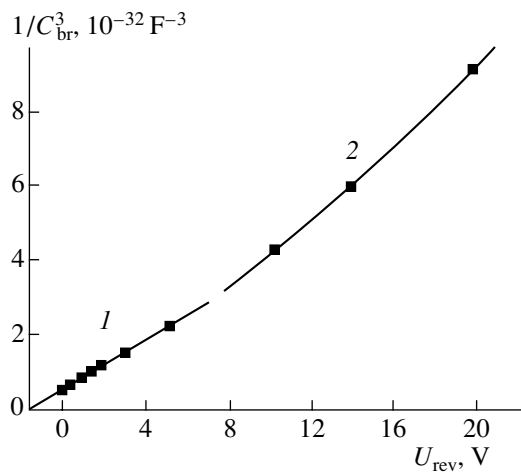$1/C_{br}^3$, 10^{-32} F^{-3}

Fig. 2. A capacitance–voltage characteristic of p^+–n structure implanted with Al ions.
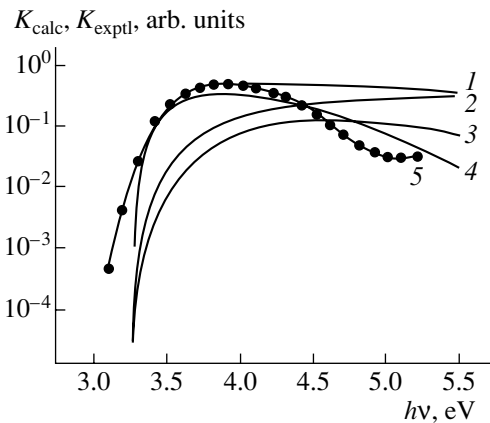
K_{calc}, K_{exptl}, arb. units

Fig. 3. Experimental (*5*) and calculated (*1–4*) spectral characteristics of photosensitivity of p^+–n structures implanted with Al ions. Curve (*1*) represents the total efficiency of the charge-carrier collection; curves (*2*), (*3*), and (*4*) correspond to the efficiencies of charge-carrier collection in the *p*-type region, in the space-charge region, and in the *n*-type region, respectively.

The junction periphery was not specially protected; reverse currents lower than 10^{-7} A were observed for reverse voltages of 20–30 V at a temperature of 20°C. At a temperature of 500°C, reverse currents lower than 10^{-6} A were observed for bias voltages as high as 10 V.

The obtained experimental spectral characteristics of photosensitivity are shown in Fig. 3 (curve *5*) in relative units normalized to an equal number of photoactive quanta.

4. CALCULATIONS AND DISCUSSION

We based our calculations on the method outlined in [10]. In that paper, it was suggested that the efficiency of collection of nonequilibrium charge carriers K be used as the parameter characterizing the spectral sensi-

tivity of *p–n* structures. The use of this method seems to be justified since the measured photocurrent varies linearly with the excitation intensity F; i.e.,

$$I_{ph} \propto qF(1 - R)K, \qquad (2)$$

where R is the reflection coefficient and K is the efficiency of collection of nonequilibrium charge carriers. The excitation intensity was varied in the range of 10^{13}–10^{16} photon/(cm^2 s).

In what follows, we represent K as

$$K = K_n + K_p + K_{pn}, \qquad (3)$$

where K_n is the efficiency of electron collection in the *p*-type region, K_p is the efficiency of hole collection in the *n*-type region, and K_{pn} is the efficiency of charge-carrier collection in the SCR.

When calculating the efficiency of collection of non-equilibrium charge carriers in the ion-implanted *p–n* structures under investigation, we considered a gradient *p–n* junction in accordance with the data shown in Fig. 2. In calculations, we took into account the effects of the built-in field, the volume recombination in the *n*- and *p*-type regions of the structure, and the charge-carrier collection in the SCR.

In calculations, we used the following experimental parameters of the structure: the junction depth $x_{pn} = 0.6$ μm; the SCR width $\delta_{SCR} = 0.5$ μm (at $U = 0$ V); and the diffusion length of the minority charge carriers in the *n*-type region $L_p = 3.5$ μm, which corresponds to the hole lifetime $t_p \approx 10^{-8}$ s. The use of the model of a gradient *p–n* junction allowed us to estimate the strength of the built-in electric field at $\varepsilon_{pn} \approx 10^2$ V/cm. In calculations, the surface-recombination velocity s was varied in the range of 10^3–10^6 cm/s. These variations do not have an appreciable effect on the features of the spectrum. The calculated spectral dependences of the collection efficiencies obtained for $s = 10^4$ cm/s are shown in Fig. 3 (curves *1–4*). As can be seen, the calculation results are in good agreement with experimental data (Fig. 3, curve *5*). According to our calculations, the total efficiency of collection of photogenerated charge carriers in the structure under investigation (the internal quantum yield) is close to 100% in the photon-energy range of 3.5–4.25 eV. The calculation of collection-efficiency components shows that the collection of holes in the *n*-type region is dominant at low photon energies 3.2–4.0 eV (in the region of the quasi-uniform irradiation of the sample) (Fig. 3, curve *4*).

It is well known that the lifetime of minority charge carriers in SiC increases by an order of magnitude as the temperature increases from 20 to 500°C [9]. According to preliminary data, the short-circuit photocurrent increases by a factor of 10–15 as the temperature increases in the above range; at the same time, the open-circuit voltage decreases by three to five times. According to the measurements of electrical characteristics at various temperatures, the studied structures

with the above-described ohmic contacts retained their operating capacity and did not degrade at temperatures as high as 500°C. Therefore, one may expect that the sensitivity of photodetectors based on ion-implanted p^+–n junctions is not reduced at these temperatures.

5. CONCLUSION

Thus, we obtained the following important results.

(i) According to the results of calculations, which are in good agreement with experimental data, the efficiency of collection of the minority charge carriers (i.e., the internal quantum yield) in the structure under investigation is close to 100% in the photon-energy range $h\nu = 3.5$–4.25 eV.

(ii) We observed an increase in the hole diffusion length (L_p) in the n-4H-SiC CVD-grown layers if p–n junctions were formed in these layers using Al-ion implantation.

(iii) It is shown that such p^+–n junctions show the greatest promise for high-temperature detectors of ultraviolet radiation: they combine the merits of epitaxial SiC-based p–n photodetectors [11, 12] with those of the detectors based on Cr–n-SiC Schottky barriers [4]. Varying the energy of the implanted Al ions, and thus optimally bringing the p–n junction closer to the surface, one can ensure that the spectral photosensitivity is similar to that of the Cr–n-SiC Schottky barriers.

(iv) It is expected that the photosensitivity of the structures under consideration does not degrade at temperatures as high as 500°C because the ohmic contacts can reliably operate at these temperatures.

ACKNOWLEDGMENTS

REFERENCES

1. G. F. Kholuyanov, Fiz. Tverd. Tela (Leningrad) **2**, 1909 (1960) [Sov. Phys. Solid State **2**, 1722 (1961)].
2. G. N. Violina and G. F. Kholuyanov, Radiotekh. Élektron. (Moscow) **11**, 2034 (1966).
3. P. Glosow, G. Ziegler, W. Suttrop, *et al.*, Proc. SPIE **868**, 40 (1988).
4. R. G. Verenchikova and V. Ya. Sankin, Pis'ma Zh. Tekh. Fiz. **14** (19), 1742 (1988) [Sov. Tech. Phys. Lett. **14**, 756 (1988)].
5. E. V. Kalinina, A. V. Suvorov, and G. F. Kholuyanov, Fiz. Tekh. Poluprovodn. (Leningrad) **14** (6), 1099 (1980) [Sov. Phys. Semicond. **14**, 652 (1980)].
6. E. Kalinina, G. Kholujanov, V. Solov'ev, *et al.*, Appl. Phys. Lett. **77** (19), 3051 (2000).
7. V. S. Ballandovich, O. A. Omar, and V. A. Popov, Izv. Leningr. Élektrotekh. Inst. im. V. I. Ul'yanova **250**, 20 (1979).
8. E. Kalinina, G. Kholujanov, V. Solov'ev, *et al.*, in *Proceedings of the E-MRS Spring Meeting 2001, Strasbourg, France, 2001*, F-VI.2.
9. A. M. Strel'chuk, Fiz. Tekh. Poluprovodn. (St. Petersburg) **29** (7), 1190 (1995) [Semiconductors **29**, 614 (1995)].
10. G. F. Kholuyanov, Fiz. Tekh. Poluprovodn. (Leningrad) **3** (5), 658 (1969) [Sov. Phys. Semicond. **3**, 560 (1969)].
11. D. M. Brown, E. T. Downey, M. Ghezzo, *et al.*, IEEE Trans. Electron Devices **40** (2), 325 (1993).
12. J. A. Edmond, H. S. Kong, and S. H. Carter, Jr., Phys. Rev. B **185**, 453 (1993).

Translated by A. Spitsyn

Silicon Carbide Detectors of High-Energy Particles

G. N. Violina*, E. V. Kalinina**, G. F. Kholujanov**, V. G. Kossov***,
R. R. Yafaev***, A. Hallén****, and A. O. Konstantinov*****

* St. Petersburg State University of Electrical Engineering, St. Petersburg, 197376 Russia

** Ioffe Physicotechnical Institute, Russian Academy of Sciences,
Politekhnicheskaya ul. 26, St. Petersburg, 194021 Russia

e-mail: evk@pop.ioffe.rssi.ru

*** Elektron Optronik, St. Petersburg, 194223 Russia

**** Royal Institute of Technology, Department of Electronics, Electrum 229, SE 164 40 Kista, Sweden

***** ACREO AB, Electrum 236, SE 164 40 Kista, Sweden

Submitted November 29, 2001; accepted for publication December 4, 2001

Abstract—The results of studying $4H$-SiC p^+–n junctions ion-implanted with aluminum as detectors of high-energy particles are reported. The junctions were formed in SiC epitaxial films grown by chemical vapor deposition. The concentration of uncompensated donors was $(3–5) \times 10^{15}$ cm^{-3}, and the charge-carrier diffusion length was $L_p = 2.5$ µm. The detectors were irradiated with 4.8–5.5-MeV alpha particles at 20°C. The efficiency of collection of the induced charge was as high as 0.35. The possibilities of operating SiC detectors at elevated temperatures (~500°C) are analyzed. © 2002 MAIK "Nauka/Interperiodica".

INTRODUCTION

Silicon carbide is one of the most promising of the wide-gap semiconductors which have high electric and mechanical strength, high thermal stability, and high radiation resistance. Taking into account this unique combination of properties, SiC can be used for the production of electron devices that can operate under extreme conditions, i.e., at high temperatures and high radiation levels and in aggressive media. The promising potential for using the SiC-based p^+–n junctions as the basis for the development of high-temperature detectors and spectrometers of high-energy particles was demonstrated even in early studies of silicon carbide and is confirmed at present. Previously, alpha-particle detectors for the reliable detection of high-energy particles at temperatures as high as 500°C were fabricated on the basis of single-crystal SiC grown by the Lely method [1–3]. However, high concentrations of defects in the Lely crystals were responsible for the short lifetimes of nonequilibrium charge carriers due to the recombination processes and brought about a low efficiency of the counting-rate characteristics of the detectors. The high concentrations of defects in the Lely crystals and the small sizes of these crystals prohibited the fabrication of large-area devices, which also resulted in the lowering of the efficiency of detectors of high-energy particles. In addition, the relatively high concentrations of uncompensated donors in the Lely crystals gave no way of extending the region of collection of nonequilibrium charge carriers so that the width of this region would be comparable with the alpha-particle range, which drastically lowered the collection efficiency. Recently, due to progress in the technology of growing high-purity epitaxial layers of SiC of different polytypes with low concentrations of defects, it became possible to appreciably enhance the efficiency of detectors of high-energy particles [4, 5].

Another important problem in the fabrication of SiC-based devices is related to the fact that it is impossible to form low-resistivity p-type material using conventional equilibrium methods for doping since the acceptor concentration cannot be higher than that governed by the solubility limit in SiC. This gives rise to high resistances of both contacts and the structures formed, which reduces the operation efficiency of the devices. However, a nonequilibrium method for doping of semiconductors is known; this method involves ion implantation, which makes it possible to introduce an impurity in amounts exceeding the corresponding limit of solubility in a material. Using the doping of n-6H-SiC with ion-implanted Al with subsequent high-temperature annealing, Kalinina *et al*. [6] managed to obtain p^+-type layers which did not introduce additional resistance into the structures with p^+–n structures.

Currently, it is of indubitable interest to consider the potentialities of SiC fast-particle counters based on currently available higher quality SiC and on ion-implantation doping.

EXPERIMENTAL

The p^+–n structures to be studied were formed on the basis of n-4H-SiC epitaxial layers grown by chemical vapor deposition (CVD) on commercial n-4H-SiC substrates. The substrates had a concentration of

uncompensated donors equal to $N_d - N_a \approx 10^{19}$ cm^{-3}. The CVD epitaxial layers were 26 µm thick and had $N_d - N_a = (3-5) \times 10^{15}$ cm^{-3}. In order to study the CVD epitaxial layers, we used thermal evaporation to form Schottky barriers with Cr on these layers. The structures with p^+–n junctions were formed using the implantation of 150-keV Al ions at a dose of 5×10^{16} cm^{-2}. We then annealed the samples for 15 s at 1700°C in an Ar atmosphere in order to activate the implanted impurity. Ohmic contacts were formed by vacuum deposition of Al and Cr/Al on the p- and n-type regions, respectively. Diode structures with areas of 10^{-3} and 4×10^{-3} cm^2 were formed using ion-plasma etching, with Al serving as the mask. In order to obtain detector structures with low leakage currents, we etched the periphery of p^+–n junctions using an alkali melt at the final stage of the technological process.

The samples were irradiated with 4.8–5.5-MeV alpha particles at 20°C. The detector signal was preliminarily amplified and was then recorded using conventional spectrometric equipment. The energy calibration of the channels was performed using a silicon reference counter. The energy interval per channel was 2.85 keV.

Diffusion lengths L_p of minority charge carriers (holes in the n-type region) in the initial CVD layer and after formation of p^+–n junctions were determined using a scanning electron microscope (SEM) and the conventional method for signal processing of the signal of the electron-beam-induced current (EBIC). The depth of ion-implanted p^+–n junctions was determined from the SEM measurements performed on the cleaved surface of the structure.

Data on the electrical parameters of the detector structures were obtained from an analysis of the current–voltage (I–V), capacitance–voltage (C–V), and photoelectric characteristics of p^+–n junctions in the temperature range from 20 to 500°C. The measurement methods and a detailed consideration of the aforementioned characteristics were reported in [7].

RESULTS AND DISCUSSION

In Fig. 1, we show the counting-rate characteristics of structures with ion-implanted p^+–n junctions; these characteristics were measured at a reverse voltage of 390 V and a temperature of 20°C. As can be seen, the detected signal is observed within the channel-number range of 520–900. The number of detected events per unit time did not exceed 2–3 per second, which was probably caused by the small areas of the structures under investigation. The fourfold increase in the area of the structures resulted in an increase in the number of counts to 10–12; i.e., a linear dependence of the number of detected events on the detector area was observed.

The background level in the counters under investigation was extremely low (about 1 count/s), which, taking into account the low leakage currents in the p^+–n junction, indicated that there was no "dead window" in the
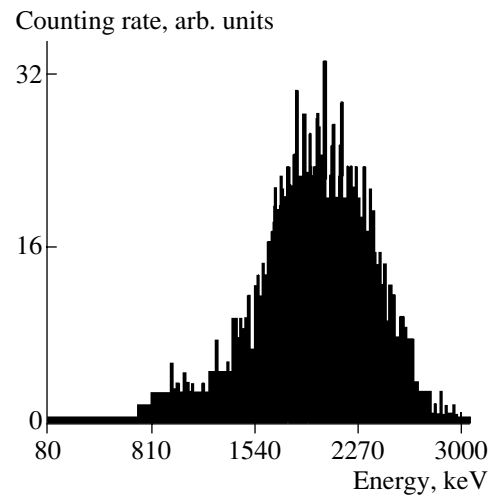

Fig. 1. The counting-rate characteristics of 4*H*-SiC structures doped using implantation of Al ions.

structure, which is similar to what is observed in the detectors based on Schottky barriers.

Taking into account that there is 2.2 keV per channel, we can see that the efficiency of collection of the induced charge (r) in the structures under investigation is no higher than 0.35. It is noteworthy that the increase in the reverse voltage at the p^+–n junction from 0 to 390 V brought about an increase in the collection efficiency from 0.22 to 0.35. We now consider the causes of a decrease in the efficiency of collection of induced charge in the structure under consideration.

It is known that the efficiency of collection of induced charge in the detectors in which the range of a high-energy particle corresponds to the width of the sensitive region W is given by

$$r = \frac{\mu\tau V_r}{W^2}\left[1 - \exp\left(-\frac{W^2}{\mu\tau V_r}\right)\right],$$

where τ is the charge-carrier lifetime, μ is the effective mobility of the charge carriers, and V_r is the reverse voltage applied to the p^+–n structure.

The diffusion length of charge carriers in the starting epitaxial layer was equal to $L_p \approx 2.5$ µm. The diffusion length of holes in the CVD layer increased to $L_p \approx 5$ µm after the formation of p^+–n junctions as a result of the implantation of Al ions [8]. The lifetime of charge carriers amounts to $\tau = 10^{-7}$ s for the above values of the diffusion length. The width of the space-charge region (SCR) in the studied p^+–n structures varied in the range from 1–1.5 to 7–10 µm when the reverse voltage was changed from 0 to 400 V. Let us assume that the effective mobility of charge carriers (holes) in the collection region is equal to $\mu = 0.01$ m^2 V^{-1} s^{-1}.

Taking into account the parameters of the studied p^+–n structures, we have $W^2/\mu\tau V_r \ll 1$, so that almost all the charge induced within W should be collected; i.e.,
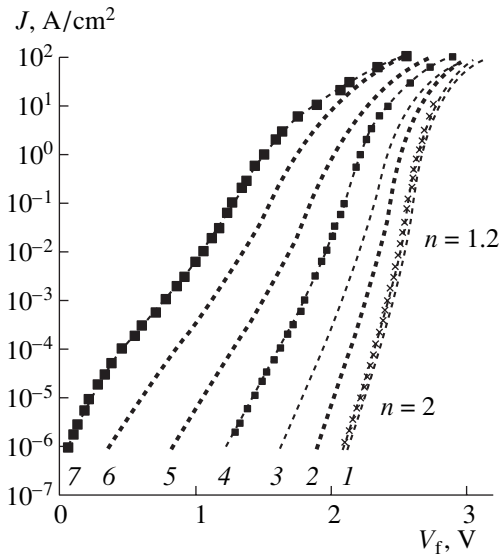
Fig. 2. The forward current–voltage characteristics of 4*H*-SiC structures implanted with Al ions at temperatures of (*1*) 300, (*2*) 342, (*3*) 391, (*4*) 476, (*5*) 561, (*6*) 676, and (*7*) 781 K.

we should have $r = 1$. However, experimentally we observed $r < 1$, which may be caused by several factors. First, according to our estimates, the range of alpha particles was not equal to the SCR width in the structures under consideration. Unfortunately, there are no data available on the range of high-energy particles in SiC. However, we can roughly estimate this parameter using the data on the ranges of high-energy particles in Si and C. The range of alpha particles in these materials varies from 3.27 to 25.46 μm when the alpha-particle energy changes from 1 to 5.5 MeV. Evidently, the range of the 4.8- to 5.5-MeV alpha particles used in this study exceeded the SCR width in the investigated p^+–n structures even if the highest reverse voltage (390 V) was applied. We might also mention another factor which tends to decrease the experimental value of the charge-collection efficiency in the detector; this factor is the limitation of the detected signal due to the series resistance of the base in the p^+–n structure.

In view of the above, the experimental data we obtained seem to be quite encouraging. They suggest that it is possible to fabricate detectors of high-energy particles on the basis of the current technology of SiC.

Let us evaluate the potentialities of the suggested detectors from the standpoint of operation temperatures. Unfortunately, the counting-rate characteristics in a wide temperature range have not been studied; this remains to be done. Nevertheless, we can indirectly assess the potentialities of SiC-based p^+–n structures by analyzing the temperature dependences of the measured I–V characteristics. In Fig. 2, we show the forward portions of I–V characteristics for ion-implanted p^+–n structures in the temperature range of 20–500°C. As can be seen, the base resistance of the p^+–n junction

decreases with increasing temperature. Thus, the effect of this factor limiting the carrier-collection efficiency in the detector becomes less profound with increasing temperature. Furthermore, as has been shown previously, the lifetimes of charge carriers in SiC increase with increasing temperature [9]. Taking into account the aforesaid, we may conclude that the carrier-collection efficiency in the ion-implanted p^+–n structures may increase as the temperature increases from 20 to 500°C.

Let us assess the properties of SiC detectors with respect to the temperature dependence of the reverse I–V characteristic. Tests of the counters showed that they reliably detected the particle if the reverse currents in the structures I_r were no higher than 10^{-8} A. At $T = 20°C$, the studied structures had $I_r \lesssim 10^{-8}$ A for absolute values of reverse voltage as large as ~400 V. These reverse currents exceed by many orders of magnitude the generation currents in the SiC-based p^+–n junctions and represent the surface and bulk leakage currents. The I_r currents increased with increasing temperature, and, as was shown previously, the I_r currents of $\approx 10^{-8}$ A in similar structures were observed at 250°C under the reverse bias of 100 V [10].

Thus, the behavior of I–V characteristics of the ion-implanted SiC-based p^+–n junctions in a wide temperature range suggests that it is possible to use current high-quality SiC in the fabrication of high-temperature detector structures aimed at detecting high-energy particles.

CONCLUSION

It is shown that n-4*H*-SiC epitaxial films lightly doped using the implantation of Al ions can be used for the formation of structures with shallow p^+–n junctions designed for the detection of high-energy particles (~5 MeV). These structures combine the almost complete absence of a dead layer with reliable operation in the temperature range from 20 to 500°C.

ACKNOWLEDGMENTS

REFERENCES

1. C. P. Capera, P. Malinaric, R. B. Campbell, and J. Ostroski, IEEE Trans. Nucl. Sci. **11** (6), 262 (1964).
2. G. F. Kholuyanov and B. V. Gavrilovskiĭ, Fiz. Tekh. Poluprovodn. (Leningrad) **2** (4), 573 (1968) [Sov. Phys. Semicond. **2**, 472 (1968)].

3. V. A. Tikhomirova, O. P. Fedoseeva, and G. F. Kholu-yanov, Fiz. Tekh. Poluprovodn. (Leningrad) **6** (5), 957 (1972) [Sov. Phys. Semicond. **6**, 831 (1972)].

4. A. A. Lebedev, N. S. Savkina, A. M. Ivanov, *et al.*, Fiz. Tekh. Poluprovodn. (St. Petersburg) **34** (2), 249 (2000) [Semiconductors **34**, 243 (2000)].

5. G. Violina, P. Shkrebiĭ, E. Kalinina, *et al.*, in *Proceedings of the III International Workshop "Silicon Carbide and Related Materials", Novgorod, 2000*, p. 213.

6. E. V. Kalinina, A. V. Suvorov, and G. F. Kholuyanov, Fiz. Tekh. Poluprovodn. (Leningrad) **14** (6), 1099 (1980) [Sov. Phys. Semicond. **14**, 652 (1980)].

7. E. Kalinina, G. Kholujanov, V. Solov'ev, *et al.*, Appl. Phys. Lett. **77** (19), 3051 (2000).

8. E. Kalinina, G. Kholujanov, V. Solov'ev, *et al.*, in *Proceedings of the E-MRS Spring Meeting 2001, Strasbourg, France, 2001*, F-VI.2.

9. A. M. Strel'chuk, Fiz. Tekh. Poluprovodn. (St. Petersburg) **29** (7), 1190 (1995) [Semiconductors **29**, 614 (1995)].

10. Yu. A. Vodakov, K. D. Dumakov, E. V. Kalinina, *et al.*, Fiz. Tekh. Poluprovodn. (Leningrad) **21** (9), 1685 (1987) [Sov. Phys. Semicond. **21**, 1017 (1987)].

Translated by A. Spitsyn

PHYSICS
OF SEMICONDUCTOR DEVICES

Waveguide InGaAsP/InP Photodetectors for Low-Power Autocorrelation Measurements at 1.55 μm

**N. Yu. Gordeev^, L. Ya. Karachinsky, I. I. Novikov, A. V. Lyutetsky,
N. A. Pikhtin, N. V. Fetisova, I. S. Tarasov, and P. S. Kop'ev**

*Ioffe Physicotechnical Institute, Russian Academy of Sciences,
Politekhnicheskaya ul. 26, St. Petersburg, 194021 Russia*
^ e-mail: gordeev@switch.ioffe.rssi.ru

Abstract—Two-photon absorption of 1.55 μm light in quantum-well InGaAs/InP laser heterostructures has been studied. The highest achieved nonlinear response was 0.78 nA/mW^2. The minimum detectable peak power of 60 μW allows for the effective use of waveguides of this type as detectors in optical autocorrelators for studying temporal characteristics of low-power signals. © *2002 MAIK "Nauka/Interperiodica"*.

1. INTRODUCTION

Correlation techniques have long been used to measure the parameters of ultrashort light pulses [1]. These methods replace the conventional stroboscopic techniques in studying pulses in the subpicosecond and femtosecond ranges [1]. Measurements of autocorrelation functions rely upon the nonlinearity of the detector, which can be ensured by such effects as second harmonic generation [2], two-photon fluorescence [3], and two-photo absorption [4]. The two-photon absorption is a nonresonant nonlinear process involving photons with energy $h\nu$ lower than the energy gap E_g of a semiconductor, but exceeding $E_g/2$. For photons with such energies, the probability of single-photon absorption is exceedingly low. When high-intensity light is incident on a semiconductor, an electron can be excited into the conduction band as a result of successive absorption of two photons. In this case, a transiting electron occupies, for a certain time, a virtual level in the band gap [5]. The condition for electron transition to this level is momentum conservation, and the electron lifetime at the level is governed by the Heisenberg uncertainty principle [6].

In the case when light with energy $h\nu$ such that $E_g/2 < h\nu < E_g$ is incident on the semiconductor, virtually all the generated nonequilibrium carriers result from two-photon absorption. This can be ascertained by measuring the photocurrent, since the dependence of the photocurrent on incident power will be quadratic in the case when two-photon absorption is predominant over linear absorption. As a result, the given mechanism can be used in the autocorrelation technique together with other mechanisms, such as second harmonic generation. Of fundamental importance is the use of waveguide structures, since the longer path of light in the waveguide, compared with that in a planar device, greatly enhances absorption [7]. It is the effect of two-photon absorption in a semiconductor waveguide

that has been successfully used for studying the temporal characteristics of injection semiconductor lasers (see, e.g., [8, 9]). In particular, superradiation pulses from InGaAs/InP lasers (emission wavelength 1.3 μm) were studied in [10], both above and below the lasing threshold, using an optical autocorrelator with AlGaAs/GaAs waveguide as nonlinear detector.

The aim of this study was to develop a waveguide photodetector operating on the two-photon absorption principle at a wavelength of 1.55 μm, which made it possible to record signals with a peak power of ~1 mW.

2. EXPERIMENT

For the present study, we used quantum-well separate-confinement InGaAs/InP heterostructures (λ = 1.3 μm) grown by liquid-phase epitaxy (structure 1) [11] and metal-organic vapor-phase epitaxy (structures 2 and 3) [12]. It should be noted that a record-breaking continuous-wave emission power was obtained with wide-stripe lasers fabricated on the basis of these structures [12, 13]. Our investigations have shown that structures 2 and 3 possess high internal quantum efficiency of stimulated emission (90%) and low internal optical loss (~3 cm^{-1}) [14]. Structure 1 had a single unstrained InGaAsP quantum well (QW) 300 Å thick and a 0.6-μm-thick waveguide. In structures 2 and 3, the active region comprised two strained QWs (with a compression strain of 1%) each 50 Å thick. The waveguide thicknesses were 0.6 and 0.72 μm in structures 2 and 3, respectively.

To study two-photon absorption, we fabricated, on the basis of these structures, samples whose design was similar to that of single-mode "shallow-mesa" lasers with stripe width W = 5 μm [15]. The waveguide length was 350 μm (structure 1) and 1000 μm (structures 2 and 3). For effective coupling of light into the waveguide,

samples were mounted on a heat sink in such a way that their front part projected beyond the heat sink limits. On the whole, the technique used for sample mounting on the heat sink was the same as in the case of laser crystals, which made it possible to pass forward current through the samples, i.e., to use them as an emission source.

The use of laser structures as a detector in an optical autocorrelator makes the process of its alignment much simpler, since a possibility arises of adjusting the auto-correlator in the inverse mode [9]. The basic concept of the given method consists in using the nonlinear photo-detector as an emission source in the initial stage of alignment, whereas the laser under study is a linear waveguide photodetector. Further alignment is done in the normal mode to achieve the highest photocurrent in the two-photon photodetector.

The two-photo absorption in waveguides was measured on the setup shown in Fig. 1. A single-mode injection laser (*1*) with an emission wavelength of 1.55 μm was used as the emission source. The driving current was quasi-continuous (pulse duration 10 μs, pulse repetition frequency 7 kHz). The intensity of light incident on the photodetector (*2*) was attenuated with a polarizer (*P*). The waveguide under study was attached to a three-axis positioning device with a minimum displacement step of 0.5 μm. The photocurrent was recorded with a Unipan 232B lock-in nanovoltmeter (*3*). It should be noted that all photodetectors were studied without applying reverse bias. This lowered the electric noise level and thereby improved the signal-to-noise ratio. The already mentioned inverse mode was used for the adjustment of the experimental setup.

3. RESULTS AND DISCUSSION

The efficiency of two-photon absorption in a semiconductor waveguide is commonly evaluated by such a parameter as nonlinear response. This parameter is defined as the coefficient of the quadratic term in the nonlinear dependence of the photocurrent in the waveguide on the power of light incident on the waveguide edge [16] and has the dimensionality [current]/[power]^2.

The dependence of the photocurrent on the power of incident light is presented in Fig. 2. As the dependence is nonlinear, it is conveniently plotted on the log–log scale. For the structures studied, the nonlinear response varied rather widely, with minimum and maximum values of 4.5×10^{-3} and 0.78 nA/mW^2, respectively. These values are in agreement with those observed previously in structures of the same kind [16].

At relatively high (~1 W) and ultralow (~1 mW) peak power values, the use of waveguides is restricted by the considerable fraction of linear absorption. The nature of this effect has not yet been clearly accounted for [16]. Apparently, the lower limit of light power at which a photodetector can be used is determined,
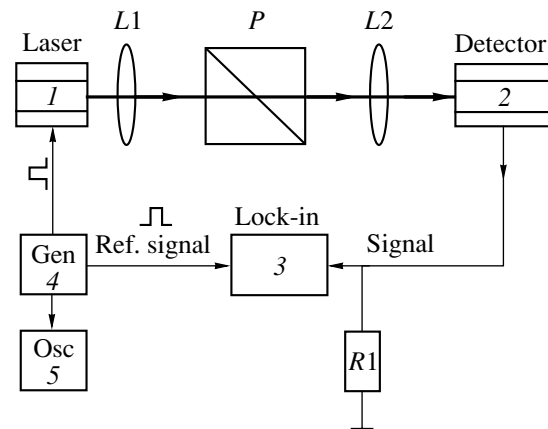

Fig. 1. Setup for studying the two-photon absorption. (*1*) Laser diode, (*2*) waveguide InGaAsP photodetector operating on the two-photon absorption principle, (*L*1, *L*2) lenses, (*P*) polarizer, (*3*) lock-in nanovoltmeter, (*4*) square-wave generator, (*5*) oscilloscope, and (*R*1) measuring resistor.
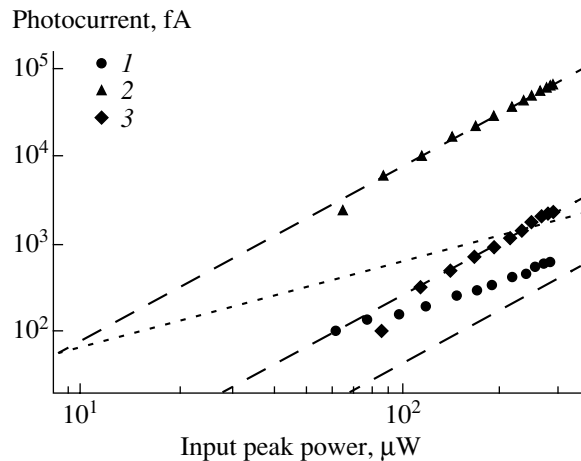

Fig. 2. Dependence of photocurrent on incident light power in the case of two-photon absorption in the waveguide InGaAs/InP heterostructure. Structure numbers are indicated. The quadratic component is shown for each structure (dashed lines); for structure 2 the linear component is also presented (dotted line). The nonlinear response for structure nos. 1–3 is 4.5×10^{-3}, 0.78, and 3.4×10^{-2} nA/mW^2, respectively.

firstly, by its nonlinear response, i.e., by the photocurrent produced, and, secondly, by the relative contributions of nonlinear and linear absorption. The best values were obtained for a waveguide structure with two QWs in the active region. In this case, the minimum detectable peak power immediately in front of the photodetector was 60 μW. It should be noted that the real power fed into the waveguide is, at the very most, no higher than this value. The use of a positioning device with a smaller displacement step, e.g., of the piezoelectric type, can improve the efficiency of light coupling into the waveguide. Extrapolation of the dependence of

the photocurrent to the input power (Fig. 2) for structure 2 shows that the linear absorption is lower than the nonlinear absorption down to powers on the order of 10 μW. No direct relationship between the design of the active region and the coefficient of nonlinear absorption was revealed. In structures with similar active regions, the coefficients differed by more than an order of magnitude. We believe that this circumstance can be accounted for by the presence of defects and impurities in the active region and in the waveguide as a whole, since the relative fraction of linear absorption becomes higher at lower total photocurrent.

4. CONCLUSION

The two-photon absorption of 1.55 μm light has been studied in a set of InGaAs/InP laser heterostructures with QWs. It was found that the considerable fraction of linear absorption at low emission power leads to a significant decrease in the total photocurrent. It is shown that the nonlinear absorption component may exceed the linear component down to ~10 μW. The minimum detectable peak power may be as low as 60 μW.

The results obtained enable the use of the investigated structures as nonlinear photodetectors in an optical autocorrelator for studying the fine temporal structure of emission from LEDs, superluminescent diodes, and laser diodes at a wavelength of 1.55 μm.

ACKNOWLEDGMENTS

REFERENCES

1. J. Herrman and B. Wilhelmi, *Lasers für Ultrakurze Lichtempulse* (Akademie-Verlag, Berlin, 1984; Mir, Moscow, 1986).
2. H. P. Weber, J. Appl. Phys. **38**, 2231 (1967).
3. J. A. Giordmaine, P. M. Rentzepis, S. L. Shapiro, and K. W. Wecht, Appl. Phys. Lett. **11**, 216 (1967).
4. Y. Takagi, T. Kobayashi, K. Yoshihara, and S. Imamura, Opt. Lett. **17**, 658 (1992).
5. H. N. Spector, Phys. Rev. B **35**, 5876 (1987).
6. A. Miller, D. A. B. Miller, and S. D. Smith, Adv. Phys. **30**, 697 (1981).
7. F. R. Laughton, J. H. Marsh, D. A. Barrow, and E. L. Portnoi, IEEE J. Quantum Electron. **30**, 838 (1994).
8. H. K. Tsang, L. Y. Chan, J. B. D. Soole, *et al.*, Electron. Lett. **31**, 1773 (1995).
9. A. M. Georgievskiĭ and S. V. Zaĭtsev, Prib. Tekh. Éksp. **39**, 132 (1996).
10. S. V. Zaitsev and A. M. Georgievski, Jpn. J. Appl. Phys. **36**, 4209 (1997).
11. A. V. Ovchinnikov, Author's Abstract of Candidate's Dissertation (Leningrad, 1988).
12. E. G. Golikova, V. A. Gorbylev, N. Yu. Davydyuk, *et al.*, Pis'ma Zh. Tekh. Fiz. **26** (6), 5 (2000) [Tech. Phys. Lett. **26**, 225 (2000)].
13. D. Z. Garbuzov, S. E. Goncharov, Yu. V. Il'in, *et al.*, in *Proceedings of the ISFOC, Leningrad, 1991*, Vol. 1, p. 144.
14. A. Yu. Leshko, A. V. Lyutetskiĭ, N. A. Pikhtin, *et al.*, Fiz. Tekh. Poluprovodn. (St. Petersburg) **34**, 1457 (2000) [Semiconductors **34**, 1397 (2000)].
15. E. G. Golikova, V. A. Gorbylev, Yu. V. Il'in, *et al.*, Pis'ma Zh. Tekh. Fiz. **26** (7), 57 (2000) [Tech. Phys. Lett. **26**, 295 (2000)].
16. D. T. Reid, W. Sibbett, J. M. Dudley, *et al.*, Engineering and Laboratory Notes, Suppl. to Optics and Photonics (OSA) **9**, 8142 (1998).

Translated by M. Tagirdzhanov